APPLIED COMPUTATIONAL ELECTROMAGNETICS SOCIETY JOURNAL

February 2022
Vol. 37 No. 2
ISSN 1054-4887

The ACES Journal is abstracted in INSPEC, in Engineering Index, DTIC, Science Citation Index Expanded, the Research Alert, and to Current Contents/Engineering, Computing & Technology.

The illustrations on the front cover have been obtained from the ARC research group at the Department of Electrical Engineering, Colorado School of Mines

Published, sold and distributed by: River Publishers, Alsbjergvej 10, 9260 Gistrup, Denmark

FEBRUARY 2022 REVIEWERS

Marco Arjona
Alireza Baghai-Wadji
Mohammad Sajjad Bayati
Aysu Belen
Amir Boag
Syed Sabir Hussain Bukhari
Nunzia Fontana
Piotr Gas
Zi He
Bernhard J. Hoenders
Shian Hwu
Fatih Kaburcuk
I. Kathir
Erhan Kurt
Brian LaRocca
Wang-Sang Lee
Yang Liu
Fabrizio Loreto
Biswa Binayak Mangaraj
Adam Mock
Kumutha N.
Mahdi Oliaei
Mirjana Peric
Cheng Qian
Alain Reineix
Thennarasan Sabapathy
Leonardo Sandrolini
Sayidmarie
Abhishek Sharma
Kouji Shibata
Marsellas Waller
Guanjun Xu
Abubakar Yakubu
Yujuan Zhao

THE APPLIED COMPUTATIONAL ELECTROMAGNETICS SOCIETY JOURNAL

Vol. 37 No. 2 February 2022

TABLE OF CONTENTS

Formulation of Iterative Finite-Difference Method for Generating Large Spatially Variant Lattices

Manuel F. Martinez[1], Jesus J. Gutierrez[1], Jimmy E. Touma[2], and Raymond C. Rumpf[1]

[1]Department of Electrical and Computer Engineering,
University of Texas at El Paso, El Paso, TX 79968, USA
mfmartinez4@miners.utep.edu, jjgutierrez4@utep.edu, rcrumpf@utep.edu

[2]Air Force Research Laboratory, Integrated Sensing and Processing,
Eglin Air Force Base, Eglin, FL 32542, USA
jimmy.touma.1@us.af.mil

Abstract – A new numerical method to generate spatially variant lattices (SVLs) is derived and implemented. The algorithm proposed solves the underlying partial differential equations iteratively with an update equation derived using the finite-difference method to obtain an SVL that is continuous, smooth, and free of unintended defects while maintaining the unit cell geometry throughout the lattice. This iterative approach is shown to be more memory-efficient when compared to the matrix-based approach and is, thus, suitable for the calculation of large-scale SVLs. The iterative nature of the solver allows it to be easily implemented in graphics processing unit to parallelize the computation of SVLs. Two spatially variant self-collimating photonic crystals are generated and simulated to demonstrate the functionality of the algorithm as a tool to generate fully three-dimensional photonic devices of realistic size.

Keywords – Iterative finite-difference method, functionally graded, metamaterials, photonic crystals, spatial variance.

I. INTRODUCTION

Self-collimating photonic crystals (SCPCs) are devices in which an electromagnetic wave travels through a volume of material without any diffraction and only moves along an axis of the lattice regardless of angle of incidence [1]. Attempts to control power flow inside these structures in an arbitrary manner in 3D SCPCs have been limited to the introduction of defects or deformations [2], which often weaken or destroy the overall electromagnetic properties of the SCPC. Spatial variance is a process to spatially adjust the geometrical aspects of periodic structures like photonic crystals (PhCs) [3]. The algorithm for spatial variance introduces geometrical changes to the PhC in a way that makes the PhC smooth, continuous, and free of unintentional defects [4] while retaining the geometry of the unit cells so that electromagnetic response is maintained. Most approaches to incorporate spatial variance in SCPCs [5–7] do so in either planar SCPCs or with devices in which the third dimension is not spatially varied. The method described in [3] suffers from the major drawback of being memory inefficient due to its reliance on large full storage matrices and computationally expensive lower–upper (LU) decomposition operations, thus limiting the size of spatially variant lattices (SVLs) that can be generated. Although other methods such as Galerkin, Crank-Nicolson, and Fourier methods [8] exist to solve partial differential equations, these run into the similar drawbacks of memory inefficiency when solving large problems. The present body of work discusses the formulation of an iterative algorithm to compute SVLs based on similar approaches to those used in electromagnetic simulation tools such as the finite-difference time-domain (FDTD) method, in which an update equation is used to explicitly solve the underlying system of partial differential equations point-by-point throughout the problem space [9]. Approaches with similar formulations to the one presented in this body of work have been successfully implemented with the use of general purpose graphics processing units (GPGPUs) to accelerate and scale execution [10].

II. GENERATION OF SPATIALLY VARIANT LATTICES

In this section, the step-by-step description of the overall algorithm to generate SVLs is presented. The first two subsections discuss the mathematical background of spatially variant gratings and SVLs. The following subsections define the steps necessary to calculate an SVL using the iterative algorithm as well as presenting the flow-diagram of the proposed algorithm.

Submitted On: August 31, 2021
Accepted On: February 8, 2022

https://doi.org/10.13052/2022.ACES.J.370201

A. Spatially variant planar gratings and lattices

Consider a simple sinusoidal grating described by a grating vector $\vec{K}$. The grating vector has a direction perpendicular to the planes of the grating and has a magnitude of $2\pi/\Lambda$, where Λ is the period of the grating. Given a grating vector, the sinusoidal grating is calculated by

$$\varepsilon_a(\vec{s}) = \cos(\vec{K} \bullet \vec{s}), \tag{1}$$

where $\vec{s} = x\hat{a}_x + y\hat{a}_y + x\hat{a}_z$ and $\varepsilon_a(\vec{s})$ is called the analog grating because of its continuous variation between the values of -1 and 1.

When attributes of the grating such as period or the orientation are spatially varied, the grating vector $\vec{K}$ becomes a function of position. When this happens, $\vec{K}$ becomes $\vec{K}(\vec{s})$ and the calculation in eqn (1) fails to properly compute the analog grating [3]

$$\varepsilon_a(\vec{s}) \neq \cos\left[\vec{K}(\vec{s}) \bullet \vec{s}\right]. \tag{2}$$

Spatial variance is incorporated through an intermediate parameter called the grating phase $\Phi(\vec{s})$ [3]. The equation shown in eqn (3) is solved numerically through a best fit approach of least squares since there are more equations than unknowns. Then, the analog grating can be calculated by eqn (4)

$$\nabla\Phi(\vec{s}) = \vec{K}(\vec{s}), \tag{3}$$

$$\varepsilon_a(\vec{s}) = \cos\left[\Phi(\vec{s})\right]. \tag{4}$$

To extend the functionality of eqn (3) and (4) from planar gratings to general lattices, Rumpf [3] states that the unit cell that describes the periodic structure to be spatially varied is decomposed into a complex Fourier series. Each term in the Fourier series is a spatial harmonic that can be interpreted as a one-dimensional planar grating. Given the infinite nature of Fourier transforms, this complex series is truncated to only a finite set of M planar gratings. Each planar grating in the truncated series is spatially varied and the overall SVL is obtained by summing each 1D grating.

B. A general solution for $\nabla\Phi(\vec{s}) = \vec{K}(\vec{s})$

Rumpf [3] presented a matrix-based numerical solution for the expression in eqn (3) in the framework of least squares with the use of $[A]^{-1}[b] = [x]$. This implementation is a brute force approach that provides fast and accurate results for small-sized problems. The issue with this approach to the solution arises when large-scale lattices are being generated since the $[A]^{-1}[b] = [x]$ is a matrix problem that increases memory and computational requirements. This poor scaling with larger lattices leads to a hard-set limit of the size of lattice that can be computationally generated.

III. ITERATIVE SOLUTION TO $\nabla\Phi(\vec{s}) = \vec{K}(\vec{s})$

A. The update equation

The derivation of the fundamental equations to iteratively generate SVLs begins by expanding the expression to be solved in eqn (3) into Cartesian coordinates

$$\frac{\partial\Phi(\vec{s})}{\partial x} + \frac{\partial\Phi(\vec{s})}{\partial y} + \frac{\partial\Phi(\vec{s})}{\partial z} = K_x(\vec{s})\hat{a}_x + K_y(\vec{s})\hat{a}_y + K_z(\vec{s})\hat{a}_z. \tag{5}$$

This vector equation can be separated into three independent scalar equations by setting the vector components on each side of the equation equal

$$\frac{\partial\Phi(\vec{s})}{\partial x} = K_x(\vec{s}), \tag{6}$$

$$\frac{\partial\Phi(\vec{s})}{\partial y} = K_y(\vec{s}), \tag{7}$$

$$\frac{\partial\Phi(\vec{s})}{\partial z} = K_z(\vec{s}). \tag{8}$$

For brevity, the following formulation focuses on eqn (6) as the basic building block for the update equation and then applied by inspection to the other equations. Eqn (6) can be approximated by a central finite-difference to the $i-1$ side or a central finite-difference to the $i+1$ side

$$\frac{\Phi|_{i,j,k} - \Phi|_{i-1,j,k}}{\Delta x} = \frac{K_x|_{i,j,k} + K_x|_{i-1,j,k}}{2} i - 1. \tag{9}$$

$$\frac{\Phi|_{i+1,j,k} - \Phi|_{i,j,k}}{\Delta x} = \frac{K_x|_{i+1,j,k} + K_x|_{i,j,k}}{2} i + 1. \tag{10}$$

Solving eqn (9) and (10) for $\Phi|_{i,j,k}$ results in

$$\Phi|_{i,j,k} = \frac{\Phi|_{i-1,j,k} + \Phi|_{i+1,j,k}}{2} + \frac{\Delta x}{4}(K_x|_{i-1,j,k} - K_x|_{i+1,j,k}). \tag{11}$$

In order to generate the grating phase term iteratively, eqn (11) needs to be interpreted as an update equation, where a new term of $\Phi|_{i,j,k}$ is calculated at each iteration based on an old value of $\Phi|_{i,j,k}$ at a previous iteration. Then, eqn (11) is written as

$$\Phi_{\text{new}}|_{i,j,k} = \frac{\Phi_{\text{old}}|_{i-1,j,k} + \Phi_{\text{old}}|_{i+1,j,k}}{2} + \frac{\Delta x}{4}(K_x|_{i-1,j,k} - K_x|_{i+1,j,k}). \tag{12}$$

Observing eqn (12), this problem consists of a system with more equations than unknowns. It is not possible to satisfy this system of equations exactly to obtain $\Phi_{\text{new}}|_{i,j,k}$. Instead, a least-squares approach was used to solve this system of equations. To incorporate the least-squares framework into eqn (12), three error terms are included in the formulation that should be minimized

$$\begin{aligned}
\Phi_{\text{new}}|_{i,j,k} &= \frac{\Phi_{\text{old}}|_{i-1,j,k} + \Phi_{\text{old}}|_{i+1,j,k}}{2} + \frac{\Delta x}{4}(K_x|_{i-1,j,k} - K_x|_{i+1,j,k}) + \varepsilon_1. \\
\Phi_{\text{new}}|_{i,j,k} &= \frac{\Phi_{\text{old}}|_{i,j-1,k} + \Phi_{\text{old}}|_{i,j+1,k}}{2} + \frac{\Delta y}{4}(K_y|_{i,j-1,k} - K_y|_{i,j+1,k}) + \varepsilon_2. \\
\Phi_{\text{new}}|_{i,j,k} &= \frac{\Phi_{\text{old}}|_{i,j,k-1} + \Phi_{\text{old}}|_{i,j,k+1}}{2} + \frac{\Delta z}{4}(K_z|_{i,j,k-1} - K_y|_{i,j,k+1}) + \varepsilon_3.
\end{aligned} \tag{13}$$

Solving for each error term in eqn (13) yields

$$\begin{aligned}
\varepsilon_1 &= \Phi_{\text{new}}|_{i,j,k} - \frac{\Phi_{\text{old}}|_{i-1,j,k} + \Phi_{\text{old}}|_{i+1,j,k}}{2} - \frac{\Delta x}{4}(K_x|_{i-1,j,k} - K_x|_{i+1,j,k}). \\
\varepsilon_2 &= \Phi_{\text{new}}|_{i,j,k} - \frac{\Phi_{\text{old}}|_{i,j-1,k} + \Phi_{\text{old}}|_{i,j+1,k}}{2} - \frac{\Delta x}{4}(K_x|_{i,j-1,k} - K_x|_{i,j+1,k}). \\
\varepsilon_3 &= \Phi_{\text{new}}|_{i,j,k} - \frac{\Phi_{\text{old}}|_{i,j,k-1} + \Phi_{\text{old}}|_{i,j,k+1}}{2} - \frac{\Delta x}{4}(K_x|_{i,j,k-1} - K_x|_{i,j,k+1}).
\end{aligned} \tag{14}$$

In the least-squares framework, the overall error metric E to minimize is defined as

$$E = \varepsilon_1^2 + \varepsilon_2^2 + \varepsilon_3^2. \tag{15}$$

To minimize the error in eqn (15), the first-derivative rule is used, resulting in

$$0 = \frac{d}{d\Phi_{\text{new}}|_{i,j,k}}(\varepsilon_1^2 + \varepsilon_2^2 + \varepsilon_3^2). \tag{16}$$

Incorporating the error term into eqn (14)

$$\begin{aligned}
&\Phi_{\text{new}}|_{i,j,k} = \\
&\frac{1}{3}[\frac{\Phi_{\text{old}}|_{i-1.j,k} + \Phi_{\text{old}}|_{i+1,j,k}}{2} + \frac{\Delta x}{4}(K_x|_{1-1,j,k} - K_x|_{1+1,j,k})] \\
&+ \frac{1}{3}[\frac{\Phi_{\text{old}}|_{i,j,-1,k} + \Phi_{\text{old}}|_{i,j+1,k}}{2} + \frac{\Delta x}{4}(K_x|_{1,j-1,k} - K_x|_{1,j+1,k})] \\
&+ \frac{1}{3}[\frac{\Phi_{\text{old}}|_{i,j,k-1} + \Phi_{\text{old}}|_{i,j,k+1}}{2} + \frac{\Delta x}{4}(K_x|_{1,j,k-1} - K_x|_{1,j,k+1})].
\end{aligned} \tag{17}$$

Comparing the terms inside the square brackets in eqn (17) to eqn (12) shows that solving the system of equations in eqn (17) by least squares is the same as calculating the arithmetic mean of the value of $\Phi_{\text{new}}|_{i,j,k}$ generated by solving eqn (12) individually. Therefore, the calculation for $\Phi_{\text{new}}|_{i,j,k}$ can be written as

$$\Phi_{\text{new}}|_{i,j,k} = \frac{\Phi_x|_{i,j,k} + \Phi_y|_{i,j,k} + \Phi_z|_{i,j,k}}{3} \tag{18}$$

where

$$\begin{aligned}
\Phi_x|_{i,j,k} &= \frac{\Phi_{\text{old}}|_{i-1,j,k} + \Phi_{\text{old}}|_{i+1,j,k}}{2} \\
&+ \frac{\Delta x}{4}(K_x|_{i-1,j,k} - K_x|_{i+1,j,k}). \\
\Phi_y|_{i,j,k} &= \frac{\Phi_{\text{old}}|_{i,j-1,k} + \Phi_{\text{old}}|_{i,j+1,k}}{2} \\
&+ \frac{\Delta y}{4}(K_y|_{i,j-1,k} - K_y|_{i,j+1,k}). \\
\Phi_z|_{i,j,k} &= \frac{\Phi_{\text{old}}|_{i,j,k-1} + \Phi_{\text{old}}|_{i,j,k+1}}{2} \\
&+ \frac{\Delta z}{4}(K_z|_{i,j,k-1} - K_z|_{i,j,k+1}).
\end{aligned} \tag{19}$$

B. Boundary conditions

The terms used to calculate $\Phi_{\text{new}}|_{i,j,k}$ in eqn (19) fail to properly compute at the edges of the grid due to the equations needing data from outside of the problem grid that does not exist. The following section describes how to introduce Neumann boundary conditions into eqn (19). Since the devices being created with this algorithm are finite in volume, the Neumann boundary condition was chosen because it prescribes a continuation of the function of the boundary for values outside of it. For the rest of this formulation, a finite discretized grid of $N_x \times N_y \times N_z \times$ points with $1 \le i \le N_x$, $1 \le j \le N_y$, and $1 \le k \le N_z$, respectively, is used.

The first condition where $\Phi_x|_{i,j,k}$ fails to compute is when i=1 since the calculation becomes

$$\begin{aligned}
\Phi_x|_{1,j,k} &= \frac{\Phi_{\text{old}}|_{0,j,k} + \Phi_{\text{old}|2,j,k}}{2} + \\
&\frac{\Delta x}{4}(K_x|_{0,j,k} - K_x|_{2,j,k}).
\end{aligned} \tag{20}$$

which is attempting to access elements $\Phi_{\text{old}}|_{0,j,k}$ and $K_x|_{0,j,k}$ which are out of the range $1 \le i \le N_x$ for the discretized grid.

In a similar manner, the second boundary problem occurs when $i = N_x$; the calculation becomes

$$\begin{aligned}
\Phi_x|_{N,j,k} &= \frac{\Phi_{\text{old}}|_{N_x-1,j,k} + \Phi_{\text{old}}|_{N_x+1,j,k}}{2} + \\
&\frac{\Delta x}{4}(K_x|_{N_x-1,j,k} - K_x|_{N_x+1,j,k}).
\end{aligned} \tag{21}$$

where $\Phi_{\text{old}}|_{N_x+1,j,k}$ and $K_x|_{N_x+1,j,k}$ are attempting to access values from outside of the $1 \le i \le N_x$ range of the discretized grid.

To reformulate eqn(19) to avoid out-of-bound access, only eqn(10) is interpreted as the update equation for values of $i = 0$

$$\Phi_x|_{1,j,k} = 4\Phi_{\text{old}}|_{2,j,k} - 2\Delta x(K_x|_{2,j,k} + K_x|_{1,j,k}). \tag{22}$$

When $i = N_x$, the terms attempting to access values outside of the grid are dropped and eqn (9) is then interpreted as the update equation

$$\Phi_x|_{N_x,j,k} = 4\Phi_{\text{old}}|_{N_x-1,j,k} - 2\Delta x(K_x|_{N_x,j,k} + K_x|_{N_x-1,j,k}) \tag{23}$$

The formulation for Φ_x that makes use of eqn (19), (22), and (23) is

$$\Phi_x|_{i,j,k} = \begin{cases}
\begin{aligned}&4\Phi_{\text{old}}|_{2,j,k} - \\ &2\Delta x\left(K_x|_{2,j,k} + K_x|_{1,j,k}\right)\end{aligned} & i = 1 \\
\begin{aligned}&\frac{\Phi_{\text{old}}|_{i-1,j,k} + \Phi_{\text{old}}|_{i+1,j,k}}{2} + \\ &\frac{\Delta x}{4}\left(K_x|_{i-1,j,k} + K_x|_{i+1,j,k}\right)\end{aligned} & 2 \le i \le N_x - 1. \\
\begin{aligned}&4\Phi_{\text{old}}|_{N_x-1,j,k} - \\ &2\Delta x\left(K_x|_{N_x,j,k} + K_x|_{N_x-1,j,k}\right)\end{aligned} & i = N_x
\end{cases} \tag{24}$$

By inspection of eqn (24), the expressions for Φ_y and Φ_z that include boundary conditions are

$$\Phi_y|_{i,j,k} = \begin{cases}
\begin{aligned}&4\Phi_{\text{old}}|_{i,2,k} - \\ &2\Delta y\left(K_y|_{i,2,k} + K_y|_{i,1,k}\right)\end{aligned} & j = 1 \\
\begin{aligned}&\frac{\Phi_{\text{old}}|_{i,j-1,k} + \Phi_{\text{old}}|_{i,j+1,k}}{2} + \\ &\frac{\Delta y}{4}\left(K_y|_{i,j-1,k} - K_y|_{i,j+1,k}\right)\end{aligned} & 2 \le j \le N_y - 1. \\
\begin{aligned}&4\Phi_{\text{old}}|_{i,N_y-1,k} - \\ &2\Delta y\left(K_y|_{i,N_y,k} + K_y|_{i,N_y-1,k}\right)\end{aligned} & i = N_y
\end{cases} \tag{25}$$

$$\Phi_z|_{i,j,k} = \begin{cases} \dfrac{4\Phi_{\text{old}}|_{i,j,2} - 2\Delta z\left(K_z|_{i,j,2} + K_z|_{i,j,1}\right)}{} & k = 1 \\ \dfrac{\Phi_{\text{old}}|_{i,j,k-1} + \Phi_{\text{old}}|_{i,j,k+1}}{2} + \dfrac{\Delta z}{4}\left(K_z|_{i,j,k-1} + K_z|_{i,j,k+1}\right) & 2 \le k \le N_z - 1. \\ \dfrac{4\Phi_{\text{old}}|_{i,j,N_z-1} - 2\Delta z\left(K_z|_{i,j,N_z} + K_z|_{i,j,N_z-1}\right)}{} & k = N_z \end{cases} \quad (26)$$

IV. IMPLEMENTATION

A. Algorithm flowchart

To summarize the implementation of the algorithm, the flowchart in Figure 1 presents the algorithm behavior, along with highlighting in gray the iterative nature of the solver used to obtain SVLs. A general overview of the algorithm will be presented here, with more explanation to follow in the upcoming sections. The flowchart begins with the definition of the baseline unit cell of the lattice $\varepsilon_{uc}(\vec{s})$ and the spatially variant $\vec{K}$ function $\vec{K}(\vec{s})$. Then, $\varepsilon_{uc}(\vec{s})$ is decomposed into a complex Fourier series truncated into a set of $P \times Q \times R$ spatial harmonics. Each one of these truncated spatial harmonics is then spatially varied to obtain the overall SVL. The gray area in the flowchart of Figure 1 represents the iterative solver to spatially vary each spatial harmonic. Each iteration in the solver checks for the difference between the grating phase, the current, and previous iterations and compares it to a tolerance term, tol. Once this tolerance is reached, the iterative solver stops executing and the next spatial harmonic is spatially varied. Once all spatial harmonics are processed, the algorithm finishes execution.

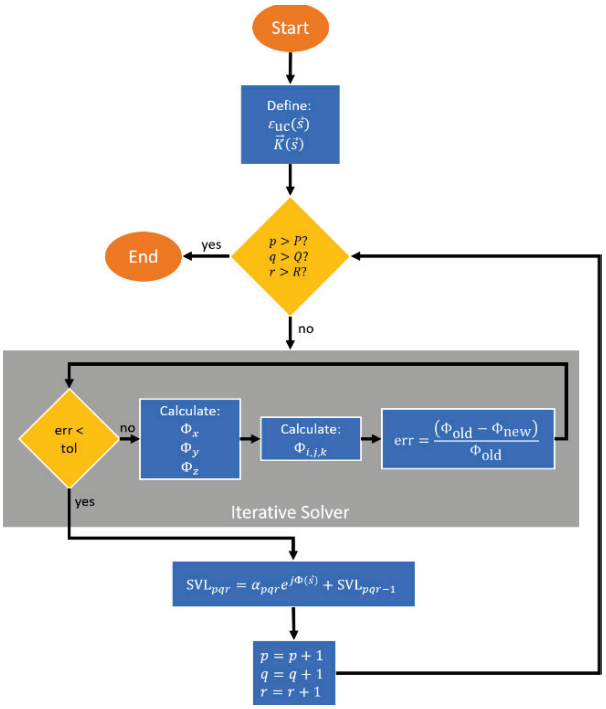

Fig. 1. Flowchart describing the algorithm and its steps. The area inside of the gray box represents the iterative solver for the grating phase. A grating phase is calculated for every Cartesian direction and then combined into a singular global grating phase.

B. Algorithm inputs

In the first presentation of the algorithm to generate SVLs, Rumpf [5] described the most common inputs to the algorithm. The first input consists of the function representing the baseline periodic element that describes the lattice, $\varepsilon_{uc}(\vec{s})$. In this paper, this function is set to 0 for all areas describing air and 1 for areas where material exists.

This baseline unit cell is then decomposed into a complex Fourier series via a fast Fourier transform (FFT). Each term in the Fourier series is a spatial harmonic with its own direction, amplitude, and period and, thus, can be considered as a single sinusoidal grating. $\varepsilon_{uc}(\vec{s})$ then becomes a weighted sum of sinusoidal gratings of the form

$$\varepsilon_{uc}(\vec{s}) = \sum_{p}^{P}\sum_{q}^{Q}\sum_{r}^{R} \alpha_{pqr} e^{j\vec{K}_{pqr}\vec{s}}. \quad (27)$$

where $\vec{s}$ is position, α_{pqr} is the complex Fourier coefficient of the pqr^{th} term, and $\vec{K}_{pqr}$ is the grating vector associated with the pqr^{th} term. The associated grating vectors are calculated analytically according to

$$\vec{K}_{pqr} = p\vec{T}_1 + q\vec{T}_2 + r\vec{T}_3. \quad (28)$$

The second set of data in [11] consists of a series of functions that define the spatial variance of the lattice parameters. Separate functions for lattice spacing, fill fraction, and unit cell orientation need to be constructed that describe the intended behavior for the final lattice. The examples of input functions described in Figure 2 show a lattice orientation that changes based on the direction of a line path as well as the lattice spacing being spatially varied in a Gaussian profile to go from 0 to 1 of the nominal lattice spacing; finally, the fill fraction of the device is changed radially outward to go from 1% to 100%. It is important to note that these input maps can take any shape the end-user requires for their application. The examples in Figure 2 is a graphical representation of a subset of possible maps.

C. Build spatially variant $\vec{K}$ function

To compute the spatially variant $\vec{K}$ function, an array that encompasses the problem space is constructed. The $\vec{K}_{pqr}$ grating vector associated with the pqr^{th} spatial harmonic is extracted and applied to the whole grid. A rotation matrix is generated to aid in the addition of the tilt

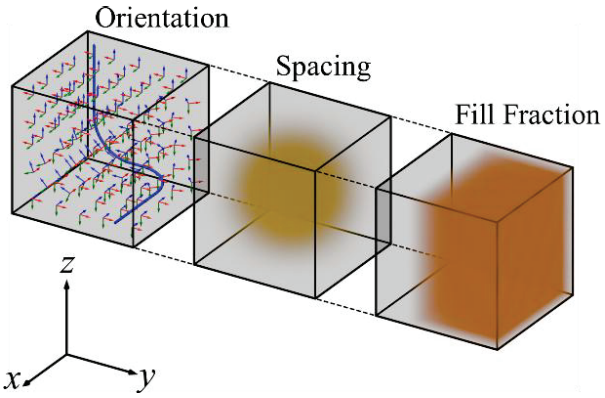

Fig. 2. Sample algorithm inputs. From left to right: lattice orientation, lattice spacing, and lattice fill fraction. Any of these input maps can be drawn graphically on a Cartesian grid to represent arbitrary shapes.

of the orientation to an intermediary $\vec{K}$ value at a point in the grid.

In order to calculate the spatially variant $\vec{K}$, the iterative solver shown in the flowchart in Figure 1 first needs to calculate the grating phase in accordance with eqn (3). The grating phase is solved iteratively in accordance with eqn (24)–(26), and at each iteration, Φ_{old} and Φ_{new} are compared to each other. This comparison is done to determine when the iteration process to calculate the grating phase stops. In this implementation, this criteria for stopping the iterative process is controlled by a tolerance factor; this means that once the numerical difference between Φ_{old} and Φ_{new} is negligible, the answer for the grating phase is considered complete.

D. Calculate spatially variant grating

After computing the overall grating phase throughout the problem space, the spatially variant grating, $\varepsilon_{pqr}(\vec{s})$, is calculated with the use of

$$\varepsilon_{pqr}(\vec{s}) = \alpha_{pqr} e^{j\Phi_{pqr}(\vec{s})} \tag{29}$$

where α_{pqr} represents the Fourier coefficient for the pqr^{th} planar grating of the unit cell.

E. Calculate overall lattice

Having calculated each spatially variant grating, the overall lattice is obtained from their sum

$$\varepsilon_a(\vec{s}) = \mathbb{R}\left[\sum_{pqr=1}^{PQR} \varepsilon_{pqr}(\vec{s})\right] \tag{30}$$

The numerical noise caused by the use of the FFT and the construction of the lattice via the use of eqn (30) can cause the values in $\varepsilon_a(\vec{s})$ to contain an imaginary component, which should be dropped by retaining only the real part of the summation.

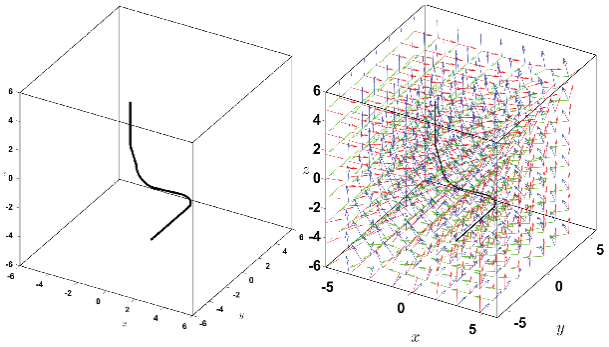

Fig. 3. Line path used as nominal unit cell orientation (left) and the output lattice orientation (right). The figure on the left represents the nominal path an electromagnetic beam would follow inside of the lattice. The figure on the right represents the orientation vectors of each unit cell as a function of position based on the orientation line.

V. GENERATION AND SIMULATION OF FULLY 3D SVLs

As mentioned in Section I, a potential application of SVLs is a spatially variant SCPC to direct the flow of light through a volume. The algorithm will be demonstrated here by generating and simulating this type of lattice. In the sections that follow, a technique for generating the input maps for this type of lattice is described. Then, two different spatially variant SCPC structures are generated with the iterative algorithm described in this paper. Finally, the results of an FDTD simulation of these structures are presented to demonstrate that functional lattices can be generated.

A. Line-path algorithm: An intuitive lattice orientation generator for SCPCs

This section describes the approach used to calculate the lattice orientation input map for flowing an electromagnetic wave around a double bend. The algorithm begins by creating a line path that the electromagnetic wave should follow. This is shown in Figure 3.

For each discrete point along the line, three vectors $\vec{a}$, $\vec{b}$, and $\vec{c}$ are defined that set the ideal orientation of the unit cells along the line. From here, the unit cell orientation of any other point within the lattice is set equal to the orientation defined at the closest point on the line. A loop is set up that iterates through every point in the lattice and calculates the three vectors $\vec{a}$, $\vec{b}$, and $\vec{c}$ for each point. The lattice orientation function that results from this process is shown in Figure 3.

B. Large lattice simulations

Two spatially variant SCPCs were generated from the two different unit cells, as shown in Figure 4. The unit cell in the left portion of Figure 4 is a simple cubic

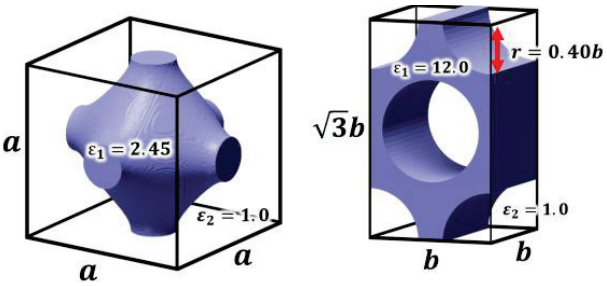

Fig. 4. Unit cells used to generate the two spatially variant SCPCs with their respective materials and dimensions. Cubic unit cell (left) has dimensions a = 1.59 cm and hexagonal unit cell (right) has dimensions b = 1.00 cm.

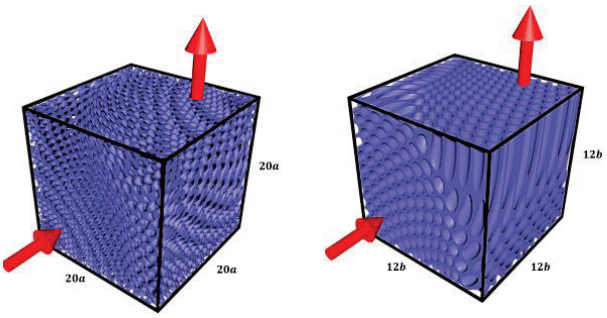

Fig. 5. Generated spatially variant SCPCs. The arrows show the input and output directions of the electromagnetic waves. Left generated with a cubic unit cell, total dimensions $20a$ = 31.90 cm. Right generated with a hexagonal unit cell, total dimensions $12b$ = 12.00 cm.

unit cell with the same dimensions and material parameters shown in [5]. The second lattice uses a hexagonal unit cell, as shown in the right portion of Figure 4, which exhibits broadband, omnidirectional, out-of-plane, and self-collimation as described in [12] . These structures were selected for generation with this algorithm due to their sensitivity to lattice spacing and overall structure [5, 12]. The final generated lattices are shown in Figure 5. In Figure 5, red arrows represent the input and output ports of the electromagnetic wave.

Full-wave simulations were performed using Remcom's XFDTD software. The source used was a Gaussian beam that was linearly polarized along the z-axis impinging the input face of each self-collimating SCPC as shown in Figure 5. Each lattice was simulated at two difference frequencies and these were $f_1 = 15$ GHz and $f_2 = 22.5$ GHz. The beam inside of the lattice was expected to follow the orientation of the unit cells due to propagating through an SC crystal. Results for both the simple cubic and hexagonal spatially variant SCPCs are shown in Figures 6 and 7.

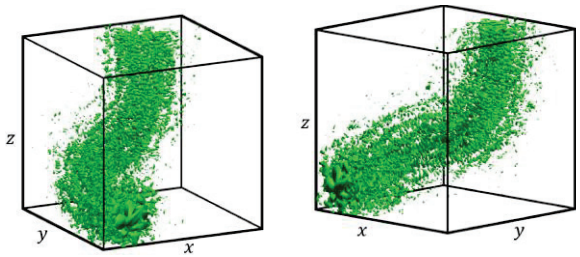

Fig. 6. FDTD simulation of electric field intensity in a spatially variant lattice generated with a cubic unit cell at f_1 = 15 GHz with a Gaussian beam (ω = 2.985cm).

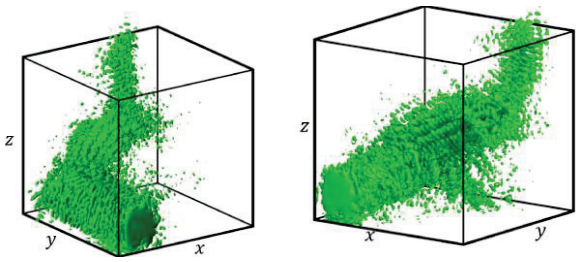

Fig. 7. FDTD simulation of electric field intensity in a spatially variant lattice generated with a hexagonal unit cell at f_2 = 22.5 GHz with a Gaussian beam (ω = 1.333cm).

Both simulations shown in Figures 6 and 7 show the electromagnetic wave traveling through the lattice following the curvature defined in Figure 3 and exiting through the output face. The simulation shown in Figure 6 exhibits greater spurious scattering. There are two main reasons for this. First, the cubic unit cell has weaker self-collimation; so it has a limited range of angles, or field-of-view (FOV), in which a wave can self-collimate. The waves outside this FOV will scatter into different directions and will not follow the defined path of SC. Second, the lattice orientation function fed into the SV algorithm was not enforcing the vectors perpendicular to the direction of SC, and, thus, the unit cell orientation across the three axes of freedom was not enforced. This can further change or reduce the limited FOV of the unit cell, leading to unwanted scattering. It is hypothesized that the performance of the lattice with the cubic unit cell can be improved by enforcing all three axes of freedom to follow the curvature, along with a deformation control [13] algorithm to further suppress any deformations along the path. The simulation of the hexagonal unit cell shows much better performance with almost zero spurious scattering. The hexagonal unit cell exhibits omnidirectional SC along the main axis of propagation, allowing the beam to exit the intended output face with minimal scattering loss.

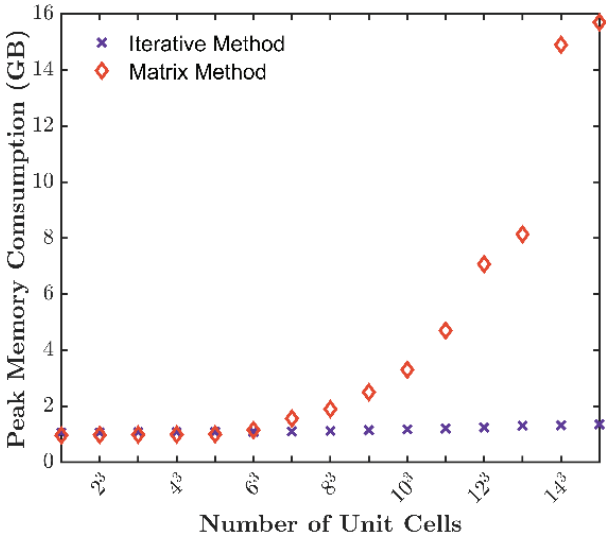

Fig. 8. Iterative solver vs. matrix solver memory usage.

VI. RESULTS

The algorithm was benchmarked against the matrix-based SVL computation approach for memory consumption. Figure 8 presents the results of the benchmark when the number of unit cells in a simple cubic lattice is increased in the x, y, and z directions. These results were obtained by calculating the total memory space allocated inside of MATLAB® for the working variables of the grating phase, input maps, and intermediate parameters used in MATLAB's LU decomposition algorithm.

Figure 8 shows that there is a linear trend in the peak memory utilization while using the iterative SVL solver, whereas the peak memory usage when using the matrix solver shows an exponential growth. These trends in memory usage are a clear indication that the iterative solver presented is an excellent tool to generate large-scale lattices, while the matrix solver falls behind in memory consumption due to the computationally expensive LU decomposition.

VII. CONCLUSION

It was shown that the formulation of an iterative SVL algorithm can be used to produce fully three-dimensional SVLs with greater memory efficiency. A line path algorithm was used to convey the unit cell orientation as a function of position in an easy and intuitive manner. Large-scale SVLs were able to be generated to be used in electromagnetic applications as spatially variant PhCs. Two lattices consisting of $20 \times 20 \times 20$ and $12 \times 12 \times 12$ unit cells, respectively, were generated and simulated using the FDTD method to confirm the device functionality. The low memory requirements of the iterative approach to generating SVLs allow for the realization of much larger photonic devices. Further, many geometrical properties in addition to unit cell orientation can be spatially varied to control multiple aspects of the wave at once in a 3D volume. This may prove valuable for unlocking the full potential that PhCs can offer to arbitrarily control electromagnetic waves throughout a volume.

ACKNOWLEDGMENT

Distribution A: Approved for public release - distribution unlimited (96TW-2021-0104)

REFERENCES

[1] H. Kosaka, T. Kawashima, A. Tomita, M. Notomi, T. Tatamura, T. Sato, and S. Kawakami, "Self-collimating phenomena in photonic crystals," vol. 74, no. 9, pp. 1212-1214, 1999.

[2] M. Notomi, K. Yamada, A. Shinya, J. Takahashi, C. Takahashi, and I. Yokohama, "Extremely large group-velocity dispersion of line-defect waveguides in photonic crystal slabs," *Phys. Rev. Lett.*, vol. 87, no. 25, pp. 253902-253902-4, Dec. 2001.

[3] R. C. Rumpf and J. Pazos, "Synthesis of spatially variant lattices," *Opt. Express*, vol. 20, no. 14, pp. 15263, Jun. 2012.

[4] R. C. Rumpf, "Engineering the dispersion and anisotropy of periodic electromagnetic structures," in *Solid State Physics - Advances in Research and Applications*, vol. 66, pp. 1212-1214, 2015.

[5] R. C. Rumpf, J. Pazos, C. R. Garcia, L. Ochoa, and R. Wicker, "3D printed lattices with spatially variant self-collimation," *Prog. Electromagn. Res.*, vol. 138, pp. 1-14, 2013.

[6] J. L. Digaum, R. Sharma, D. Batista, J. J. Pazos, R. C. Rumpf, and S. M. Kuebler, "Beam-bending in spatially variant photonic crystals at telecommunications wavelengths," *Advanced Fabrication Technologies for Micro/Nano Optics and Photonics IX,* vol. 9759, pp. 975911, 2016.

[7] J. J. Gutierrez, N. P. Martinez, and R. C. Rumpf, "Independent control of phase and power in spatially variant self-collimating photonic crystals," *J. Opt. Soc. Am. A*, vol. 36, no. 9, pp. 1534-1539, 2019.

[8] K. David and C. Ward, *Numerical analysis | mathematics | Britannica*, 3rd ed. Pacific Grove: American Mathematical Sociecty, 2000.

[9] S. D. Gedney, "Introduction to the Finite-Difference Time-Domain (FDTD) Method for Electromagnetics," *Synth. Lect. Comput. Electromagn.*, vol. 6, no. 1, pp. 1-250, Jan. 2011.

[10] D. De Donno, a. Esposito, L. Tarricone, and L. Catarinucci, "Introduction to GPU Computing and CUDA Programming: A Case Study on FDTD [EM Programmer's Notebook]," *IEEE Antennas Propag. Mag.*, vol. 52, no. 3, pp. 116-122, 2010.

[11] R. C. Rumpf and J. Pazos, "Synthesis of spatially variant lattices," *Opt. Express*, vol. 20, no. 14, pp. 15263-15274, 2012.

[12] Y. C. Chuang and T. J. Suleski, "Photonic crystals for broadband, omnidirectional self-collimation," *J. Opt.*, vol. 13, no. 3, pp. 1-8, 2011.

[13] R. C. Rumpf, J. J. Pazos, J. L. Digaum, and S. M. Kuebler, "Spatially variant periodic structures in electromagnetics," *Philos. Trans. R. Soc. A Math. Phys. Eng. Sci.*, vol. 373, no. 2049, p. 20140359, Jul. 2015.

A Memory-Efficient Hybrid Implicit–Explicit FDTD Method for Electromagnetic Simulation

Faxiang Chen and Kang Li

School of Information Science and Engineering, Shandong University, Qingdao 266237, China
cfxlongman@163.com, kangli@sdu.edu.cn

Abstract **–** As the explicit finite-difference time-domain (FDTD) method is restricted by the Courant−Friedrich−Levy (CFL) stability condition and inefficient for simulation in some situations, implicit methods are developed. The hybrid implicit−explicit (HIE) FDTD method is one popular method among them. In this paper, a memory-efficient HIE FDTD method is designed for electromagnetic simulation. The proposed HIE-FDTD method is based upon the divergence relationship of electric fields, nearly reduces one field component, and realizes a memory reduction rate of 33% approximately. Two numerical experiments are carried out to validate the proposed method and the results indicate that the proposed memory-efficient HIE-FDTD method can work well.

Index Terms **–** Finite-difference time-domain (FDTD), hybrid implicit−explicit FDTD (HIE-FDTD), memory-efficient.

I. INTRODUCTION

Solving electromagnetic (EM) field is a necessary part in device design and analysis of EM phenomena, and many methods such as ray tracing method [1], scatter matrix method (SMM) [2–4], and Wentzel−Kramers−Brillouin (WKB) method [5] have been proposed. Methods with analytical approximation are relatively accurate and full of physical information, while their scopes are limited. As a result, numerical methods are also developed. The finite-difference time-domain (FDTD) method [6] has been regarded as one of the most effective and versatile methodologies [7, 8] mainly due to its direct temporal computing and simplicity. However, the explicit FDTD method is constrained by the Courant−Friedrich−Levy (CFL) stability condition [9]. As a result, when there are fine structures in the computation task, the FDTD method has to employ relatively small cell sizes and, thus, unavoidably takes a relatively small time step and consequently is confronted with heavy burden of long running time. In order to solve the issue, researchers resort to implicit schemes and have proposed a series of methods such as alternating-direction implicit (ADI) FDTD method [10, 11], locally one-dimensional (LOD) FDTD method [12, 13], Crank−Nicolson (CN) FDTD method [14, 15], weighted Laguerre polynomial (WLP) FDTD method [16, 17], and hybrid implicit−explicit (HIE) FDTD method [18, 19]. Among those methods, the ADI-FDTD method and the LOD-FDTD method both employ time split schemes and seem somewhat complex. The CN-FDTD method and the WLP-FDTD method both adopt fully implicit schemes and result in a huge sparse matrix which is expensive to handle. Whereas, the HIE-FDTD method only executes implicit difference schemes for the spatial partial derivatives in the direction along which there are fine structures and takes general explicit difference schemes for the remaining spatial partial derivatives in the directions along which there are no fine elements. In such an arrangement, the HIE-FDTD method finishes the restriction of the fine spatial cell sizes on time step size, acquires the ability to improve computational efficiency, and has drawn much attention in recent years [19–22]. Compared with the conventional FDTD method and even some other absolutely stable FDTD methods such as the ADI-FDTD method in some situations [23], the HIE-FDTD method showed higher efficiency, and a lot of work including but not limited to simulations of designing devices, implementations of PML, and reducing numerical dispersion error [19–22, 24] have been put forward.

Compared with the FDTD method, the HIE-FDTD method becomes more complex and needs more memory to implement, and, recently, the authors in [25] also point out that the character exists in some previous algorithms that employ implicit schemes. As a result, a form of HIE-FDTD method that is both free of strict CFL stability condition and is also of low memory requirements without bringing much complexity may be of value. In the paper [26], the authors proposed a scheme based on divergence relationship and achieved a memory reduction rate near to 33%. Then the thought of memory saving was adopted into some other situations [27–29] in different ways.

Submitted On: August 15, 2021
Accepted On: February 8, 2022

https://doi.org/10.13052/2022.ACES.J.370202

In this paper, based on the work proposed in [18] and [26], a memory-efficient HIE-FDTD method is developed based on the divergence relationship of electric fields. It will be seen that the proposed HIE-FDTD method nearly only stores two field components in computation, reduces 33.33% of memory approximately, and maintains the accuracy and efficiency of the original method.

II. ALGORITHM FORMULATION

In simple, isotropic, and lossless media, according to [18], the HIE FDTD method is

$$E_x^{n+1} = E_x^n + \frac{\Delta t}{2\varepsilon}\frac{\partial\left(H_z^{n+1}+H_z^n\right)}{\partial y} \tag{1}$$

$$E_y^{n+1/2} = E_y^{n-1/2} - \frac{\Delta t}{\varepsilon}\frac{\partial H_z^n}{\partial x} \tag{2}$$

$$H_z^{n+1} = H_z^n + \frac{\Delta t}{2\mu}\frac{\partial\left(E_x^{n+1}+E_x^n\right)}{\partial y} - \frac{\Delta t}{\mu}\frac{\partial E_y^{n+1/2}}{\partial x}. \tag{3}$$

In order to acquire the solutions, a user either replaces H_z^{n+1} in eqn (1) with H_z^{n+1} in eqn (3), solves matrix equations, and acquires E_x^{n+1} or inserts eqn (1) into eqn (3), handles matrix equations, and solves H_z^{n+1} and, in the end, calculates the remaining field variables explicitly. We term them as HIE-E-FDTD method and HIE-H-FDTD method, respectively.

The divergence relationship of electric fields can be directly written as

$$\begin{aligned}&\frac{\partial E_x^{n+1}}{\partial x}+\frac{\partial E_y^{n+1/2}}{\partial y}\\ &=\frac{\partial E_x^{n}}{\partial x}+\frac{\partial E_y^{n-1/2}}{\partial y}+\frac{\Delta t}{2\varepsilon}\frac{\partial^2\left(H_z^{n+1}-H_z^n\right)}{\partial x\partial y}.\end{aligned} \tag{4}$$

Eqn (4) can also be rewritten as

$$\begin{aligned}&\frac{\partial E_x^{n+1}}{\partial x}+\frac{\partial E_y^{n+1/2}}{\partial y}-\frac{\Delta t}{2\varepsilon}\frac{\partial H_z^{n+1}}{\partial x\partial y}\\ &=\frac{\partial E_x^{n}}{\partial x}+\frac{\partial E_y^{n-1/2}}{\partial y}-\frac{\Delta t}{2\varepsilon}\frac{\partial^2 H_z^{n}}{\partial x\partial y}.\end{aligned} \tag{5}$$

Clearly, the divergence relationship is time invariant. The initial condition is 0; so eqn (5) can be further rewritten as

$$\frac{\partial E_x^{n}}{\partial x}+\frac{\partial E_y^{n-1/2}}{\partial y}-\frac{\Delta t}{2\varepsilon}\frac{\partial^2 H_z^{n}}{\partial x\partial y}=0. \tag{6}$$

In fact, eqn (6) is just the result of linear combination of the two curl equations of electric field components in the HIE-FDTD method. In the region containing source, eqn (6) may fail; so one can directly apply the HIE-FDTD method without any change and construct linear equations to solve the fields or get the discrete divergence relationship by directly adding the numerical expressions of the two field components in the conventional HIE-FDTD method according to the regular form of divergence relationship.

Conductor (PEC) will also destroy eqn (6). On the surface of conductor, tangential E is 0; so eqn (6) is omitted. As to normal E, we recommend using the HIE-FDTD method on surface of conductor directly.

After applying finite difference approximation to spatial derivatives, the full numerical form of eqn (6) can be written as

$$\begin{aligned}E_x^n(i,j) &= E_x^n(i-1,j)-\frac{\Delta x}{\Delta y}\left(E_y^{n-1/2}(i,j)-E_y^{n-1/2}(i,j-1)\right)\\ &+\frac{\Delta t}{2\varepsilon}\left(\begin{array}{c}\dfrac{H_z^n(i,j)-H_z^n(i,j-1)}{\Delta y}\\ -\dfrac{H_z^n(i-1,j)-H_z^n(i-1,j-1)}{\Delta y}\end{array}\right).\end{aligned} \tag{7}$$

In the computation domain, cells with the same x coordinate are defined as a sub-region registered as $x = i$. In this paper, each sub-region is rectangle, and the domain consists of $M \times N$ cells and is grouped into many rectangles like $x = i - 1$, $x = i$, and $x = i + 1$, which is shown in Figure 1.

Fields in these regions are expressed as vectors and registered as $E_y(i)$, $E_x(i)$, and $H_z(i)$. From eqn (7), it can be seen that E_x^n in $x = i$ only requires E_x^n in $x = i - 1$ except $E_y^{n-1/2}$ in $x = i$ and H_z^n in $x = i$ and in $x = i - 1$. In this paper, E_y fields are at sides of cells in y direction, E_x fields are at sides of grids in x direction, and H_z fields are at the centers of each cell. As a result, eqn (7) can also be rewritten as a matrix form

$$E_x^n(i) = E_x^n(i-1) + A\,E_y^{n-1/2}(i) + B\,H_z^n(i) + C\,H_z^n(i-1) \tag{8}$$

where A, B, and C are matrices determined by coefficients in front of fields in eqn (7).

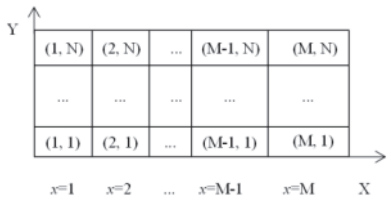

(a)

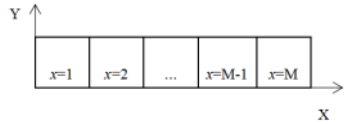

(b)

Fig. 1. (a) The computation domain with cells and sub-regions. (b) The computation domain with sub-regions.

Suppose $x = i - 1$ is the initial position where our calculation begins. We define $E_y(k)$ and $H_z(k)$ where k can be each rectangle in the whole domain. As to E_x, only two vectors e_{x1} that can store E_x^n in $x = i - 1$ and e_{x2} that has the memory sufficient to store E_x in $x = i$ are defined.

First, as e_{x1} is equal to E_x^n in $x = i - 1$, e_{x2} can be valued through eqn (8) and is equal to E_x^n in $x = i$. As E_x^n, $E_y^{n-1/2}$, and H_z^n are known in $x = i - 1$, $E_y^{n+1/2}$ and H_z^{n+1} can be solved by the conventional HIE-FDTD procedure in $x = i - 1$. Then e_{x1}=e_{x2} which is equal toE_x^n in $x = i$, and E_x^n in $x = i + 1$ can be valued by eqn (8) and can reuse the memory occupied by e_{x2}. And now as E_x^n, $E_y^{n-1/2}$ and H_z^n are known in $x = i$, and $E_y^{n+1/2}$ and H_z^{n+1} can be solved by the conventional HIE-FDTD procedure in $x = i$ again. Repeating this process to the last rectangle, it will be seen that all $E_y^{n+1/2}$ and H_z^{n+1} have been solved, and only two vectors that store E_x^n in each sub-region temporarily and are alternatively used are sufficient to finish the calculation, while in the conventional HIE-FDTD method, all field components are required to store. As a result, in the proposed method, one electric field component is nearly eliminated and the aim of memory reduction is realized in such a way.

A short pseudo-code is written below. Some terms in this content will be explained. In this part, $T_{\max}$ is the last time step, each value of x presents the rectangle corresponding to cells with the same coordinate of x in the computation domain, and $X_{\max}$ presents the last rectangle. e_{x1} and $e_{x2}$are both vectors, and E_x and H_z are matrices. t presents the current time step in iteration.

Pseudo-code of the proposed method:

Vector v stores $E_x^1(1)$(=0); $H_z^1 = 0$; $E_y^{1/2} = 0$.

for $t = 2:T_{\max}$

  $e_{x1} = v$;

  e_{x1} works as $E_x^{t-1}(1)$;

  $e_{x2} = e_{x1} + A E_y^{t-1-1/2}(2) + B H_z^{t-1}(2) + C H_z^{t-1}(1)$;

  e_{x2} works as $E_x^{t-1}(2)$;

  $E_y^{t-1/2}(1)$, $H_z^t(1)$, and $E_x^t(1)$ are solved by regular HIE FDTD procedure;

  $v = E_x^t(1)$;

  for i=2:$X_{\max}$-1

    $e_{x1} = e_{x2}$;

    e_{x1} works as $E_x^{t-1}(i)$;

    $e_{x2} = e_{x1} + A E_y^{t-1-1/2}(i+1) + B H_z^{t-1}(i+1) + C H_z^{t-1}(i)$;

    e_{x2} works as $E_x^{t-1}(i+1)$;

    $E_y^{t-1/2}(i)$ and $H_z^t(i)$ are solved by regular HIE-FDTD procedure;

  end

  $i = X_{\max}$;

  $E_y^{t-1/2}(i)$ and $H_z^t(i)$ are solved by regular HIE-FDTD procedure.

end

It must be pointed out that E_x and it with identifications of different time steps and space positions both in the description above and in the proposed method only indicate electric fields of x component and does not mean a matrix that is defined, occupies memory and stores fields covering the whole calculation domain.

From the description above, it can be stated that in an arbitrary iteration at $(n + 1)$th time step, the proposed method does not need to store all the E_x^nfields beforehand; only two vectors e_{x1} and e_{x2} that are repeatedly used are sufficient for the run of the algorithm, and, in such a way, the memory reduction is realized. In this description, E_x are chosen as unknown variables in linear equations. For the case that H_z works as unknown variables, the algorithm is implemented in a similar way.

In fact, in the proposed method, at each time step, E_x appear in each sub-region by eqn (7) but do not need to store after fields in this region are solved. Supposing E_x in some regions are required, one only needs to store those solutions when the run goes through the local regions.

III. NUMERICAL VALIDATION

In order to validate the proposed method, two numerical experiments that both use 2D parallel plate waveguides [15] are carried out. The structures used in the two examples are shown in Figure 2.

The excitation for the two numerical tests taken from [11] is

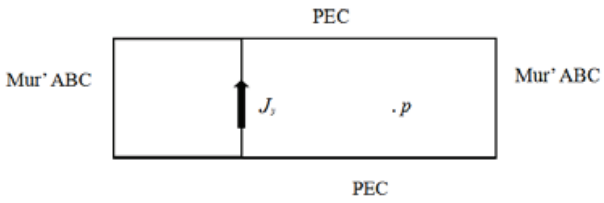

(a)

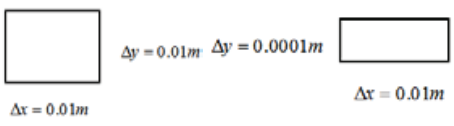

(b) (c)

Fig. 2. (a) The structures in the two numerical examples, (b) one cell in the first example, and (c) one cell in the second example.

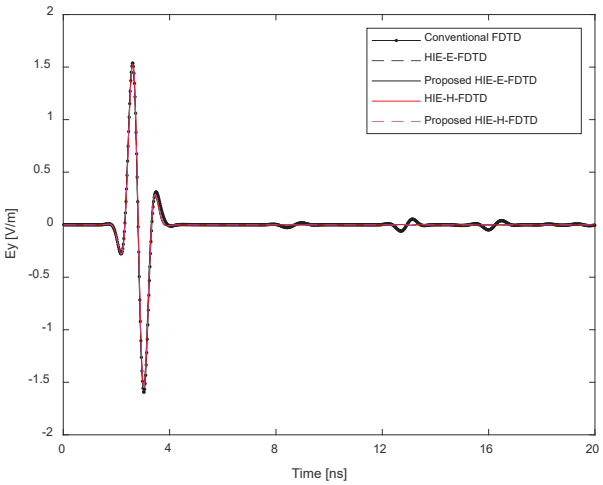

Fig. 3. Transient E_y at p point.

$$J_y(t) = \exp\left(-\left(\frac{t-T_c}{T_d}\right)^2\right)\sin\left(2\pi f_c(t-T_c)\right), \quad (9)$$

where

$$T_d = \frac{1}{2f_c}$$
$$T_c = 3T_d. \quad (10)$$

In the structure, p is the probe point recording fields at different time step, and $_{J_y}$ is the excitation current.

In the first example, there are 200 and 100 cells with the sizes set as $\Delta x = 0.01$ m and $\Delta y = 0.01$ m along x and y directions, respectively. The source is placed on line of x = 10 and the point p(50,5) is chosen as observation point recording E_y at each time step and the two sides of the extended waveguide are both truncated by first-order Mur' absorbing boundary condition. In this situation, according to the CFL stability condition, the largest time step sizes for the conventional FDTD method and the HIE-FDTD method are 23.57 and 33.33 ps, respectively. For the convenience of comparative analysis, the time steps for conventional FDTD and HIE-FDTD methods in this case are both simply set as 20 ps.

Figure 3 shows E_y at p point and Table 1 records the running time consumed by the FDTD method, HIE-FDTD method, and the proposed memory-efficient version of the later method with the uniform time step size. From Figure 3, we can see that the numerical results supplied by several algorithms are all in good agreement and, thus, validate the correctness of the new memory-efficient version of HIE-FDTD method. It can be seen that different implementations of the HIE-FDTD methods show a little difference in computation time. As the HIE-FDTD method is an implicit method, it costs more time than the conventional FDTD method when a uniform time step is used.

Table 1: Comparison of computation time of different methods with uniform time step size

FDTD methods	Time step	Iteration numbers	CPU time (s)
Conventional FDTD	20 ps	1000	1.23
Original HIE-E-FDTD	20 ps	1000	33.35
Proposed HIE-E-FDTD	20 ps	1000	33.76
Original HIE-H-FDTD	20 ps	1000	35.58
Proposed HIE-H-FDTD	20 ps	1000	35.71

In order to measure the accuracy of the proposed method, error $= \sqrt{\sum_{i=1}^{T}\left(E_y^i - E_{y,Ref}^i\right)^2 / \sum_{i=1}^{T}\left(E_{y,Ref}^i\right)^2}$ is defined as error function. In this function, T stands for the total number of time step iterations and equals 1000. The solutions of the original HIE-E-FDTD method and original HIE-H-FDTD method are set as reference solutions when the errors of two implementations of the proposed memory-efficient method are discussed. Setting the solution from the original HIE-E-FDTD method as standard, the error between the original HIE-E-FDTD method and the proposed HIE-E-FDTD method is 0. Setting the solution from the original HIE-H-FDTD method as standard, the error between the original HIE-H-FDTD method and the proposed original HIE-H-FDTD method is 3.59×10^{-15}. It can be seen that the errors are very small and show almost no difference. So the accuracy of the proposed method can be seen as the same as that of the original HIE-FDTD method.

In the second numerical example, we still employ the extended plate waveguide as test model mentioned above but fine the mesh size along y direction to 0.0001 m, and all the other conditions stay the same. The relevant results and time cost are shown in Figure 4 and Table 2.

Figure 4 still shows that the results calculated by the conventional FDTD method, HIE-FDTD method, and the proposed memory-efficient HIE-FDTD method are all in good agreement.

Table 2 represents the CPU time for the simulations run by different methods. In this situation, it can be seen that different implementations of the HIE-FDTD methods show a little difference in computation time. The proposed method takes almost the same time as the original HIE-FDTD method, while it is still much faster than the conventional FDTD method. As a result, the

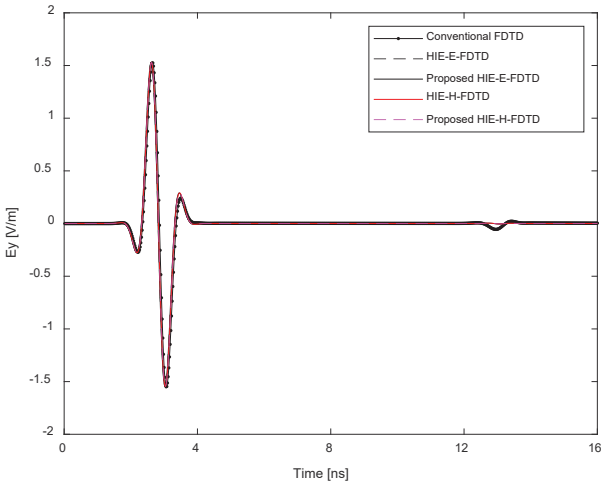

Fig. 4. Transient E_y at p point.

Table 2: Comparison of computation time of different methods with nonuniform time step sizes

FDTD methods	Time step	Iteration numbers	CPU time (s)
Conventional FDTD	0.2 ps	80,000	69.60
Original HIE-E-FDTD	20 ps	800	32.85
Proposed HIE-E-FDTD	20 ps	800	32.82
Original HIE-H-FDTD	20 ps	800	29.75
Proposed HIE-H-FDTD	20 ps	800	29.65

proposed memory-efficient HIE-FDTD method can both work well for problems with or without fine structures in one direction.

Using the same method of measuring the accuracy of the proposed method adopted in the first example, and setting the solution from the original HIE-E-FDTD method as standard, the error between the original HIE-E-FDTD method and the proposed HIE-E-FDTD method is 0. Setting the solution from the original HIE-H-FDTD method as standard, the error between the original HIE-H-FDTD method and the proposed HIE-H-FDTD method is 6.99×10^{-14}. In this function, T stands for the total number of time step iterations and equals 800. It can be seen that the errors both are very small and show almost no difference. So the accuracy of the proposed method is the same as that of the original HIE-FDTD method.

Table 3 shows the memory cost in different methods. As the numbers of cells in two numerical examples are

Table 3: Memory cost (KB) in different methods

	FDTD (KB)	HIE-E-FDTD	HIE-H-FDTD	Proposed HIE-E-FDTD	Proposed HIE-H-FDTD
A	468.75	468.75	468.75	314.06	314.06
B	468.75	468.75	468.75	314.06	314.06

equal, the memory of storing fields they require is also equal and listed in Table 3 where A presents the first numerical example and B presents the second one. It is clear that $1-312.50/468{,}075 \approx 33\%$; so the memory reduction rate is near to 33%.

IV. CONCLUSION

The analytic and semi-analytical methods are accurate and can also show physical aspects of a system explicitly. At the same time, numerical methods are also developed and are available in a wider range. Numerical methods require more memory than analytic methods in most situations. The HIE-FDTD method shows higher computation efficiency than the FDTD method in problems with fine elements in one direction. In this paper, efforts are made to reduce memory cost and a memory-efficient HIE FDTD method is proposed based on divergence relationship of electric fields. The proposed algorithm nearly eliminates one electric field component, saves nearly 33% of memory, and the implementation of the proposed method is not much more complex than the conventional HIE-FDTD method. Numerical experiments are carried out and validate that the proposed memory-efficient HIE-FDTD method can solve EM fields correctly and runs almost as fast as the original HIE-FDTD method, and in those situations, the computational efficiency can be interpreted as unchanged. The accuracy of the proposed memory-efficient HIE-FDTD method is also very close to that of the original HIE-FDTD method.

REFERENCES

[1] L. J. Guo, L. X. Guo, and L. P. Gan, "Influence of dusty plasma on antenna radiation," *Physics of Plasmas*, vol. 28, no. 8, p. 083701, Aug. 2021.

[2] L. X. Guo and L. J. Guo, "The effect of the inhomogeneous collision frequency on the absorption of electromagnetic waves in a magnetized plasma," *Physics of Plasmas*, vol. 24, no. 11, p. 112119, Nov. 2017.

[3] Q. W. Rao, G. J. Xu, P. F. Wang, and Z. Q. Zheng, "Study on the propagation characteristics of terahertz waves in dusty plasma with a ceramic substrate by the scattering matrix method," *Sensors*, vol. 21, no. 263, pp. 1-11, Jan. 2021.

[4] Q. W. Rao, G. J. Xu, P. F. Wang, and Z. Q. Zheng, "Study on the propagation characteristics of terahertz waves in dusty plasma with a ceramic substrate by the scattering matrix method," *International Journal of Antennas and Propagation*, vol. 2021, no. 6625530, pp. 1-9, Jan. 2021.

[5] Y. Y. Chen, H. B. Wang, and D. L. Zhao, "The applicability of WKB method in studying inhomogeneous dusty plasma," *IEEE Transactions on Plasma Science*, vol. 48, no. 1, pp. 275-279, Jan. 2020.

[6] K. Yee, "Numerical solution of initial boundary value problems involving Maxwell's equations in isotropic media", *IEEE Trans. Antennas Propag*., vol. AP-14, no. 3, pp. 302-307, May 1966.

[7] A. Taflove and S. C. Hagness, "Computational electrodynamics: the finite-difference time-domain method," Norwood, MA, USA: Artech House, 2005.

[8] D. M. Sullivan, Electromagnetic Simulation Using the FDTD Method, Hoboken, NJ, USA:Wiley, 2013.

[9] F. L. Teixeira, "A summary review on 25 years of progress and future challenges in FDTD and FETD techniques," *Applied Computational Electromagnetics Society (ACES) Journal*, vol. 25, no. 1, pp. 1-14, Jan. 2010.

[10] T. Namiki, "A new FDTD algorithm based on alternating-direction implicit method", *IEEE Trans. Microw. Theory Techn.*, vol. 47, no. 10, pp. 2003-2007, Oct. 1999.

[11] J. Chen, "New alternating direction implicit finite-difference time-domain method with higher efficiency," *Applied Computational Electromagnetics Society (ACES) Journal*, vol. 27, no. 11, pp. 903-907, Nov. 2012.

[12] T. L. Liang, W. Shao, and S. B. Shi, "Complex-envelope ADE-LOD-FDTD for band gap analysis of plasma photonic crystals," *Applied Computational Electromagnetics Society (ACES) Journal*, vol. 33, no. 4, pp. 443-449, Apr. 2018.

[13] A. K. Saxena and K. V. Srivastava, "Three-dimensional unconditionally stable LOD-FDTD methods with low numerical dispersion in the desired directions," *IEEE Transactions on Antennas and Propagation*, vol. 64, no. 7, pp. 3055-3067, Jul. 2016.

[14] G. L. Sun and C. W. Trueman, "Unconditionally stable Crank–Nicolson scheme for solving two-dimensional Maxwell's equations", *Electron. Lett*., vol. 39, no. 7, pp. 595-597, Apr. 2003.

[15] J. X. Li, H. L. Jiang, and N. X. Feng, "Efficient FDTD implementation of the ADE-based CN-PML for the two dimensional TMz waves," *Applied Computational Electromagnetics Society (ACES) Journal*, vol. 30, no. 6, pp. 688-691, Jun. 2015.

[16] Y. S. Chung, T. K. Sarkar, B. H. Jung, and M. Salazar-Palma, "An unconditionally stable scheme for the finite-difference time-domain method", *IEEE Trans. Microw. Theory Techn*., vol. 51, no. 3, pp. 697-704, Mar. 2003.

[17] W. Shao and J. L. Li , "An efficient laguerre-FDTD algorithm for exact parameter extraction of lossy transmission lines," *Applied Computational Electromagnetics Society (ACES) Journal*, vol. 27, no. 3, pp. 223-228, Mar. 2012.

[18] B. Huang, G. Wang, Y. Jiang, and W. Wang, "A hybrid implicit-explicit FDTD scheme with weakly conditional stability", *Microw. Opt. Technol. Lett.*, vol. 39, no. 2, pp. 97-101, Oct. 2003.

[19] L. J. Y. Guo, J. Chen, J. G. Wang, and A. X. Zhan, "A new HIE-PSTD method for solving problems with fine and electrically large structures simultaneously," *Applied Computational Electromagnetics Society (ACES) Journal*, vol. 31, no. 12, pp. 1397-1340, Dec. 2016.

[20] F. Moharrami and Z. Atlasbaf, "Simulation of multilayer graphene–dielectric metamaterial by implementing SBC model of graphene in the HIE-FDTD method," *IEEE Transactions on Antennas and Propagation*, vol. 68, no. 3, pp. 2238-2245, Mar. 2020.

[21] J. Chen, "A review of hybrid implicit explicit finite difference time domain method," *J. Computat. Phys*., vol. 363, pp. 256-267, Jun. 2018.

[22] Y. Kong, C. Zhang, and Q. Chu, "An optimized one-step leapfrog HIE-FDTD method with the artificial anisotropy parameters," *IEEE Transactions on Antennas and Propagation*, vol. 68, no. 2, pp. 1198-1203, Feb. 2020.

[23] J. Chen and J. Wang, "Comparison between HIE-FDTD method and ADI-FDTD method," *Microw. Opti. Technol. Lett.*, vol. 49, no. 5, pp. 1001–1005, Mar. 2007.

[24] P. Wu, Y. Xie, H. Jiang, H. Di, and T. Natsuki, "Complex envelope hybrid implicit-explicit procedure with enhanced absorption for bandpass nonreciprocal application," *IEEE Microwave and Wireless Components Letters,* vol. 31, no. 6, pp. 533-536, Jun. 2021.

[25] K. L. Zhang, L. Wang, R. P. Li, M. J. Wang, C. Fan, H. X. Zheng, and E. P. Li., "Low-dispersion leapfrog WCS-FDTD with artificial anisotropy

parameters and simulation of hollow dielectric resonator antenna array," *IEEE Transactions on Antennas and Propagation*. vol. 69, no, 9, pp. 5810-5811, Sep. 2021.

[26] G. D. Kondylis, F. De Flaviis, G. J. Pottie, and T. Itoh, "A memory-efficient formulation of the finite-difference time-domain method for the solution of Maxwell equations," *IEEE Transactions on Microwave Theory and Techniques*, vol. 49, no. 7, pp. 1310-1320, Jul. 2001.

[27] Y. Yi, B. Chen, W. Sheng, and Y. Pei, "A memory-efficient formulation of the unconditionally stable FDTD method for solving Maxwell's equations," *IEEE Transactions on Antennas and Propagation*, vol. 55, no. 12, pp. 3729-3733, Dec. 2007.

[28] B. Liu, B. Q. Gao, W. Tan, and W. Ren, "A new FDTD algorithm - ADI/R-FDTD", *Electromagnetic Compatibility 2002 3rd International Symposium*, pp. 250-253, May 2002.

[29] T. B. Yu and B. H Zhou, "A memory-efficient FDTD algorithm for solving Maxwell equations in cylindrical grids," *IEEE Transactions on Antennas and Propagation*, vol. 52, no. 5, pp. 1382-1384, May 2004.

Kang Li was born in Jinan, China, in 1962. He received the B.S. and M.S. degrees in electrical engineering and the Ph.D. degree in optical engineering from Shandong University, Jinan, China, in 1984, 1987, and 2006, respectively.

He is currently a Professor with the School of Information Science and Engineering, Shandong University. His current research interests include computational electromagnetics and fiber-optic communications.

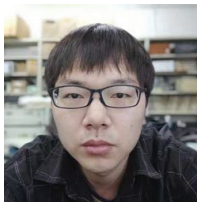

Faxiang Chen received the master's degree in electromagnetic field and microwave technology from Shanghai Maritime University, Shanghai, China, in 2015. He is currently working toward the Ph.D. degree in electronic science and technology with the Shandong University, Qingdao, China.

His current research interest includes computational electromagnetics.

Scalable and Fast Characteristic Mode Analysis using GPUs

Khulud Alsultan[1,2], Mohamed Z. M. Hamdalla[1], Sumitra Dey[1], Praveen Rao[3], and Ahmed M. Hassan[1]

[1]Department of Computer Science Electrical Engineering, University of Missouri-Kansas City, Kansas City, MO 64110, USA

[2]Department of Computer Science and Engineering, King Saud University, Riyadh 11451, Saudi Arabia

[3]University of Missouri-Columbia, Columbia, MO 65211, USA

Abstract – Characteristic mode analysis (CMA) is used in the design and analysis of a wide range of electromagnetic devices such as antennas and nanostructures. The implementation of CMA involves the evaluation of a large method of moments (MoM) complex impedance matrix at every frequency. In this work, we use different open-source software for the GPU acceleration of the CMA. This open-source software comprises a wide range of computer science numerical and machine learning libraries not typically used for electromagnetic applications. Specifically, this paper shows how these different Python-based libraries can optimize the computational time of the matrix operations that compose the CMA algorithm. Based on our computational experiments and optimizations, we propose an approach using a GPU platform that is able to achieve up to 16× and 26× speedup for the CMA processing of a single 15k × 15k MoM matrix of a perfect electric conductor scatterer and a single 30k × 30k MoM matrix of a dielectric scatterer, respectively. In addition to improving the processing speed of CMA, our approach provided the same accuracy as independent CMA simulations. The speedup, efficiency, and accuracy of our CMA implementation will enable the analysis of electromagnetic systems much larger than what was previously possible at a fraction of the computational time.

Index Terms – Big data applications, characteristic mode analysis, graphics processing unit, method of moments, scalability.

I. INTRODUCTION

The theory of characteristic modes (TCM), also termed characteristic mode analysis (CMA), is a computational technique that is used in a wide range of electromagnetic applications such as antenna design [1–7], electromagnetic compatibility [8–13], and nano-antenna analysis and design [14–17]. The numerical recipe of the CMA implementation involves the numerical analysis of the method of moments (MoM) impedance matrix using operations such as the singular value decomposition (SVD), multiplication, inverse, slicing, and matrix transpose [18]. CMA of electrically large scatterers or multi-scale scatterers with fine details is challenging since it can generate large MoM impedance matrices that can cause out-of-memory issues, limited resource errors, or longer time to execute [19]. Moreover, if an application requires the CMA of hundreds of frequencies to accurately quantify the electromagnetic response over a wide frequency range, terabytes (TBs) of RAM and storage and high-speed processors are needed since CMA typically involves the processing of one dense matrix per frequency. Therefore, CMA creates a *classical big data problem* that needs advanced computer science and Big Data tools to address efficiently.

A wide range of Big Data tools has recently been developed to accelerate matrix operations in different applications. For example, Lee and Cichocki [20] proposed algorithms for calculating SVD on large-scale matrices based on low-rank tensor train decomposition. Their approach outperformed MATLAB and LOBPCG (locally optimal block preconditioned conjugate gradient). Gu *et al*. designed the Marlin library, which includes three matrix multiplication algorithms to improve the efficiency of large matrix computations [21]. Liu and Ansari used Apache Spark for processing matrix inversions to reduce the computation and space complexity of large-scale matrices [22]. They developed a scalable lower−upper decomposition-based block-recursive algorithm called SparkInverse, which outperformed MRInverse [23] and MPInverse [24] on large matrices (e.g., 102,400 × 102,400 matrices). Yu *et al*. developed MatFast, a scalable matrix processing for in-memory distributed cluster on Apache Hadoop [25] and Spark for large-scale matrices [26]. MatFast supports matrix transpose and multiplication. Recently,

Submitted On: June 29, 2021
Accepted On: January 1, 2022

https://doi.org/10.13052/2022.ACES.J.370203

Misra *et al.* developed Stark, which is a distributed matrix multiplication algorithm using Apache Spark for large-scale matrices [27]. Stark is based on Strassen's matrix multiplication scheme, which is faster than the standard one. It was tested on matrices of size up to 16,384 × 16,384. While Stark was faster than Marlin and Spark MLlib [28], it has high space complexity.

In this work, motivated by the computational complexity of CMA [41], we used some of the new open-source software for GPU computing previously mentioned, as well as different Python-based numerical libraries, to accelerate the CMA of large-scale matrices. The performance of Python-based numerical libraries was recently reported for simple matrix operations and in an angle of arrival calculation example [42]. However, to the best of our knowledge, these tools are not commonly used in computational electromagnetic applications, and the novelty in this work is to explore their efficacy in accelerating the CMA implementation. We start our optimization by decomposing the CMA algorithm into basic matrix operations. We perform exhaustive computational experiments to study the optimum numerical library to execute each matrix operation and explore whether each operation is better executed on multi-core CPUs or on a GPU. By allocating the operations accordingly, the acceleration of the CMA can be maximized.

It is important to emphasize that, in this work, we do not use electromagnetic concepts such as the multilevel fast multi-pole approximation (MLFMA) [19] or the symmetry and Toeplitz properties of the MoM matrix for arrays [43] to accelerate the CMA implementation. Moreover, there are alternative electromagnetic decompositions that reduce the computational time and improve the accuracy of the CMA [44]. However, in this work, we develop an alternative approach to accelerate the CMA that is based on brute force computer science techniques. To the best of our knowledge, this work is the first time that the acceleration of the CMA implementation was performed using open-source software for GPU computing. Related work had been recently reported for the acceleration of other electromagnetic techniques such as the MoM and the MLFMA. Yang *et al*. accelerated the MLFMA for more than 10 billion unknowns using 2560 processors and more than 30 TB of RAM [45]. However, in this work, we limit our focus to GPU-based acceleration techniques. To put our CMA acceleration work into context, Table 1 summarizes some of this recent work classified by the electromagnetic method that is accelerated, the maximum size of the impedance matrix considered, the acceleration technique, and the speedup achieved. It is important to emphasize that, for conciseness, we limit Table 1 to the studies that used GPUs to accelerate the frequency-domain MoM and other closely related techniques. Therefore, Table 1 does not include acceleration studies that did not report the use of GPUs or studies that used GPUs to accelerate computational electromagnetic techniques that are not related to the MoM. GPU acceleration of the MoM implementation is also available in commercial solvers such as WIPL-D [46].

The rest of this paper is organized as follows. We begin with an overview of CMA in Section II. In Section III, we present our GPU implementation for CMA using different Python numerical libraries. We present the results, including the computational time and validation of the numerical results, followed by a discussion in Section IV. Section V concludes the paper.

II. OVERVIEW OF CMA

CMA decomposes the total surface current generated on a scatterer into a set of fundamental real and orthogonal modes and calculates the relative importance of each mode at each frequency [47]. The modes can be calculated by solving the eigenvalue problem given by

$$\mathbf{X}\mathbf{J}_n = \lambda_n \mathbf{R}\mathbf{J}_n, \tag{1}$$

where $\mathbf{X}$ and $\mathbf{R}$ are the imaginary and real components of the impedance operator $\mathbf{Z}$ [18]. The vectors $\mathbf{J}n$ are the eigenvectors or the eigen-currents, and λ_n are the eigenvalues. The resulting eigenvalues and eigenvectors are independent of the excitation. By applying the MoM [48], eqn (1) can be converted into the matrix equation:

$$[\mathbf{X}]\,[\mathbf{J}_n] = \lambda_n\,[\mathbf{R}]\,[\mathbf{J}_n]. \tag{2}$$

Two approaches have been reported to obtain the impedance matrix $\mathbf{Z}$, namely, the volume integral equation (VIE) formulation [18] and the surface integral equation (SIE) formulation [47]. In this work, we adopt the SIE formulation that requires the surface discretization of the scatterer.

CMA is applied extensively for conducting bodies [47, 49]. However, applying CMA for complex shapes, composed of one or more dielectric materials, is still under development [50]. The CMA analysis of dielectric materials requires post-processing of the impedance matrix because the solution includes both electric and magnetic induced currents ($\mathbf{J}$ and $\mathbf{M}$). Applying the Galerkin methods to the integral equation of SIE, it can be expressed into the following equivalent system of matrix equations [51]:

$$\begin{bmatrix} \mathbf{Z}^{\mathrm{EJ}} & \mathbf{Z}^{\mathrm{EM}} \\ \mathbf{Z}^{\mathrm{HJ}} & \mathbf{Z}^{\mathrm{HM}} \end{bmatrix} \begin{bmatrix} \mathbf{J} \\ \mathbf{M} \end{bmatrix} = \begin{bmatrix} \mathbf{V}^{\mathrm{E}} \\ \mathbf{V}^{\mathrm{H}} \end{bmatrix} \tag{3}$$

To solve the equation for only the electric currents, the system of the matrix in eqn (3) can be modified by replacing the magnetic currents in this equation as follows [51]:

$$\mathbf{M} = \left(\mathbf{Z}^{\mathrm{HM}}\right)^{-1} \left(\mathbf{V}^{\mathrm{H}} - \mathbf{Z}^{\mathrm{HJ}}\mathbf{J}\right). \tag{4}$$

Table 1: Review of recent research on the acceleration of various electromagnetic techniques

Ref.	Electromagnetic technique/comments	Maximum size of the impedance matrix	Acceleration technique	Speedup ratio (with respect to single CPU)		
				Impedance matrix assembly	Solution of linear system	Total
[29]	Conventional MoM/ Single precision NVIDIA GeForce 7600GT (675 MHz) GPU with 256 MB video memory and an AMD Athlon 64 3000+ (1.81 GHz) CPU with 1 GB memory	~ 9.9k	GPU acceleration on Brook platform	17.33	NA	NA
[30]	Conventional MoM/ Complex double-precision A CUDA-capable device, GeForce GTX 280 built on the GT200 architecture was used	~ 7.7k	GPU CUDA acceleration	~ 140	~ 13	~ 45
[31]	Conventional MoM/ Complex double-precision Intel Core i7, GeForce GTX 275 and the CUDA API, PGI Fortran+CULA, Intel Fortran + MKL were used	~ 7k	GPU CUDA acceleration	~ 9	~ 5	~ 6
[32]	Conventional MoM/ Complex double-precision NVIDIA GT200 (GeForce GTX 275) CUDA-capable device was used as an external math coprocessor to the host CPU (2.66-GHz Intel Core i7)	~ 7k	GPU CUDA acceleration	~ 13	~ 5	~ 8.5
[33]	Conventional MoM/ Single precision Intel Core i7 CPU 930 @2.8GHz, 24 GB of RAM, Windows 7 Professional 64-bit. Up to three identical GPUs GeForce GTX 480, 1536 MB of VRAM (each), VRAM access speed 177 GB/s. Four hard-disk drives (HDD) with I/O speed 100 MB/s (per HDD, without buffering).	~ 152k	Out-of-core solver accelerated with multiple GPUs	NA	NA	20
[34]	Single-level fast multi-pole method (FMM) Complex double-precision Multi-node GPU cluster of 13 nodes, and Nvidia Tesla M2090 GPU per node. An MVAPICH2 implementation of MPI was used for cluster parallel programming.	~ 245k	13 nodes GPU cluster	NA	NA	~ 700
[35]	MLFMA Single precision The CPU-MLFMA is parallelized and executed by eight threads on a workstation with a four-core Intel Xeon processor W3550 (with a clock speed of 3.06 GHz). The OpenMP-CUDA-MLFMA is executed on four Nvidia Tesla C2050 GPUs.	~ 342k	OpenMP-CUDA on multiple GPUs	124	NA	21
[36]	Higher-order MoM (HMoM)/ Complex double-precision A Dell Precision 5400 equipped with two Intel Xeon quad-core CPUs (2.5 GHz clock speed), 16 GB RAM, and one NVIDIA GTX 660 GPU card was used. GPU's architecture is Kepler GK104 with a core frequency of 1015 MHz, 960 Stream Processors (SPs). CUDA version 4.2 was used.	~ 70k	Optimized parallel out-of-core LU solver on hybrid GPU/CPU platform	6	9.78	NA
[37]	FMM-FFT/ Dual Xeon system with four R9 280X cards	~ 1100k	GPU/CPU hybrid platform	NA	NA	~ 30
[38]	MLFMA/ Single precision Intel i7 processor with 8 GB RAM, a TESLA C2075 GPU with 6 GB of RAM, a Windows 7 64-bit license, and the 3.1 CUDA toolkit were used.	~ 694k	Parallelization using CUDA	189	–	84
[39]	Load-balanced out-of-GPU memory implementation of MoM/ Double-precision Intel quad-core i7 3820 CPU running at 3.6 GHz with64 GB RAM, and a GeForce GTX 680 GPU with 4 GB of on-board memory running at 1006 MHz were used	–	GPU CUDA acceleration	2.21 (when compared to four-core CPU)	NA	NA
[40]	MoM Intel Xeon E5-2698 v3 processor with 16 cores and 25 GB of RAM and an NVIDIA Tesla K40 GPU were used	~ 1M	FMM/GPU	NA	2.5	NA

Substituting eqn (4) back into eqn (3), it can be expressed as [51]

$$\left[\mathbf{Z}^{\mathrm{EJ}}-\mathbf{Z}^{\mathrm{EM}}\left(\mathbf{Z}^{\mathrm{HM}}\right)^{-1}\mathbf{Z}^{\mathrm{HJ}}\right]\mathbf{J}=\mathbf{V}^{\mathrm{E}}-\mathbf{Z}^{\mathrm{EM}}\left(\mathbf{Z}^{\mathrm{HM}}\right)^{-1}\mathbf{V}^{\mathrm{H}}. \tag{5}$$

From eqn (5), a new effective impedance matrix can be expressed as

$$\mathbf{Z}^{\mathrm{E}}=\mathbf{Z}^{\mathrm{EJ}}-\mathbf{Z}^{\mathrm{EM}}\left(\mathbf{Z}^{\mathrm{HM}}\right)^{-1}\mathbf{Z}^{\mathrm{HJ}}. \tag{6}$$

It is worth noting that the previous equation involves the processing of complex matrices. Most of the conventional Big Data tools can only handle pure-real matrices, especially on GPUs. However, recently, Big Data tools were developed to handle complex matrices on GPU [52]. Therefore, one of the main contributions of this work is to identify, in the following sections, the Big Data tools compatible with complex matrices necessary for the CMA of dielectric scatterers, as shown in eqn (6) [51]. Using the new equivalent impedance matrix shown in eqn (6), a new generalized eigenvalue equation can be formulated by [51]

$$[\mathbf{X}^{\mathrm{E}}][\mathbf{J}_n]=\lambda_n[\mathbf{R}^{\mathrm{E}}][\mathbf{J}_n], \tag{7}$$

where λ_n and $\mathbf{J}n$ are the eigenvalues and eigenvectors calculated using $\mathbf{R}^E$ and $\mathbf{X}^E$, which are the real and imaginary parts, respectively, of the equivalent impedance matrix $\mathbf{Z}^E$. The eigenvalues λ_n can be used to calculate the modal significance MSn of each mode as

$$\mathrm{MS}n=1/|1+j\lambda_{\mathrm{n}}|. \tag{8}$$

The modal significance is independent of the excitation, and it identifies the relative weight of each mode at any given frequency. The modal significance varies between 0 and 1, reaching 1 typically at the resonance frequency of the mode [14]. It is important to emphasize that there are alternative implementations for performing the CMA of dielectric scatterers. Huang *et al.* performed an excellent review and comparison in [53]. However, the goal of this work is to explore GPU-based acceleration, and the techniques developed herein have the potential to yield similar acceleration levels in alternative dielectric CMA implementations.

A scatterer that is highly complex in shape or electrically large needs a detailed mesh that yields a large MoM impedance matrix containing thousands of rows and columns. These matrices consume gigabytes of disk space and RAM for storage during analysis. Computing CMA for hundreds of frequencies needs the analysis of hundreds of large MoM impedance matrices, which also pose a Big Data challenge.

With the availability of high-end CPUs and hardware accelerators such as GPUs, one can cope with the Big Data challenge in CMA. CPU cores and GPUs provide internal parallelism inside their architecture [54]. This can speed up the matrix computations in CMA. A GPU computing platform provides promising support toward improving resource utilization [54]. Today, open-source software such as TensorFlow [55], designed originally for large-scale machine learning, and Python libraries such as NumPy [52] and CuPy [56] can be exploited for CMA.

Thus, a hybrid CPU/GPU platform provides ample opportunities to test different techniques for accelerating different matrix operations using open-source software that can handle large datasets.

Algorithm 1 CMA pseudocode based on Harrington's method [18]

Input: Real part of input MoM matrix $\mathbf{R}$, imaginary part of input MoM matrix $\mathbf{X}$, matrix size n_cols
Result: Eigenvalues λ_n and eigenvectors $\mathbf{J}_n$
Using CPU (TensorFlow):
    read $\mathbf{R}$; read $\mathbf{X}$
Using GPU (CuPy):
    $\mathbf{Z}=\mathbf{R}+\mathbf{X}$ ▷ Create complex matrix
    Slice $\mathbf{Z}$ into four parts $\mathbf{Z}_{EJ}, \mathbf{Z}_{EM}, \mathbf{Z}_{HJ}$, and $\mathbf{Z}_{HM}$
    $\mathbf{ZZ}=\mathbf{Z}_{EJ}-\mathbf{Z}_{EM}*\mathbf{Z}_{HM}^{-1}*\mathbf{Z}_{HJ}$
    $\mathbf{RR}$= real($\mathbf{ZZ}$)
    $\mathbf{XX}$ = imag($\mathbf{ZZ}$)
    $\mathbf{U}, \mathbf{S}, \mathbf{V}$=SVD($\mathbf{RR}$)
    $si=len(\mathbf{S})$
    $u_{11}=\mathbf{S}^{-0.5}$ ▷ $u_{11}=1/sqrt(S)$
    $\mathbf{A}=\mathbf{U}^{\mathbf{T}}*\mathbf{XX}*\mathbf{U}$
    Slice $\mathbf{A}$ into four parts $\mathbf{A}_{11}, \mathbf{A}_{12}, \mathbf{A}_{21}$, and $\mathbf{A}_{22}$
    $\mathbf{B}=u_{11}*(\mathbf{A}_{11}-\mathbf{A}_{12}*\mathbf{A}_{22}^{-1}*\mathbf{A}_{12}^{T})*u_{11}$
    $\mathbf{UB}, \mathbf{SB}, \mathbf{HB}=SVD(\mathbf{B})$
    $\mathbf{VB}=\mathbf{U}*concat(eye(si), (-\mathbf{A}_{22}^{-1}*\mathbf{A}_{12}^{T}))*u_{11}*\mathbf{HB}$
    $\mathbf{J}_n$ = flip $\mathbf{VB}$
    for $jm=1,2,\ldots,n\_cols$ **do**
        $\lambda_n[jm]=imag(\mathbf{J}_n[:,jm]^T*\mathbf{ZZ}*\mathbf{J}_n[:,jm])$
    end for
return

III. ACCELERATION OF THE CMA IMPLEMENTATION ON A GPU PLATFORM

In this section, we develop multiple different CMA implementations using different hardware setups and different numerical libraries. We then perform extensive experiments to identify the optimum implementation for each matrix size and for each hardware setup. We used three different hardware setups for our CMA implementation: (1) a multi-core CPU, (2) a GPU platform, and (3) a hybrid CPU/GPU platform. We used the following numerical libraries: (1) TensorFlow2.0 (TF), (2) Numpy Python library, and (3) CuPy Python library. TF is an open-source platform for machine learning, and it can be executed on both CPUs and GPUs. On a hybrid CPU/GPU platform, TF will assign all operations to the GPU by default. To instruct TF to execute a certain operation on a CPU, the following statement needs to be added before the operation:

```
with tf.device (device name):
```

TF has application programming interfaces (APIs) in several languages such as C++, Python, and Java. In this work, we used Python to implement CMA with TF. The NumPy python library can run on a multi-core CPU, whereas the CuPy python library can only run on GPUs. Therefore, we developed five different CMA evaluations as follows: (1) TF where all matrix operations are executed only on CPUs, (2) TF where all matrix operations are executed only on GPUs, (3) hybrid TF implementation where some matrix operations are executed on CPUs and some matrix operations are executed on GPUs, (4) NumPy where all matrix operations are executed only on CPUs, and (5) CuPy where all matrix operations are executed only on GPUs. The goal is to identify the fastest implementation out of the five for different matrix sizes. Moreover, the five implementations will guide future CMA users who have access to only CPUs or GPUs and will also guide users who prefer to use one of the previously described Python libraries.

Our CMA implementation is based on the method described in Algorithm 1 [18]. We chose this particular implementation since it is capable of accurately handling a wide range of scatterers, including wires and wire-like nanostructures [14]. First, we read the real and imaginary parts of the input MoM matrix using TensorFlow (Lines 3−4). Next, we construct the complex matrix $\mathbf{Z}$ followed by slicing it into four equal parts and then computing $\mathbf{ZZ}$ (Lines 5−10). This step is only performed for dielectric targets following the approach in [51]. For PEC scatterers, this step is skipped, and $\mathbf{ZZ}$ is set equal to $\mathbf{Z}$. The SVD process is then performed (Lines 10 and 11). After that, matrices $\mathbf{A}$ and $\mathbf{B}$ are computed as detailed in Lines 13−16. The remaining steps are to compute the eigenvalues λ_n as shown in Lines 17−22.

Algorithm 2 Mode tracking pseudocode

1: **Input:** Real part of $\mathbf{Z}$ matrix $\mathbf{RR}$, eigenvectors at the previous frequency $\mathbf{oldM}$, no. of requested modes $\mathbf{numM}$
2: **Result:** Ordered eigenvalues $\mathbf{CM}$
3: **for** $im = 1, 2, \ldots,$ $\mathbf{numM}$ **do**
4: **for** $jm = 1, 2, \ldots,$ $\mathbf{numM}$ **do**
5: $\mathbf{CM}[im, jm] = abs(\mathbf{oldM}[:, im]^T * \mathbf{RR} * \mathbf{J}_n[:, jm])$
6: **end for**
7: $[temp, It] = max(\mathbf{CM}[im, :])$
8: **if** $It \neq im$ **then**
9: $temp1 = \lambda_n[It]$
10: $\lambda_n[It] = \lambda_n[im]$
11: $\lambda_n[im] = temp1$
12: $temp2 = \mathbf{J}_n[:, It]$
13: $\mathbf{J}_n[:, It] = \mathbf{J}_n[:, im]$
14: $\mathbf{J}_n[:, im] = temp2$
15: **end if**
16: **end for**
17: **return**

The modes and eigenvalues generated by the CMA (Algorithm 1) are not ordered in the same way over the entire frequency range [57–59]. Mode tracking is, therefore, performed to find the correct mode ordering throughout the frequency range of interest. Our implementation of mode tracking, which can be run on a CPU or a GPU, is based on calculating the correlation between the modes of the current frequency and the modes of the previous frequency [57] (see Algorithm 2).

IV. EXPERIMENTAL SETUP, RESULTS, AND DISCUSSION

In this section, we report the performance of the five CMA implementations previously described. We ran all experiments on CloudLab [60], an experimental testbed for cloud computing. We used a machine in CloudLab's Wisconsin data center with two Intel Xeon E5-2667 8-core CPUs (3.20 GHz) and an NVIDIA Tesla V100 SMX2 GPU (16 GB). All the algorithms were implemented and evaluated using the following software and tools: Linux Ubuntu 16.04, TensorFlow 2.0.0, CUDA 10.0.130, Python 3.7.10., NumPy1.20.1, CuPy 8.3.0, and Pandas 1.2.3.

Table 2 breaks down the computational time for the different CMA matrix operations for a 14k $\times$ 14k matrix using the five implementations previously described: TF on CPU, TF on GPU, TF on hybrid CPU/GPU, NumPy on CPU, and CuPy on GPU. All CPU computational experiments in Table 2 used 32 cores. Comparing the computational time for the TF on CPU and TF on GPU in Table 2, we see that TF on GPU is faster than TF on CPU for all matrix operations except for the SVD and the writing of the eigenvector operation. Therefore, to optimize the TF on a hybrid CPU/GPU platform, we assigned all CMA matrix operations to GPU except the SVD and the writing of the eigenvectors operation, which were assigned to the CPU. Table 2 shows that the TF on hybrid CPU/GPU is faster than the TF on CPU or TF on GPU.

The fourth implementation, NumPy on CPU, is faster than the three TF implementations in Table 2. The main advantage of the NumPy on CPU is its acceleration of the matrix multiplications and the SVD, even though it is slower than TF in terms of the matrix inverse operation and writing the eigenvectors. Finally, the CuPy on GPU is the fastest implementation with a significant acceleration in the matrix multiplication and the SVD compared to the other four implementations. The CuPy on GPU can provide a speedup of 80$\times$ compared to other implementations in Table 2, highlighting the importance of selecting the optimum numerical library for the CMA implementation. The analysis in Table 2 shows that different numerical libraries generate drastic differences in the computation time of different matrix

Table 2: Time distribution (minutes) for 14k × 14k dielectric object over TF CPU, TF-GPU, hybrid TF, NumPy with multi-core CPU, and CuPy with GPU implementation

Matrix operation	TF CPU	TF GPU	TF Hybrid	NumPy with multi-core CPU	CuPy with GPU
Reading the matrix	0.33	0.25	0.28	0.20	0.22
Assembling real and imaginary parts	0.25	0.03	0.03	0.10	0.08
Multiplications	151.07	6.33	6.38	1.22	0.25
Inverse	3	0.03	0.02	0.17	0.05
SVDs	9.78	28.23	9.75	0.92	0.35
Writing eigenvectors	0.27	0.92	0.23	0.93	0.90
Total time	164.83	38.7	16.79	3.45	1.91

Table 3: MOM matrix memory requirements for different formats

Matrix type	Matrix size	CSV file size	Binary file size
4k × 4k	4776 × 4776	1.5 GB	350 MB
14k × 14k	14,183 × 14,183	27 GB	3.0 GB
15k × 15k	15,279 × 15,279	32.4 GB	3.6 GB
16k × 16k	16,608 × 16,608	36 GB	4.2 GB
30k × 30k	33,024 × 33,024	138 GB	16.2 GB

operations, which, to the best of our knowledge, was not documented for large dense MoM matrices processed by CMA. If GPUs are not available, the NumPy implementation provides the fastest implementation of CMA, whereas if GPUs are available, the CuPy implementation is the fastest. Therefore, Table 2 can be used as a guide for choosing the optimum numerical library for any computational electromagnetic technique based on the dominant matrix operations of its algorithm.

To quantify the scalability of the CMA implementation, we tested MoM impedance matrices, of different sizes, generated by the commercial electromagnetic solver FEKO [61]. Matrices of both dielectric and PEC matrices were tested. Details of these matrices, including the matrix size, the size of the CSV file, and the binary file size, are shown in Table 3. We used the binary files storing the MoM matrices for these experiments. The advantage of the binary format is that it requires approximately 10%−20% of the storage hard drive memory required by the ASCII and CSV file formats, as shown in Table 3. This reduction in storage memory is particularly important for the CMA of large MoM matrices and/or for the simulation of many matrices to cover multiple frequencies.

Tables 4 and 5 show the computational time required by our implementation for dielectric and PEC scatterers, respectively. We tested the computational time of the

Table 4: Time taken by our CMA implementations on a multi-core CPU and GPU (minutes) for dielectric

Matrix type	No. of cores used on the multi-core CPU (NumPy)					GPU (CuPy)
	1	4	8	16	32	
4k × 4k	0.88	0.44	0.36	0.34	0.34	0.29
14k × 14k	20.44	6.74	4.38	3.48	3.48	1.90
16k × 16k	33.69	10.81	6.86	5.23	5.26	2.83
30k × 30k	257.13	79.43	47.14	45.11	32.29	15.60

Table 5: Time taken by our CMA implementations on a multi-core CPU and GPU (minutes) for PEC

Matrix type	No. of cores used on the multi-core CPU (NumPy)					GPU (CuPy)
	1	4	8	16	32	
15k × 15k	128.98	38.25	23.82	17.92	18.12	12.38

CMA NumPy implementation using 1, 2, 4, 8, 16, and 32 cores without GPU, and we also added the computational time required when only a GPU and the CuPy implementation were employed. As we increased the number of cores, the computational time decreased. For instance, it took 257 minutes to process the 30k × 30k matrix on 1 core but only 32 minutes on 32 cores. For a PEC scatterer, represented by a 15k × 15k matrix, it took 130 minutes to process the matrix on 1 core but only 18 minutes on 16 cores. Tables 4 and 5 show that moving from 16 cores to 32 cores showed no decrease in the computational time for matrix sizes of 16k × 16k and smaller. Therefore, for matrices that are 16k × 16k and smaller, the maximum speedup is achieved at 16 cores. However, Table 4 shows that, for the 30k × 30k matrix, increasing the number of cores from 16 to 32 lowered the computational time and enhanced the speedup, indicating the potential of our implementation to scale for matrices 30k × 30k and larger.

In Tables 4 and 5, we also report the computational time required by our CMA CuPy implementation on a GPU. While our implementation required around 32.29 minutes to process a 30k × 30k matrix of a dielectric scatterer using a 32-CPU cores, it took only 15.6 minutes on the GPU platform. We also tested our CMA implementation for a PEC scatterer represented by a 15k × 15k matrix. Again, the CMA implementation on a GPU platform was the fastest, as shown in Table 5. Using a GPU achieved a speedup of 16× and 10× for the dielectric and the PEC object, respectively, in comparison to a single CPU core. The computational time and speedup are shown in Figure 1. Moreover, if we do not consider the time needed to write the eigenvectors in the speedup calculations, the speedup will be 26× and 16× for the dielectric and the PEC object, as shown in Figure 2.

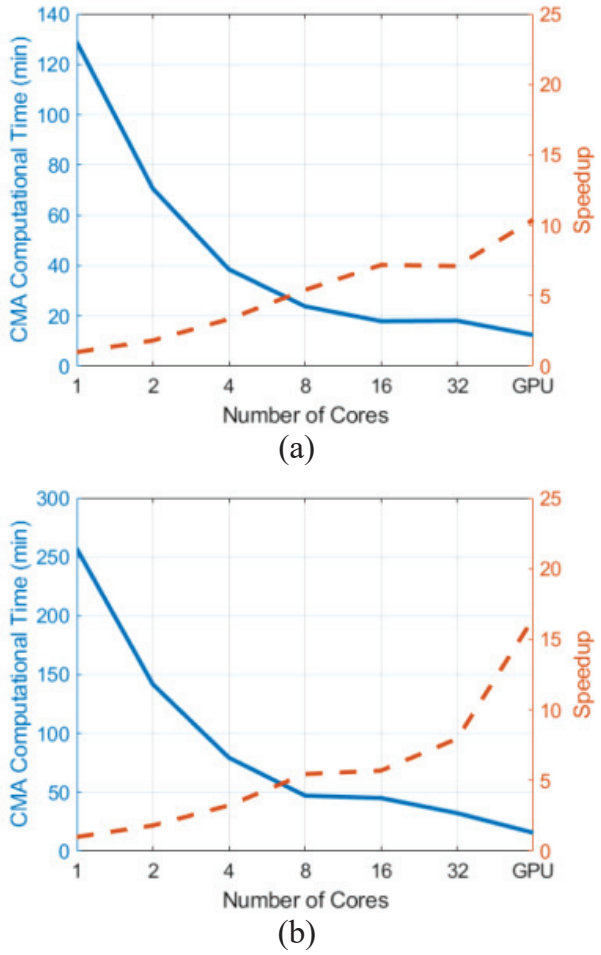

Fig. 1. Speedup and time taken for CMA with writing the eigenvalues and eigenvectors vs. different number of cores for (a) PEC (15k × 15k) and (b) dielectric object (30k × 30k).

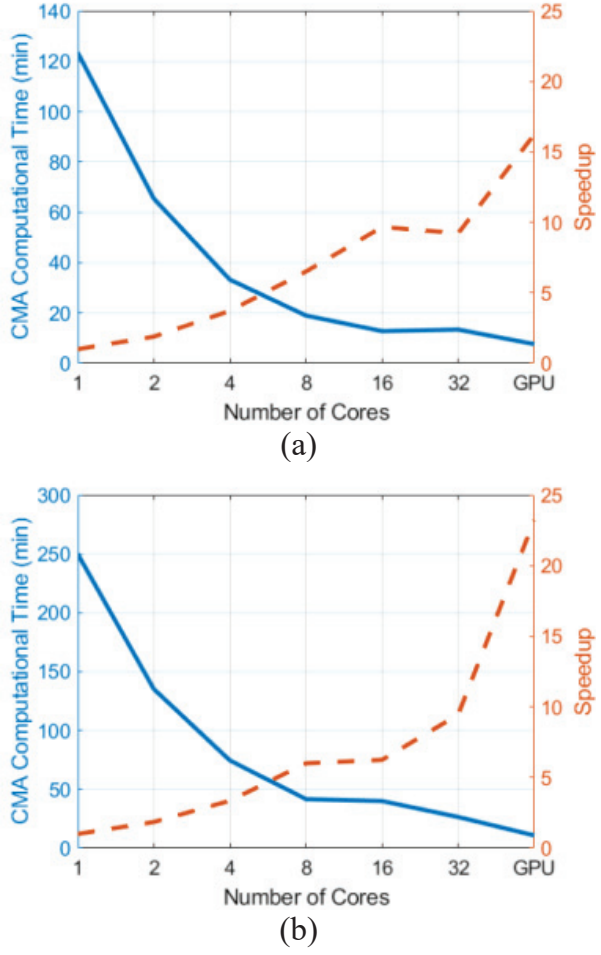

Fig. 2. Speedup and time taken for CMA without writing the eigenvalues and eigenvectors vs. different number of cores for (a) PEC (15k × 15k) and (b) dielectric object (30k × 30k).

Lastly, we validated the numerical results produced by our CMA implementation to demonstrate that it does not compromise accuracy. We tested our implementation for two different cases. For PEC scatterers, we used the horn antenna in [see Figure 3(a)]. The eigenvalues λ_n of the horn antenna calculated using our implementation perfectly match the eigenvalues calculated using FEKO, as shown in Figure 4. We also used a lossless dielectric cylinder of radius 5.25 mm, height 4.6 mm, ε_r = 38, and μ_r = 1 [see Figure 3(b)]. The frequency range was chosen from 4.5 to 7.5 GHz with a 50-MHz interval. This case is often used to verify the results of CMA formulations for real materials [53]. Figure 5 presents the modal significance of the dielectric cylinder, which matches with the results reported by Chen *et al.* [62]. The previous two cases demonstrate the validity of our accelerated CMA implementation.

In this work, we limited our computational experiments to common Big Data tools such as TensorFlow, Python-based CuPy, and Python-based NumPy. Many additional algorithms have been previously reported for speeding matrix operations [63, 64]. In future work, we plan to investigate these implementations and

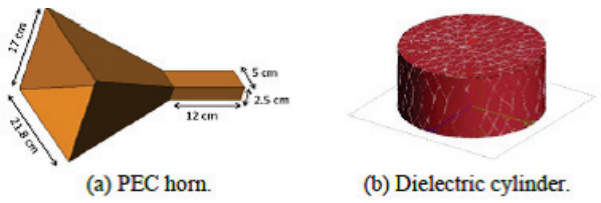

Fig. 3. Different scatterers used to validate the accuracy of our accelerated CMA implementation. (a) PEC horn antenna. (b) Dielectric cylinder.

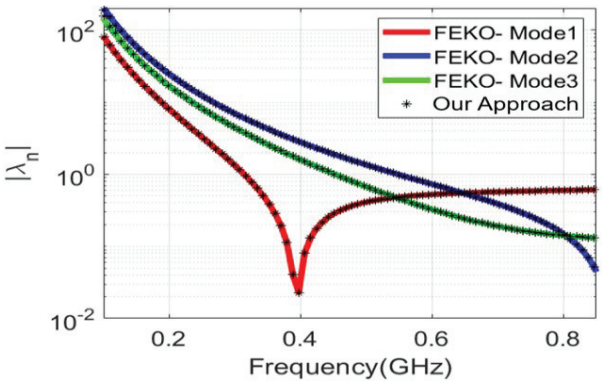

Fig. 4. Eigenvalues for a horn-shaped PEC.

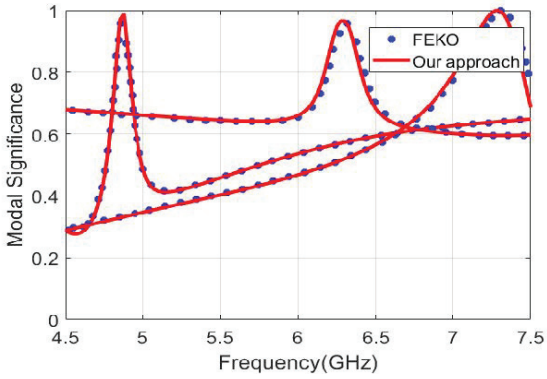

Fig. 5. Modal significance for a cylinder-shaped dielectric.

other alternatives, for further acceleration of the CMA implementation.

V. CONCLUSION

In this paper, we tested different numerical implementations of the CMA algorithm using open-source software for GPU computing. We showed that different numerical implementations can have drastically different computational times for the different matrix operations that make up the CMA algorithm. Therefore, it is important to select the optimum numerical library since the computational time can vary for large matrices by up to approximately two orders of magnitude. From our computational experiments, we showed that the CuPy implementation on GPU delivered the largest speedup. In comparison to the execution on a single CPU core, the CuPy implementation on GPU was capable of achieving 26× and 16× speedup for processing a single MoM matrix of a dielectric and a PEC object, respectively. In addition to faster execution, our implementation provided the same accuracy as theoretical solutions and independent commercial CMA simulations.

ACKNOWLEDGMENT

Khulud Alsultan would like to acknowledge the support of the Saudi Arabian Cultural Mission. This work was supported in part by Office of Naval Research (ONR) grants: #N00014-17-1-2932 and #N00014-17-1-3016. "Distribution Statement A. – Approved for public release. Distribution is unlimited."

REFERENCES

[1] M. Cabedo-Fabres, E. Antonino-Daviu, A. Valero-Nogueira, and M. F. Bataller, "The theory of characteristic modes revisited: A contribution to the design of antennas for modern applications," *IEEE Antennas and Propagation Magazine*, vol. 49, no. 5, pp. 52–68, 2007.

[2] M. Vogel, G. Gampala, D. Ludick, U. Jakobus, and C. Reddy, "Characteristic mode analysis: Putting physics back into simulation," *IEEE Antennas and Propagation Magazine*, vol. 57, no. 2, pp. 307–317, 2015.

[3] G. Angiulli, G. Amendola, and G. Di Massa, "Application of characteristic modes to the analysis of scattering from microstrip antennas," *Journal of Electromagnetic Waves and Applications*, vol. 14, no. 8, pp. 1063–1081, 2000.

[4] L. Guan, Z. He, D. Ding, and R. Chen, "Efficient characteristic mode analysis for radiation problems of antenna arrays," *IEEE Transactions on Antennas and Propagation*, vol. 67, no. 1, pp. 199–206, 2019.

[5] N. Michishita and H. Morishita, "Helmet antenna design using characteristic mode analysis," *Applied Computational Electromagnetics Society (ACES) Journal*, vol. 35, no. 2, p. 6, 2020.

[6] M. M. Elsewe and D. Chatterjee, "Ultra-wide bandwidth enhancement of single-layer single-feed patch antenna using the theory of characteristic modes," *Applied Computational Electromagnetics Society (ACES) Journal*, vol. 33, no. 3, p. 4, 2018.

[7] A. Araghi and G. Dadashzadeh, "Detail-oriented design of a dual-mode antenna with orthogonal radiation patterns utilizing theory of characteristic modes," *Applied Computational Electromagnetics Society (ACES) Journal*, vol. 28, no. 10, p. 8, 2013.

[8] Q. Wu, H.-D. Bruns, and C. Schuster, "Characteristic mode analysis of radiating structures in digital systems," *IEEE Electromagnetic Compatibility Magazine*, vol. 5, no. 4, pp. 56–63, 2016.

[9] X. Yang, Y. S. Cao, X. Wang, L. Zhang, S. He, H. Zhao, J. Hu, L. Jiang, A. Ruehli, J. Fan, and J. L. Drewniak, "EMI radiation mitigation for heatsinks using characteristic mode analysis," *in 2018 IEEE Symposium on Electromagnetic Compatibility, Signal Integrity and Power Integrity (EMC, SI & PI)*. IEEE, pp. 374–378, 2018.

[10] S. H. Yeung and C.-F. Wang, "Exploration of characteristic mode theory for electromagnetic compatibility modeling," *in 2018 IEEE International Symposium on Electromagnetic Compatibility and 2018 IEEE Asia-Pacific Symposium on Electromagnetic Compatibility (EMC/APEMC)*. IEEE, pp. 1278–1282, 2018.

[11] M. Z. Hamdalla, B. Bissen, A. N. Caruso, and A. M. Hassan, "Experimental validations of characteristic mode analysis predictions using GTEM measurements," *in 2020 IEEE International Symposium on Antennas and Propagation and USNC-URSI Radio Science Meeting*. IEEE, 2020.

[12] M. Z. Hamdalla, A. M. Hassan, and A. N. Caruso, "Characteristic mode analysis of the effect of the UAV frame material on coupling and interference," *in 2019 IEEE International Symposium on Antennas and Propagation and USNC-URSI Radio Science Meeting*. IEEE, pp. 1497–1498, 2019.

[13] M. Z. Hamdalla, A. M. Hassan, A. Caruso, J. D. Hunter, Y. Liu, V. Khilkevich, and D. G. Beetner, "Electromagnetic interference of unmanned aerial vehicles: A characteristic mode analysis approach," *in 2019 IEEE International Symposium on Antennas and Propagation and USNC-URSI Radio Science Meeting*. IEEE, pp. 553–554, 2019.

[14] A. M. Hassan, F. Vargas-Lara, J. F. Douglas, and E. J. Garboczi, "Electromagnetic resonances of individual single-walled carbon nanotubes with realistic shapes: A characteristic modes approach," *IEEE Transactions on Antennas and Propagation*, vol. 64, no. 7, pp. 2743–2757, 2016.

[15] P. Ylä-Oijala, D. C. Tzarouchis, E. Raninen, and A. Sihvola, "Characteristic mode analysis of plasmonic nanoantennas," *IEEE Transactions on Antennas and Propagation*, vol. 65, no. 5, pp. 2165–2172, 2017.

[16] K. C. Durbhakula, A. M. Hassan, F. Vargas-Lara, D. Chatterjee, M. Gaffar, J. F. Douglas, and E. J. Garboczi, "Electromagnetic scattering from individual crumpled graphene flakes: a characteristic modes approach," *IEEE Transactions on Antennas and Propagation*, vol. 65, no. 11, pp. 6035–6047, 2017.

[17] S. Dey, D. Chatterjee, E. J. Garboczi, and A. M. Hassan, "Plasmonic nanoantenna optimization using characteristic mode analysis," *IEEE Transactions on Antennas and Propagation*, vol. 68, no. 1, pp. 43–53, 2019.

[18] R. Harrington and J. Mautz, "Computation of characteristic modes for conducting bodies," *IEEE Transactions on Antennas and Propagation*, vol. 19, no. 5, pp. 629–639, 1971.

[19] Q. I. Dai, J. Wu, H. Gan, Q. S. Liu, W. C. Chew, and E. Wei, "Large-scale characteristic mode analysis with fast multipole algorithms," *IEEE Transactions on Antennas and Propagation*, vol. 64, no. 7, pp. 2608–2616, 2016.

[20] N. Lee and A. Cichocki, "Big data matrix singular value decomposition based on low-rank tensor train decomposition," *in International Symposium on Neural Networks*. Springer, pp. 121–130, 2014.

[21] R. Gu, Y. Tang, Z. Wang, S. Wang, X. Yin, C. Yuan, and Y. Huang, "Efficient large scale distributed matrix computation with Spark," *in 2015 IEEE International Conference on Big Data (Big Data)*. IEEE, pp. 2327–2336, 2015.

[22] J. Liu, Y. Liang, and N. Ansari, "Spark-based large-scale matrix inversion for big data processing," *IEEE Access*, vol. 4, pp. 2166– 2176, 2016.

[23] J. Xiang, H. Meng, and A. Aboulnaga, "Scalable matrix inversion using mapreduce," *in Proceedings of the 23rd International Symposium on High-Performance Parallel and Distributed Computing*, pp. 177–190, 2014.

[24] L. S. Blackford, J. Choi, A. Cleary, E. D'Azeuedo, J. Demmel, I. Dhillon, S. Hammarling, G. Henry, A. Petitet, K. Stanley, D. Walker, R. C. Whaley, and J. J. Dongarra, ScaLAPACK User's Guide. USA: Society for Industrial and Applied Mathematics, 1997.

[25] T. White, Hadoop: The Definitive Guide, 1st ed. O'Reilly Media, Inc., 2009.

[26] Y. Yu, M. Tang, W. G. Aref, Q. M. Malluhi, M. M. Abbas, and M. Ouzzani, "In-memory distributed matrix computation processing and optimization," *in 2017 IEEE 33rd International Conference on Data Engineering (ICDE)*. IEEE, pp. 1047–1058, 2017.

[27] C. Misra, S. Bhattacharya, and S. K. Ghosh, "Stark: Fast and scalable Strassen's matrix multiplication using Apache Spark," IEEE Transactions on Big Data, 2020.

[28] X. Meng, J. Bradley, B. Yavuz, E. Sparks, S. Venkataraman, D. Liu, J. Freeman, D. Tsai, M. Amde, S. Owen, D. Xin, X. Reynold, M. Franklin, R. Zadeh, M. Zaharia, and A. Talwalkar, "Mllib: machine learning in apache spark," *The Journal of Machine Learning Research*, vol. 17, no. 1, pp. 1235–1241, 2016.

[29] S. Peng and Z. Nie, "Acceleration of the method of moments calculations by using graphics processing units," *IEEE Transactions on Antennas and Propagation*, vol. 56, no. 7, pp. 2130–2133, 2008.

[30] E. Lezar and D. B. Davidson, "GPU-accelerated method of moments by example: Monostatic

scattering," *IEEE Antennas and Propagation Magazine*, vol. 52, no. 6, pp. 120–135, 2010.

[31] T. Topa, A. Karwowski, and A. Noga, "Using GPU with CUDA to accelerate MoM-based electromagnetic simulation of wiregrid models," *IEEE Antennas and Wireless Propagation Letters*, vol. 10, pp. 342–345, 2011.

[32] T. Topa, A. Noga, and A. Karwowski, "Adapting MoM with RWG basis functions to GPU technology using CUDA," *IEEE Antennas and Wireless Propagation Letters*, vol. 10, pp. 480–483, 2011.

[33] D. P. Zoric, D. I. Olcan, and B. M. Kolundzija, "Solving electrically large EM problems by using out-of-core solver accelerated with multiple graphical processing units," *in 2011 IEEE International Symposium on Antennas and Propagation (APSURSI)*. IEEE, pp. 1–4, 2011.

[34] Q. M. Nguyen, V. Dang, O. Kilic, and E. El-Araby, "Parallelizing fast multipole method for large-scale electromagnetic problems using GPU clusters," *IEEE Antennas and Wireless Propagation Letters*, vol. 12, pp. 868–871, 2013.

[35] J. Guan, S. Yan, and J.-M. Jin, "An openMP-CUDA implementation of multilevel fast multipole algorithm for electromagnetic simulation on multi-GPU computing systems," *IEEE Transactions on Antennas and Propagation*, vol. 61, no. 7, pp. 3607–3616, 2013.

[36] X. Mu, H.-X. Zhou, K. Chen, and W. Hong, "Higher order method of moments with a parallel out-of-core LU solver on GPU/CPU platform," *IEEE Transactions on Antennas and Propagation*, vol. 62, no. 11, pp. 5634–5646, 2014.

[37] M. J. Miranda, T. Ö zdemir, and R. J. Burkholder, "Hardware acceleration of an FMM-FFT solver using consumer-grade GPUs," *in 2016 United States National Committee of URSI National Radio Science Meeting (USNC-URSI NRSM)*. IEEE, pp. 1–2, 2016.

[38] E. Garćıa, C. Delgado, L. Lozano, and F. Ćatedra, "Efficient strategy for parallelisation of multilevel fast multipole algorithm using CUDA," *IET Microwaves, Antennas & Propagation*, vol. 13, no. 10, pp. 1554–1563, 2019.

[39] T. Topa, "Load-balanced fortran-based out-of-GPU memory implementation of the method of moments," *IEEE Antennas and Wireless Propagation Letters*, vol. 16, pp. 813–816, 2017.

[40] R. Adelman, N. A. Gumerov, and R. Duraiswami, "FMM/GPUaccelerated boundary element method for computational magnetics and electrostatics," *IEEE Transactions on Magnetics*, vol. 53, no. 12, pp. 1–11, 2017.

[41] K. Alsultan, P. Rao, A. Caruso, and A. Hassan, "Scalable Characteristic Mode Analysis: Requirements and Challenges," *in Large Scale Networking (LSN) Workshop on Huge Data: A Computing, Networking and Distributed Systems Perspective*, pp. 1–2, 2020.

[42] A. Weiss and A. Elsherbeni, "Computational performance of matlab and python for electromagnetic applications." *Applied Computational Electromagnetics Society (ACES) Journal*, vol. 35, no. 11, 2020.

[43] S. Kaffash, R. Faraji-Dana, M. Shahabadi, and S. Safavi-Naeini, "A fast computational method for characteristic modes and eigenvalues of array antennas," *IEEE Transactions on Antennas and Propagation*, 2020.

[44] D. Tayli, M. Capek, L. Akrou, V. Losenicky, L. Jelinek, and M. Gustafsson, "Accurate and efficient evaluation of characteristic modes," *IEEE Transactions on Antennas and Propagation*, vol. 66, no. 12, pp. 7066–7075, 2018.

[45] M.-L. Yang, B.-Y. Wu, H.-W. Gao, and X.-Q. Sheng, "A ternary parallelization approach of mlfma for solving electromagnetic scattering problems with over 10 billion unknowns," *IEEE Transactions on Antennas and Propagation*, vol. 67, no. 11, pp. 6965– 6978, 2019.

[46] B. L. Mrdakovic, M. M. Kostic, D. I. Olcan, and B. M. Kolundzija, "New generation of wipld in-core multi-gpu solver," *in 2018 IEEE International Symposium on Antennas and Propagation & USNC/URSI National Radio Science Meeting*. IEEE, pp. 413–414, 2018.

[47] Y. Chang and R. Harrington, "A surface formulation for characteristic modes of material bodies," *IEEE Transactions on Antennas and Propagation*, vol. 25, no. 6, pp. 789–795, 1977.

[48] R. F. Harrington, "Matrix methods for field problems," Proceedings of the IEEE, vol. 55, no. 2, pp. 136–149, 1967.

[49] M. Khan and D. Chatterjee, "Characteristic mode analysis of a class of empirical design techniques for probe-fed, U-slot microstrip patch antennas," *IEEE Transactions on Antennas and Propagation*, vol. 64, no. 7, pp. 2758–2770, 2016.

[50] Q. Wu, "Characteristic mode assisted design of dielectric resonator antennas with feedings," *IEEE Transactions on Antennas and Propagation*, vol. 67, no. 8, pp. 5294–5304, 2019.

[51] Y. Chen and C.-F. Wang, "Surface integral equation based characteristic mode formulation for dielectric resonators," *in 2014 IEEE Antennas and Propagation Society International Symposium (APSURSI)*. IEEE, pp. 846–847, 2014.

[52] T. E. Oliphant, A guide to NumPy. Trelgol Publishing USA, vol. 1, 2006.

[53] S. Huang, J. Pan, C.-F. Wang, Y. Luo, and D. Yang, "Unified implementation and cross-validation of the integral equationbased formulations for the characteristic modes of dielectric bodies," *IEEE Access*, vol. 8, pp. 5655–5666, 2019.

[54] S. Mittal and J. S. Vetter, "A survey of CPU-GPU heterogeneous computing techniques," *ACM Computing Surveys (CSUR)*, vol. 47, no. 4, pp. 1–35, 2015.

[55] M. Abadi, A. Agarwal, P. Barham, E. Brevdo, Z. Chen, C. Citro, G. S. Corrado, A. Davis, J. Dean, M. Devin, S. Ghemawat, I. Goodfellow, A. Harp, G. Irving, M. Isard, Y. Jia, R. Jozefowicz, L. Kaiser, M. Kudlur, J. Levenberg, D. Mane, R. Monga, S. Moore, D. Murray, C. Olah, M. Schuster, J. Shlens, B. Steiner, I. Sutskever, K. Talwar, P. Tucker, V. Vanhoucke, V. Vasudevan, F. Viegas, O. Vinyals, P. Warden, M. Wattenberg, M. Wicke, Y. Yu, and X. Zheng, "Tensorflow: Large-scale machine learning on heterogeneous distributed systems," arXiv preprint arXiv:1603.04467, 2016.

[56] R. Nishino and S. H. C. Loomis, "Cupy: A numpy-compatible library for NVIDIA GPU calculations," *in Proceedings of Workshop on Machine Learning Systems (LearningSys) in the Thirty first Annual Conference on Neural Information Processing Systems (NIPS)*, 2017.

[57] M. Capek, P. Hazdra, P. Hamouz, and J. Eichler, "A method for tracking characteristic numbers and vectors," *Progress In Electromagnetics Research*, vol. 33, pp. 115–134, 2011.

[58] J. Zhu, W. Li, and L. Zhang, "Broadband Tracking of Characteristic Modes," *Applied Computational Electromagnetics Society (ACES) Journal*, vol. 34, no. 11, p. 6, 2019.

[59] Q. He, Z. Gong, H. Ke, and L. Guan, "A Double Modal Parameter Tracking Method To Characteristic Modes Analysis," *Applied Computational Electromagnetics Society (ACES) Journal*, vol. 32, no. 12, p. 8, 2017.

[60] D. Duplyakin, R. Ricci, A. Maricq, G. Wong, J. Duerig, E. Eide, L. Stoller, M. Hibler, D. Johnson, K. Webb, A. Akella, K. Wang, G. Ricart, L. Landweber, C. Elliott, M. Zink, E. Cecchet, S. Kar, and P. Mishra, "The design and operation of CloudLab," in 2019 USENIX Annual Technical Conference (USENIX ATC 19). Renton, WA: USENIX Association, pp. 1–14, Jul. 2019. [Online]. Available: https://www.usenix.org/conference/atc19/presentation/duplyakin

[61] 2021. [Online]. Available: https://www.altair.com/feko/

[62] Y. Chen, "Alternative surface integral equation-based characteristic mode analysis of dielectric resonator antennas," *IET Microwaves, Antennas & Propagation*, vol. 10, no. 2, pp. 193– 201, 2016.

[63] R. Solca, A. Haidar, S. Tomov, T. C. Schulthess, and J. Dongarra, "Poster: A novel hybrid cpu-gpu generalized eigensolver for electronic structure calculations based on fine grained memory aware tasks," *in 2012 SC Companion: High Performance Computing, Networking Storage and Analysis*. IEEE, pp. 1340–1340, 2012.

[64] D. Liu, R. Li, D. J. Lilja, and W. Xiao, "A divide-and-conquer approach for solving singular value decomposition on a heterogeneous system," *in Proceedings of the ACM International Conference on Computing Frontiers*, pp. 1–10, 2013.

Khulud Alsultan received the B.S. degree in computer science from King Saud University, Riyadh, Saudi Arabia in 2006, the M.Sc. degree in computer science from Kent State University, Kent, OH, USA, in 2013, and the Ph.D. degree in computer science and telecommunication and computer networking from the University of Missouri-Kansas City, Kansas City, MO, USA, in 2021.

She is currently a Lecturer with the Department of Computer Science, King Saud University (KSU). Her research interest includes Big Data and data analysis, and its applications in healthcare and electrical engineering. She served as an external reviewer for several conferences, such as *BEXA 2019* and *BDA 2019*. While being an active researcher, she obtained the Preparing Future Faculty program (PFF) graduate certificate at UMKC. Moreover, Dr. Alsultan received awards including the Grace Hopper Celebration Student Scholarship in 2018, and the Graduate Student Travel Grant, UMKC, Kansas City, MO, USA, in 2019.

Mohamed Hamdalla received the B.Sc. and M.Sc. degrees from the Arab Academy for Science, Technology and Maritime Transport, Alexandria, Egypt, in 2012 and 2016, respectively, both in electronics and communications engineering, and the Ph.D. degree in electrical engineering from the University of Missouri-Kansas City, Kansas City, MO, USA, in 2021.

His current research interests include antennas, metamaterials, microwave filters, electromagnetic compatibility and interference, characteristic mode theory, and applications.

Sumitra Dey received the B.Tech. degree in radio physics and electronics from the University of Calcutta, Kolkata, India, in 2014, the M.Tech. degree in RF and microwave communication engineering from IIEST Shibpur, West Bengal, India, in 2016, and the Ph.D. degree in electrical engineering from the University of Missouri-Kansas City, Kansas City, MO, USA, in 2021.

She is currently a Lead Product Engineer with Multiphysics System Analysis Group, Cadence Design Systems, San Jose, CA, USA. Her research interests include computational electromagnetics, signal/power integrity in high frequency, nano-electromagnetics, nondestructive evaluation, experimental microwave and terahertz imaging, AI/ML based optimization of electromagnetic response, multilayer Green's functions, characteristic mode theory, and applications.

Dr. Dey was awarded the Honorable Mention in Student paper competition in *2020 Applied Computational Electromagnetic Society (ACES) Conference*, Monterey, CA, USA, Honorable Mention in Student paper competition in *2019 IEEE APS/USNC URSI Symposium*, Atlanta, GA, USA, Honorable Mention in 2018 Altair FEKO Student Design Competition, and the Best Student Paper in *IEEE CALCON 2015*, Kolkata, India.

Praveen Rao received the M.S. and Ph.D. degrees in computer science from the University of Arizona, Tucson, AZ, USA, in 2007 and 2001, respectively.

He is currently a tenured Associate Professor with joint appointment in the Department of Health Management & Informatics and the Department of Electrical Engineering & Computer Science at the University of Missouri (MU), Columbia, MO, USA. His research interests are in the areas of Big Data management, data science, health informatics, and cybersecurity. He directs the Scalable Data Science (SDS) Lab at MU. His research, teaching, and outreach activities have been supported by the National Science Foundation (NSF), Air Force Research Lab (AFRL), the National Endowment for the Humanities (NEH), the National Institutes of Health (NIH), the University of Missouri System (Tier 1 grant, Tier 3 grant), University of Missouri Research Board, and companies. He is a Co-PI for the NSF IUCRC Center for Big Learning. At MU, he is a core faculty of the Center for Biomedical Informatics (CBMI), the Cybersecurity Center, the MU Institute for Data Science and Informatics, and the CERI Center. He is a core scientist of the Washington University Center for Diabetes Translation Research funded by NIH. He is a Senior Member of the ACM (2020) and IEEE (2015).

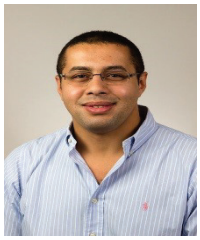

Ahmed M. Hassan received the B.Sc. (with highest honors) and M.Sc. degrees from Cairo University, Giza, Egypt, in 2004 and 2006, respectively, both in electronics and communications engineering. He received the Ph.D. degree in electrical engineering from the University of Arkansas, Fayetteville, AR, USA, in 2010.

From 2011 to 2012, he was a Postdoctoral Researcher with the Department of Electrical Engineering, University of Arkansas. From 2012 to 2015, he was a Postdoctoral Researcher with the National Institute of Standards and Technology, Gaithersburg, MD, USA. He is currently an Assistant Professor with the Computer Science Electrical Engineering Department, University of Missouri-Kansas City. His current research interests include nanoelectromagnetics, bioelectromagnetics, electromagnetic compatibility and interference, nondestructive evaluation, experimental microwave, and terahertz imaging.

A Difference Subgridding Method for Solving Multiscale Electro-Thermal Problems

Xiaoyan Zhang, Ruilong Chen, and Aiyun Zhan

School of Information Engineering
East China Jiaotong University, Nanchang 330013, China
xy_zhang3129@ecjtu.edu.cn, 2465246593@qq.com, 707290432@qq.com

***Abstract* –** Because of less memory costs and time consumption, a finite difference subgrid technique can effectively deal with multiscale problems in electromagnetic fields. When used in Maxwell equation, symmetric elements of the matrix are required; otherwise, the algorithm will be unstable. Usually, the electro-thermal problem also contains multiscale structures. However, the coefficient matrix of the heat transfer equation is asymmetric because the parameters of the equation vary with temperature and the Robbin boundary condition is used as well. In this paper, a three-dimensional (3D) finite difference subgridding method is proposed to simulate the electro-thermal coupling process of the multiscale circuits. The stability condition of the algorithm is deduced with a matrix method. And the efficiency and the effectiveness of the proposed subgridding approach are verified through square- and *n*-shaped resistances. Compared with the results of the COMSOL software and the traditional finite difference method (FDM), the proposed subgridding method has less unknowns and faster speed.

***Index Terms* –** Electro-thermal problems, finite-difference method (FDM), multiscale, subgridding method.

I. INTRODUCTION

With the increase of the integration of the electronic components, Joule heat of the circuits becomes a severe problem; sometimes, it will lead to the decline of the reliability of the circuit [1, 2]. In order to solve this problem, the variation of the electromagnetic component parameters with the temperature [1–4], the distribution of the temperature in the circuit [5–7], and the influence of the high temperature on circuit performance [1, 2, 8] arouse the researchers' study interests to guide circuit design and improve its stability. The difficulty of this study is that the electricity is the cause of the Joule heat, and the heat will affect the electrical parameters in return. They are coupled with each other.

Using the commercial software COMSOL to establish an electro-thermal model is one of the effective methods to solve this issue [9, 10]. However, the COMSOL is based on a finite-element method (FEM); so it has the shortcomings of low efficiency and heavy calculation burden in commutating the transient temperature field [11].

In the last decades, some algorithms have been further developed and used to study the variation of the circuit's temperature and its effects on the device performance. In 2005, the heat transfer equation was analytically solved to evaluate the changes of temperature and thermal resistance of a microwave power field effect transistor (FET) unit [3]. However, the analytical method is only suitable for solving the electro-thermal problems of some specific structures. In 2008, a semi-analytical method was proposed based on the assumption that the substrate is half infinite. The method was applied to observe the nonlinear characteristics of an integrated resistance by considering the changes of the electrical conductivity (σ) and the thermal conductivity (K) with temperature [4]. Due to the limitation of the analytical method, this approach is not suitable for modeling a model of finite substrate. In 2011, a numerical method of a finite-volume method (FVM) was presented and applied to estimate the temperature distribution profile of a three-dimensional (3D) power delivery network (PDN) package [1]. Only the variation of σ with temperature is considered. In 2016, our group developed a two-dimensional (2D) radial point interpolation method (RPIM) for electro-thermal coupling modeling. Although the temperature variation of the σ and K were taken into account, the instability of the 3D meshless method of the RPIM still needs to be solved [5]. In 2018, a finite difference time domain method (FDTD) and a volume-element method (VEM) were combined for the transient analysis of gas-insulated transmission lines' (GILs) electro-thermal performance [6]. Similarly, the change of resistance with temperature is introduced into the modeling process. In 2019, a 3D RPIM was presented to study the temperature response from

Submitted On: January 13, 2021
Accepted On: February 20, 2022

https://doi.org/10.13052/2022.ACES.J.370204

a through-silicon via (TSV). And the effects of the σ, K, and the specific heat C were taken into account [7]. Whereas, the problem of meshless algorithm, which we mentioned earlier, still needs to be faced. In 2020, the finite difference method (FDM) was introduced into a SPICE simulation tool for observing the characteristics of an insulated gate bipolar transistor (IGBT) at different temperatures. The charge motion of the semiconductor materials was introduced into the voltage equations [8].

Among the above algorithms, the FDM has the advantages of numerical stability and relatively simple implementation; so it is widely used in temperature field modeling [6, 8, 12]. One of the disadvantages of the FDM is difficulty in dealing with multiscale problems. Because the uniformly fine mesh of the FDM will result in a very large memory cost and the extension of the iterations. To solve this issue, some subgridding algorithms, such as a variable step size method (VSSM) [13], a spatial subgridding algorithm with separated temporal and spatial interfaces [14], a hybrid implicit–explicit FDTD method (HIE-FDTD) [15], and a Huygens subgridding FDTD method [16] were proposed and successfully applied in solving Maxwell equations. Since at least two sizes of grids are applied to the subgridding algorithm and the time steps of the domains with different grid sizes can be different, the simulations of the coarse grid and the fine grid can be carried out separately. In this way, the subgridding method can reduce the number of the unknowns and shorten the simulation time. Unfortunately, the data on the grids' boundary needs to be obtained by the interpolation approach, which will destroy the symmetry of the algorithm. In order to ensure the stability of the subgridding approach, an effective solution is to make the element distribution of its coefficient matrix symmetrical [17], but it is difficult in mathematics; another simpler way is to derive the stability conditions of the algorithm so that it can run under certain conditions [18].

Usually, multiscale structures are often included in a circuit. Especially, for solving such an electro-thermal problem, electrical insulation and thermal radiation boundary conditions exist. In addition, the values of the electrical conductivity and the thermal conductivity of the circuit are related to the temperature. All these lead to an asymmetric coefficient matrix of the subgridding algorithm.

In this paper, a finite difference subgridding method for modeling the coupled electro-thermal equations is presented. In the subgridding scheme, the iterations in coarse grid and fine grid are performed respectively; and the spatial and the temporal linear interpolations are applied to obtain the values on the boundary surface. A matrix method [18] is introduced to derive the stability condition of the algorithm. In each march-on-in-time process, the coefficient matrix of the algorithm is updated as σ and K change. And the σ and K will vary with the temperature T. To validate the efficiency of the proposed method, the transient temperature distributions of a square and an n-shaped copper resistances are simulated and compared with the results of the commercial software COMSOL and the traditional FDM, which demonstrate its effectiveness and efficiency.

This paper is arranged in the following manner. In Section II, theories and mathematics of the proposed method for the 3D electro-thermal problems as well as the stability condition are derived. In Section III, the numerical results are compared with those of the COMSOL software and the traditional FDM. In Section IV, conclusion is drawn.

II. THEORIES AND NUMERICAL METHODS

A. The coupled electro-thermal equations

A multiscale structure as shown in Figure 1 is considered in this research. In this model, a copper resistor with a smaller size of $L_{\text{cu}} \times W_{\text{cu}} \times d$ is integrated on a cuboid silicon substrate ($L_s \times W_s \times D_s$). This device is assumed to be physically small. And because the speed of thermal change is far less than the speed of the electromagnetic field transmission, the electromagnetic field on the resistance is regarded as a static field. Therefore, the problem of the electro-thermal mutual coupling can be regarded as an electrostatic field producing Joule heat losses of P, and then the P becomes the thermal source and leads to heat conduction. In turn, the spatial distributions of the temperature will change the parameters of the device.

This physical mechanism can be described by the following mathematical equation:

$$\rho C \frac{\partial T}{\partial t} = \nabla \cdot (K(x,y,z,T)\nabla T) + P(x,y,z,T), \quad (1)$$

where the constants ρ and C represent a density and a specific heat capacity of a material, respectively, K stands for the material's thermal conductivity, T is the temperature, and t represents the time. The power density P is calculated by

$$P = \sigma(x,y,T)\,|\nabla\phi|^2 d. \quad (2)$$

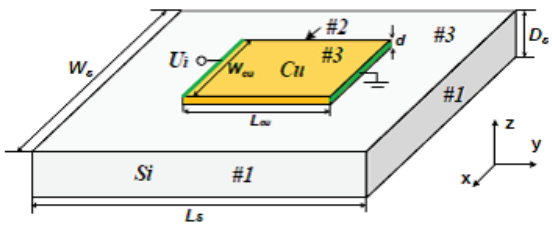

Fig. 1. Electro-thermal model of a resistor.

Here, ϕ represents the copper's electric potential, and it is estimated by

$$\nabla \cdot (\sigma \nabla \phi) = 0. \tag{3}$$

d is the height of the copper. Its conductivity is defined as

$$\sigma(x,y,T) = 1/\rho_0 (1 + \alpha T(x,y)) , \tag{4}$$

where ρ_0 is an electrical resistivity and α represents a temperature coefficient.

As Figure 1 shows, the positive electrode (Γ_{e+}) of the copper is impinged on an U_s voltage and its negative electrode (Γ_{e-}) is grounded (i.e., Dirichlet boundary or first-type boundary). In addition, the electrical insulation (Neumann boundary or second-type boundary) at $\Gamma_{\#2}$, the thermal radiation (the third-type boundary or Robbin boundary) at boundary $\Gamma_{\#3}$, and the other edges of the circuit that are cooled to T_0 are supposed. These conditions are expressed as

$$\phi|_{\Gamma_{e+}} = U_s, \phi|_{\Gamma_{e-}} = 0, \text{ and } \frac{\partial \phi}{\partial \hat{n}}|_{\Gamma_{\#2}} = 0, \tag{5a}$$

and

$$T|_{\Gamma_{\#1}} = T_0, K\frac{\partial T}{\partial \hat{n}}|_{\Gamma_{\#3}} = h(T_\infty - T), \tag{5b}$$

where $\hat{n}$ is the norm of the boundary, h is the convective heat transfer coefficient, and T_∞ is the ambient temperature. The empirical formula for $K(x,y,z,T)$ can be found in [4].

B. Application of the finite difference subgridding method to the coupled electro-thermal equations

In this electro-thermal model, only copper is partitioned with a uniform fine grid of Δl_f, while the substrate is divided by a uniform coarse grid of Δl_c. Therefore, when calculating ϕ, there is only one kind of grid in the computational domain. After using the central difference method to eqn (3) to estimate its derivatives, ϕ at the fine cell (i, j) can be estimated by

$$\phi_{i,j} = \left(c^e_{1,i}, c^e_{2,i}, c^e_{1,j}, c^e_{2,j}\right)\left(\phi_{i-1,j}, \phi_{i+1,j}, \phi_{i,j-1}, \phi_{i,j+1}\right)^{\mathrm{T}}, \tag{6}$$

where $c^e_{p,q} = (4 + (-1)^p \Delta\sigma_q)/16$, ($p$=1, 2. q=i, j), $\Delta\sigma_q$= $\left(\sigma_{q+1} - \sigma_{q-1}\right)/\sigma_q$..

On Neumann boundary of eqn (5a), eqn (6) becomes

$$\phi_{i,j}|_{\Gamma_{\#2}} = \left(\frac{1}{2} + \frac{\Delta\sigma_j}{8}\right)\phi_{i,j+1} + \left(\frac{1}{2} - \frac{\Delta\sigma_j}{8}\right)\phi_{i,j-1}. \tag{7}$$

Then, the Joule heat losses of P is

$$P = \frac{d}{\Delta l_f^2} \cdot \left[\left(\phi_{i+1,j} - \phi_{i-1,j}\right)^2 + \left(\phi_{i,j+1} - \phi_{i,j-1}\right)^2\right]. \tag{8}$$

Whereas, there are two grid sizes on the Si substrate. To describe the subgridding algorithm clearly, the FDM of the temperature field on an upper left corner of the top surface in Figure 1 is cut out to be discussed in detail. This is typical because the grids on the top surface are constrained by the third-type boundary condition.

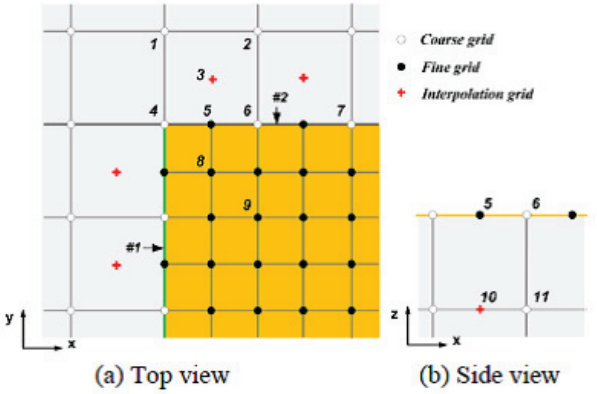

Fig. 2. An interface of the coarse grids and subgrids on an upper left corner of the top surface.

The key of a subgridding method is the field coupling between the coarse mesh and the fine mesh. In this paper, the coupling is realized by linear interpolation. For simplicity and illustration purpose, the 2:1 ratio of the coarse cell and the fine cell is used as Figure 2. The coarse grid borders the fine grid. There are three types of grids: coarse grid, fine grid, and interpolation grid.

The cells "1, 2, 4, 6, 7" in Figure 2(a) and "11" in Figure 2(b) are coarse grids, where "6, 7" on the subgridding interface; the "5, 8, 9" are fine grids, where "5" on the interface, and the point "3, 10" is extra added to estimate its value. All the unknown temperature fields in Figure 2(a) are constrained by the Robbin boundary conditions of eqn (5b). Besides, the temperature fields of the other grids in the substrate, such as "11," have no constraints.

Similarly, the T of these grids, except for "3, 10," can be obtained by applying the FDM approach. After some manipulations, their formulas can be written as

$$T^{n+1/m}_{i,j,k} = \boldsymbol{R}^{xy}_T \boldsymbol{T}^n_{xy} + \boldsymbol{R}^z_T \boldsymbol{T}^n_z + P, \tag{9}$$

where P = 0. But for the grids in the copper area, P is calculated by eqn (8); n is the iteration time step, and the time step ratio m is also the ratio of the spatial step, which is defined by

$$m = \Delta t_c / \Delta t_f = \Delta l_c / \Delta l_f. \tag{10}$$

The $\boldsymbol{R}^{xy}_T$ = (c^T_0, $c^T_{1,i}$, $c^T_{2,i}$, $c^T_{1,j}$, $c^T_{2,j}$), $\boldsymbol{T}^n_{xy}$ =($T^n_{i,j,k}$, $T^n_{i-1,j,k}$, $T^n_{i+1,j,k}$, $T^n_{i,j-1,k}$, $T^n_{i,j+1,k}$)^T, where

$$\begin{cases} c^T_0 = 1 - 4K_q a_\varsigma \\ c^T_{p,q} = a_\varsigma (K_q + (-1)^p \Delta K_q) \end{cases} \tag{11}$$

Here, $a_\varsigma = \Delta t_\varsigma / \rho C \Delta l^2_\varsigma$, ς=c or f; p=1, 2, q=i, j, k; ΔK_q =$(K_{q+1} - K_{q-1})/4$.

For the grids in different regions, m, $\boldsymbol{R}^z_T$, and $\boldsymbol{T}^n_z$ are different.

For the grid "1, 2, 4, 6, 7," m=1, $\varsigma = c$, $\boldsymbol{R}_T^z = (-(c_{1b,k}^T + c_{2b,k}^T), c_{1b,k}^T, c_{2b,k}^T)$, where $c_{1b,k}^T = 2K_q a_\varsigma$, $c_{2b,k}^T = ha_\varsigma \Delta l_\varsigma (3 - K_{k-1}/K_k)$; $\boldsymbol{T}_z^n = (T_{i,j,k}^n, T_{i,j,k-1}^n, T_\infty)^T$.

For the grid "5, 8, 9," m is defined by eqn (10), and $\varsigma = f$, $\boldsymbol{R}_T^z$, and $\boldsymbol{T}_z^n$ are the same as above; in particular, T_3 is interpolated by

$$T_3 = \frac{T_1 + T_2 + T_4 + T_6}{4}, \tag{12}$$

and is introduced to estimate T_5. T_{10} is also introduced to estimate T_5, which is interpolated by the two adjacent coarse grids along x-axis.

For the grid "11," m = 1, $\varsigma = c$, $\boldsymbol{R}_T^z = (c_{1,k}^T, c_{2,k}^T)$, $\boldsymbol{T}_z^n = (T_{i,j,k-1}^n, T_{i,j,k+1}^n)^T$.

Since "6" is located on the boundary of the grid, when calculating T_6, T_9 should be known at the same time. However, "9" is located on a fine cell. Due to the different time steps between the fine grid and the coarse grid, T_9 needs to be iterated m times to reach the same time as T_6. Therefore, the two grids are coupled with each other.

To facilitate understanding, suppose that the current time step is n and all the fields are known. We summarize the update process of the proposed subgridding scheme into the following steps.

Step #1: Compute the electric potential equations of eqn (6)–(8) to obtain the Joule heat losses of P.

Step #2: Compute eqn (9) with Δt=Δt_c to update T_1^n, T_2^n, and T_{11}^n of the coarse grid and T_4^n, T_6^n, and T_7^n of the interface grid to be T_1^{n+1}, T_2^{n+1}, T_{11}^{n+1}, T_4^{n+1}, T_6^{n+1}, and T_7^{n+1}. Then, compute eqn (12) to obtain T_3^n and T_3^{n+1}, T_{10}^n, and T_{10}^{n+1}. Similarly, eqn (9) with Δt=Δt_f is executed to calculate $T_5^{n+1/m}$, $T_8^{n+1/m}$, and $T_9^{n+1/m}$ of the fine grid. Take T_6 as an example:

$$\begin{aligned} T_6^{n+1} &= (1 - 6K_6 a_c + ha_c \Delta l_c (3 - K_{11}/K_6))\, T_6^n \\ &\quad + a_c (K_6 - (K_7 - K_4)/4) T_4^n \\ &\quad + a_c (K_6 - (K_7 - K_4)/4) T_7^n \\ &\quad + a_c (K_6 - (K_2 - K_9)/4) T_9^n \\ &\quad + a_c (K_6 - (K_2 - K_9)/4) T_2^n \\ &\quad + 2K_6 a_c T_{11}^n + ha_c \Delta l_c (3 - K_{11}/K_6) T_\infty + a_c \Delta l_c^2 P_6 \end{aligned} \tag{13}$$

Step #3: Update the temperature fields of the fine grids from the time step n+1/m to n+2/m. It should be noted that in order to obtain $T_5^{n+2/m}$, $T_3^{n+1/m}$, and $T_{10}^{n+1/m}$needs to be interpolated in advance through T_3^n and T_3^{n+1}, T_{10}^n and T_{10}^{n+1}. This process will be repeated until the time step increases to n+1. Take T_5 as an example:

$$\begin{aligned} T_5^{n+\frac{i+1}{m}} &= \left(1 - 6K_5 a_f + ha_f \Delta l_f (3 - K_{10}/K_5)\right) T_5^{n+\frac{i}{m}} \\ &\quad + a_f (K_5 - (K_6 - K_4)/4) T_4^{n+\frac{1}{m}} \\ &\quad + a_f (K_5 - (K_6 - K_4)/4) T_6^{n+\frac{1}{m}} \\ &\quad + a_f (K_5 - (K_3 - K_8)/4) T_8^{n+\frac{1}{m}} \\ &\quad + a_f (K_6 - (K_3 - K_8)/4) T_3^{n+\frac{1}{m}} \\ &\quad + 2K_5 a_f T_{10}^{n+\frac{1}{m}} + ha_f \Delta l_f (3 - K_{10}/K_5) T_\infty \\ &\quad + a_f \Delta l_f^2 P_5, \end{aligned} \tag{14}$$

where $1 \le i \le m - 1$.

Step #4: Renew both σ and K with the temperatures calculated in Step #2 and Step #3. Go to Step #1.

C. Stability analysis

The explicit equation of (9) is conditionally stable. In this paper, the fine cell's time step is first derived to be Δt_f^1 by using the matrix method, and then Δt_c is determined by using the same method and considering the relationship with Δt_f^1 at the same time. Finally, Δt_f is updated to 1/m times of Δt_c as eqn (10).

Specifically, the source-free form of eqn (9) is arranged into the following equation:

$$T^{n+1} = \begin{pmatrix} M_c & M_f \end{pmatrix}_{N \times N} T^n, \tag{15}$$

where $\boldsymbol{T} = (T_1, T_2, \ldots, T_N)^T$, N is the total number of the grids, and $\boldsymbol{M}_c$ and $\boldsymbol{M}_f$ denote the coefficient matrix of the coarse grids and fine grids, respectively. It can be obtained by

$$M_\varsigma = I + \Delta t_f^1 D_\varsigma, \ \ (\varsigma = c, f), \tag{16}$$

where $\boldsymbol{I}$ is an identity matrix, and $\boldsymbol{D}$ represents the operator $(\rho C)^{-1} \nabla \cdot K \nabla$. It is a sparse matrix.

A necessary condition for T^{n+1} is that when $n \to \infty$, the spectral radius of the coefficient matrix must satisfy

$$\left|\lambda_i^M\right| \le 1, \tag{17}$$

where $\lambda_i^M = 1 + \Delta t_f^1 \lambda_i^D$, and λ_i^M and λ_i^D represent the eigenvalue element of $\boldsymbol{M}$ and $\boldsymbol{D}$, respectively. Due to the Robbin boundary condition, M is unsymmetric but full rank. λ_i^D is negative real or complex whose imaginary part is small enough to be ignored.

From eqn (17), we have

$$\Delta t_f^1 \le 2/(\max|\lambda_i^D|). \tag{18}$$

By applying the same method, Δt_c^1 can be preliminarily determined. In this case, only $\boldsymbol{M}_c$ is considered in eqn (15). Besides, the time step of the coarse grid has m times of that of the fine grid as well. So, we take

$$\Delta t_c = \min(\Delta t_c^1, m\Delta t_f^1). \tag{19}$$

Therefore,Δt_f can be updated to

$$\Delta t_f = \min(\Delta t_f^1, \Delta t_c/m), \tag{20}$$

in turn.

Theoretically, Δt will change with T, but this change is negligible and can be ignored. To reduce the time loss, a fixed time step is used in the program execution.

Table 1: Parameters of Figure 1

Parameter	Value	Parameter	Value
L_{cu},W_{cu},d	20,20,0.01 mm	$T_0 = T_\infty$	20 ℃
L_s,W_s,D_s	40,40,20 mm	h	24 W/m^2·K
ρ	2.329 g/cm^3	C	700 J/kg·K
Δl_c	2.5 mm	U_i	5 V
Δt_c	0.004 s	m	4

III. NUMERICAL EXPERIMENTS

A. Cuboid resistor integrated on a Si substrate

The main parameters of Figure 1 are listed in Table 1. The parameters of σ and K can be found in [4]. A square wave signal with a voltage of 5 V is impinged on the resistor. The voltage period is 0.08 s. m sets to 4 in this experiment.

Figure 3(a) shows the element distribution characteristics of $\boldsymbol{M}$. The data shows that $\boldsymbol{M}$ is an asymmetric matrix with dominant main diagonal elements. The eigenvalues of the matrix, which equal λ^M, are given in Figure 3(b).

The resistor's σ and K on the top surface at $t = 5$ s is simulated and given in Figure 4(a) and (b), respectively. Obviously, they are spatially distributed, which is caused by the temperature change in space.

The transient temperatures at (20, 20, and 20 mm) are observed and illustrated in Figure 5. These results are compared with those of the conventional FDM, which adopts a uniform fine grid with $\Delta l_s = 0.625$ mm and its time step is 0.001 s. From the figure, we can see that their numerical results agree well.

Figure 6 shows the temperature distributions on the top surface of the substrate at $t = 5$ s. We can clearly see that on the boundary of the coarse and fine grids, the temperatures of the coarse grids naturally transit to the fine grids.

In order to further verify the efficiency of the proposed algorithm, the temperatures on the top surface, whose grid numbers are 1576–1800, are also compared with the results from COMSOL software ($t = 5$ s). Figure 7 shows the numerical results of the

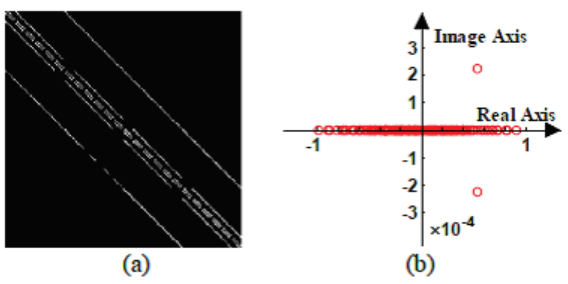

Fig. 3. The characteristics of $\boldsymbol{M}$. (a) Its element distribution. (b) Its eigenvalues.

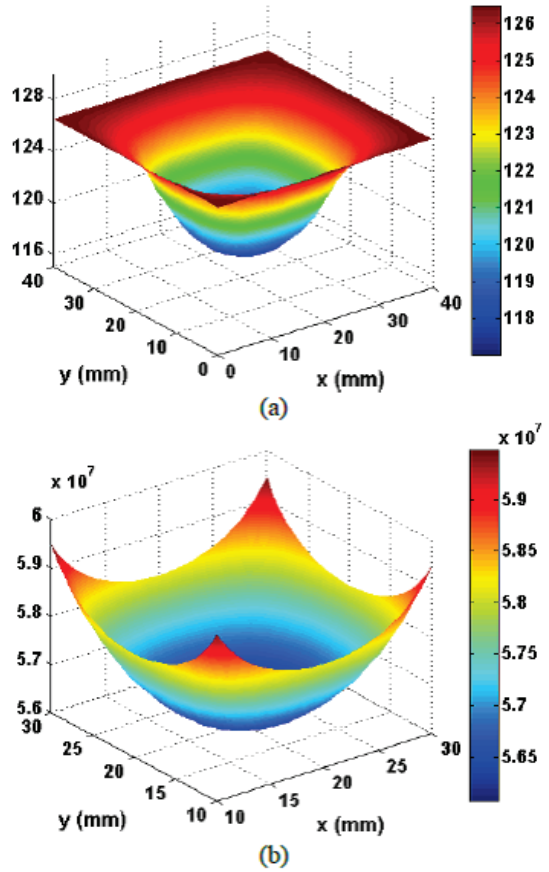

Fig. 4. Temperature-dependent parameters of the resistor. (a) σ. (b) K.

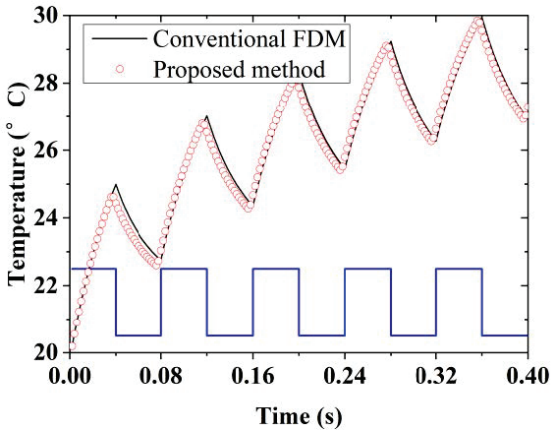

Fig. 5. Comparison of the temperatures obtained with the different methods at (20, 20, and 20 mm).

three methods. Obviously, they are in good agreement. It verifies the effectiveness of the proposed subgridding approach in modeling the multiscale electro-thermal structure.

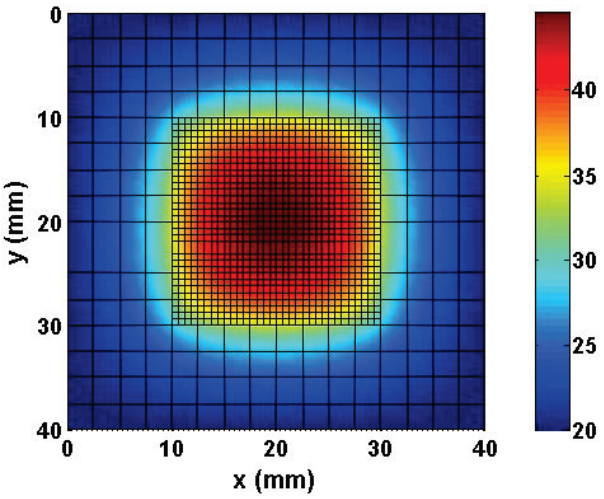

Fig. 6. Temperature distribution on the top surface.

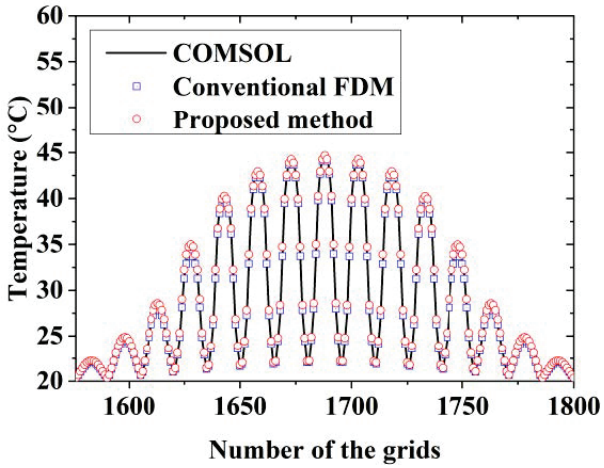

Fig. 7. Temperature distribution obtained by COMSOL, conventional method, and the proposed method.

Table 2 lists the computational expenditures of three methods. Based on the table, the following observations are made.

- The proposed algorithm with subgrids reduces the number of unknowns by about 91% and the computational time by about 49.6% compared to the traditional FDM with uniform fine mesh.
- The proposed finite difference subgridding method reduces the number of unknowns by about 70% and the computational time by about 10.7% compared to the COMSOL software.

B. N-shaped resistor integrated on a Si substrate

To further study the adaptability of the proposed algorithm, an n-shaped copper resistor ($L_{cu} = W_{cu} = 20$ mm, $L_{arc} = 5$ mm, $d = 0.1$ mm) integrated on a square silicon film substrate ($L_s = W_s = 40$ mm) is illustrated as Figure 8 shows. This model has a multiscale structure. In this case, the square wave voltage changes to be 5 V and its period is 1 s. Other parameters are the same as the square resistance above.

Table 2: Computational expenditures of different methods

Numerical method	Total number of unknowns	Total number of iterations	CPU time (s)
Conventional FDM	31,752	5000	21.27
COMSOL	9391	N/A	12.00
Proposed subgridding method	2825	1250	10.72

Figure 9 shows the temperature distributions of the substrate at $t = 20$ s. Also, the obvious reflection of

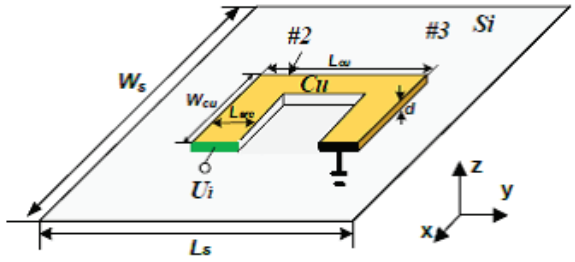

Fig. 8. N-shaped resistor integrated on a Si substrate.

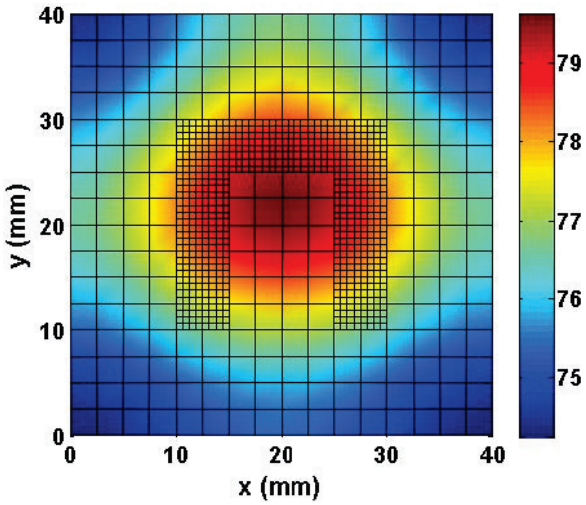

Fig. 9. Temperature distribution of the substrate at $t = 20$ s.

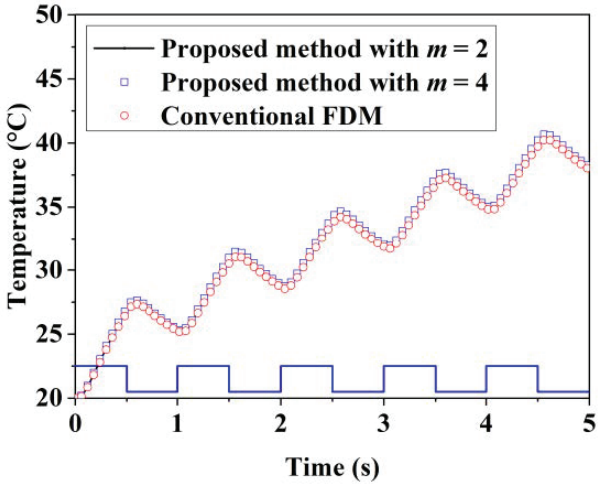

Fig. 10. Comparison of the temperatures obtained with the different methods at (20 and 20 mm).

the temperature field on the boundary was not observed. These results are compared with those of the conventional FDM, which adopts a uniform fine grid with $\Delta l_s =$ 0.625 mm and its time step is 0.001 s. Figure 10 gives the comparison of the transient temperatures obtained with the two different methods at the observed point (20 and 20 mm). From the figure, we can see that the three temperature patterns tend to be in good agreement. It verifies the effectiveness of the proposed subgridding approach again.

IV. CONCLUSION

In this paper, a 3D explicit finite difference subgridding method is proposed and applied to study the electro-thermal problems of electronic components and ICs with multiscale structures. Square- and n-shaped resistances are used as examples. In order to agree with the actual problems, the temperature-dependent electrical conductivity and thermal conductivity are considered in this research. In addition, the Robbin boundary condition is used in the model. Therefore, the coefficient matrix of the subgridding algorithm is asymmetric. Fortunately, its main diagonal elements are dominant and symmetric; the imaginary part of the other asymmetric elements is close to 0. Based on these properties, the stability condition of the algorithm is derived by matrix method. The numerical results are compared with those of the traditional FDM with fine mesh and the COMSOL software as well. They are in good agreement. In addition, the proposed method can reduce the number of unknowns by about 91% and 70% and the computational time by about 49.6% and 10.7%, compared to the traditional FDM and the COMSOL software, respectively. All of the above show the efficiency of the proposed method.

ACKNOWLEDGMENT

The authors wish to acknowledge the support of the National Natural Science Foundation of China under Grant 61761017.

REFERENCES

[1] J. Xie and M. Swaminathan, "Electrical-thermal Co-simulation of 3D Integrated Systems with Micro-fluidic Cooling and Joule Heating Effects," *IEEE Transactions on Components, Packaging, and Manufacturing Technology,* vol. 1, no. 2, pp. 234-246, Feb. 2011.

[2] X. Guan, X. Wei, X. Song, N. Shu, and H. Peng, "FE Analysis on Temperature, Electromagnetic Force and Load Capacities of Imperfect Assembled GIB Plug-in Connectors," *Applied Computational Electromagnetics Society Journal*, vol. 33, no. 6, pp. 697-705, Jun. 2018.

[3] S. Yanagawa, "Analytical Approach to Evaluate Thermal Reduction Effects of Peripheral Structures on Microwave Power GaAs Device Chips," *IEEE Microwave and Wireless Components Letters*, vol. 15, no. 5, pp. 324-326, May 2005.

[4] B. Vermeersch and G. De Mey, "Dynamic Electrothermal Simulation of Integrated Resistors at Device Level," *Microelectronics Journal*, vol. 40, no. 9, pp. 1411-1416, Dec. 2008.

[5] X. Zhang, Z. Chen, and Y. Yu, "An Unconditional Stable Meshless ADI-RPIM for Simulation of Coupled Transient Electrothermal Problems," *IEEE Journal on Multiscale and Multiphysics Computational Techniques*, vol. 1, pp. 98-106, Nov. 2016.

[6] D. I. Doukas, T. A. Papadopoulos, A. I. Chrysochos, D. P. Labridis, and G. K. Papagiannis, "Multiphysics Modeling for Transient Analysis of Gas-insulated Lines," *IEEE Transactions on Power Delivery*, vol. 33, no. 6, pp. 2786-2793, Dec. 2018.

[7] J. Chai, G. Dong, and Y. Yang, "Nonlinear Electrothermal Model for Investigating Transient Temperature Responses of a Through-silicon via Array Applied with Gaussian Pulses in 3-D IC," *IEEE Transactions on Electron Devices*, vol. 66, no. 2, pp. 1032-1040, Feb. 2019.

[8] H. Cao, P. Ning, X. Wen, T. Yuan, and H. Li, "An Electro-thermal Model for IGBT Based on Finite Differential Method," *IEEE Journal of Emerging and Selected Topics in Power Electronics,* vol. 8, no. 1, pp. 673-684, Mar. 2020.

[9] A. M. Milovanovic, B. M. Koprivica, A. S. Peulic, and I. L. Milankovic, "Analysis of Square Coaxial Line Family," *Applied Computational Electromagnetics Society Journal*, vol. 30, no. 1, pp. 99-108, Jan. 2015.

[10] M. Moradi, R. S. Shirazi, and A. Abdipour, "Design and Non-linear Modeling of a wide Tuning Range Four-plate MEMS Varactor with High Q-factor for RF Application," *Applied Computational Electromagnetics Society Journal*, vol. 31, no. 2, pp. 180-186, Feb. 2016.

[11] J. Chen, S. Yang, and Z. Ren, "A Network Topological Approach-based Transient 3-D Electrothermal Model of Insulated-gate Bipolar Transistor," *IEEE Transactions on Magnetics*, vol. 56, no. 2, pp. 1-4, Feb. 2020.

[12] F. Kaburcuk and A. Z. Elsherbeni, "Temperature Rise and SAR Distribution at Wide Range of Frequencies in a Human Head due to an Antenna Radiation," *Applied Computational Electromagnetics Society Journal*, vol. 33, no. 4, pp. 367-372, Apr. 2018.

[13] S. S. Zivanovic, K. S. Yee and K. K. Mei, "A Subgridding Method for the Time-domain Finite-difference Method to Solve Maxwell's Equations," *IEEE Transactions on Microwave Theory and Techniques*, vol. 39, no. 3, pp. 471-479, Mar. 1991.

[14] K. Xiao, D. J. Pommerenke and J. L. Drewniak, "A Three-dimensional FDTD Subgridding Algorithm with Separated Temporal and Spatial Interfaces and Related Stability Analysis," *IEEE Transactions on Antennas and Propagation*, vol. 55, no. 7, pp. 1981-1990, Jul. 2007.

[15] J. Chen, A. Zhang, "A Subgridding Scheme Based on the FDTD Method and HIE-FDTD Method," *Applied Computational Electromagnetics Society journal*, vol. 26, no. 1, pp. 1-7, Jan. 2011.

[16] H. AL-Tameemi, J. Bérenger, and F. Costen, "Singularity Problem with the One-sheet Huygens Subgridding Method," *IEEE Transactions on Electromagnetic Compatibility*, vol. 59, no. 3, pp. 992-995, Jun. 2017.

[17] K. Zeng, and D. Jiao, "Symmetric Positive Semi-definite FDTD Subgridding Algorithms in Both Space and Time for Accurate Analysis of Inhomogeneous Problems," *IEEE Transactions on Antennas and Propagation*, vol. 68, no. 4, pp. 3047-3059, Jan. 2020.

[18] S. Wang, "Numerical Examinations of the Stability of FDTD Subgridding Schemes," *Applied Computational Electromagnetics Society Journal*, vol. 22, no. 2, pp. 189-194, Jul. 2007.

Xianyan Zhang received the B.S. degree in applied physics and the M.S. degree in physical electronics from Yunnan University, Kunming, China, in 2001 and 2004, respectively, and the Ph.D. degree in electromagnetic field and microwave technology from the Institute of Electronics, Chinese Academy of Sciences, Beijing, China, in 2007.

Her research interests include electromagnetic computation, antenna design and wireless power transmission structure design.

Ruilong Chen was born in Hengyang, Hunan, China, in 1996. He received the B.S. degree in communication engineering from Beijing Union University, Beijing, China, in 2018, and the M.S. degree in communication engineering from East China Jiaotong University, Nanchang, China, in 2021.

He is currently working with Wuxi Leihua Science and Technology Co., Ltd. His research interests focus on electromagnetic computation and radar signal processing.

Aiyun Zhan was born in Nantong, Jiangsu, China, in 1973. She received the B.S. degree from Southwest Jiaotong University, Chengdu, China, in 1997, and he M.S. degree from East China Jiaotong University, Nanchang, China, in 2008. She is currently working with the School of Information Engineering, East China Jiaotong University. Her research interests focus on channel coding and optical communication.

Electromagnetic Characteristics Calculation of FSS by the Mixed Method FDTD/Extrapolation/Cascade Method

Yangyang Wang, Dongfang Zhou, Qikun Liu, and Dewei Zhang

PLA Strategic Support Information Engineering University, Zhengzhou 450001, China
zd96882@sina.com, 1107293517@qq.com, liuqikun@163.com, box66@163.com

Abstract – In this paper, a mixed method (MM) combining the advantages of finite difference time domain (FDTD), extrapolation, and matrix cascade methods is proposed. First, the hybrid algorithm combining the FDTD and extrapolation method is used to compute the electromagnetic characteristics of the single-layer frequency selective surface (FSS). Subsequently, matrix cascade method is used to calculate the electromagnetic characteristics of the multi-layer FSS. By introducing the Floquet theorem and considering the periodic boundary condition (PBC), absorbing boundary conditions (ABC) of the FSS, a three-dimensional model, is established. The computational results show that, while maintaining the same level of accuracy, the hybrid method greatly improves the computation speed and reduces the computer memory compared with the simulation software. It can provide an important reference for the subsequent study of the electromagnetic characteristics of the FSS.

Index Terms – FDTD, extrapolation method, matrix cascade, FSS, electromagnetic characteristics.

I. INTRODUCTION

At present, radome is widely used for military and civil fields [1-3]. However, the traditional dielectric radome does not have the stealth function and cannot meet the requirements of high in-band wave transmission and strong out-of-band stealth. In order to overcome the shortcomings of traditional dielectric radome, frequency selective surface (FSS) is adopted by the researchers [4-10] and implanted in the radome to obtain specific electromagnetic (EM) characteristics. Therefore, studying the EM properties of the FSS is a key indicator for the design of FSS.

The commercially available simulation packages, e.g., HFSS and CST [11-13], do not offer the desired level of flexibility for calculating the EM properties of FSS. Therefore, a customized simulation package needs to be pursued.

At present, the numerical computation methods for the EM properties of FSS mainly include finite element method (FEM) [14] and finite difference time domain method (FDTD) [15]. The FEM divides the entire computational domain into a mesh, which takes up a large amount of computer memory. It is generally the case that the speed of computations slows down with increasing memory requirement. Therefore, the FEM is not suitable for large-sized objects.

The FDTD method has the advantage of increasing the computation accuracy and reducing the memory requirements. It is used to compute the EM characteristics of the FSS. However, it has certain limitations. For example, iteration number depends on the relationship between step size and time, and in order to improve the accuracy, it is necessary to encrypt the grid. To solve this problem, researchers have proposed many methods, such as second-order time approximation [16, 17]. However, the derivation processes are usually very complicated. Therefore, the extrapolation method is adopted in this paper.

Based on the extrapolation method, a new algorithm is proposed in this paper. The computation mainly includes two steps. First, the result is obtained under the original mesh density (#1). Then, in order to improve the accuracy, the mesh density is increased to twice the original mesh density, and the result is obtained while keeping the computation region unchanged (#2). For the above two results, the extrapolated solution can be obtained by the extrapolation formula. This method not only greatly improves the computation accuracy but also reduces the computer memory [18]. It is widely used in the field of mathematics and EM field.

A mixed method (MM) combining FDTD, extrapolation method, and cascading to compute the EM properties of multi-layer FSS is proposed in this paper. It has the advantages of fast computational speed of FDTD, matrix cascade, and high computational accuracy of extrapolation method, while avoiding the disadvantages of increasing the grid density to improve the accuracy. Therefore, the hybrid method promises to be a favorable candidate for computing EM properties of FSS. In Section II, the computation process of the EM characteristics of the single-layer FSS is introduced in detail. Then,

Submitted On: October 28, 2021
Accepted On: February 26, 2022

https://doi.org/10.13052/2022.ACES.J.370205

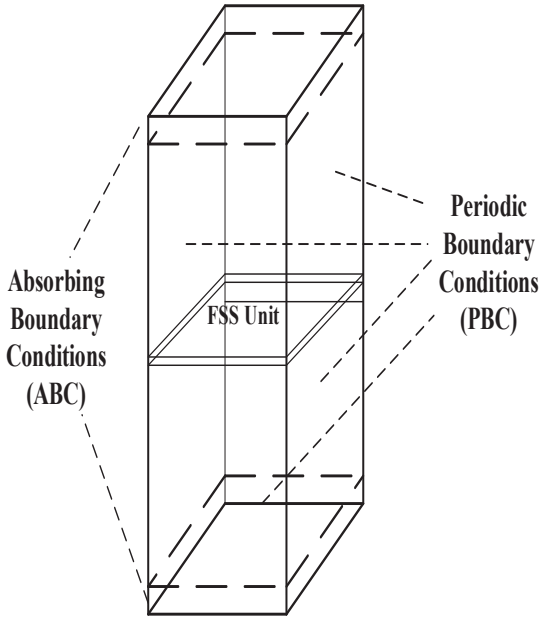

Fig. 1. FSS model.

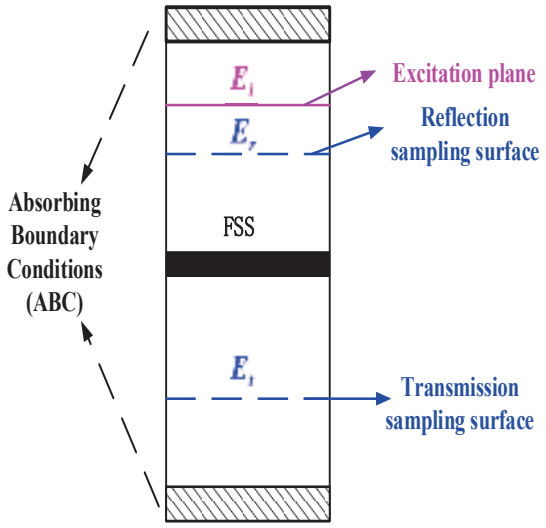

Fig. 2. Computation model.

considering cascading, the expression of the EM characteristics of the multi-layer FSS is derived. In Section III, the dielectric plate and FSS, having an infinite periodic structure, are used to verify the accuracy of the hybrid method. In Section IV, influence factors of reflection coefficient are analyzed.

II. HYBRID FDTD/EXTRAPOLATION/CASCADE METHOD

A. The basic principle of FDTD

The basic principle of FDTD is to use the idea of central difference to discretize Maxwell's equations in space and time [19]. From Maxwell's equations, iterative formulas for electric and magnetic field components can be derived by employing the central difference formula.

To compute the EM properties of the infinite periodic FSS, the Floquet theorem is introduced. Thus, the EM characteristic of the entire FSS structure is obtained by calculating only one unit of the FSS. Figure 1 shows the model of the FSS. Periodic boundaries are applied to the four sides of the model, and absorbing boundaries are applied to the upper and lower sides.

Periodic boundary condition (PBC) is explained in detail in [4]. At present, the common methods to achieve absorbing boundary condition (ABC) mainly include perfectly matched layer (PML), convolution perfectly matched layer (CPML), and uniaxial perfectly matched layer (UPML). When dealing with decay pattern, PML needs to be placed sufficiently far away from the obstacle so that the decay pattern is fully attenuated. However, this will increase the number of grids and reduce the computation speed. Therefore, PML has low efficiency when dealing with decay pattern. CPML is an improved version based on PML [19]. In addition, the parameter ranges of CPML only apply to individual special cases. In actual computations, to satisfy the ABC, a larger range of adjustment coefficients is required, which is not conducive to obtaining results quickly. Therefore, UPML ABCs are adopted in this paper.

Under the excitation of a Gaussian pulse, EM waves propagate along the upper and lower sides of the excitation loading surface. We set the reflection sampling surface and the transmission sampling surface on the upper and lower sides of the FSS structure, respectively. The schematic diagram of the computation model is shown in Figure 2.

It can be seen from Figure 2 that the transmission field E_t is calculated on the transmission sampling surface, and the total field is calculated on the reflection sampling surface, which includes the reflected field E_r and the incident field E_i. Therefore, the expressions for the reflection and transmission coefficients of FSS are shown in the following equation:

$$R = \frac{E_r}{E_i}, T = \frac{E_t}{E_i}, \tag{1}$$

where E_r is the reflected field, E_t is the transmission field, and E_i is the incident field.

B. The basic principle of extrapolation method

The basic principle of the extrapolation method is to first calculate the result under the original mesh density (#1). The time step size $dt = \min(ds)/(4c)$, where, ds is the space step and c is the wave velocity in space. Then, in order to improve the accuracy, the mesh density is increased to twice the original mesh density, and the result

is obtained (#2). At this time, the time step size remains unchanged and still meets the requirements of computational stability. Since the two space divisions before and after are different, but the time step remains the same, the results of these two times can be combined.

For the above two results, a simple extrapolation formula is performed. Extrapolation solution is obtained. This method not only greatly improves the computation accuracy but also reduces the computer memory requirements. The following discussion briefly introduces the reason why the extrapolation method can improve the computation accuracy.

Assuming that f is a function of the independent variable x and time t, and the spacing on the x-axis is h, Taylor expansion of $f(x_{i+1})$ at t_n is

$$f(x_{i+1})|_{t_n} = f(x_i)|_{t_n} + h\left.\frac{\partial f}{\partial x}\right|_{x=x_i,t_n} + \left.\frac{h^2\partial^2 f}{2!\partial x^2}\right|_{x=x_i,t_n} + O(h^3). \quad (2)$$

Furthermore, Taylor expansion at $x_{i+1/2}$ is

$$f(x_{i+1/2})|_{t_n} = f(x_i)|_{t_n} + \left.\frac{h\partial f}{2\partial x}\right|_{x=x_i,t_n} + \left(\frac{h}{2}\right)^2 \left.\frac{\partial^2 f}{2!\partial x^2}\right|_{x=x_i,t_n} + O(h^3). \quad (3)$$

From Equation (2) and (3)

$$4f(x_{i+1/2})|_{t_n} - f(x_{i+1})|_{t_n} = 3\,f(x_i)|_{t_n} + h\left.\frac{\partial f}{\partial x}\right|_{x=x_i,t_n} - \frac{h^3}{2}\left.\frac{\partial^3 f}{3!\partial x^3}\right|_{x=x_i,t_n} + O(h^4). \quad (4)$$

Similarly,

$$4f(x_{i-1/2})|_{t_n} - f(x_{i-1})|_{t_n} = 3\,f(x_i)|_{t_n} - h\left.\frac{\partial f}{\partial x}\right|_{x=x_i,t_n} + \frac{h^3}{2}\left.\frac{\partial^3 f}{3!\partial x^3}\right|_{x=x_i,t_n} + O(h^4). \quad (5)$$

From Equation (4) and (5),

$$4\left(f(x_{i+1/2})|_{t_n} + f(x_{i-1/2})|_{t_n}\right) - \left(f(x_{i+1})|_{t_n} + f(x_{i-1})|_{t_n}\right) = 6\,f(x_i)|_{t_n} + O(h^4). \quad (6)$$

Besides,

$$f(x_{i+1/2})|_{t_n} + f(x_{i-1/2})|_{t_n} = 2\,f_f(x_i)|_{t_n}, \quad (7a)$$

$$f(x_{i+1})|_{t_n} + f(x_{i-1})|_{t_n} = 2\,f_c(x_i)|_{t_n}. \quad (7b)$$

Substituting Equation (7) into eqn (6),

$$f(x_i)|_{t_n} = \frac{1}{3}\left[4\,f_{\mathrm{enc}}(x_i)|_{t_n} - f_{\mathrm{org}}(x_i)|_{t_n}\right] + O(h^4). \quad (8)$$

Here, f_{enc} is the results calculated by encrypting the grid (twice the original mesh density) and f_{org} is the results under the original mesh density.

It can be seen from Equation (8) that the remaining term is the fourth-order of the space step, so that the extrapolation solution has higher computation accuracy.

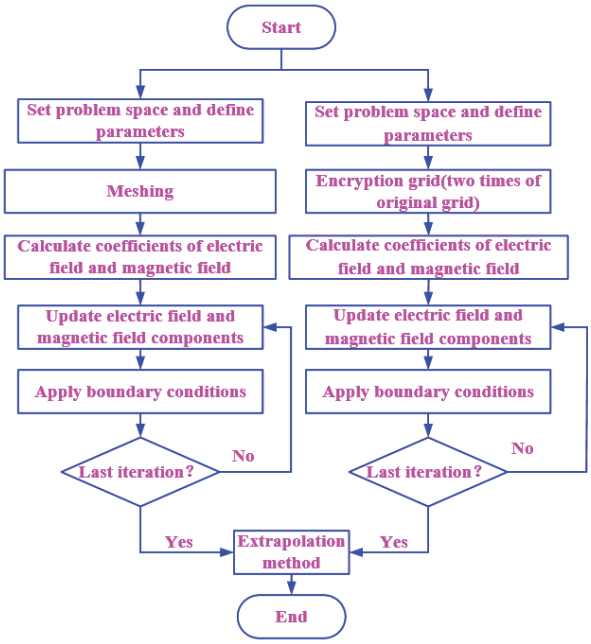

Fig. 3. The computation flow chart of the hybrid method.

C. Hybrid FDTD/extrapolation method

When performing the three-dimensional (3D) numerical computation of the reflection coefficients of the FSS, first, the FDTD/ extrapolation method is used to calculate the EM field, given a certain grid density. Due to space limitations, take the electric and magnetic field components in the x-direction as an example. The updated equations of the electric field and magnetic field are shown in the following equations:

$$\begin{aligned} E_x^{n+1}(i,j,k) &= \tfrac{2\varepsilon_x-\Delta t\sigma_x}{2\varepsilon_x+\Delta t\sigma_x}E_x^n(i,j,k) \\ &+ \tfrac{2\Delta t}{(2\varepsilon_x+\Delta t\sigma_x)\Delta y}(H_z^{n+1/2}(i,j,k) - H_z^{n+1/2}(i,j-1,k)) \\ &- \tfrac{2\Delta t}{(2\varepsilon_x+\Delta t\sigma_x)\Delta z}(H_y^{n+1/2}(i,j,k) - H_y^{n+1/2}(i,j,k-1)), \end{aligned} \quad (9)$$

$$\begin{aligned} H_x^{n+1/2}(i,j,k) &= H_x^{n-1/2}(i,j,k) \\ &+ \tfrac{\Delta t}{\mu_x\Delta z}(E_y^n(i,j,k+1) - E_y^n(i,j,k)) \\ &- \tfrac{\Delta t}{\mu_x\Delta y}(E_z^n(i,j+1,k) - E_z^n(i,j,k)), \end{aligned} \quad (10)$$

where ε_x is the dielectric constant, σ_x is the electrical conductivity, μ_x is the magnetic permeability, Δt is the time step, and Δy and Δz are space steps, respectively.

Take the electric field component along the x-direction as an example, denoted as $E_x^{org}(i,j,k)$. Then, the grid is encrypted. At this time, the calculated result is recorded as $E_x^{enc}(i,j,k)$. The computation flow chart of the hybrid method combining FDTD and extrapolation method is shown in Figure 3.

From Equation (8), the extrapolation solution is

$$E_x^{\mathrm{ext}}(i,j,k) = \frac{1}{3}[4E_x^{\mathrm{enc}}(i,j,k) - E_x^{\mathrm{org}}(i,j,k)]. \quad (11)$$

D. Cascading

The scattering matrix for each independent periodic structure is calculated. Then, all independent scattering matrices are cascaded. Figure 4 shows the schematic diagram of the N-layer FSS. In addition, when the spacing is small ($d/\lambda < 1$), the propagation constant of the cross-polarization is negative imaginary, and the field decays exponentially away from the FSS. Thus, the quantities of practical interest are the reflection coefficient of the main polarization, and the cross-polarization is ignored. The reflection coefficients of a single-layer FSS are calculated using the method in Section II-C. Then, the single-layer scattering matrix according to the computation results of the reflection and transmission coefficients is deduced by the following expression:

$$\overline{\overline{S}}_n = \begin{bmatrix} T_n\left(1-\frac{R_n^2}{T_n^2}\right) & \frac{R_n}{T_n}e^{j2kd_n} \\ -\frac{R_n}{T_n}e^{-j2kd_n} & \frac{1}{T_n} \end{bmatrix}, \det\left(\overline{\overline{S}}_n\right) = 1, \quad (12)$$

$$d_n = d_1 + d_2 + \cdots + d_{n-1},\ n = 1,2,\ldots,N.$$

From Equation (12), the expression of the cascaded transmission matrix $\overline{\overline{T}}$ can be obtained as

$$\overline{\overline{T}} = \begin{bmatrix} A & B \\ C & D \end{bmatrix} = \overline{\overline{S}}_N \overline{\overline{S}}_{N-1} \cdots \overline{\overline{S}}_2 \overline{\overline{S}}_1. \quad (13)$$

When the second port is open circuit, A is the ratio of the voltage of the first port to the voltage of the second port and C is the ratio of the current of the first port to the voltage of the second port; when the second port is short circuit, B is the ratio of the voltage of the first port to the current of the second port and D is the ratio of the current of the first port to the current of the second port.

After cascading, the reflection and transmission coefficients of the multi-layer FSS turn out to be

$$R = -(C/D), \quad (14)$$

$$T = A - (BC/D). \quad (15)$$

III. VERIFICATION OF COMPUTATION METHOD

A. Verification of hybrid method

In order to test the accuracy of the hybrid method, a dielectric plate and FSS with infinite periodic structure are considered. The period of the dielectric plate along the x-axis and y-axis is 15 mm, its thickness is 6 mm, and the relative permittivity is 4.3. Metal patch with a length of 12 mm and a width of 3 mm on the surface of the above-mentioned dielectric layer. The model is shown in Figure 5. A Gaussian pulse excitation with the center frequency of 8 GHz is applied to the structure. The reflection coefficient comparison chart is shown in Figure 6(a) and (b), respectively. The extrapolated solution of Figure 6(a) is calculated from the grid size r = 1.5 mm and r = 3 mm. Figure 6(b) is calculated from the grid size r = 0.3 mm and r = 0.6 mm. Tables 1 and 2 show the comparing results of the dielectric plate and the FSS.

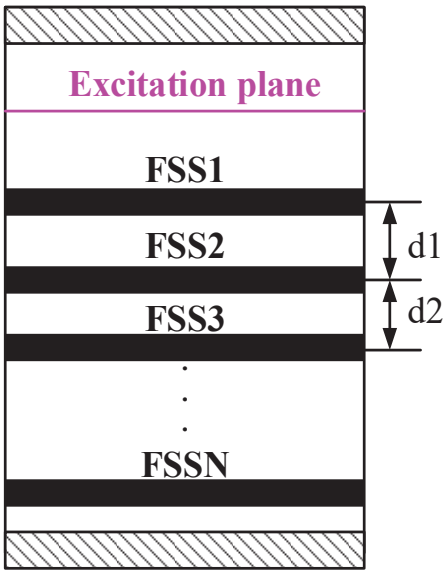

Fig. 4. The N-layer FSS.

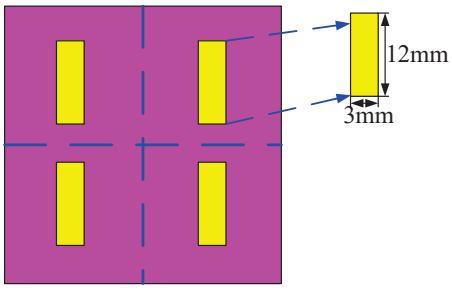

Fig. 5. Structure model.

The expression of maximum relative error is

$$R_r = \frac{\max|R_{\text{cst}} - R_i|}{R_{\text{cst}}}, \quad (16)$$

where R_{cst} is the simulation result (CST) and R_i is the computational result.

It can be seen from Figure 6 that the denser the grid, the higher the computation accuracy of the FDTD. However, if the computation accuracy is improved by encrypting the grid, the memory requirement will be greatly increased, thus reducing the computation speed. In engineering applications, not only high computation accuracy but also fast computation speed is required. Therefore, the method needs to be improved. In addition, it can be seen from Figure 6 that the sparser the grid, the worse the computation accuracy of the FDTD, but the extrapolation solution can greatly improve the computation accuracy without increasing the grid density.

It can be seen from Tables 1 and 2 that within the range of errors permitted, the computation speed of the hybrid method is superior. The proposed method can

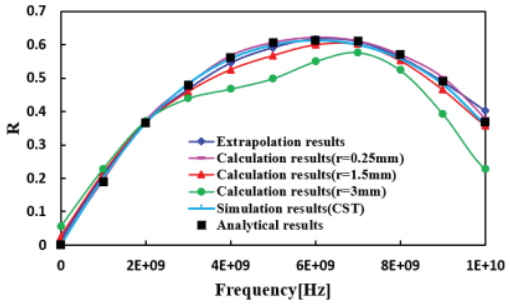

(a) Comparing methods for calculating reflection coefficient of periodic dielectric plate.

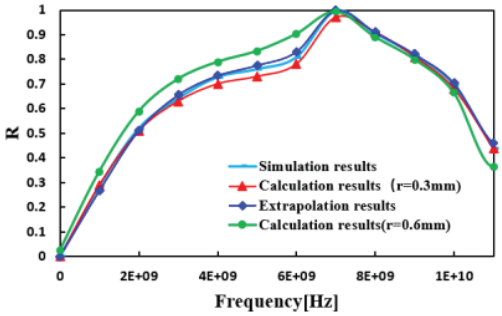

(b) Comparing methods for calculating reflection coefficient of FSS.

Fig. 6. Comparison chart of computation results.

Table 2: Comparison of the efficiency (FSS)

	Spacing	Running time	Memory requirement	Maximum relative error
FDTD	0.6 mm	233.5 s	7406 M	7.05%
	0.3 mm	1025.1 s	12,853 M	5.9%
MM	Running time		Memory requirement	Maximum relative error
	1256.2 s		14,855 M	1.8%
CST	4267.8 s		266,761 M	

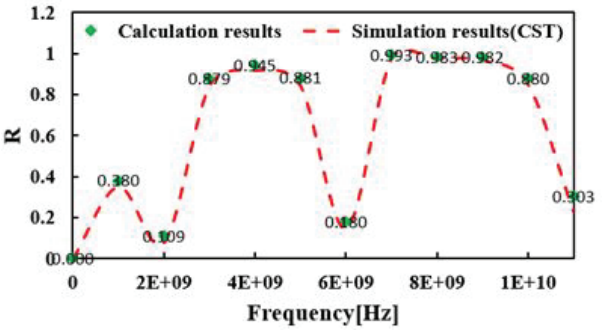

Fig. 7. Reflection coefficient comparison diagram.

greatly save the computation time and improve accuracy of the EM properties of the FSS.

B. Verification of cascade method for multi-layer FSS

The above method is extended to the computation of EM characteristics of multi-layer FSS. The two-layer FSS structure is considered. The distance between the two-layer structures is 24 mm, and the structural parameters of the FSS are the same as those in Section III-A. The computation results are shown in Figure 7.

As shown in Figure 7, the hybrid method is used to calculate the reflection coefficient of the multi-layer FSS. The calculated result is very close to the simulation result, and the error between the two is small. In addition, the matrix cascading technology can greatly reduce the number of grids and the computer memory requirements and increase the computation speed. Through comparison, we can see that the computation method in this paper is correct and reasonable.

Table 1: Comparison of the efficiency (dielectric plate)

	Spacing	Running time	Memory requirement	Maximum relative error
FDTD	3 mm	4.906 s	7306 M	17.5%
	1.5 mm	8.342 s	7322 M	7.1%
	0.25 mm	858.66 s	8476 M	1.4%
MM	Running time		Memory requirement	Maximum relative error
	12.436 s		7886 M	1.5%
CST	120.86 s		16998 M	

IV. EXAMPLES AND ANALYSIS

A. Computation of FSS with different patches

The structural parameters of the dielectric layer are the same as above, and the length and width of the upper patch are both 12 mm. And the length and width of the lower patch are 12 and 3 mm, respectively. The 3D model is shown in Figure 8, the Gaussian excitation source is the same as above, and the computational result is shown in Figure 9. The FSS with different patch geometries are shown in Table 3.

From Table 3, we can see that the computation speed of the hybrid method is superior. In the same way, the algorithm proposed in the paper is suitable for the com-

Table 3: Comparing methods

	Running time	Occupy memory
MM	2625.1 s	26,988 M
CST	8468.6 s	47,899 M

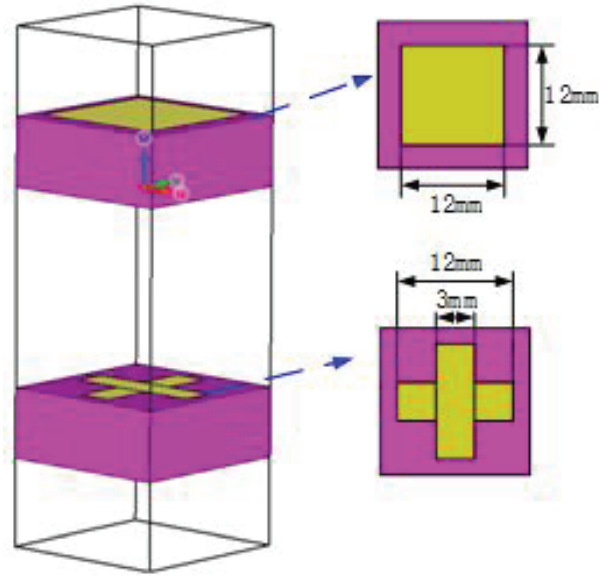

Fig. 8. Structure model.

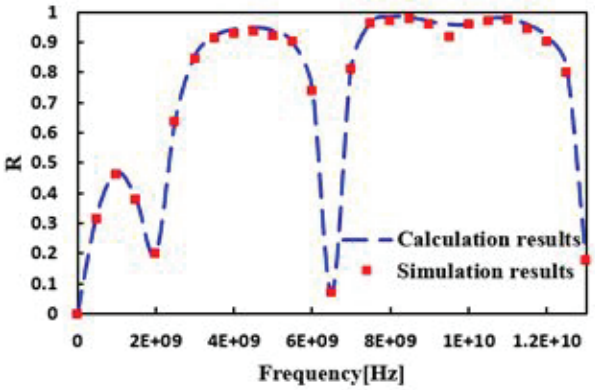

Fig. 9. Computation results.

putation of EM characteristics of the FSS with different patch geometry.

B. Factors influencing reflection coefficient

1) The impact of dielectric constant

The reflection coefficient of the FSS is closely related to the dielectric constant of the dielectric layer. Suppose the structural parameters of FSS are the same as Section III-A. Keep the excitation source and the length and width of the dielectric layer unchanged. Change the dielectric constant of the dielectric layer and observe the change of reflection coefficient. The computed reflection coefficients are shown in Figure 10.

From Figure 10, within 1-5 of dielectric constant, it can be concluded that the resonance frequency decreases with increasing dielectric constant. It can be seen that

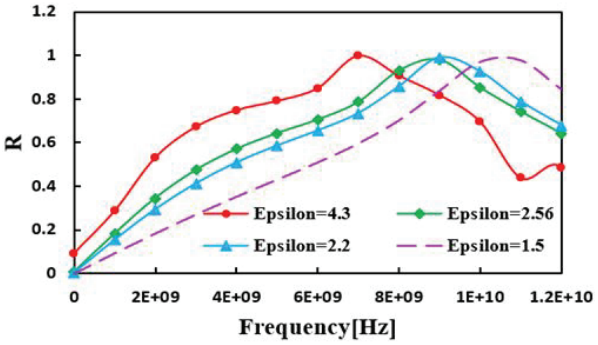

Fig. 10. The effect of dielectric constant on results.

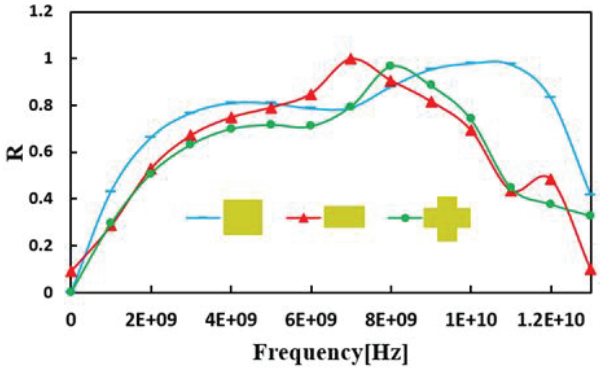

Fig. 11. The effect of patch geometry on results.

the dielectric layer mainly affects the resonant frequency. Therefore, by loading FSS, the transmission frequency of the radome can be adjusted effectively.

2) The impact of patch geometry parameters

The reflection coefficient of the FSS is not only closely related to the dielectric constant but also tightly dependent on the structure of the patch. As in the previous case, keeping the excitation source, the size of the dielectric layer, and the material characteristics unaltered, and changing the patch geometry to square, monopole, and cross shape, the computed results are shown in Figure 11.

As shown in Figure 11, the resonance frequency depends on the patch geometry; the larger the patch geometry covers the area of the dielectric layer, the larger the resonance point of frequency. It provides an important reference basis for the design of passband range of the FSS.

V. CONCLUSION

1. In this paper, a hybrid method combining FDTD, extrapolation, and cascading is proposed to compute the reflection coefficient of the multi-layer FSS. By means of an example, it is shown that the

algorithm has the advantages of increasing the computation speed and accuracy, and reducing the computer memory.

2. The EM characteristics of the FSS are computed. The results show that the proposed method in this paper is also applicable to multi-layer FSS with different patch geometry.
3. Within 1-5 of dielectric constant, the resonance frequency decreases with increasing the dielectric constant.
4. The resonance frequency depends on the patch geometry. The larger the area of the patch geometry covering the dielectric layer, the larger the resonance frequency; a property which provides an important reference for the design of the FSS.

ACKNOWLEDGMENTS

This work was supported by the National Natural Science Foundation of China under Grant 61871405.

REFERENCES

[1] D. M. Guo, Y. W. Sun, and Z. Y. Jia, "Methods and research progress of high performance manufacturing," *journal of mechanical engineering*. vol. 51, no.11, pp. 119-134, 2014.

[2] D. J. Kozakoff, *Analysis of Radome Enclosed Antennas*. Boston: Artech House, 2009.

[3] B. L. Cannon, and J. W. Jordan, "Integration of an equivalent aperture method into full-wave electromagnetic simulation of airborne radomes," *Journal of the Applied Computational Electromagnetic Society*, vol. 31, no. 5, pp. 473-480, 2016.

[4] R. Panwar, and J. R. Lee, "Progress in frequency selective surface-based smart electromagnetic structures: a critical review," *Aerospace Science & Technology*, vol. 66, no. 1, pp. 216-234, 2017.

[5] Q. Chen, L. Chen, J. Bai, and Y. Fu, "Design of absorptive frequency selective surface with good transmission at high frequency," *Electronics Letters*, vol. 51, no. 12, pp. 885-886, 2015.

[6] W. Wu, X. Liu, K. Cui, Y. Ma, and Y. Yuan, "An ultrathin and polarization-insensitive frequency selective surface at Ka-band," *IEEE Antennas and Wireless Propagation Letters*, vol. 17, no. 1, pp. 74-77, 2018.

[7] K. Payne, K. Xu, and J. H. Choi, "Generalized synthesized technique for the design of thickness customizable high-order bandpass frequency-selective surface," *IEEE Transactions on Microwave Theory and Techniques*, vol. 99, no. 1, pp. 1-11, 2018.

[8] K. Zhang, W. Jiang, J. Ren, and S.-X. Gong, "Design of frequency selective absorber based on parallel LC resonators," *Progress in Electromagnetics Research*, vol. 65, no. 1, pp. 91-100, 2018.

[9] S. Narayan, G. Gulati, B. Sangeetha, and R. U. Nair, "Novel metamaterial-element-based FSS for airborne radome applications," *IEEE Transactions on Antennas and Propagation*, vol. 66, no. 9, pp. 4695-4707, 2018.

[10] M. Bai, B. Liang, and H. Ma, "An efficient FDTD algorithm to analyze skewed periodic structures impinged by obliquely incident wave," *Journal of the Applied Computational Electromagnetic Society*, vol. 30, no. 10, pp. 1068-1073, 2015.

[11] N. Liu, Study on rapid design method for high performance frequency selective surface radome. Department of Mechanical Engineering, Dalian university of technology, Ph.D, Spring 2019.

[12] K. Fan, Design and research on active FSS radome. Department of Electronic Information Engineering, Nanjing university of aeronautics and astronautics, MS, Spring 2014.

[13] H. Y. Chen and S. H. Wen, "An empirical formula for resonant frequency shift due to Jerusalem-cross FSS with substrate on one side," *Applied Computational Electromagnetic Society*, vol. 30, no. 7, pp. 730-737, 2018.

[14] K. S. Feng, C. J. Xie, and J. D. Xu, "Finite element method analysis of frequency selective characteristics of periodic structure of medium," *Journal of Microwaves*, vol. 24, no. 1, pp. 1-8, 2008.

[15] M. Jin and M. Bai, "On the transmitted beam degradation through FSS in the working band by plane-wave spectrum computation and evaluation," *Applied Computational Electromagnetic Society*, vol. 31, no. 9, pp. 1135-1143, 2016.

[16] P. Monk, "Sub-gridding FDTD schemes," *Applied Computational Electromagnetic Society*, vol. 11, no. 1, pp. 37-46, 1996.

[17] C. M. Chen, "Extrapolation of triangular linear element in general domain," *Numerical Mathematics A Journal of Chinese*, vol. 3, no. 1, pp. 1-6, 1989.

[18] Y. M. Li, "A new algorithm for improving computation precision in finite difference time domain," *Proceedings of the 10^{th} national conference on electrical engineering mathematics*, 2005.

[19] Z. Y. Yu, *The Finite-Difference Time-domain Method for Electromagnetics with MATLAB Simulations*. National defense industry press, 2012.

Yangyang Wang was born in 1990. She received the Ph.D. degree from Chongqing University, Chongqing, China, in 2020. She is currently working with the National Digital Switching System Engineering and Technological Research Center, Zhengzhou, China. Her current research interests include antenna and radome analysis and design, computational electromagnetics, etc.

Dongfang Zhou was born in 1963. He received the Ph.D. degree from Zhejiang University, Hangzhou, China, in 2005. He is currently working with the National Digital Switching System Engineering and Technological Research Center, Zhengzhou, China. His current research interests include antenna and propagation, radio frequency and microwave circuits and systems, and high power microwave and radome.

Qikun Liu was born in 1985. He received the Ph.D. degree from PLA Strategic Support Information Engineering University. He is currently working with the National Digital Switching System Engineering and Technological Research Center, Zhengzhou, China. His current research interests include antenna and propagation, radio frequency, and radome.

Dewei Zhang received the Ph.D. degree from the National Digital Switching System Engineering and Technological Research Center, Zhengzhou, China, in 2005. He is currently working with the National Digital Switching System Engineering and Technological Research Center. His current research interests include RF/microwave devices, such as antennas, filters, and power amplifier, for wireless communications, and radar systems.

Bi-Static Radar Cross-Section Test Method by using Historic Marconi Set-up and Time Gating

Yousef Azizi[1], Mohammad Soleimani[2], Seyed Hasan Sedighy[3], and Ladislau Matekovits[4]

[1,2]Department of Electrical Engineering
Iran University of Science and Technology, Tehran 1684613114, Iran

[3]School of Advanced Technologies
Iran University of Science and Technology, Tehran 1684613114, Iran

[1,4]Department of Electronics and Telecommunications
Politecnico di Torino, Turin 10129, Italy

[4]Department of Measurements and Optical Electronics,
Politehnica University Timisoara, Timisoara 300006, Romania

[4]Istituto di Elettronica e di Ingegneria del
l'Informazione e delle Telecomunicazioni, National Research Council, Turin 10129, Italy

***Abstract* –** In this paper, a low-cost, simple, and reliable bi-static radar cross-section (RCS) measurement method by using a historic Marconi set-up is presented. It uses a transmitting (Tx) antenna (located at a constant position, at a reference angle of $\theta = 0^\circ$) and a moving receiver (Rx) antenna. A time gating method is used to extract the information from the reflection in the time domain; applying time filter allows removing the antenna side-lobe effects and other ambient noises. In this method, the Rx antenna (on the movable arm) is used to measure the reflected field in the angular range from 1° to 90° from the structure (printed circuit board, PCB) and the reference configuration represented by a ground (GND) plane of the same dimension. The time gating method is then applied to each pair of PCB/GND measurements to extract the bi-static RCS pattern of the structure at a given frequency. Here, a comparison of measurement results is carried out at 18 and 32 GHz with simulation ones indicating successful performance of the proposed method. It can be used as a low-cost, reliable, and available option in future measurement and scientific research.

***Index Terms* –** RCS Measurement, Marconi Set-Up, Time Gating.

I. INTRODUCTION

Radar cross-section (RCS) measurement is one of the essential requirements in the field of telecommunication engineering, of which evaluation is always controversial due to the existence of measurement errors, environmental noise, post-processing requirements to extract results, and expensive automation measuring equipment [1]. RCS was first discussed in the military field [2–4]. This concept was introduced in non-military applications in 1965 [5]. Accurate modeling and analysis of structures is a basic need in the design of radar cross-section reduction (RCSR) structures. For this purpose, physical optics (PO) analyses of small structures are an effective method for RCS estimation of small structures [6]. In [7], investigation of the RCS of finite frequency selective surface (FSS) has been presented and compared with the infinite size FSS, which is helpful for the design of FSS structures with low RCS. The RCS measurement techniques have been well presented in [8]. Performing RCS measurement in a laboratory requires hardware such as shielded chamber, absorbers, Tx/Rx antennas, radio frequency (RF) signal sources, and receivers [9]. Also, extracting and processing measurement information to eliminate background noise, antenna side-lobe effects, and other environmental reflection factors require using numerical techniques, such as time gating, which is well discussed in the literature, for example in [10]. Based on the optical theorem, the wideband RCS measurements method that uses a forward RCS of structure has been presented in [11]. The RCS measurement methods for static and dynamic facilities were presented in [12] and [13], respectively. By using spectral extrapolation technique, one can eliminate the end of band errors of RCS measurement, which is an appropriate technique in minimizing of the noise [14]. During the last decades, many methods, such

Submitted On: October 16, 2021
Accepted On: January 28, 2022

https://doi.org/10.13052/2022.ACES.J.370206

as the method of moment (MOM), geometrical theory of diffraction (GTD), and PO have been proposed [15]. Moreover, many numerical tools such as finite element method (FEM), boundary element method, and software packages implementing a combination of them were developed to easily calculate the RCS of structures [16]. Bi-static RCS measurement by using some special equipment (synchronized Tx/Rx, source and receiver equipment, and moving rails) is expensive, and, therefore, only a few laboratories can measure it [17, 18]. To solve the problem of expensive automation set-ups, using Marconi training set-up can be effective as a simple and reliable solution in the static RCS measurement. The Marconi set-up, which is used as one of the teaching aids in laboratories, has a movable arm and an angled calibrator (protractor) whose rotation rate can be adjusted and controlled [19]. However, both automatic and manual solutions for RCS measurement are possible.

In this paper, a simple, cost-effective, and reliable numerical bi-static RCS measurement method is presented to extract the RCS results by mounting the Marconi set-up inside of the anechoic chamber and using the time gating method. In this measurement, the Tx antenna is placed in front of the printed circuit board (PCB) and GND of the sample structure, and the Rx antenna is moved manually on the rotating-angular calibrated arm to extract the reflection information at all angles from 1° to 90° for different frequencies. Then, the PCB/GND measurement information at each angle is post-processed, by converting them from frequency domain to time domain by using inverse fast Fourier transform (IFFT). The data are then time filtered and reconverted to the frequency domain by using FFT. The procedure is applied to data obtained from both PCB and GND reflections at each angle. The bi-static pattern is then extracted at each frequency. The measurement results and the results obtained from the numerical tools of CST Suite software are in good agreement with the IEEE 1502 recommended [16] (known as the main reference for RCS measurement). Comparison of simulation and measurement results of a sample structure indicates that this simple, reliable, and cost-effective test method could be used as a measurement method instead of the conventional automated test procedure that needs software automation for controlling the hardware (rail, Tx, and Rx antennas).

II. BI-STATIC TEST METHOD

The Marconi test set-up as one of the oldest equipment in the communication laboratory is shown in Figure 1(a). This set-up has a central stand for placing the device under test (DUT) on it, ad a rotating and calibrated arm where the amount of rotation can be seen and controlled (see Figure 1(b) and (c)). To measure bi-static RCS, the Tx antenna is placed in front of the target at the same height as the DUT, while the Rx antenna is placed on the rotating arm at the same height. The RX antenna is rotating to cover any angle needed for the measurement of RCS, storing and processing the reflection signal from the target. The prototype of the sample metasurface for RCSR test is shown in Figure 1(d). The metasurface under test has a dimension of $250 \times 250\text{mm}^2$, and it is printed on a single layer grounded RO4003 substrate with 1.6-mm thickness (Figure 1(d)).

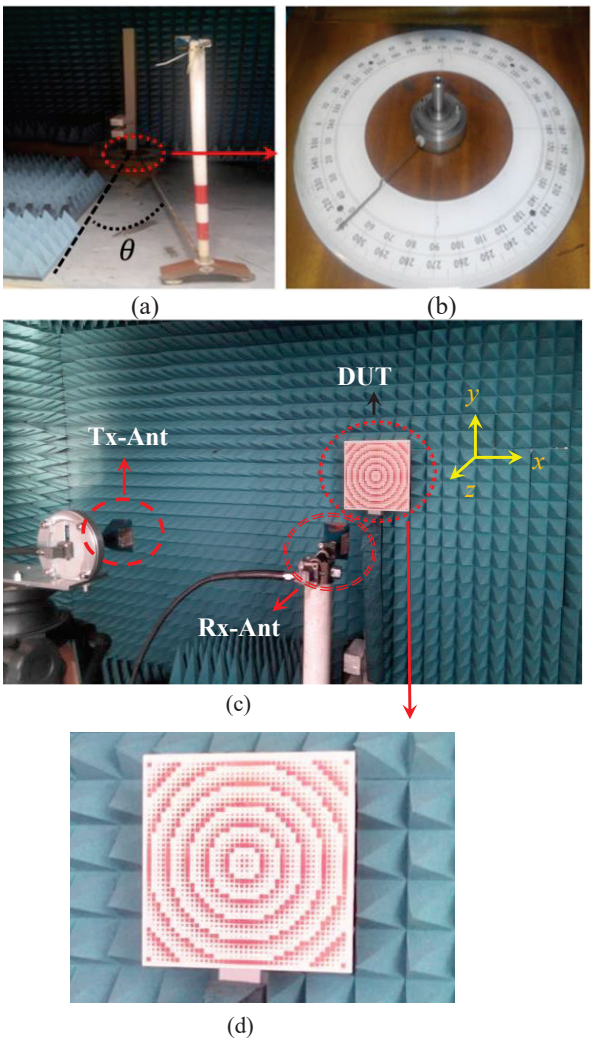

Fig. 1. Photograph of the measurement set-up and DUT. (a) Schematic of the Marconi set-up in anechoic chamber. (b) Angular calibrated surface of the Marconi set-up. (c) Bi-static set-up using Marconi set-up, Tx/Rx antenna, and DUT.(d) Sample metasurface under test

To measure the bi-static pattern of the sample structure by using the Marconi set-up, it is necessary to fix the Tx antenna in front of the target and then measure

the reflection from PCB/GND of DUT by the Rx antenna mounted on a movable arm at any angle. The Rx antenna is rotated manually by using the calibrated screen of the set-up protractor (see Figure 1(b)) to minimize the angular error. Since the structure of the sample metasurface has symmetry with respect to x/y axes (horizontal and vertical axes in Figure 1), it is appropriate to measure the reflection from the PCB/GND of the metasurface in the angle range of $1^\circ \div 90^\circ$.

III. POST-PROCESSING PROCEDURE

After measuring the reflection from PCB/GND at all desired angles ($\theta = \pm 1^\circ \pm 90^\circ$) by using the time gating method, the PCB/GND reflection signals (both real and imaginary parts) at any specific angle θ are converted from the frequency domain to the time domain. The discrete IFFT equation is used [20].

$$X_k = \frac{1}{N}\sum_{n=0}^{N-1} x_n e^{i2\pi kn/N}, k = 0, \ldots, N-1 \qquad (1)$$

where x_n is the nth value of the reflection signal (real and imaginary) in the frequency domain, N is the number of frequency samples, and X_k is the kth value of the signal in the time domain. Then, by applying a suitable time filter (here Kaiser) in the time domain, noise and other existing environmental reflections are removed. At this stage, only the PCB/GND reflection signals remain, and by FFT, the reflection rate from the PCB/GND is calculated in terms of frequency. The FFT equation that is used reads [20]

$$x_k = \sum_{n=0}^{N-1} X_k e^{i2\pi kn/N}, k = 0, \ldots, N-1 \qquad (2)$$

where X_k is the kth value of the signal in the time domain, N is the number of time steps, and x_n is the nth value of the complex value signal in the frequency domain. This coordinate loop shown in Figure 2 flowchart is used to extract the PCB/GND reflection at all angles ($\theta = 1^\circ - 90^\circ$).

In order to apply the measurement flowchart presented in Figure 2 and measure the bi-static RCS of the metasurface at 18 and 32 GHz, N5227A PNA Network Analyzer was used. The 30-GHz bandwidth (from 10 to 40 GHz) has been covered by three sets of TX/Rx antennas, in 1601 frequency points in each frequency band, and considering 100 Hz PNA resolution bandwidth. The frequency bandwidth, steps, and resolution bandwidth are chosen so that the reflected signal from PCB/GND in the time domain might be detected [1]. It should also be noted that the radial distance between Tx/Rx antenna to PCB/GND is equal to 2.5 m, which gives rise to high spatial attenuation, especially at high frequencies.

To depict the RCS results of the structure in the entire band of interest ($10-40$ GHz), the RCS results from three measurements (in three separate frequency bands of $10-18$, $18-22$, and $22-40$ GHz) are merged in one single plot and presented as the final RCS result of the proposed structure. By starting from $\theta = 1^\circ$, the reflection from PCB/GND was measured at all angles between 1° and 90°. It should be noted that the reflection measurement from DUT is done by the same configuration of the network analyzer, and, in this case, the reflection of both PCB and GND in the frequency domain has the same power range, as depicted in Figure 3(a). In this case, it is impossible to distinguish between the reflection signal of PCB and GND due to the similar amplitude of their reflection power. At this stage, the distinction between the reflection signals and consequently the time gate required to apply the time filter is determined by applying IFFT and transmitting the PCB and GND reflection signals from the frequency domain to the time domain. Figure 3(b) shows the PCB/GND reflection at $\theta = 1^\circ$ in the time domain (which corresponds to the $22-40$ GHz band).

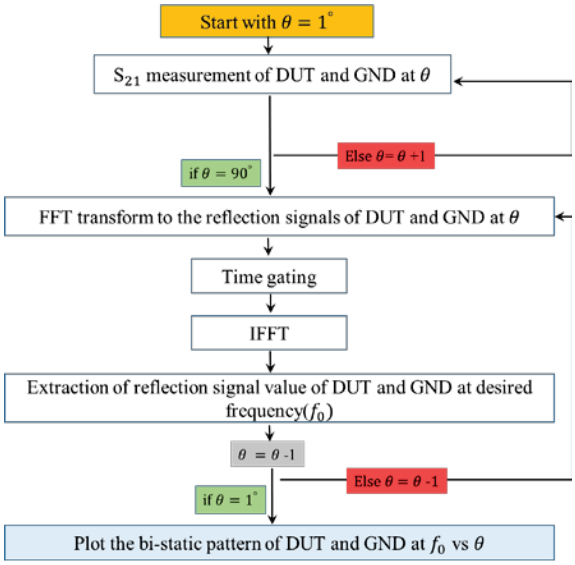

Fig. 2. Flowchart of RCSR measurement using the Marconi set-up and time gating method.

It can be seen that there is a difference in the reflection amplitude of PCB and GND in the time interval of $27-29$ ns. Applying a proper time filter to the reflection signals in this time interval reduces the background noise, side-lobe signals (especially at $6-10$ ns range that is related to the side-lobes), and reflection from other environmental factors with more than 80 dB. Figure 3(c) shows the PCB/GND reflection results after the application of the high order (400) Kaiser time filter. The difference between the reflection signal of PCB and GND in the period of $27-29$ ns can be seen in Figure 3(c).

By applying the appropriate time filter (Kaiser) as well as FFT to the signals of this time period, the

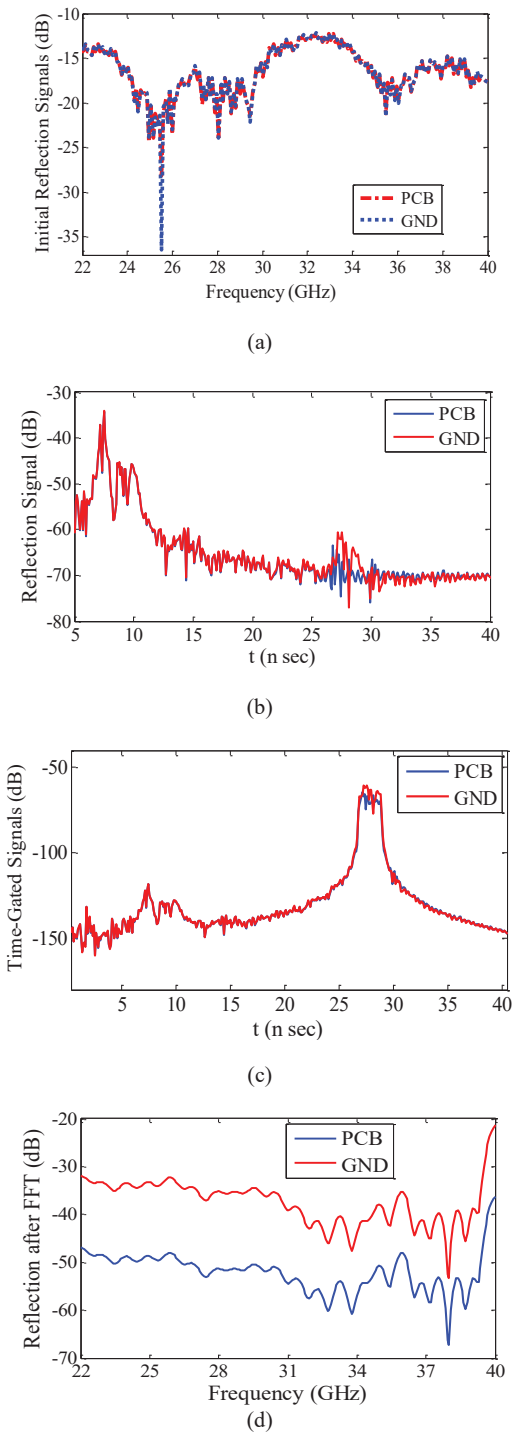

Fig. 3. Time and frequency domain reflection results of the PCB/GND and RCS results. (a) Initial reflection signal of PCB/GND in frequency domain. (b) Time domain measurement results of PCB/GND. (c) PCB/GND reflection results after applying Kaiser time gating filter. (d) Reflection signal of PCB/GND after FFT. (e) RCSR measurement and simulation of the sample metasurface at $\theta = 1^\circ$.

reflection of PCB and GND in the frequency domain and subsequently RCS result of considered sub-band, here 22−40 GHz, can be calculated. It should be noted that all post-processing steps, i.e., IFFT, FFT, and Kaiser filter calculation, have been implemented in Matlab.

In the next step, the PCB/GND reflection for the considered frequency band (22−40 GHz) at $\theta = 1^\circ$ is obtained by applying the IFFT which is plotted in Figure 3 (d). It can be appreciated that in the frequency range, 22–40 GHz, the reflection from the PCB surface is less than that from the GND one. One can conclude that by considering the metasurface, a broadband RCSR performance has been achieved. At this stage, the difference between PCB and GND signal is extracted as a measured RCSR, which is plotted in Figure 3 (e). The simulation and measurement results in Figure 3 (e) are in good agreement with each other and there are small differences (lower than 1.5 dB) between simulated and measured results at 18 and 32 GHz, which indicate the efficiency of the proposed test method. Comparison of the simulation results provided by the full-wave CST Microwave Studio software with the measured ones proves the accuracy and reliability of the proposed method.

In the same manner, RCS measurement of the metasurface in the other two frequency bands (10−18 and 18−22 GHz) has been carried out and the final RCS result was merged in Figure 4(a) and (b). Reflections of PCB and GND are plotted in Figure 4(a). Comparison between simulation and measurement results of sample metasurface is shown in Figure 4(b). It can be seen that there is a good agreement between measurement and simulation results in the overall 10−40 GHz frequency band.

A. Bi-static RCS pattern extraction

In the following, the reflection values are extracted from other angles as shown in Figure 2. By performing the above-described procedure for all of the other angles and extracting the reflection values from PCB/GND at 18 and 32 GHz (at any angle), the bi-static RCS pattern of sample metasurface was plotted in Figure 5(a) and (b), respectively.

For better presenting and validating the test method, the simulated and measured normalized PCB/GND RCS patterns are compared with each other. Due to the symmetry of the structure, the measurement results from $\theta = 1^\circ$ to 90° are mirrored to $\theta = -1^\circ$ to -90°. Note that the measurement results for $\theta = 0^\circ$ are not applicable (because the Tx and Rx antennas should have shared the same location); when using two Tx/Rx antennas, the minimum measurable angle is 1°.

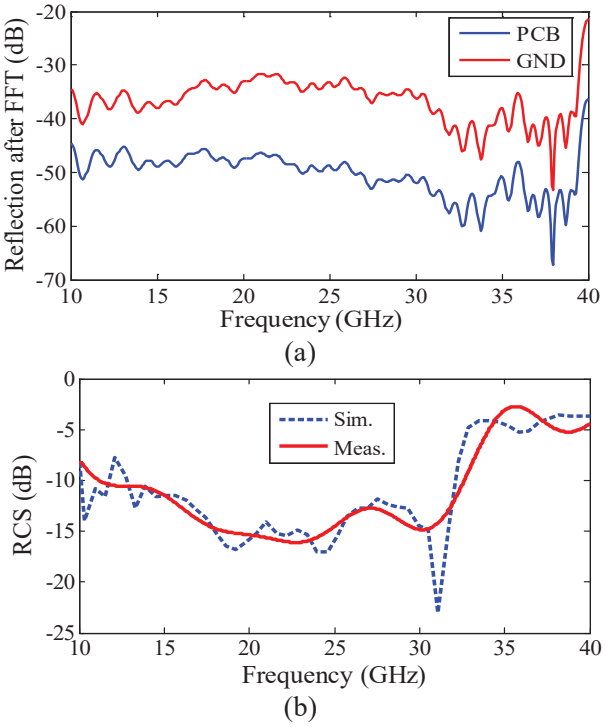

Fig. 4. Frequencydomain reflection results of the PCB/GND and RCS results. (a) Initial reflection signal of PCB/GND in frequency domain. (b) Frequencydomain measurement results of PCB/GND.

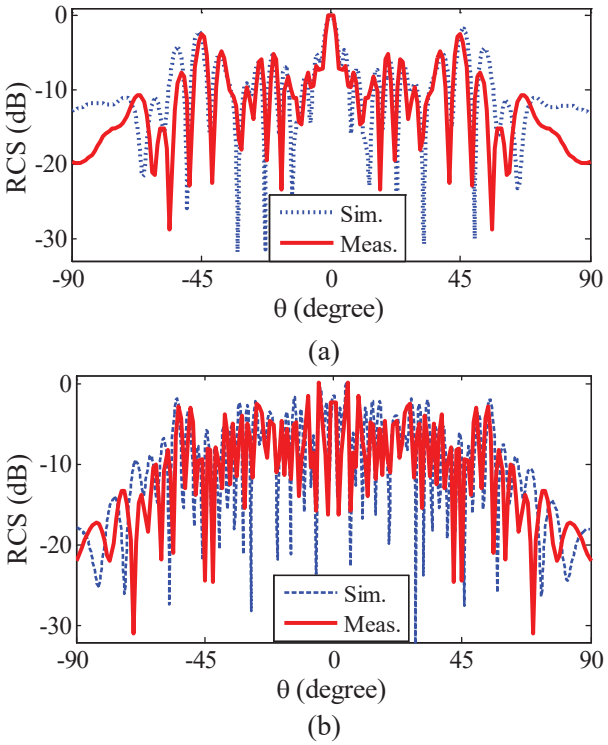

Fig. 5. Measurement and simulation bi-static results of the proposed metasurface at (a) 18 and (b) 32GHz.

Comparison of measurement and simulation results at 18 GHz shows that there is a good agreement between them in the angular range of $1^\circ - 60^\circ$. According to 5(a), there is a difference up to several dB between the simulation results and the measurement at angles greater than 60°. The reason for this difference can be the errors in the environmental factors such as set-up vibration, and errors related to the construction of metasurfaces and calibration of test equipment. In general, there is a good similarity and agreement between the measurement results with the proposed method and the simulation results at 18 GHz, which is due to the following reasons: (1) accurate angular calibration that is achieved using the Marconi set-up allowing accurate measurement of reflection at any angle; (2) elimination of the reflection noise effect from the environment by the high-order time filter, which reduces a significant part of the environmental measurement error (intrinsic advantage of time gating method). Similarly, a comparison between the measurement and simulation RCS pattern at 32 GHz shows that the proposed method has good accuracy. In this case, the number of resonances in the RCS pattern of the structure has increased, as can be seen in the measurement results. A comparison between the RCS pattern measurement and simulation results at 32 GHz proves that the proposed method has good accuracy. In this case, the number of resonances in the RCS pattern of the structure has increased, which can be appreciated in the measurement results.

Unlike the simulation results at 18 GHz and $60^\circ - 90^\circ$ incident angles, there is good agreement between the measurement and simulation results.

IV. CONCLUSION

A low-cost, simple, and reliable bi-static test method was proposed using a calibrated Marconi scientific-educational test set-up to perform the measurements and post-process by time-gating method (using FFT, time filtering, and IFFT) used to extract scattering pattern of objects and structures. This method can be used as a suitable alternative to expensive bi-static measurement methods that require expensive hardware and software equipment. Using time gate and applying appropriate time filtering (in this case, the Kaiser filter was used) leads to eliminating the background and environment reflection, also. The performance of the proposed method is confirmed by testing a sample metasurface and comparing it with the simulation results. The sample metasurface has dimensions of 250×250 mm^2, which is printed on the Rogers 4003 substrate with a thickness of 1.6 mm. Comparison of simulation and measurement

results shows that the proposed method has the potential to be widely used in laboratory and scientific applications by students and researchers. Also, the comparison between bi-static measurement results and simulation results (in accordance with the IEEE 1502 standard) validates the accuracy of the proposed method.

ACKNOWLEDGMENT

This work was supported by Iranian national science foundation (INSF) with grant number of 4003152. The authors are willing to express their gratitude to Mr. Gianluca Dassano and Gianfranco Albis for their cooperation and assistance in mounting the RCS measurement test set-up and extraction of results with the time gating method.

REFERENCES

[1] E. F. Knott, "Calibration," in Radar Cross Section Measurements. New York, NY, USA: Van Nostrand Reinhold, pp. 183-187, 1993.

[2] C. G. Bachman, H. E. King, and R. C. Hansen, "Techniques for Measurement of Reduced Radar Cross-sections", *Microwave Journal,* vol. 6, no. 1, pp. 61-67, Feb. 1963.

[3] W. A. Cummings, "Radiation Measurements at Radio Frequencies: A Survey of Current Techniques," 27 Proceedings of the IRE, vol. 47, no. 5, pp. 705-735, May 1959.

[4] P. D. Kennedy, "Equipment and Techniques for the Measurement of Radar Reflections from Model Targets," WESCON Convention Record, pt. 1, pp. 208-215, 1957.

[5] Special Issue on Ra2dar Reflectivity, Proceedings of the IEEE, vol. 53, no. 8, Aug. 1965.

[6] A. Gorji, B. Zakeri, and R. C. Janalizadeh, "Physical Optics Analysis for RCS Computation of a Relatively Small Complex Structure," *Applied Computational Electromagnetics Society Journal,* vol. 29, pp. 530-540, July 2014.

[7] C. Fang, X. Ye, Y. Zhang, Q. Wang, J. Zhao, N. Zhang, H. Jiang, C. Jin, and M. Bai, "Investigation of the RCS for Finite Bandpass Frequency Selective Surface," *Applied Computational Electromagnetics Society Journal,* vol. 34, no. 6, Jun. 2019.

[8] J. R. Huynen, "Measurement of the Target Scattering Matrix," *Proceedings of the IEEE,* vol. 53, no. 8, pp. 936-946, Aug. 1965.

[9] U. K. Chung, H. T. Chuah, and J. W. Bredow, "A Microwave Anechoic Chamber for Radar-cross Section Measurement," *IEEE Antenna and Propagation Magazine,* 39, 3, pp. 21-26, June 1997.

[10] A. Soltane, G. Andrieu, and A. Reineix, "Monostatic Radar Cross-Section Estimation of Canonical Targets in Reverberating Room Using Time-Gating Technique," in 2018 International Symposium on Electromagnetic Compatibility (EMC EUROPE), *IEEE,* pp. 355-359, 2018.

[11] C. Larsson, M. Gustafsson, "Wideband Measurements of the Forward RCS and the Extinction Cross Section," *Applied Computational Electromagnetics Society Journal,* vol. 28, no. 12, Dec. 2013.

[12] H. C. Marlow, D. C. Watson, C. H. Van Hoozer, and C. C. Freeny, "The RAT SCAT Cross-section Facility," *Proceedings of the IEEE,* vol. 53, no. 8, pp. 946-954, Aug. 1965.

[13] I. D. Olin and F. D. Queen, "Dynamic Measurement of Radar Cross-sections," *Proc. IEEE,* vol. 53, no. 8, pp. 954-961, Aug. 1965.

[14] C. F. Hu, N. J. Li, and C. H. Fang, "Application of Spectral Extrapolation Technique to Stepped-Frequency RCS Measurement," *Applied Computational Electromagnetics Society Journal,* vol. 35, no. 9, Oct. 2020.

[15] IEEE, 1502TM, "IEEE Recommended Practice for Radar Cross-Section Test Procedures," pp. 106-106, 1997.

[16] M. G. Cote, "Automated Swept-angle Bistatic Scattering Measurements using Continuous-wave Radar," *IEEE Trans. Instrum. Meas.,* vol. 41, no. 2, pp. 185-192, Apr. 1992.

[17] M. Z. Joozdani, M. K. Amirhosseini, and A. Abdolali, "Wideband Radar Cross-section Reduction of Patch Array Antenna with Miniaturised Hexagonal Loop Frequency Selective Surface," *Electron. Lett.,* vol. 52, no. 9, pp. 767-768, Apr. 2016.

[18] A. A. Toscano, "Marconi's Representations of the Wireless, In Marconi's Wireless and the Rhetoric of a New Technology," *Springer, Dordrecht,* pp. 57-85, 2012.

[19] G. C. Corazza, "Marconi's history," *Proc. IEEE,* vol. 86, pp. 1307-1311, July 1998.

[20] A. V. Oppenheim and R. W. Schafer, Discrete-Time Signal Processing, NJ, Upper Saddle River: Prentice-Hall, 1989.

Yousef Azizi was born in Kermanshah, Iran, in 1989. He received his B.Ss degree in Electrical Engineering from Urmia University (UU), Urmia, Iran, in 2013. He also received his M.Sc. and Ph.D. degree all in Electrical Engineering from Iran University of Science and Technology (IUST), Tehran, Iran, in 2016 and 2021, respectively. He is currently a postdoctoral researcher in the Department of Electrical Engineering at ISUT. His major research interests are the design of Metasurface, Superstrate Antenna, planar and conformal Modulated surface for Radar Cross Section Reduction (RCSR).

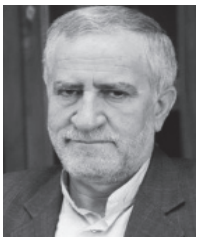

Mohammad Soleimani received the B.Sc. degree in electrical engineering from the University of Shiraz, Shiraz, Iran, in 1978, and the M.Sc. and Ph.D. degrees from Pierre and Marie Curie University, Paris, France, in 1981 and 1983, respectively.

He is currently a Professor with the School of Electrical Engineering, Iran University of Sciences and Technology, Tehran, Iran and serves as the Director with the Antenna and Microwave Research Laboratory. He has also served in many executive and research positions. He has authored and coauthored 19 books (in Persian) and more than 200 journal and conference papers. His research interests include electromagnetics and high-frequency electronics and antennas.

Seyed Hassan Sedighy received the B.Sc., M.Sc., and Ph.D. degrees in electrical engineering from the Iran University of Science and Technology (IUST) in 2006, 2008, and 2012, respectively.

He is currently an Associate Professor with the School of Advanced Technologies, Iran University of Sciences and Technology. His current research interests include microstrips antenna, optical transformation, design and application of metamaterials, and RF radio links.

Ladislau Matekovits received the degree in electronic engineering from Institutul Politehnic din Bucureşti, Bucureşti, Romania, and the Ph.D. degree (Dottorato di Ricerca) in electronic engineering from Politecnico di Torino, Torino, Italy, in 1992 and 1995, respectively.

Since 1995, he has been with the Department of Electronics and Telecommunications, Politecnico di Torino, first with a post-doctoral fellowship, then as a Research Assistant. He joined the same department as an Assistant Professor in 2002 and was appointed as a Senior Assistant Professor in 2005 and as an Associate Professor in 2014. In February 2017, he received the Full Professor qualification (Italy). In late 2005, he was a Visiting Scientist with the Antennas and Scattering Department, FGAN-FHR (now Fraunhofer Institute), Wachtberg, Germany. From July 1, 2009, for two years, he has been a Marie Curie Fellow with Macquarie University, Sydney, NSW, Australia, where, in 2013, he also held a Visiting Academic position and, in 2014, was appointed as an Honorary Fellow. Since 2020, he has been an Honorary Professor with the Polytechnic University of Timisoara, Romania and an Associate of the Italian National Research Council. He has been appointed as a Member of the National Council for the Attestation of University Degrees, Diplomas, and Certificates (CNATDCU), Romania, for the term 2020–2024.

His main research activities concern numerical analysis of printed antennas and, in particular, development of new, numerically efficient full-wave techniques to analyze large arrays, and active and passive metamaterials for cloaking applications. Material parameter retrieval of these structures by inverse methods and different optimization techniques has also been considered. In the last years, bio-electromagnetic aspects have also been contemplated, as, for example, design of implantable antennas or development of nano-antennas, for example, for drug delivery applications.

He has published 375+ papers, including 100+ journal contributions, and delivered seminars on these topics all around the world: Europe, USA (AFRL/MIT-Boston), Australia, China, Russia, etc. Prof. Matekovits has been invited to serve as Research Grant Assessor for government funding calls (Romania, Italy, Croatia, and Kazakhstan) and as International Expert in Ph.D. thesis evaluation by several universities from Australia, India, Pakistan, Spain, etc.

Dr. Matekovits has been a recipient of various awards in international conferences, including the 1998 URSI Young Scientist Award (Thessaloniki, Greece), the Barzilai Award 1998 (Young Scientist Award, granted every two years by the Italian National Electromagnetic Group), and the Best AP2000 Oral Paper on Antennas, ESA-EUREL Millennium Conference on Antennas and Propagation (Davos, Switzerland). He is a recipient of the Motohisa Kanda Award 2018, for the most cited paper of the *IEEE Transactions on Electromagnetic Compatibility* in the past five years, and, more recently, he has been awarded with the 2019 American Romanian Academy of Arts and Sciences (ARA) Medal of Excellence in Science and by the Ad Astra Award 2020, Senior Researcher, for excellence in research.

He has been an Assistant Chairman and Publication Chairman of the European Microwave Week 2002 (Milan, Italy) and General Chair of the *11th International Conference on Body Area Networks (BodyNets) 2016*. Since 2010, he has been a member of the organizing committee of the *International Conference on Electromagnetics in Advanced Applications (ICEAA)*, and he is a member of the technical program committees of several conferences. He serves as an Associated Editor for the *IEEE Access*, *IEEE Antennas and Wireless Propagation Letters*, and *IET Microwaves, Antennas & Propagation* and as a Reviewer for different journals.

Synthesis of Thinned Planar Arrays Using 0-1 Integer Linear Programming Method

Mingyu Wang and Xuewei Ping

College of Computer and Information Engineering,
Hohai University, Nanjing 211100, China
201307020029@hhu.edu.cn, xwping@hhu.edu.cn.

***Abstract* –** This paper proposes a fast optimization method for synthesizing thinned planar antenna arrays. A 0-1 integer linear programming (ILP) model was proposed for the antenna array optimization. This model mainly aims to minimize the peak sidelobe level (PSLL) and consider the design requirements of narrow beamwidth and high directivity, finally obtaining the optimal distribution of the turned "ON" element positions in the aperture. Several cases of planar array designs with different aperture sizes and scan angles were provided in the paper and compared with other popular algorithms. Numerical results showed that the new method can effectively optimize the thinned planar arrays, including large-scale arrays, while significantly reducing the computational cost and time.

***Index Terms* –** Antenna arrays optimization, planar array thinning, sidelobe level (SLL), 0-1 integer linear programming (ILP).

I. INTRODUCTION

Thinned antenna arrays are of great application value for many practical engineering fields such as mobile communication systems, radar antennas, and navigation systems. However, array thinning is a complex nonlinear optimization problem, which is hard to find the optimal solution in a short time.

In general, optimization methods can be divided into two main categories: heuristic algorithms and deterministic algorithms. In recent years, swarm intelligence algorithms have been favored by many researchers for their flexibility and efficiency. Stochastic algorithms such as genetic algorithm (GA) [1], particle swarm optimization (PSO) algorithm [2], cuckoo search (CS) algorithm [3], ant colony optimization (ACO) method [4], improved chicken swarm optimization (ICSO) method [5], etc., have been applied to synthesize thinned arrays. These methods have obvious advantages in solving nonlinear optimization problems, owing to their global search capabilities and the fact that they do not depend on a good initial value. However, they are computationally expensive and cannot be applied to the synthesis of large-scale antenna arrays. Moreover, the scanning performance of the thinned planar array is also an important design consideration. The random searching methods in [22] and [24] are able to obtain a low peak sidelobe level (PSLL) for a given beam scanning direction; yet, the optimization process is too time-consuming and the PSLL is not optimal.

Some deterministic algorithms have also been used to synthesize antenna arrays. In [6], Willey proposed a space tapering method that yields predictable gain, beamwidth, and sidelobe level (SLL). Skolnik *et al*. [7] proposed a statistical approach to design density taper arrays. Bucci *et al*. [8] proposed a simple deterministic method for thinning planar circular arrays. These approaches are all non-iterative procedures and computationally efficient. However, they are not global optimization methods. In [9] and [10], Keizer synthesized linear and planar arrays using the iterative Fourier technique (IFT), respectively. This algorithm has been applied to the design of large-scale thinned arrays successfully. However, it is prone to trap in local optima and needs to perform several times to seek the global optimum solution. Besides, analytic algorithms based on difference sets (DS) and almost difference sets (ADS) have been proposed in [11–13]. However, since the number of control variables in the DS and ADS sequences is limited, those methods apply only to a finite number of array apertures. Recently, a new method for designing thinned antenna arrays through the quantum Fourier transform (QFT) is presented in [14]. Gu *et al*. [15] proposed a novel algorithm called the probability learning IFT (PLIFT), a method introducing an innovative adaptive learning mechanism with better global convergence and robustness. Both of these methods can be applied for large-scale array thinning.

In this paper, the 0-1 integer linear programming (ILP) method is proposed for planar antenna array thinning. In this method, the optimization model is built with maximized directivity as the objective function and maximum acceptable SLL as the constraints. The intlinprog

Submitted On: December 16, 2021
Accepted On: February 14, 2022

https://doi.org/10.13052/2022.ACES.J.370207

function in MATLAB was utilized to solve this linear model. The 0-1 ILP method is a global optimization algorithm, which has been successfully applied to solve many engineering problems, such as the design of homogeneous magnets [16]. However, to the best of the authors' knowledge, the 0-1 ILP technique has not been used to optimize thinned antenna arrays. Compared with the stochastic methods, the new approach has a distinct advantage in computational efficiency, especially in high-dimensional, large-scale problems.

II. MATHEMATICAL FORMULATION AND METHOD

It is assumed that the size of the array is $M \times N$; d_x and d_y are the row spacing and column spacing between elements, respectively. They are both equal to 0.5λ. The coordinates of the element in row m, column n can be expressed as (md_x, nd_y), $1 \le m \le M$, $1 \le n \le N$.

The far-field radiated by this planar antenna array is given as

$$E(I_{mn},\theta,\varphi) = EF(\theta,\varphi)\cdot AF(I_{mn},\theta,\varphi), \tag{1}$$

$$\mathrm{AF}(I_{mn},\theta,\varphi) = \sum_{m=1}^{M}\sum_{n=1}^{N} I_{mn}\cdot e^{jk\cdot\left[(m-1)d_x u+(n-1)d_y v\right]} \tag{2}$$

where:

$$\begin{aligned} u &= \sin(\theta)\cos(\varphi) - \sin(\theta_0)\cos(\varphi_0) \\ v &= \sin(\theta)\sin(\varphi) - \sin(\theta_0)\sin(\varphi_0) \end{aligned} \tag{3}$$

where $EF(\theta, \varphi)$ is the radiation pattern of individual elements, AF $(I_{mn}, \theta, \varphi)$ is the array factor, $k = (2\pi/\lambda)$ is the wavenumber, and λ is the wavelength of electromagnetic wave. $\theta \in [0, \pi/2)$ and$\varphi \in [0, 2\pi)$ are the elevation angle and the azimuth angle, respectively. (θ_0, ϕ_0) is the scanning direction of the main beam. $I_{mn} \in \{0, 1\}$ is the amplitude excitation of the element in row m, column n, where "0" and "1" represent the states of a turned "OFF" element and a turned "ON" element, respectively. Suppose that N_{on} is the number of turned "ON" elements and N_{tot} is the total number of element positions in the aperture. The fill factor of the array ξ can be denoted as

$$\xi = \frac{N_{\mathrm{on}}}{N_{\mathrm{tot}}}. \tag{4}$$

The directivity and normalized PSLL can be calculated by eqn (5) and (6), respectively

$$F_{\mathrm{Dir}}(I_{mn}) = 10\lg\left[\frac{4\pi\cdot|\mathrm{AF}_{\max}|^2}{\int_{\varphi=0}^{2\pi}\int_{\theta=0}^{\frac{\pi}{2}}|\mathrm{AF}(I_{mn},\theta,\varphi)|^2\sin\theta d\theta d\varphi}\right], \tag{5}$$

$$F_{\mathrm{PSLL}}(I_{mn},\theta,\varphi) = \max_{(\theta,\varphi)\in \mathrm{SR}}\left\{20\log_{10}\left|\frac{\mathrm{AF}(I_{mn},\theta,\varphi)}{\mathrm{AF}_{\max}}\right|\right\} \tag{6}$$

where AF_{max} is the maximum antenna array factor, and SR denotes the sidelobe region. This paper aims to minimize the PSLL while maintaining high directivity. For this purpose, taking the maximum antenna directivity as the objective function and the acceptable maximum SLL as constraints, the mathematical optimization model can be established as

$$\text{Maximize}: \left[F_{\mathrm{Dir}}(I_{mn})\right], \tag{7a}$$

$$\text{Subject to}: \begin{cases} F_{\mathrm{PSLL}}(I_{mn},\theta,0) \le \varepsilon \ \ (\text{if } |\theta| \ge \Delta\theta_0) \\ F_{\mathrm{PSLL}}(I_{mn},\theta,\pi/2) \le \varepsilon \ \ (\text{if } |\theta| \ge \Delta\theta_{90}) \\ \sum_{m=1}^{M}\sum_{n=1}^{N} I_{mn} = \mathrm{round}\left[(M\times N)\cdot\xi\right] \\ I_{1,1} = 1, I_{1,N} = 1, I_{M,1} = 1, I_{M,N} = 1 \end{cases} \tag{7b}$$

where ε represents a given maximum SLL, $\Delta\theta_0$ and $\Delta\theta_{90}$ denote one-half of the main beamwidth in φ = 0° and φ = 90° directions, respectively, and round(.) means rounding objects toward the nearest integer. To improve the speed of program execution, here, we only constrained the SLL in φ = 0° and φ = 90° planes. Moreover, since the main beamwidth of the array mainly depends on the aperture size, the four corners of the rectangle aperture contain turned "ON" elements to ensure that the beamwidth remains nearly unchanged. Eqn (7a) can be equivalently converted to the following form:

$$\text{Minimize}: \left[\int_{\varphi=0}^{2\pi}\int_{\theta=0}^{\frac{\pi}{2}}\left|\frac{\mathrm{AF}(I_{mn},\theta,\varphi)}{\mathrm{AF}_{\max}}\right|^2\sin\theta d\theta d\varphi\right]. \tag{8}$$

However, it is hard to solve the model directly because its objective function and constraints are nonlinear. For this reason, an approximate linearization technique is adopted to change the nonlinear programming into linear programming. The above model can be rewritten as

$$\text{Minimize}: \left[2\xi\cdot\sum_{m=1}^{M}\sum_{n=1}^{N}\mu_{mn}\cdot I_{mn} - \sum_{m=1}^{M}\sum_{n=1}^{N}\eta_{mn}\cdot I_{mn}\right], \tag{9a}$$

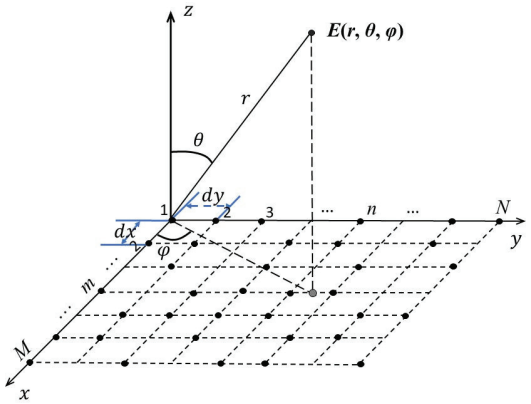

Fig. 1. The geometry of a rectangular planar antenna.

$$\text{Subject to}: \begin{cases} \text{real}\left[F_{\text{PSLL}}\left(I_{mn},\theta,0\right)\right] \le \varepsilon' \ (\text{if } |\theta| \ge \Delta\theta_0) \\ \text{imag}\left[F_{\text{PSLL}}\left(I_{mn},\theta,0\right)\right] \le \varepsilon' \ (\text{if } |\theta| \ge \Delta\theta_0) \\ \text{real}\left[F_{\text{PSLL}}(I_{mn},\theta,\frac{\pi}{2})\right] \le \varepsilon' \ (\text{if } |\theta| \ge \Delta\theta_{90}) \\ \text{imag}\left[F_{\text{PSLL}}(I_{mn},\theta,\frac{\pi}{2})\right] \le \varepsilon' \ (\text{if } |\theta| \ge \Delta\theta_{90}) \\ \sum_{m=1}^{M}\sum_{n=1}^{N} I_{mn} = \text{round}\left[(M\times N)\cdot\xi\right] \\ I_{1,1}=1, I_{1,N}=1, I_{M,1}=1, I_{M,N}=1 \end{cases} \tag{9b}$$

where real(.) represents the real part of the complex number, imag(.) denotes the imaginary part of the complex number, and the expressions of μ_{mn} and η_{mn} are given in eqn (10) and (11), respectively

$$\mu_{mn} = \frac{\int_{\varphi=0}^{2\pi}\int_{\theta=0}^{\frac{\pi}{2}} \alpha_{mn}(\theta,\varphi)\cdot\sum_{m=1}^{M}\sum_{n=1}^{N}\alpha_{mn}(\theta,\varphi)\sin\theta d\theta d\varphi}{|\text{AF}_{\max}|^2}, \tag{10}$$

$$\eta_{mn} = \frac{\int_{\varphi=0}^{2\pi}\int_{\theta=0}^{\frac{\pi}{2}}\left[|\alpha_{mn}(\theta,\varphi)|^2\right]\cdot\sin\theta d\theta d\varphi}{|\text{AF}_{\max}|^2} \tag{11}$$

where

$$\alpha_{mn}(\theta,\varphi) = e^{jk\cdot\left[(m-1)d_x u(\theta,\varphi)+(n-1)d_y v(\theta,\varphi)\right]}. \tag{12}$$

The mathematical model above is a canonical linear programming model, which is much easier to solve than the nonlinear model. It can be solved effectively by using the MATLAB (R) INTLINPROG optimization toolbox. In the above linear programming model, the main beamwidth in the $\varphi = 0^\circ$ and $\varphi = 90^\circ$ planes are set to $\Delta\theta_0$and $\Delta\theta_{90}$, and the PSLL is constrained by ε'.

III. RESULTS AND NUMERICAL ANALYSIS

In this section, several representative simulation examples are proposed to demonstrate the effectiveness of the 0-1 ILP method in thinning planar arrays. Here, we assumed that the element factor satisfies isotropic. The results obtained by the 0-1 ILP algorithm present in this section are the best ones among 30 independent trials. All simulation results below were obtained with a PC equipped with an AMD R74800H (3.2 GHz) processor and 16–GB RAM. In order to compare the runtime, the population size and iteration number of all the following algorithms are the same as those set in the original literature.

A. Square array design

In the first case, the 0-1 ILP method was applied to optimize the 12 × 12 elements planar square arrays with different fill factors. In order to compare the obtained results with that of other algorithms, we considered only the symmetrical antenna array with no populated turned "ON" elements at the four corners of the aperture. The fill factors for the arrays are consistent with those in the existing literature and present in the second column of Table 1. It also lists the maximum value of SLL in the two principal planes and the total runtime for each algorithm. The PSLL attained with the proposed method is lower than that of the other algorithms. The computational time is about 0.2–0.3 s for a single trial using the 0-1 ILP approach, and the total time of 30 runs ranges from 7.8 to 8.4s, which is far less than several hundred seconds for other algorithms. Actually, only a few runs are required for small arrays to obtain the optimal solution. The above results validated the effectiveness of the proposed algorithm in synthesizing small-sized arrays.

Table 1: Comparison of the PSLL and the total runtime of 12 × 12-element symmetric planar array synthesized using different algorithms

Method	filling Factor	PSLL (dB) ($\varphi = 0^\circ$)	PSLL (dB) ($\varphi = 90^\circ$)	Total run time (s)
MPT [17]	34.1%	−17.60	−17.60	–
0-1 ILP	34.1%	−19.54	−19.54	8.0
MBc-GA [18]	47.9%	−19.40	−19.40	–
0-1 ILP	47.9%	−23.20	−23.20	8.3
MBC-GA [19]	52.8%	−23.07	−23.07	453.8
0-1 ILP	52.8%	−24.26	−24.56	8.1
BPSO [20]	61.1%	−18.65	−16.83	101.7
0-1 ILP	61.1%	−23.77	−23.77	7.8

In yet another example, a 16 × 16-element asymmetric array with a 50% fill factor was considered. In order to further validate the performance of the proposed method when the main lobe scanning direction is off normal, the patterns were simulated for the beam scanning directions of (θ_0= 0°, φ_0= 0°), (θ_0= 15°, φ_0= 0°), and (θ_0= 30°, φ_0= 90°), respectively. The methods in [22] and [24] were reproduced to compare with the proposed method. Figures 2(a) and 2(b) give 2D normalized pattern obtained by the IBc-GA [24], BIL-PSO [22], and the 0-1 ILP methods when the main beam points at broadside, namely (θ_0= 0°, φ_0= 0°). Figures 2(c) and 2(d) are the optimization results when the main lobe direction points to (θ_0= 15°, φ_0= 0°) and (θ_0= 30°, φ_0= 90°), respectively. For comparison, the main lobe widths obtained with these three methods at the same scanning angle were set to the same value. The first null beamwidth (FNBW) of the broadside pattern in both principal planes is 23°. When steering the main beam toward (θ_0= 15°, φ_0= 0°), the beamwidth in $\varphi = 0^\circ$ plane is increased to 26°. When the main beam points at (θ_0= 30°, φ_0= 90°), the FNBW in φ = 90° plane grows to 27°. Figure 3 gives the 3D normalized power pattern

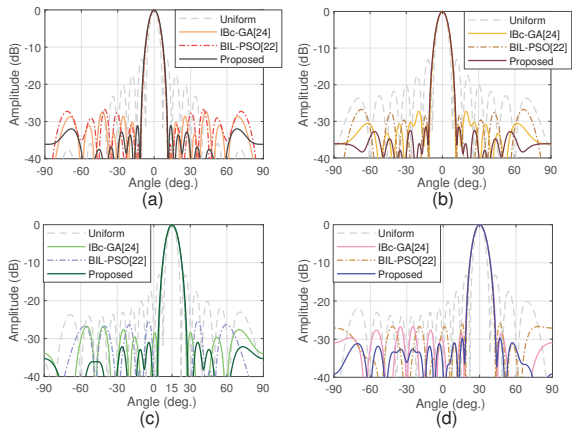

Fig. 2. 2D far-field patterns of the 16 × 16 asymmetric planar array with a 50% fill factor. (a) Broadside pattern in $\varphi = 0^\circ$ plane. (b) Broadside pattern in $\varphi = 90^\circ$ plane. (c) Scanned pattern in $\varphi = 0^\circ$ plane with the main beam pointing at ($\theta_0 = 15^\circ$, $\varphi_0 = 0^\circ$). (d) Scanned pattern in $\varphi = 90^\circ$ plane with the main beam pointing at ($\theta_0 = 30^\circ$, $\varphi_0 = 90^\circ$).

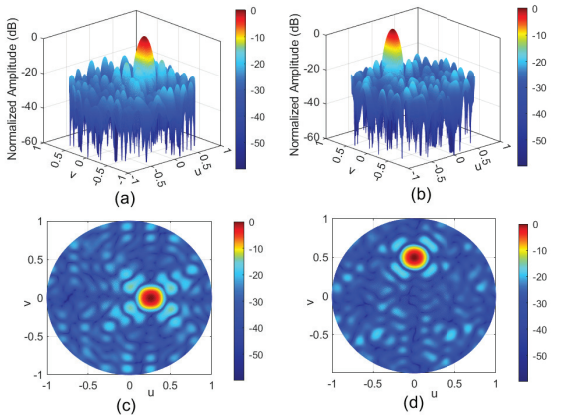

Fig. 3. 3D far-field patterns of the 16 × 16 asymmetric planar array with a 50% fill factor. (a) and (c) Steering the main beam toward ($\theta_0 = 15^\circ$, $\varphi_0 = 0^\circ$). (b) and (d) Steering the main beam toward ($\theta_0 = 30^\circ$, $\varphi_0 = 90^\circ$).

and contour plot when the main beam is scanned to the direction of ($\theta_0 = 15^\circ$, $\varphi_0 = 0^\circ$) and ($\theta_0 = 30^\circ$, $\varphi_0 = 90^\circ$), respectively. The obtained PSLL and directivity of the planar arrays corresponding to different scanning angles by the 0-1 ILP method and the methods in [22] and [24] are presented in Table 2. As can be seen that for given scanning angles, these three methods can achieve almost the same directivity and a lower PSLL with no grating lobe, yet the PSLL obtained by the proposed approach is significantly lower than that obtained by the other two methods.

Table 2: Comparison of the performance of thinned arrays using different algorithms when the main beam points at ($\theta_0 = 0^\circ$, $\varphi_0 = 0^\circ$), ($\theta_0 = 15^\circ$, $\varphi_0 = 0^\circ$), and ($\theta_0 = 30^\circ$, $\varphi_0 = 90^\circ$)

(θ_0, φ_0)	Results	IBc-GA [24]	BIL-PSO [22]	0-1 ILP
(0°, 0°)	PSLL (dB) ($\varphi = 0^\circ$)	−26.72	−27.40	−31.04
	PSLL (dB) ($\varphi = 90^\circ$)	−26.74	−27.18	−31.51
	Direct. (dBi)	25.42	25.63	25.80
(15°, 0°)	PSLL (dB) ($\varphi = 0^\circ$)	−25.30	−26.72	−30.95
	Direct. (dBi)	25.19	25.41	25.42
(30°, 90°)	PSLL (dB) ($\varphi = 90^\circ$)	−25.84	−26.73	−29.74
	Direct. (dBi)	25.11	25.06	25.15

B. Rectangular array design

In this case, a 20 × 10-element rectangular planar array was considered. In order to assess the performance of the 0-1 ILP technique, we attempted to replicate the methods published in [21–24] and compared the best results with those acquired by the proposed method. Table 3 gives the comparison between the optimization results obtained by methods in [21–23] and the 0-1 ILP algorithm. All of these methods were applied to a 20 × 10-element symmetric planar array, using fill factors from 54% to 68%. As shown in Table 3, the PSLLs obtained by OGA [21], BIL-PSO [22], and ACO [23] are nearly the same as the 0-1 ILP. However, the total optimization time of the proposed 0-1 ILP method is much shorter than that of other algorithms.

The performance comparisons of the IBc-GA [24], BIL-PSO [22], and 0-1 ILP in dealing with the 20 × 10-element asymmetric planar array with a 54% fill factor is presented in Table 4 and Figure 4. For a more accurate comparison, the FNBW values of these methods were controlled to be the same, where the FNBW in $\varphi = 0^\circ$ plane is set to 18° and the FNBW in $\varphi = 90^\circ$ plane is set to 36°. The optimized element distributions obtained using the 0-1 ILP technique are illustrated in Figure 5. The white blocks in the figure represent the ON-state, and the black blocks represent the OFF-state. From Table 4, it can be seen that the maximum SLL in principal planes of the proposed approach is −28.55 dB, which is 2.11 dB lower than that achieved through IBc-GA [24] and 3.41 dB lower than that obtained by BIL-PSO [22]; yet, there is little difference in directivity. In addition, the total runtime of each algorithm is listed in

Table 3: Comparison of the PSLL and the total runtime of 20 × 10-element symmetric planar array synthesized with different algorithms

Method	Filling factor	PSLL (dB) ($\varphi = 0°$)	PSLL (dB) ($\varphi = 90°$)	Total run time (s)
OGA [21]	54.0%	−26.09	−25.09	225.7
0-1 ILP	54.0%	−26.09	−25.09	8.9
OGA [21]	58.0%	−28.34	−26.59	227.6
BIL-PSO [22]	58.0%	−28.31	−26.57	241.5
0-1 ILP	58.0%	−28.34	−26.59	9.1
ACO [23]	68.0%	−25.67	-25.76	326.8
0-1 ILP	68.0%	−25.68	−25.77	8.6

Table 4: Comparison of the performance of the 20 × 10 asymmetric planar array synthesized with the IBC-Ga [24], BIL-PSO [22], and 0-1 ILP methods

Results	IBc-GA [24]	BIL-PSO [22]	0-1 ILP
PSLL (dB) in $\varphi = 0°$ plane	−26.64	−25.14	−28.55
PSLL (dB) in $\varphi = 90°$ plane	−26.44	−25.44	−29.37
Directivity (dBi)	25. 45	25.76	26.12
Total run time (s)	3355.6	2835.4	14.1

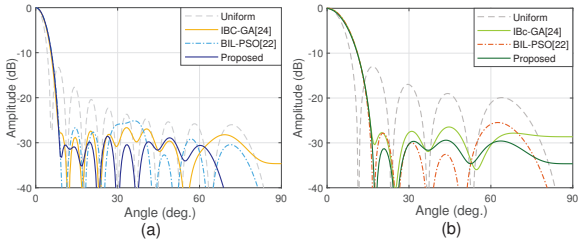

Fig. 4. Far-field patterns of the 20 × 10 asymmetric planar array with a 54% fill factor obtained by uniform excitation, IBc-GA [24], BIL-PSO [22], and the proposed method. (a) 2D pattern in $\varphi = 0°$ plane. (b) 2D pattern in $\varphi = 90°$ plane.

the fourth row of Table 4. The average time for one execution of the proposed method is 0.47 s, and the total time for 30 independent runs is about 14.1 s, which is much less than the 3355.6 s required by IBc-GA in [24] and the 2835.4 s required by BIL-PSO in [22].

Most papers on array thinning are devoted to optimizing symmetric arrays to reduce the solution space and speed up convergence. These algorithms show good performance in thinning small- and medium-scale symmetric antenna arrays and even achieve the global optimum.

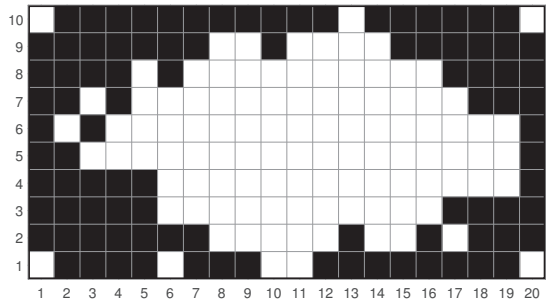

Fig. 5. Distribution of the turned "ON" element across the 20 × 10 planar array with a 54% fill factor. White blocks indicate elements that are turned "ON" and black blocks indicate elements that are turned "OFF."

Yet, they can only end up with sub-optimal solutions when optimizing asymmetric planar arrays with equal size and the same total number of iterations. That may be because the asymmetric planar array has higher degrees of freedom, which increases the difficulty of optimization. However, our simulation results demonstrated that the 0-1 ILP algorithm outperforms [21–24] by achieving lower PSLL in a much shorter time.

C. Large-scale square array design

To investigate the capabilities of the 0-1 ILP method for thinning large-scale planar arrays, we considered a 100 × 100 symmetric planar square array with a 49.52% fill factor. The obtained results are given in Table 5 and Figures 6−8. Table 5 illustrates that the performance of the 0-1 ILP technique in optimizing PSLL is better than [25]. The peak SLL decreases from −32.80 to −40.88 dB in the $\varphi = 0°$ plane and drops from −33.40 to −40.71 dB in the $\varphi = 90°$ plane. The directivity of the thinned array is 40.18 dBi, and the FNBW in both $\varphi = 0°$ plane and $\varphi = 90°$ plane is 5°. Figure 6 shows the 3D normalized far-field pattern, Figure 7 plots the 2D far-field pattern when $\varphi = 0°$ and $\varphi = 90°$, and Figure 8 gives the optimal distribution of the turned "ON" elements (white) and turned "OFF" elements (black) across the array aperture. The average time for one independent run of the proposed method is about 13.17 s, and the total time for 30 runs is about 395.1 s.

The high-dimensional optimization problem often comes with a considerable computational burden; so only a few published methods have the ability to synthesize large arrays. Although this method requires multiple adjustments of the parameters based on experience, the foregoing results and analysis demonstrated clearly that the 0-1 ILP method solves optimization problems with high-dimensional quickly and efficiently.

D. Discussion of the results

Array thinning is a complex nonlinear problem and is difficult to be solved. Stochastic algorithms are

Table 5: Comparison of the PSLL of 100 × 100 square array designed with the IW-PSO [25] and 0-1 ILP approaches

Results	IW-PSO [25]	0-1 ILP
PSLL (dB) in $\varphi = 0^\circ$ plane	−32.80	−40.88
PSLL (dB)in $\varphi = 90^\circ$ plane	−33.40	−40.71
Directivity (dBi)	–	40.18
Turned-ON elements	4951	4952

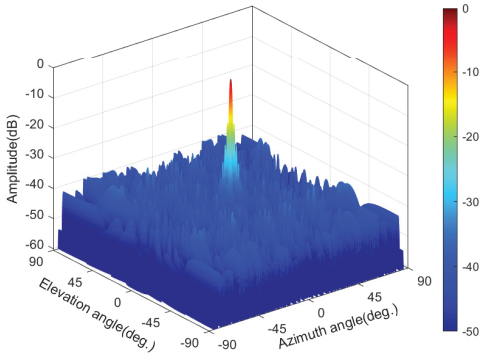

Fig. 6. 3D pattern of the symmetric planar array consisting of 100 × 100 size and a 49.52% fill factor.

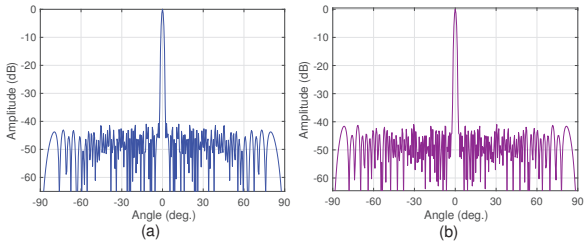

Fig. 7. Far-field patterns of the 100 × 100 symmetric planar array with a 49.52% fill factor. (a) 2D pattern in $\varphi = 0^\circ$ plane. (b) 2D pattern in $\varphi = 90^\circ$ plane.

computationally expensive, time-consuming, and may not converge to the optimal solution. In this paper, an approximate linearization technique was proposed to reduce the complexity of the model, which dramatically accelerates the calculation speed. The method is simple, efficient, and without any iterations. One drawback of the 0-1 ILP method is that the approximate linearization process may cause rounding errors. However, the numerical results evidenced that the linear programming model proposed in this paper has a high approximation accuracy, the optimizing result of which can be regarded as an approximate solution of the original model. Furthermore, since the solution accuracy of the intlinprog(.) function is limited, it could not get the optimal solution when optimizing larger arrays. Commercial optimization solvers such as Gurobi and CPLEX can be used to improve the solution accuracy of the 0-1 ILP model. The new approach has provided a novel strategy for thinning planar arrays, which has prominent advantages in solving the large-scale antenna array optimization problems with huge solution space and high complexity. In addition, it can be further applied to optimize the PSLL of the whole sidelobe region.

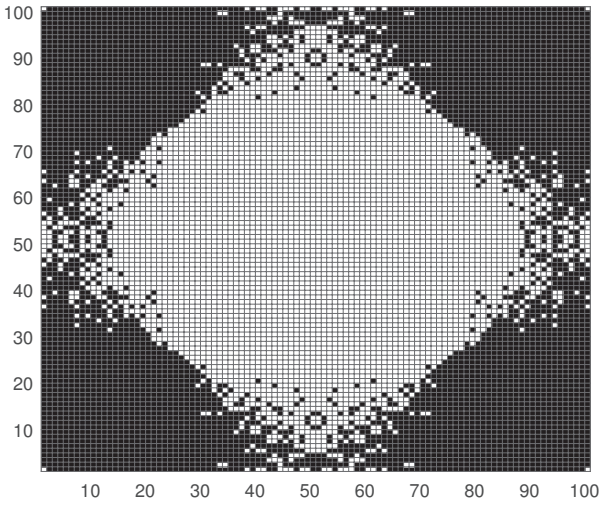

Fig. 8. Distribution of the turned "ON" element across the 100 × 100 square array with a 49.52% fill factor. White blocks indicate elements that are turned "ON," and black blocks indicate elements that are turned "OFF."

IV. CONCLUSION

This paper introduced the 0-1 ILP method for thinning planar arrays. The 0-1 ILP technique is a fast algorithm without iterative procedures. The obtained results of the new method were compared with some earlier published stochastic algorithms. Simulation results indicate that the method proposed in this paper can effectively suppress the peak SLL of planar arrays and substantially increase computational efficiency compared to the stochastic algorithm. Besides, we have successfully applied the method to optimize a beam-scannable antenna array and a 100 × 100 planar square array, demonstrating the effectiveness of the 0-1 ILP method for steerable arrays and large-scale array thinning, respectively. In future work, we will attempt to obtain lower PSLL in all φ planes and will further optimize the excitation current of the thinned planar arrays to reduce the PSLL by nonlinear programming methods.

REFERENCES

[1] R. L. Haupt, "Thinned arrays using genetic algorithms," *IEEE Trans. Antennas Propag.*, vol. 42, no. 7, pp. 993–999, Jul. 1994.

[2] N. Jin and Y. Rahmat-Samii, "Advances in particle swarm optimization for antenna designs: Real-number, binary, single-objective and multiobjective implementations," *IEEE Trans. Antennas Propag.*, vol. 55, no. 3, pp. 556–567, Mar. 2007.

[3] G. Sun, Y. Liu, Z. Chen, S. Liang, A. Wang, and Y. Zhang, "Radiation beam pattern synthesis of concentric circular antenna arrays using hybrid approach based on cuckoo search," *IEEE Trans. Antennas Propag.*, vol. 66, no. 9, pp. 4563–4576, Sep. 2018.

[4] A. S. Zare, S. Baghaiee. "Application of ant colony optimization algorithm to pattern synthesis of uniform circular antenna array". *Applied Computational Electromagnetics Society Journal*, vol. 30, no. 8, pp. 810–818 Aug. 2015.

[5] S. Liang, Z. Fang, G. Sun, Y. Liu, G. Qu, and Y. Zhang, "Sidelobe reductions of antenna arrays via an improved chicken swarm optimization approach," *IEEE Access*, vol. 8, pp. 37664–37683, 2020.

[6] R. E. Willey, "Space tapering of linear and planar arrays," *IRE Trans. Antennas Propag.*, vol. AP-10, no. 4, pp. 369–377, Jul. 1962.

[7] M. Skolnik, J. W. Sherman, III, and F. C. Ogg, Jr., "Statistically designed density-tapered arrays," *IEEE Trans. Antennas Propag.*, vol. AP-12, no. 4, pp. 408–417, Jul. 1964.

[8] O. M. Bucci, T. Isernia, and A. F. Morabito, "A deterministic approach to the synthesis of pencil beams through planar thinned arrays," *Prog. Electromagn. Res.*, vol. 101, no. 2, pp. 217–230, 2010.

[9] W. P. M. N. Keizer, "Linear array thinning using iterative FFT techniques," *IEEE Trans. Antennas Propag.*, vol. 56, no. 8, pp. 2260–2757, Aug. 2008.

[10] W. P. M. N. Keizer, "Large planar array thinning using iterative FFT techniques," *IEEE Trans. Antennas Propag.*, vol. 57, no. 10, pp. 3359–3362, Oct. 2009.

[11] M. Donelli, A. Martini, and A. Massa, "A hybrid approach based on PSO and Hadamard difference sets for the synthesis of square thinned arrays," *IEEE Trans. Antennas Propag.*, vol. 57, no. 8, pp. 2491–2495, Aug. 2009.

[12] G. Oliveri, L. Manica, and A. Massa, "ADS-based guidelines for thinned planar arrays," *IEEE Trans. Antennas Propag.*, vol. 58, no. 6, pp. 1935-1948, Jun. 2010.

[13] G. Oliveri, F. Caramanica, C. Fontanari, and A. Massa, "Rectangular thinned arrays based on McFarland difference sets," *IEEE Trans. Antennas Propag.*, vol. 59, no. 5, pp. 1546–1552, May 2011.

[14] P. Rocca, N. Anselmi, G. Oliveri, A. Polo and A. Massa, "Antenna array thinning through quantum Fourier transform," *IEEE Access*, vol. 9, pp. 124313-124323, 2021.

[15] L. Gu, Y.-W. Zhao, Z.-P. Zhang, L.-F. Wu, Q.-M. Cai, and R.-R. Zhang, "Adaptive Learning of Probability Density taper for large planar array thinning," *IEEE Trans. Antennas Propag.*, vol. 69, no. 1, pp. 155-163, Jan. 2021.

[16] H. Xu, S. M. Conolly, G. C. Scott, and A. Macovski, "Homogeneous magnet design using linear programming," *IEEE Trans. Magn.*, vol. 36, no. 2, pp. 476–483, Mar. 2000.

[17] K. Yang, Z. Zhao, and Y. Liu, "Synthesis of sparse planar arrays with matrix pencil method," in *Proc. Int. Conf. on Computational Problem-Solving (ICCP)*, 2011, pp. 82–85.

[18] B. V. Ha, M. Mussetta, P. Pirinoli, and R. E. Zich, "Modified compact genetic algorithm for thinned array synthesis," *IEEE Antennas Wireless Propag. Lett.*, vol. 15, pp. 1105–1108, 2016.

[19] M. Jijenth, K. K. Suman, V. S. Gangwar, A. K. Singh, and S. P. Singh, "A novel technique based on modified genetic algorithm for the synthesis of thinned planar antenna array with low peak sidelobe level over desired scan volume," in *IEEE MTT-S International Microwave and RF Conference (IMaRC)*, Dec 2017, pp. 251–254.

[20] K. V. Deligkaris, Z. D. Zaharis, D. G. Kampitaki, S. K. Goudos, I. T. Rekanos, and M. N. Spasos, "Thinned planar array design using Boolean PSO with velocity mutation," *IEEE Trans Magn.*, vol. 45, no. 3, pp. 1490-1493, Mar. 2009.

[21] L. Zhang, Y.-C. Jiao, B. Chen, and H. Li, "Orthogonal genetic algorithm for planar thinned array designs," *International Journal of Antennas and Propagation*, vol. 2012, 2012.

[22] D. Liu, Q. Jiang, and J. X. Chen, "Binary inheritance learning particle swarm optimisation and its application in thinned antenna array synthesis with the minimum sidelobe level," *IET Microw., Antennas Propag.*, vol. 9, no. 13, pp. 1386–1391, 2015.

[23] O. Quevedo-Teruel and E. Rajo-Iglesias, "Ant colony optimization in thinned array synthesis with minimum sidelobe level," *IEEE Antennas Wireless Propag. Lett.*, vol. 5, pp. 349–352, 2006.

[24] V. S. Gangwar, R. K. Samminga, A. K. Singh, M. Jijenth, K. K. Suman, and S. P. Singh, "A novel strategy for the synthesis of thinned planar antenna array which furnishes lowest possible peak sidelobe level without appearance of grating lobes over wide steering angles", *Journal of Electromagnetic Waves and Applications*, 2017, pp. 842-857.

[25] J. K. Modi, R. K. Gangwar, P. Ashwin and V. S. Gangwar, "An efficious strategy for the synthesis

of large arrays thinning with low PSLL," *2019 International Conference on Wireless Communications Signal Processing and Networking (WiSPNET)*, 2019, pp. 41-43.

Mingyu Wang was born in Hohhot, Inner Mongolia Autonomous Region, China. She received the B.S. degree in communication engineering from Hohai University, Nanjing, China, in 2019. She is currently working toward the master's degree in signal and information processing with the same university. Her research interests include the design of antenna arrays.

Xuewei Ping was born in Hebi of He'nan Province, China. He received the Ph.D. degree in electromagnetic field and microwave technology from the Nanjing University of Science and Technology, Nanjing, China, in 2007.

He is currently with the College of Computer and Information, Hohai University, Nanjing, China. His research interests include computational electromagnetics and the design and analysis of superconducting magnets and gradient coils.

PET-Based Instant Inkjet-Printed 4 × 4 Butler Matrix Beamforming Network

Suleiman A. Babale[1], Sharul Kamal A. Rahim[2], Kim G. Tan[3], Kashif N. Paracha[4], Arslan D. Butt[4], Irfan Ali[2], and S. H. Lawan[1]

[1]Department of Electrical Engineering
Bayero University Kano, Kano 3011, Nigeria
sababale.ele@buk.edu.ng, shlawan.ele@buk.edu.ng

[2]Wireless Communication Centre
Universiti Teknologi Malaysia (UTM), Johor Bahru 81310, Malaysia
sharulkamal@fke.utm.my, irfan_lrk_15@yahoo.com

[3]Faculty of Engineering & Technology
Multimedia University, Jalan Ayer Keroh Lama, Melaka 75450, Malaysia
kgtan@mmu.edu.my

[4]Department of Electrical Engineering
Government College University, Faisalabad 38000, Pakistan
kashifnisar@gcuf.edu.pk, arslandawood@gcuf.edu.pk

***Abstract* –** In this paper, a novel planar Butler matrix (BM) utilizing only 3 dB hybrid couplers and a crossover are implemented using a low-cost silver-nano inkjet printing technique. Unlike in the conventional design of BM where a phase shifter is required, this novel design does not need a phase shifter to be implemented. However, the use of delicate substrates like polyethylene terephthalate (PET) in the design makes it unique. This is not possible with the conventional thermal curing process, as PET substrate cannot be subjected to an excessively feverish temperature. The results obtained show good return loss and transmission coefficients better than 26.10 and 23.54 dB, respectively, at the center frequency. Similarly, an amplitude imbalance of less than 2.4 dB with phase mismatch within $\pm 0.25^\circ$ is achieved at the center frequency. The BM has a -10 dB bandwidth of 24.79% with a beam pattern produced at $+13^\circ$,-40°, $+40^\circ$, and -13° when ports 1-4 of the BM are energized.

***Index Terms* –** Modified coupler, PET substrate, Butler matrix, crossover.

I. INTRODUCTION

Previously, base-station uses an omnidirectional antenna for communications. The use of this type of antenna serves as a waste of power since most of the power radiates in all directions, instead of being directed toward the desired user. Moreover, sometimes, this radiated energy also served as an interferer to the nearby cells. With the advent of smart antenna technology (SAT), this problem was drastically minimized. Antenna beamforming network is generally known as an adaptive antenna array as per IEEE Standard. It is a type of antenna system that consists of external circuitries and radiating elements whose properties are controlled by the signal being received [1]. There are broadly two types of antenna beamforming network: the switched beam system (SBS) with fixed beam and variable phases and the adaptive antenna array with variable amplitude and phase [2]. Butler matrix (BM) falls under the category of SBS. BM is among the well-known beamforming networks because of its structural simplicity, compactness, cost-effectiveness, and easy fabrication. It is being made from hybrid couplers [3], crossing lines, and some phase delays [4-6]. It is a vital component of most array-based multiple-inputs multiple-outputs (MIMO) antenna systems. Its beam scanning is important in increasing the channel capacity of a system and reduces interference [7]. Planar BMs were reported in different technologies, such as in substrate integrated waveguides [8], [9], inkjet printing technique [10], multi-layered techniques [11, 12], composite right-left handed transmission line (CRLH TL) [13], swapped-port couplers [14], and suspended stripline technology [15]. In [16], [17], BM beamforming network was designed by integrating additional controllers and phase shifters to control the beam steering array. But the bandwidths are mostly less than 15% due to the $\lambda/4$ requirement of the couplers involved [18]. To maintain the phase difference at the

Submitted On: January 26, 2021
Accepted On: November 20, 2021

https://doi.org/10.13052/2022.ACES.J.370208

intermediate and the final stages of the design, hybrid couplers together with 135° phase shifters are used [19]. These phase shifters sometimes contributed in deterring good performances of BM due to introduction of losses [20] and untolerable phase ripples [21]. BM without crossover was presented in [22]. But the patch used in the coupler has complex nature and its field distribution does not have a closed-form equation that characterized its geometry using any well-known transmission line (TL) theory. However, the ground plane pattern, some of its variables, and their locations can only be obtained using time-consuming and complex processes. The BM presented in [23] does not use a phase shifter, but a via is needed for crossing the signals. Despite the importance of couplers in many designs like BM, little has been done on arbitrary output phase-difference characteristics [24], [25]. In [25], a hybrid coupler with arbitrary phase-difference was proposed. But, the method has some drawbacks and was corrected in [26]. This idea was conceived in this paper to propose an inkjet-printed BM.

In this paper, a novel 4 × 4 BM utilizing modified couplers and a crossover are presented. Using couplers with 45° phase difference in this design eliminates the use of phase shifters, and this, in turn, reduces the dimension and TL losses of the device by shortening the TL path. We demonstrated the BM by prototyping using instant inkjet printing technology that does not require thermal curing. One advantage of this printing process is the use of chemical sintering which paves a way for seamless and fast prototyping of electronic devices using delicate types of substrate materials. For example, the use of paper and polyethylene terephthalate (PET) substrates is not possible with the thermal curing process as they cannot be subjected to an excessively feverish temperature.

II. THE INKJET PRINTING TECHNIQUE

The technique presented in this paper uses a chemical sintering process based on conductive silver nanoparticles ink utilizing an inkjet printer by Brother Industries, Ltd. (model: DCP–J140w). The choice of this type of printer is because of its low cost and availability as compared to other chemical sintering processes [10], [27]. Another advantage of this type of printer is the effectiveness of its nozzles, which eject a moderate amount of ink volume at a given time which translates to deposition of the conductive ink in a manner that provides an undistorted conductive path [28]. Unlike other printing techniques that require thermal curing for a conductive pattern to be formed. Immediately after printing with this setup, the ink dried up and a conductive pattern is formed with a very low resistance of about 0.3 Ω/m^2 within a few seconds.

Before evaluating a complex structure with this technique, a uniform TL of 50 cm length having an impedance of 50 Ω was simulated using the properties of the silver-nano conductor as presented in [29]. Figure 1(a) shows the printer setup that was used for simulation of the uniform TL. It was terminated at both ends with 50-Ω load and was fabricated on the transparent PET substrate as shown in Figure 1(b). The simulation was carried out within a frequency range of 1-9 GHz to ascertain its workability for any design within the frequency range. The measured results shown in Figure 1(c) illustrate good return loss of about 36 dB and a transmission coefficient S_{21} of about 0 dB throughout the entire frequency band. It could be inferred that with this printing process, papers and other delicate substrates with a low melting point could be used to produce electronic circuitries as against other inkjet printing processes that required thermal curing in which the substrate materials will be subjected to very high temperature and pressure.

III. COUPLER DESIGN

To design any form of BM, the use of a coupler is inevitable. This section briefly describes the two types of couplers used in the implementation of the proposed BM.

A. Modified coupler

The concept used in the design of this novel 4 × 4 BM is centered on the design of 45° hybrid coupler shown in Figure 2. This coupler is referred to as a modified coupler because its output phase difference is at 45° as against the classical coupler whose output difference is 90°.

The design for the 45° coupler has been adapted from [30] where the derivation for the design was not presented. However, the resulting equations used in our design of the coupler are shown here as eqn (1)–(5):

$$\mathrm{Z}_1 = \mathrm{Z}_0 P\,|\sin\psi\,|, \tag{1}$$

$$Z_2 = Z_3 = \frac{Z_0 P \sin\psi}{\sqrt{1+P^2\sin^2\psi}}, \tag{2}$$

$$\theta_1 = \frac{\pi}{2} \tag{3}$$

$$\theta_2 = \tan^{-1}\left(\frac{(Z_0\tan\psi\,)}{Z_1}\right), \tag{4}$$

$$\theta_3 = \pi - \tan^{-1}\left(\frac{(Z_0\tan\psi\,)}{Z_1}\right), \tag{5}$$

where, Z_1, Z_2 , and Z_3 are normalized with the reference impedance terminating the ports Z_0. The angles θ_1, θ_2, and θ_3 can be any arbitrary angle, P^2 is the power division ratio, and the phase difference at the center frequency is ψ.

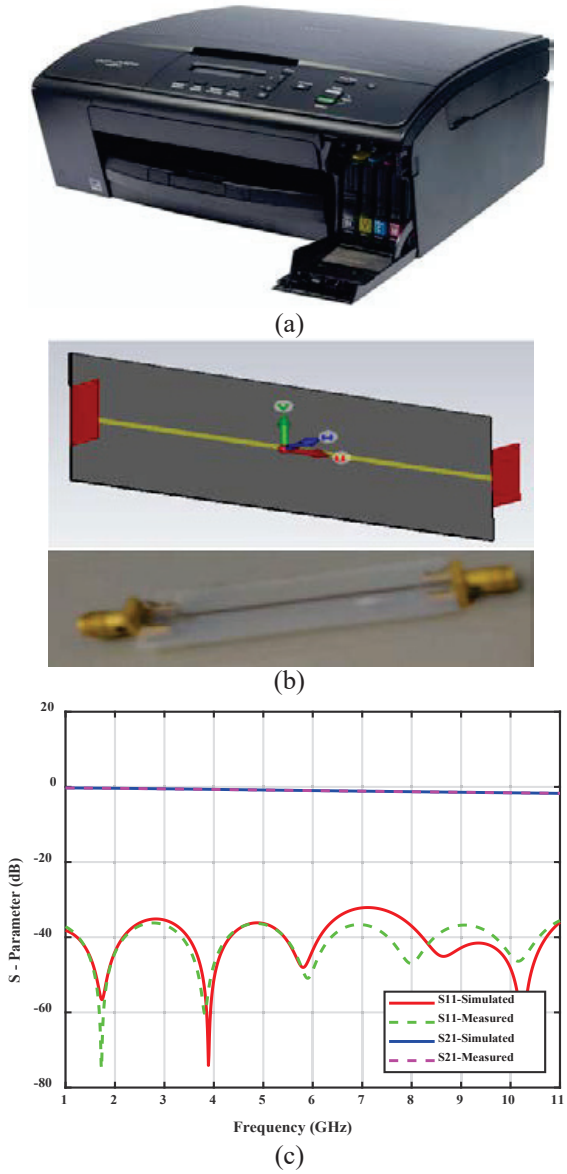

Fig. 1. (a) The Brother printer DCP–J140w, (b) layout and photograph of a 50-Ω microstrip TL simulated and prototyped with the PET substrate, and (c) the *S*-parameters for the microstrip TL.

Using these coupler design equations, a 3-dB coupler with a phase difference of 45° has been designed and simulated to operate at a frequency of 6 GHz. Using the designed equations, the phase difference between the outputs is set to be 45° and the reference impedance Z_0 is fixed at 50 Ω. Under these conditions, the impedances of the horizontal arm of the 3-dB coupler Z_1 = 28.87 Ω, whereas those of the horizontal arms are Z2 = Z3 = 35.36 Ω, with θ_1=90°, θ_2= 120°, and θ_3= 60°. The use of this coupler having 45° phase-difference eliminates

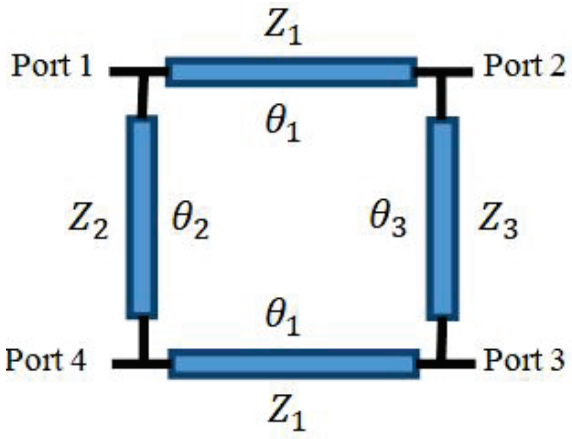

Fig. 2. Structure of the proposed 45° coupler.

Table 1: Parameters of the modified coupler

Parameters	Value (mm)
AL1	9.41
AW1	0.93
BL1	5.63
BW1	1.08
L1	1.41
L2	3.67
L3	2.82
W	1.08
PL1	10.0
PL2	3.67
PL3	2.62
PW1	0.67

the need for additional components in building the BM, thereby making it compact and retain its good performance. This is because it replaces the functions of both the quadrature coupler and phase shifter in the classical BM which gives a phase difference of either 45° or 135° at the output of the phase shifter. The physical parameters of the coupler are computed from the impedances and the electrical lengths of the coupler and are tabulated as shown in Table 1.

The optimized parameters of each section of the modified coupler are indicated on the layout as shown in Figure 3(a). The simulated *S*-parameters showing the *S*-parameter response and the output phase difference are shown in Figure 3(b).

B. Classical coupler

The second type of coupler known as the classical coupler was also designed using eqn (1)-(5) outlined in the previous section. From these equations, setting the output phase difference ψ to 90° and the characteristics

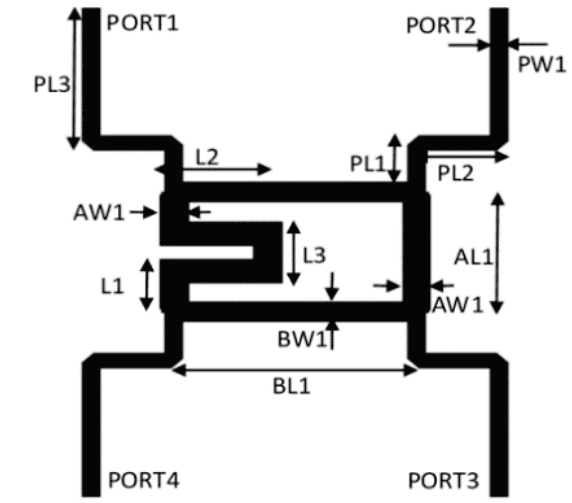

(a)

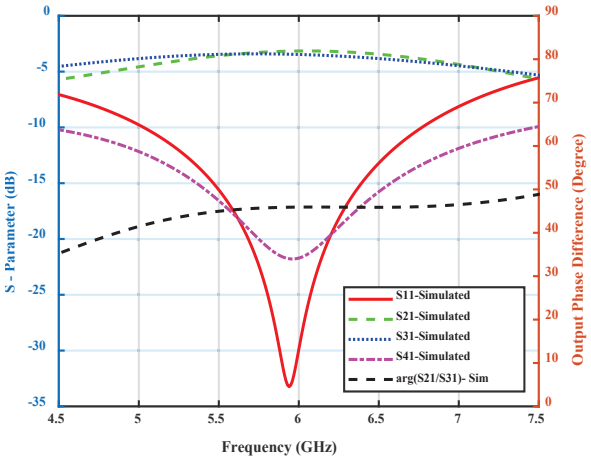

(b)

Fig. 3. (a) Layout of the modified coupler. (b) *S*-parameter results of the modified coupler.

impedance of the line Z_0 to 50 Ω, the corresponding impedances of the couplers' vertical and horizontal arms become: Z_1=Z_0= 50 Ω and Z_2=Z_3= 35.36 Ω.

The physical parameters of the coupler are computed from the impedances and the electrical lengths of the coupler and are tabulated as shown in Table 2. Also, the values of each section of the coupler are computed as indicated on the layout of Figure 4(a). Also, the *S*-parameters of the coupler are also shown in Figure 4(b).

C. Microstrip crossover

The classical coupler designed was used to obtain the crossover used in the implementation of the BM. It was implemented by cascading the two 90° couplers designed in the previous section. But sometimes, the resulting structure has to be optimized for better results. Figure 5 (a) shows the schematic of the optimized crossover, while its *S*-parameter results are shown in Figure 5 (b).

Table 2: Parameters of the classical coupler

Parameters	Value (mm)
AL1	7.70
AW1	1.10
BL1	10.50
BW	0.68
PL1	2.00
PL2	3.52
PL3	6.00
PW1	0.67

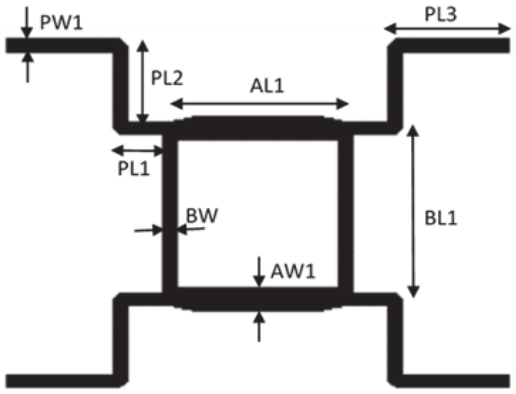

(a)

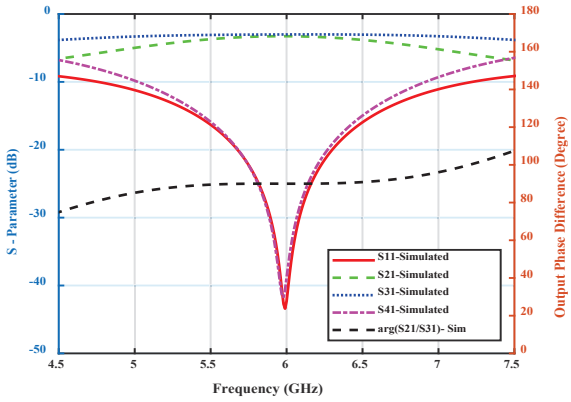

(b)

Fig. 4. (a) Layout of the quadrature coupler. (b) *S*-parameter results of the 45° coupler.

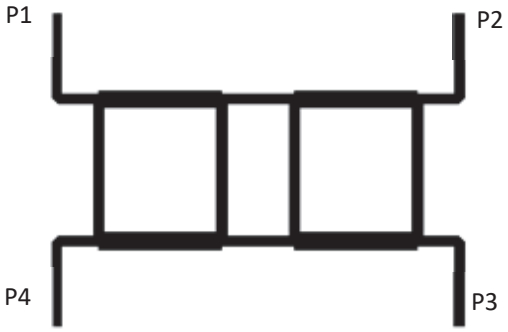

(a)

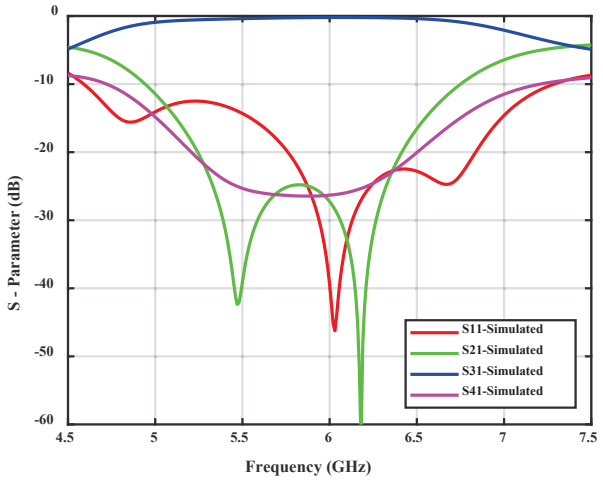

(b)

Fig. 5. (a) Layout of the microstrip crossover. (b) *S*-parameter results of the crossover.

Table 3: Parameters of the patch antenna

Parameters	Value (mm)
Substrate wavelength (λ_{sub})	0.029
Patch width (W_P)	15.45
Patch length (L_P)	16.21
Feed width (W_f)	0.613
Substrate width (W)	32.40
Substrate length (L)	30.90

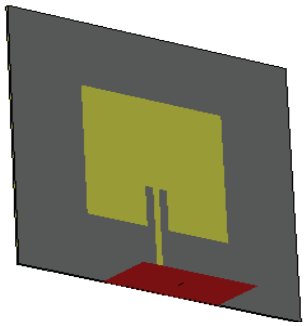

(a)

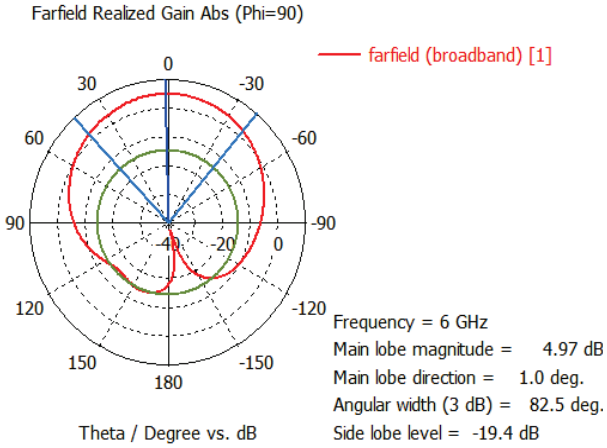

(b)

Fig. 6. (a) Layout of the patch antenna. (b) *S*-parameter results of the patch antenna.

D. Patch antenna

A square-shaped microstrip patch antenna was designed based on the equations presented in [31], and the desired resonant frequency was set to 6 GHz to rhyme with that of the proposed BM. The design parameters of the single element microstrip patch antenna is calculated and presented in Table 3.

After obtaining the physical parameters of the single element patch antenna, a commercially available software, Computer Simulation Technology (CST), was used for the simulation. Figure 6 shows the geometry and radiation pattern of the single element patch antenna. From this figure, it can be seen that an excellent radiation pattern with a realized gain of 4.97 dB, sidelobe level of -19.4 dB, and 3-dB angular beamwidth of 82.5° has been obtained.

For quick verification, in practical design, the length L of a simple patch antenna is usually taken in the range of $0.33\lambda o < L < 0.5\lambda o$, where λo is the wavelength of the free-space. Also, the thickness of the patch t which is typically the conductor thickness is usually taken such that $t \ll \lambda o$. The height of the substrate h is usually in the range of $0.01\lambda o \leq h \leq 0.05\lambda o$, and, finally, the dielectric constant of the substrate (εr) is typically in the range of $1 \leq \varepsilon r \leq 10$ [31].

IV. BUTLER MATRIX

The overall structure of the BM was obtained from the individual components designed in the previous sections. The BM was simulated and fabricated on the transparent PET substrate with a measured dielectric constant of 2.71, a thickness of 0.125 mm, and a loss tangent of 0.043. CST studio was used throughout the simulation

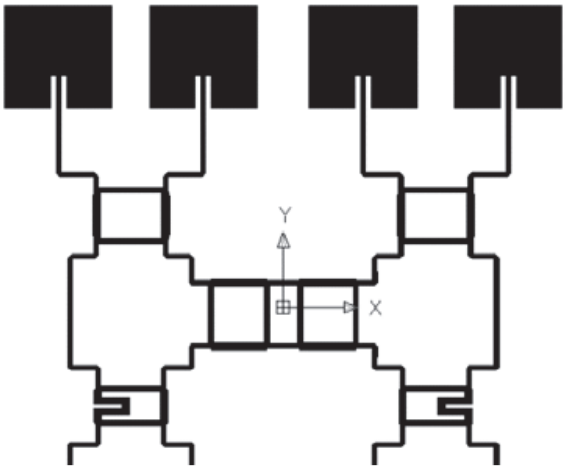

(a)

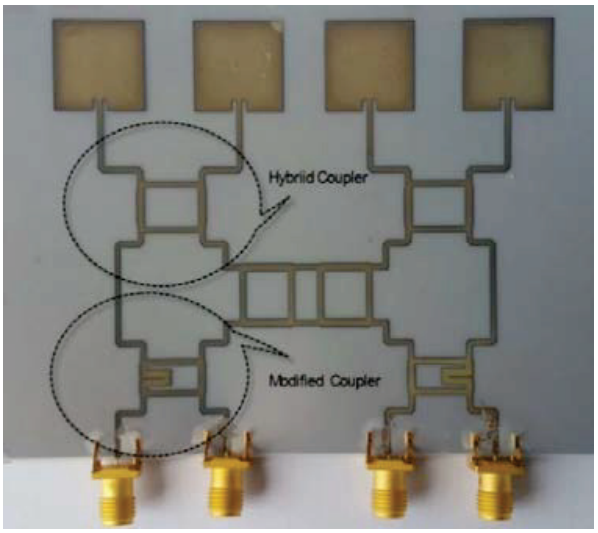

(b)

Fig. 7. The proposed 4 × 4 Butler matrix. (a) Layout. (b) Photograph.

and the silver-nano printing technology was used for the prototyping.

The layout and the photograph of the proposed BM feeding the antenna array are shown in Figure 7. It comprises the first two 45° couplers, two conventional 90° couplers, and a crossover. For ease of handling, the second crossover was eliminated in the design. This is because it only reverses the position of the signals at the output ports of the BM.

The fabricated BM was tested in an anechoic chamber to compare the radiation pattern produced as a result of exciting the BM. The experimental test stands for the measurements are shown in Figure 8.

By exciting port 1 of the beamforming network, the return loss was found to be 26.10 dB and the transmission characteristics are $S_{51} = 5.11$ dB, $S_{61} = 8.19$ dB, $S_{71} = 5.17$ dB, and $S_{81} = 8.03$ dB at the center frequency. Similarly, when a signal is applied at port 2 while terminating other ports with 50 Ω load, a return loss of 24.8 dB and transmission coefficients of $S_{52} = 8.43$, $S_{62} = 5.34$ dB, $S_{72} = 7.51$ dB, and $S_{82} = 5.27$ dB are obtained at the center frequency. Exciting ports 3 and 4 of the BM produces the same results as in ports 1 and 2. This is due to the symmetry of the beamforming network. In all the cases, the return losses are far below the 10 dB line, and the transmission coefficient results approach the theoretical value of 6.0 dB in each case with a maximum variation of less than ±2.4 dB. Figure 9(a) shows the return loss and isolation while the results of the transmission coefficients are shown in Figure 9(b). From these results, all the transmission coefficients are between −5 and −9 dB at the center frequency.

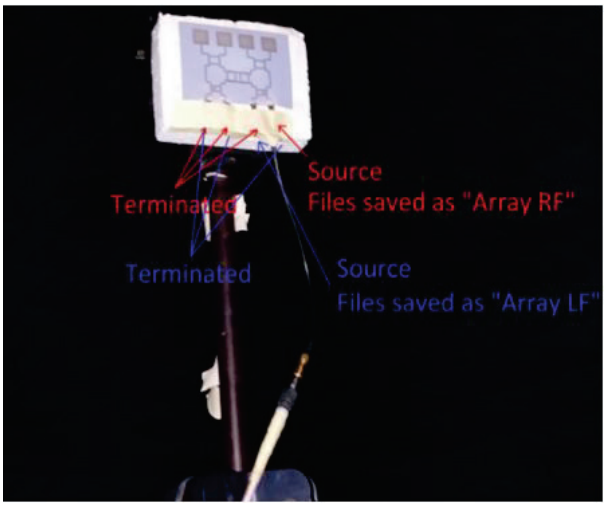

Fig. 8. Experimental test stand for the complete BM and the antenna array.

Also, when ports 3 and 4 are excited, the transmission coefficients at the various output ports are equal but in a reverse manner to those obtained when ports 2 and 1 are excited, respectively. It is worth noting that, when all the input ports are separately excited, return losses are similar in all the cases. From the results obtained, as shown in Figure 10, the progressive output phase differences, when excited separately from different input ports, are ±45° and ±135° with phase mismatch within ±0.25° at the center frequency.

The radiation patterns of the BM beamforming network from both the simulation and the measured are shown in Figure 11. From this plot, it can be observed that when a signal is applied at the inputs port 1 or 3 and 2 or 4 separately, the scanned beam angles corresponding to each phase difference are ±40.0° and ∓13.0°, respectively.

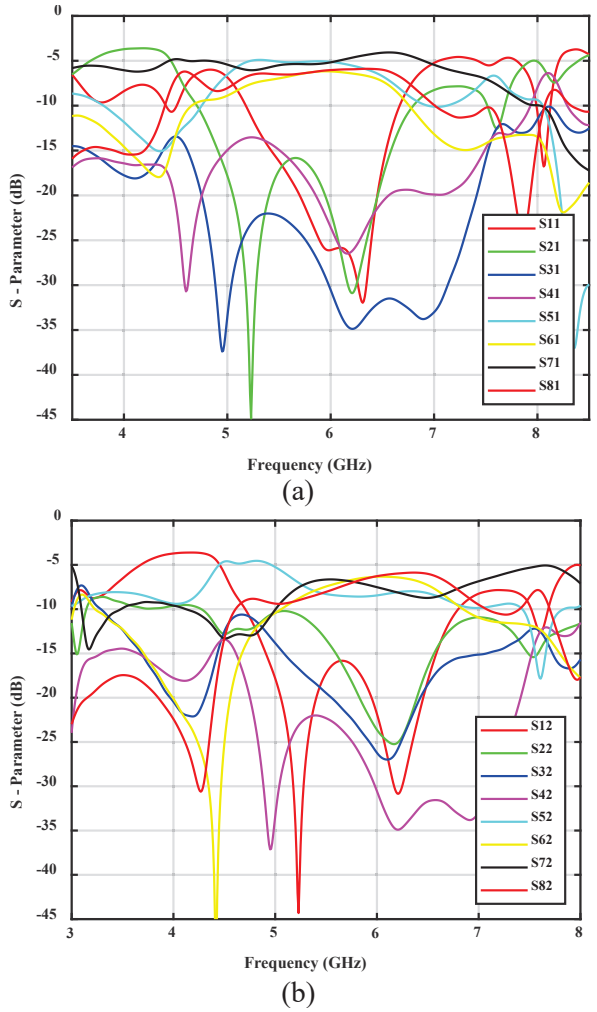

Fig. 9. *S*-parameters of the 4 × 4 Butler matrix showing the *S*-parameter responses when (a) port 1 is excited and when (b) port 2 is excited.

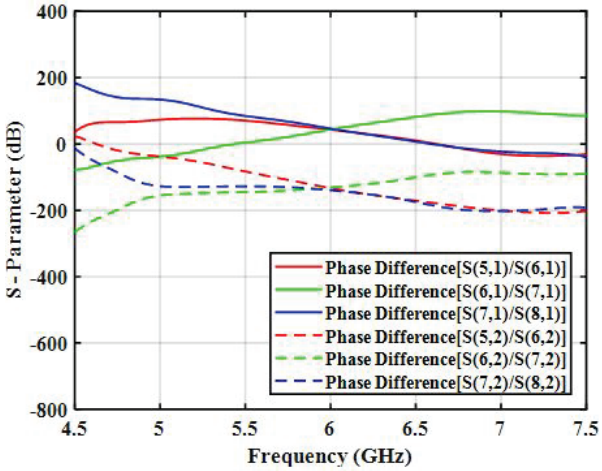

Fig. 10. Output phase difference of the proposed 4 × 4 Butler matrix when ports 1 and 2 are excited.

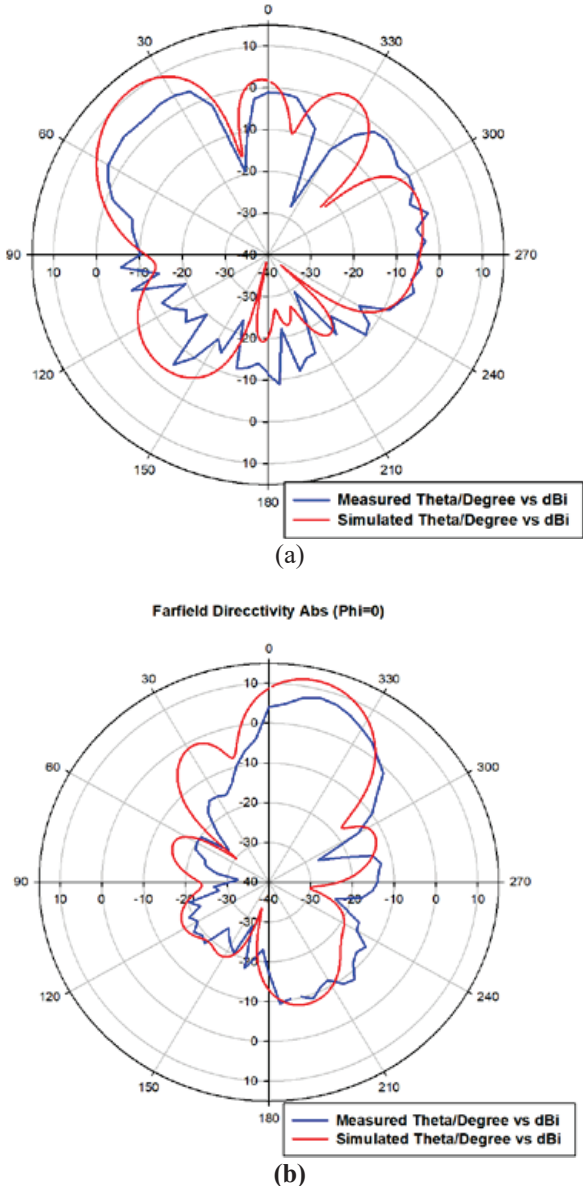

Fig. 11. The measured and simulated scanned beam angles of the proposed 4 × 4 BM: (a) when port 1 is excited; (b) when port 2 is excited.

Table 4: Comparison of the proposed BM with related BM

Ref.	Technique	−10 dB Band-width	S_{11} (dB)	Amplitude imbal-ance	Phase error
[2]	PCB	15%	−16 dB	0.75 dB	6°
[5]	SIW	3.33%	−13.5 dB	0.78 dB	11°
[20]	PCB	20.1%	−24.1 dB	0.4 dB	0.9°
[21]	TF-IPD	8%	−8 dB	4 dB	13°
This work	Inkjet printed	24.8%	−22.1 dB	2.4 dB	0.5°

V. CONCLUSION

In this work, a novel 4 × 4 BM has been designed, simulated, and fabricated using PET substrates. In terms of design, only couplers and crossover have been used without the phase shifter, typically used in case of conventional BMs. The results obtained show that the performance of the proposed design is highly reliable in terms of the radiation pattern it produced, the progressive phase difference, and amplitude imbalance at the output ports, as they are closely aligned with the theoretical predictions. From the radiation pattern measurement of the BM beamforming network, it can be observed that the beams are deposed appropriately at an angle suggested in theory. This result shows that by eliminating the phase shifter which is one of the building blocks in the design of BM, losses along the consequently shorter TL path line are minimized. Another merit of this design is the implementation of the device with a low-cost inkjet printing technique based on the chemical sintering process. With these potentials, the proposed BM can serve as a viable candidate where conformal antenna is needed and for the future 5G beamforming network.

ACKNOWLEDGEMENT

The authors acknowledge the Bayero University Kano Nigeria, Universiti Teknologi Malaysia, and Multimedia University for providing financial support under Grants 5F237, 4J414, and FRGS/1/2018/TK08/MMU/02/1.

REFERENCES

[1] R. J. Gong, Y. L. Ban, J. W. Lian, Y. Liu, and Z. Nie, "Circularly polarized multibeam antenna array of ME dipole fed by 5 × 6 Butler matrix," *IEEE Antennas Wirel. Propag. Lett.*, 2019.

[2] T. Mbarek, G. Ridha, and G. Ali, "Radiation pattern of a networks antenna supplied with Butler matrix, comparison with a multi-layer structure," *Applied Computational Electromagnetics Society (ACES) Journal*, pp. 1785-1792, 2007.

[3] A. K. Vallappil, M. K. A. Rahim, B. A. Khawaja, and M. Aminu-Baba, "Metamaterial based compact branch-line coupler with enhanced bandwidth for use in 5G applications," *Applied Computational Electromagnetics Society (ACES) Journal*, vol. 35, no. 6, pp. 700-708, 2020.

[4] Y. S. Lin and J. H. Lee, "Miniature Butler matrix design using glass-based thin-film integrated passive device technology for 2.5-GHz applications," *IEEE Trans. Microw. Theory Tech.*, 2013.

[5] T. Macnamara, "Simplified design procedures for Butler matrices incorporating 90 degree hybrids or 180 degree hybrids.," *IEE Proc. H Microwaves, Antennas Propag.*, vol. 134, no. 1, pp. 50-54, 1987.

[6] A. Karimbu Vallappil, M. K. A. Rahim, B. A. Khawaja, and M. N. Iqbal, "Compact metamaterial based 4 × 4 Butler matrix with improved bandwidth for 5G applications," *IEEE Access*, 2020.

[7] T. Y. Chen and P. L. Chi, "Bandwidth-enhanced branch-line coupler using the center-loaded vertical line and distributed capacitors," *Asia-Pacific Microw. Conf. Proceedings, APMC*, vol. 1, no. 1, pp. 989-991, 2012.

[8] C. J. Chen and T. H. Chu, "Design of a 60-GHz substrate integrated waveguide Butler matrix-a systematic approach," *IEEE Trans. Microw. Theory Tech.*, 2010.

[9] Q. L. Yang, Y. L. Ban, K. Kang, C. Y. D. Sim, and G. Wu, "SIW multibeam array for 5G mobile devices," *IEEE Access*, 2016.

[10] W. Arriola, M. Lee, Y. Kim, E. Ryu, and I. S. Kim, "New inkjet printed wideband 3 dB branch line coupler," *IEEE MTT-S Int. Microw. Symp. Dig.*, pp. 1-4, 2011.

[11] K. Tekkouk, J. Hirokawa, R. Sauleau, M. Ettorre, M. Sano, and M. Ando, "Dual-Layer ridged waveguide slot array fed by a Butler matrix with sidelobe control in the 60-GHz band," *IEEE Trans. Antennas Propag.*, 2015.

[12] K. Wincza and S. Gruszczynski, "Broadband integrated 8 × 8 Butler matrix utilizing quadrature couplers and schiffman phase shifters for multibeam antennas with broadside beam," *IEEE Trans. Microw. Theory Tech.*, 2016.

[13] H. X. Xu, G. M. Wang, and X. Wang, "Compact Butler matrix using composite right/left handed transmission line," *Electron. Lett.*, 2011.

[14] Y. S. Jeong and T. W. Kim, "Design and analysis of swapped port coupler and its application in a miniaturized Butler matrix," *IEEE Trans. Microw. Theory Tech.*, 2010.

[15] Y. M. Madany, H. M. Elkamchouchi, and A. A. Salama, "Design and analysis of miniaturized smart antenna system using 1×8 switched Butler Matrix," *2012 IEEE 13th Annu. Wirel. Microw. Technol. Conf. WAMICON 2012*, vol. 2012-Janua, 2012.

[16] L. Abdelghani, T. A. Denidni, and M. Nedil, "Design of a new ultra-wideband 4×4 Butler matrix for beamforming antenna applications," *IEEE Antennas Propag. Soc. AP-S Int. Symp.*, pp. 2-3, 2012.

[17] M. Nedil, M. A. El Cafsi, T. A. Denidni, and A. Gharsallah, "Novel UWB CB-CPW Butler matrix for wireless applications," *in IEEE Antennas and Propagation Society, AP-S International Symposium (Digest)*, pp. 1800-1801, 2014.

[18] S. A. Babale, S. K. A. Rahim, M. Jusoh, and L. Zahid, "Branch-line coupler using PDMS and shieldit super fabric conductor," *Appl. Phys. A Mater. Sci. Process.*, vol. 123, no. 2, 2017.

[19] K. Wincza and S. Gruszczynski, "Broadband integrated 8 × 8 Butler matrix utilizing quadrature couplers and schiffman phase shifters for multibeam antennas with broadside beam," *IEEE Trans. Microw. Theory Tech.*, vol. 64, no. 8, pp. 2596-2604, 2016.

[20] M. Fakharzadeh, P. Mousavi, S. Safavi-Naeini, and S. H. Jamali, "The effects of imbalanced phase shifters loss on phased array gain," *IEEE Antennas Wirel. Propag. Lett.*, vol. 7, pp. 192-196, 2008.

[21] S. Y. Zheng, W. S. Chan, and K. F. Man, "Broadband phase shifter using loaded transmission line," *IEEE Microw. Wirel. Components Lett.*, 2010.

[22] S. Sun and L. Zhu, "Miniaturised patch hybrid couplers using asymmetrically loaded cross slots," *IET Microwaves, Antennas Propag.*, 2010.

[23] G. Tian, J. P. Yang, and W. Wu, "A novel compact Butler matrix without phase shifter," *IEEE Microw. Wirel. Components Lett.*, 2014.

[24] H. Ren, B. Arigong, M. Zhou, J. Ding, and H. Zhang, "A novel design of 4 × 4 Butler matrix with relatively flexible phase differences," *IEEE Antennas Wirel. Propag. Lett.*, 2016.

[25] Y. S. Wong, S. Y. Zheng, and W. S. Chan, "Quasi-arbitrary phase-difference hybrid coupler," *IEEE Trans. Microw. Theory Tech.*, 2012.

[26] M. J. Park, "Comments on quasi-arbitrary phase-difference hybrid coupler," *IEEE Trans. Microw. Theory Tech.*, vol. 61, no. 3, pp. 1397-1398, 2013.

[27] S. Ahmed, F. A. Tahir, A. Shamim, and H. M. Cheema, "A compact kapton-based inkjet-printed multiband antenna for flexible wireless devices," *IEEE Antennas Wirel. Propag. Lett.*, vol. 14, no. c, pp. 1802-1805, 2015.

[28] Y. Kawahara, S. Hodges, B. S. Cook, C. Zhang, and G. D. Abowd, "Instant inkjet circuits: Lab-based inkjet printing to support rapid prototyping of ubicomp devices," 2013.

[29] S. A. Babale, S. K. A. Rahim, M. Himdi, S. H. Lawan, F. D. Sani, and A. D. Usman, "Implementation of inkjet-printed 3 dB coupler with equal power division and 45° output phase difference," *Microw. Opt. Technol. Lett.*, vol. 63, no. 4, pp. 1007-1011, 2021.

[30] S. A. Babale, S. K. Abdul Rahim, O. A. Barro, M. Himdi, and M. Khalily, "Single layered 4 × 4 Butler matrix without phase-shifters and crossovers," *IEEE Access*, vol. 6, pp. 77289-77298, 2018.

[31] C. Balanis, "Antenna theory: analysis and design, fourth edition," in John Wiley & Sons, Inc., 2016.

Suleiman Aliyu Babale (Member, IEEE) received the bachelor's degree in electrical engineering from Bayero University Kano, Nigeria, in 2005, the M.Sc. degree from Ahmadu Bello University Zaria, Nigeria, in 2012, and the Ph.D. degree in electrical engineering with majors in telecommunications from Universiti Teknologi Malaysia, Johor Bahru, Malaysia, in 2018.

He has published more than 25 journal papers and conference and technical proceedings on antenna arrays, smart antenna systems, and microwave devices. He has been a Lecturer with Bayero University Kano since 2009 and a registered member of the Council for the Regulation of Engineering in Nigeria (COREN) since 2011. His main research interests are in millimeter-wave multibeam antenna array with Butler matrix beamforming network for 5G wireless communications.

Sharul Kamal Abdul Rahim received the first degree from University of Tennessee, USA majoring in electrical engineering, graduating in 1996, the M.Sc. degree in engineering (communication engineering) from Universiti Teknologi Malaysia (UTM) in 2001, and the Ph.D. degree in wireless communication system from the University of Birmingham, U.K., in 2007.

Currently, he is a Professor with Wireless Communication Centre, Faculty of Electrical Engineering, UTM Skudai. His research interest is in smart antenna on communication system. He has published more than 50 journal papers and technical proceedings on rain attenuations, smart antenna system, microwave design, and reconfigurable antenna in national and international journals and conferences.

Dr. Rahim is also a member of IEEE Malaysia Section, Member Board of Engineer Malaysia (MBEM), and Member of Institute of Engineer Malaysia (MIEM) and Eta Kappa Nu Chapter (International Electrical Engineering Honor Society, University of Tennessee).

Tan Kim Geok received the B.E., M.E., and Ph.D. degrees from Universiti Teknologi Malaysia, in 1995, 1997, and 2000, respectively, all in electrical engineering.

He was a Senior R&D Engineer with EPCOS Singapore, in 2000. From 2001 to 2003, he was with DoCoMo Euro-Labs, Munich, Germany. He is currently an Academic Staff with Multimedia University. His research interests include radio propagation for outdoor and indoor, RFID, multi-user detection technique for multi-carrier technologies, and A-GPS.

Kashif Nisar Paracha received the bachelor's degree (Hons.) in electrical engineering from the University of Engineering and Technology (UET), Taxila, Pakistan, in 2004, the M.S. degree in electrical engineering from the King Fahd University of Petroleum and Mineral (KFUPM), Dhahran, Saudi Arabia, in 2008, and the Ph.D. degree in electrical engineering from the Universiti Teknologi Malaysia (UTM), Johor Bahru, Malaysia, in 2019.

He was a Research Assistant with the Electrical Engineering Department, KFUPM, from 2006 to 2008, and he taught with the Electrical Engineering Department, The University of Faisalabad (TUF), Pakistan, from 2008 to 2011. He is currently an Assistant Professor with the Electrical Engineering Department, Government College University Faisalabad (GCUF). He has authored or coauthored over eight research journal articles and three conference articles. His research interests include communication, wearable antenna design, metamaterials, inkjet printing methods, and algorithms.

Dr. Paracha is a Life-Time Professional Member of the Pakistan Engineering Council (PEC) and Senior member of IEEE, USA.

Arslan Dawood Butt received the B.Sc. degree in electrical engineering with distinction from EME College, NUST, Pakistan, in 2010. He immediately enrolled for M.Sc. in electronic systems engineering at Politecnico di Milano, Italy and received the master's degree in 2012. He later pursued the Ph.D. degree in the field of "silicon based radiation detection systems" with the same university and was awarded the Ph.D. degree with Merit in 2016. During his M.S. and Ph.D. studies, Dr. Butt worked on international projects sponsored by European Space Agency, the European Commission, and the Instituto Nazionale di Fisica Nucleare (INFN) Milan section. In 2017, Dr. Butt joined the Department of Electrical Engineering, Government College University Faisalabad (GCUF), Pakistan as an Assistant Professor to pursue a career of teaching and research in Pakistan. In GCUF, Dr. Butt has changed his field of research to motion tracking and wearable sensors for augmented reality applications. He is the author and coauthor of about 16 research journal articles, and 40 conference articles.

Irfan Ali received the B.E. degree in telecommunications from the Mehran University of Engineering and Technology (MUET), Pakistan, in 2010 and the master's degree in telecommunications engineering from the NED University of Engineering and Technology, in 2014, and the Doctor of Philosophy (Ph.D.) degree from Wireless Communication Centre (WCC), Universiti Teknologi Malaysia (UTM).

His research interests include dielectric resonator antennas, microstrip patch antennas, MIMO antennas, and mutual coupling analysis. He has published more than 20 papers in reputed journals and conference proceedings.

Sani Halliru Lawan (Member, IEEE) received the B.Eng. and M.Eng. degrees in electrical engineering from Bayero University Kano, Kano, Nigeria, in 2006 and 2013, respectively, and the Ph.D. degree in electrical engineering (photonics) from Universiti Teknologi Malaysia, in 2019.

He has been working as a Lecturer with Bayero University Kano since 2009. His research interest includes fiber propagation, optical and wireless communication systems, passive optical networks, and electrical engineering services.

Study of the Combination Method and Its Application to Shrink a Patch Antenna Operating in the UHF Band

Qianling Huang[1], Xiaofei Xu[1,2,*], and Ruiheng Zhang[1]

[1]School of Communication and Information Engineering
Shanghai University, Shanghai 200444, China

[2]Key Laboratory of Specialty Fiber Optics and Optical Access Networks, Shanghai Institute for Advanced Communication and Data Science
Shanghai University, Shanghai 200444, China
*xfxu@shu.edu.cn

***Abstract* –** This work is focused on how to efficiently shrink a patch antenna operating in the UHF band. Five typical independent methods are first introduced that were solely used to realize a small patch antenna. A potential combination method is further discussed utilizing two or more of these five methods. One miniature patch antenna is experimentally demonstrated operating at 735 MHz using the combination method, in which both of shorting wall and complementary split ring resonators are applied in a reconciling way. A two-step optimization procedure is given to show how the antenna sizes can be significantly reduced with this combination method. The antenna is fabricated on a simple dielectric with a low ε_r of 2.2. The patch size is only $0.127\lambda \times 0.123\lambda$. The antenna efficiency is considerably high as 77% in measurement.

***Index Terms* –** Combination method, patch antenna, small-sized, UHF band.

I. INTRODUCTION

Patch antennas are widely used in several gigahertz (GHz) range. Due to the resonance condition, the patch length is generally at the order of half guided wavelength ($0.5\lambda_g$) [1, 2]. The patch length is, however, physically large for an antenna operating below 1 GHz in the UHF band due to the long wavelength. In this work, we aim to shrink a patch antenna in the UHF band. We notice that a variety of miniaturization methods have been reported [3] to realize a compact patch antenna including: (I) shorting/folding technique [4–7]; (II) etching slots on the patch and/or ground planes [8–10]; (III) using natural magneto-dielectric with a higher relative permittivity ε_{rh} and/or permeability μ_r [11–14]; (IV) using planar metamaterials [15–18]; (V) bulky metamaterials with effective permittivity $\varepsilon_{r\text{eff}}$, and/or permeability $\mu_{r\text{eff}}$ [19–26], etc. Most of them were nevertheless solely used.

Inspired by these technologies, a combination method by incorporating two or more of the five methods can be utilized to reduce the antenna size as well. The combination method is more effective than a single technique used on its own. Here, with the technologies of shorting wall and planar metamaterial structures, a combination method is demonstrated to significantly compact a patch antenna operating in the UHF band. The size reduction effect is numerically examined in a two-step optimization procedure. The first step is to add a shorting wall that makes the half-wave patch reduced to quarter-wave. The second step is to further shorten the quarter-wave length by loading periodic complementary split ring resonators (CSRRs) [16, 17, 27] on the patch. One shorted patch antenna with 2×2 CSRRs is experimentally studied resonating at 735 MHz. The patch antenna is fabricated on a simple dielectric with a low ε_r of 2.2. The patch size is only $0.127\lambda \times 0.123\lambda$ (λ is free space wavelength). The measured efficiency is 77%, which is in good agreement with the simulated value. The small shorted metamaterial patch antenna can be applied in the UHF band communications.

II. CONCEPT OF THE COMBINATION METHOD

The typical five methods to shrink patch antennas are given in Table 1. The five size multipliers from M_I to M_V are also given, which are used to measure how the antenna length is reduced from the original half-wave. Note that the first three methods [3–14] have been widely used in previous decades. The latter two methods [15–26] are, however, using new conceptual metamaterials. According to the metamaterial structures, they are further differentiated into planar and bulky types. The planar metamaterials are 2D structures [15–18], e.g., CSRRs, loaded on the patch or ground plane, which are similar with etched slots on the planes since they both need metal planes to make functional patterns. Hence,

Submitted On: November 9, 2021
Accepted On: March 16, 2022

https://doi.org/10.13052/2022.ACES.J.370209

Table 1: Five typical methods to shrink a patch antenna and the associated multipliers

No.	Method	Multiplier
I	Shorting/folding technique	$M_{\mathrm{I}} \approx 0.5^n$
II	Slotted patch/ground	M_{II}
III	Natural magneto-dielectric (ε_{rh},μ_r)	$M_{\mathrm{III}} \approx \sqrt{\varepsilon_r/(\varepsilon_{rh}\mu_r)}$
IV	Planar metamaterials	M_{IV}
V	Bulky metamaterials ($\varepsilon_{r\mathrm{eff}}$,$\mu_{r\mathrm{eff}}$)	$M_{\mathrm{V}} \approx \sqrt{\varepsilon_r/(\varepsilon_{r\mathrm{eff}}\mu_{r\mathrm{eff}})}$

the second and fourth methods are sometimes incompatible. The bulky metamaterials are, however, 3D structures embedded in the dielectric substrate [19–26]. They are physically inhomogeneous included with composite subwavelength structures but work as homogeneous natural materials as if $\varepsilon_{r\mathrm{eff}} \approx \varepsilon_{rh}$ and $\mu_{r\mathrm{eff}} \approx \mu_r$.

Considering a conventional patch antenna with length L fabricated on a low loss nonmagnetic substrate with dielectric constant ε_r, the resonant frequency f_0 is predicted using a simple formula [1, 2]

$$f_0 \approx c/\left(2L\sqrt{\varepsilon_r}\right), \tag{1}$$

where c is the light speed in free space. Note that the margin effects are not accounted in eqn (1) for simplicity. The associated electric patch length is calculated as

$$L_\lambda = \frac{L}{\lambda} = \frac{L}{c} f_0. \tag{2}$$

From eqn (2), we see that the electric patch length is proportional to f_0. Hence, for a given L, the key issue to compact the antenna is to downshift f_0 with the five methods listed in Table 1.

We now discuss the multipliers for these methods. On the basis of the conventional antenna discussed above, if the antenna size is kept unchanged when using these compacting methods, it will resonate at a new but lower frequency f_1. Therefore, multiplier is approximately equal to f_1/f_0, which is smaller than 1. For the first method of the shorting/folding technique, the multiplier is $M_I \approx 0.5^n$, where n is an integer. If only a shorting wall is added to the antenna [4–6], the half-wave antenna evolves to quarter-wave, e.g., n = 1 in this case. For more complex folding techniques[7], n can be 2, 3, or even larger.

The multipliers M_{II} for the second method of adding slots on the patch or ground, and M_{IV} for the fourth method are both highly dependent on the shape and parameters of functional structures. Therefore, it will be difficult to given empirical solutions for M_{II} and M_{IV}.

For the third method when the patch antenna is loaded with a natural magneto-dielectric with ε_{rh} and μ_r, the resonant frequency becomes

$$f_1 \approx c/\left(2L\sqrt{\varepsilon_{rh}\mu_r}\right). \tag{3}$$

The associated multiplier is $M_{III} \approx [\varepsilon_r/(\varepsilon_{rh}\mu_r)]^{1/2}$. The case for the fifth method is similar with eqn (3) but using effective $\varepsilon_{r\mathrm{eff}}$ and $\mu_{r\mathrm{eff}}$, which is

$$f_1 \approx c/\left(2L\sqrt{\varepsilon_{r\mathrm{eff}}\mu_{r\mathrm{eff}}}\right). \tag{4}$$

The associated multiplier is $M_V \approx [\varepsilon_r/(\varepsilon_{r\mathrm{eff}}\mu_{r\mathrm{eff}})]^{1/2}$.

By incorporating all the five methods, we obtain

$$\begin{aligned} f_1 &= f_0 \cdot M_{\mathrm{I}}(f_1) \cdot \begin{bmatrix} M_{\mathrm{II}}(f_1) \\ M_{\mathrm{IV}}(f_1) \end{bmatrix} \cdot \begin{bmatrix} M_{\mathrm{III}}(f_1) \\ M_{\mathrm{V}}(f_1) \end{bmatrix} \\ &= f_0 \cdot M_{\mathrm{total}}(f_1). \end{aligned} \tag{5}$$

The new resonant frequency f_1 in eqn (5) is now the product of f_0 multiplied by a new size reduction operator M_{total}, which represents the total effect of the five methods. Considering the second and fourth methods are sometimes incompatible in a practical antenna design, we use a square bracket including these two multipliers, in which only one multiplier can be chosen for the same time. The case is similar for the second square bracket where the third and fifth methods are included. If the size reduction effects vary with frequency, these multipliers should be dispersive as well that only the effects around f_1 need to be taken into account.

By utilizing the five methods in a combining way, the antenna length can be reduced more significantly than only one method used solely. In the following parts, one compact patch antenna will be demonstrated by incorporating two methods, in which both of a shorting wall and planar metamaterial structures are utilized.

III. ANTENNA DESIGN

A. Step 1: From half-wave to quarter-wave

We start from a conventional rectangular patch antenna. The prototype of the conventional antenna is given in Figure 1 (a) with patch size of $L \times W$ and ground plane length G. In the side view of Figure 1 (b), we see that dielectric substrate is with thickness h, dielectric constant ε_r, and loss tangent tanδ. The patch and ground planes are both made of copper with conductivity of 5.8 $\times$ 10^7 S/m and thickness t. The shorted patch antenna is shown in Figure 1 (c). A shorting wall composed of numerous conducting vias is added at the end of the shorted antenna. The shorting wall connects the patch and ground planes, making the half-wave patch length ($\tilde{}\lambda_g$/2) reduced to quarter-wave ($\tilde{}\lambda_g$/4). Note that the sizes for both antennas are identical. And they are both coaxially fed with characteristic impedance of 50 Ω.

Assuming L = 52 mm, W = 50 mm, G = 100 mm, h = 12 mm, t = 0.035 mm, ε_r = 2.2, and tanδ = 0.001, we obtain the reflection coefficients (S11s) for the conventional and shorted patch antennas in Figure 2, using the numerical HFSS solver.

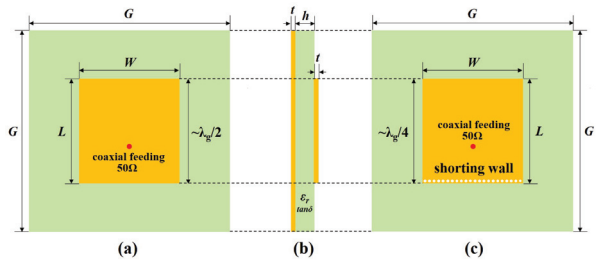

Fig. 1. Antenna prototypes. (a) Top view. (b) Side view of a conventional patch antenna. (c) Top view of a shorted patch antenna.

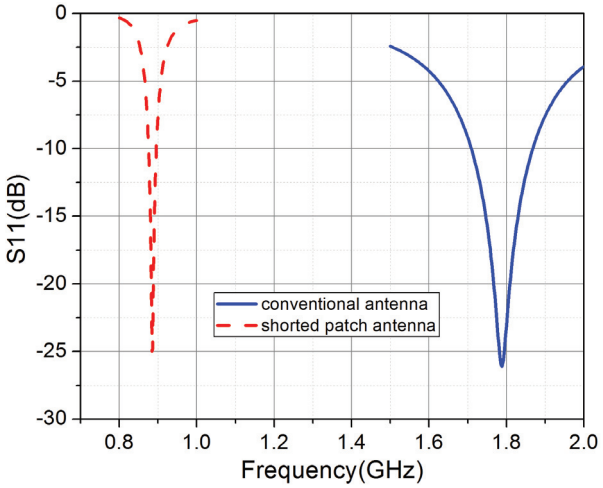

Fig. 2. The simulated S11s for the conventional and shorted patch antennas.

It is seen that the resonant frequency is 1.788 GHz for the conventional antenna and 0.885 GHz for the shorted one. The patch lengths are 0.46 λ_g and 0.23 λ_g, respectively. If the margin effects for the patches are accounted, the lengths should be better near $\lambda_g/2$ and $\lambda_g/4$.

B. Step 2: Beyond quarter-wave

To make the antenna smaller, the planar CSRRs are further added on the shorted patch. The scheme for one CSRR element is given in Figure 3 (a). They are excited by the electric fields perpendicular to the structures [16, 17], working as electric metamaterials. The mechanisms for the CSRRs can be explained using a lumped-element model (see Figure 13 in [27]) that the effective capacitance for the CSRR patch is increased than the original integrated one. The period for the CSRR element is p. Two slots are etched on the square structure. The length of the outer slot is a, while the width is g. These parameters can be tuned and adapted for different antenna applications. An array including

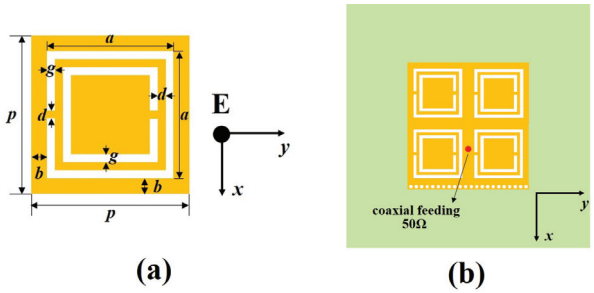

Fig. 3. (a) One CSRR element and (b) the shorted patch antenna loaded with 2 × 2 CSRRs.

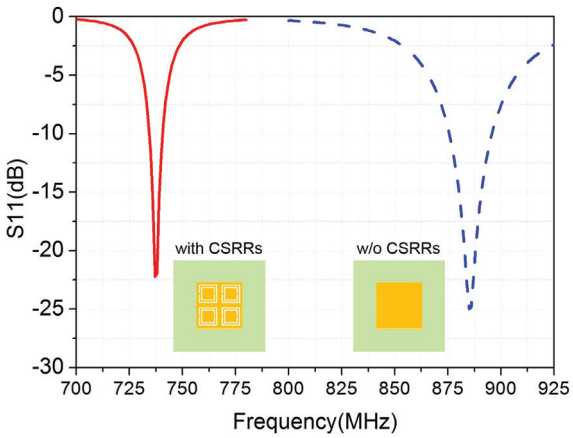

Fig. 4. The simulated S11s for the shorted patch antennas with and without CSRRs.

2 × 2 CSRRs is designed on the patch, as shown in Figure 3 (b). The metamaterial antenna size is kept the same as the aforementioned one without CSRRs.

The geometry parameters for the CSRR structure are: p = 25 mm, a = 20 mm, g = 1 mm, d = 0.5 mm, and b = 2.5 mm. The shorted antennas loaded with CSRRs are subsequently calculated in HFSS. The simulated S11s are shown in Figure 4. As is mentioned above, the original shorted antenna without CSRRs resonates at 885 MHz. However, by adding 2 × 2 CSRRs, the antenna resonant frequency is downshifted to 737 MHz. The patch length is about 0.19 λ_g, which is beyond the quarter-wave limitation for a conventional shorted patch antenna.

The two-step results provide an evident evolution map for the combination method to show its capability to effectively reduce the antenna resonant frequency. Considering the antenna volumes for these antennas are identical, it implies that the antenna with a lower resonant frequency has a smaller electrical size. Hence, a better size reduction effect can be achieved by the combination technique than only one method used solely.

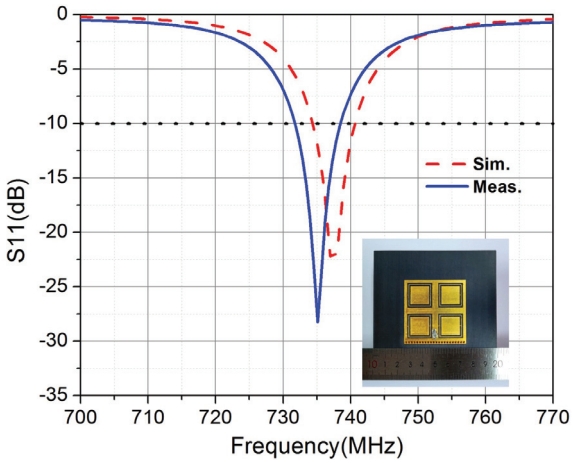

Fig. 5. The S11s for the shorted CSRR patch antenna. The inset picture shows the fabricated antenna.

IV. EXPERIMENTAL RESULTS

The designed shorted patch antenna with 2×2 CSRRs is experimentally demonstrated. The substrate is a kind of F4BMX dielectric with nominal $\varepsilon_r = 2.2$ and $\tan\delta = 0.001$, provided by Taizhou Wangling Corp. The measured S11, in contrast to the simulated one, is given in Figure 5. The fabricated shorted antenna with the CSRR metamaterial patch is also shown in the inset picture. It is fed by a 50-Ω coaxial probe. From the measured S11, it is observed to resonate at 735 MHz (λ = 408.16 mm) with the -10 dB bandwidth (BW) of 6.8 MHz (0.93%). They agree well with the simulated results. The simulated resonant frequency from HFSS is 737 MHz with BW of 6.2 MHz (0.84%). The limited BW is resulted from the small antenna size [28, 29], which can also be found in other miniature antennas [12].

The normalized antenna size is $0.127 \times 0.123\lambda$ (or $0.189\lambda_g \times 0.182\lambda_g$). The substrate thickness is 12 mm or 0.03λ. Considering the dielectric is with a low index of $\varepsilon_r = 2.2$, the size-reduction effect is remarkable.

The radiation patterns for the shorted metamaterial antenna at the resonant frequency are given in Figure 6. For the shorted antenna, there is only one slot radiating the electromagnetic waves. Hence, its patterns on the *E*-plane as shown in Figure 6 (a) exhibit quasi-omnidirectional characteristics. They are much different from the conventional patch antenna in which two parallel slots work together. The *H*-plane patterns in Figure 6 (b) are yet similar with the conventional antenna.

The miniature antenna is with a notable backlobe. It is due to the electrically small ground plane. To suppress the backlobe, an effective method is to increase the ground size. Another limitation for the antenna is that the cross-polarizations are seen very large on the *H*-plane. They seem inevitable for shorted patch antennas that were also found in other designs with shorting walls [5–7]. Fortunately, the radiation fields in the broadside are still with good polarization purity.

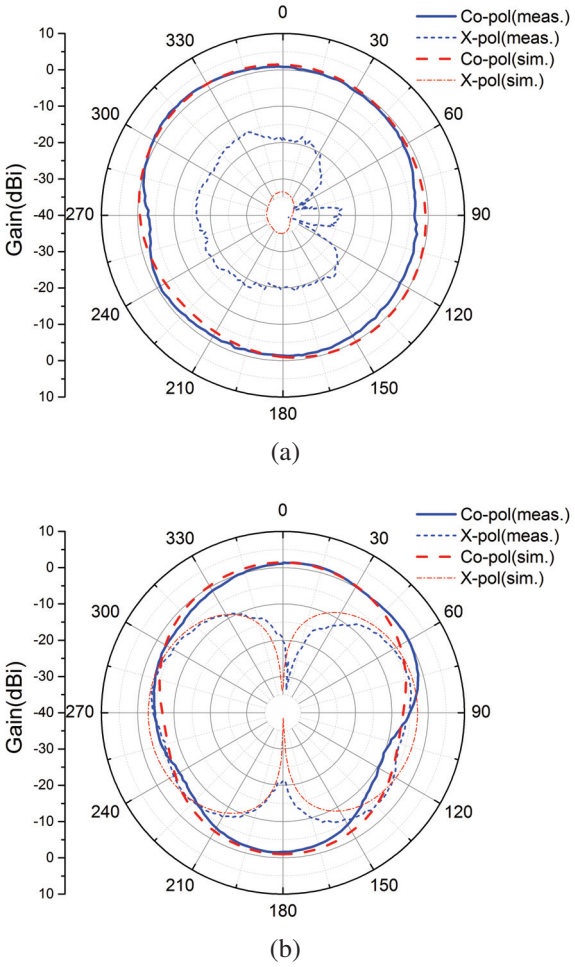

Fig. 6. The radiation patterns for the shorted metamaterial antenna on the (a) *E*-plane and (b) *H*-plane.

The peak antenna gain is at the level of 2 dBi at the resonant frequency. The antenna gain can be moderately enhanced to about 3-4 dBi by increasing the directivity. It can be realized by enlarging the ground plane as to suppress the backlobe.

Figure 7 shows the simulated and measured antenna efficiency (η). They are obtained with the G/D (gain/directivity) method. The directivity is calculated from the measured 3D radiation pattern data. The peak efficiency in measurement is about 77%. The simulated one is slightly higher as 82%. It proves that, although the new shorted antenna with CSRRs is very small, the total radiated power is still kept at an acceptably high level.

The performances for the shorted metamaterial antenna in this work are finally summarized in Table 2,

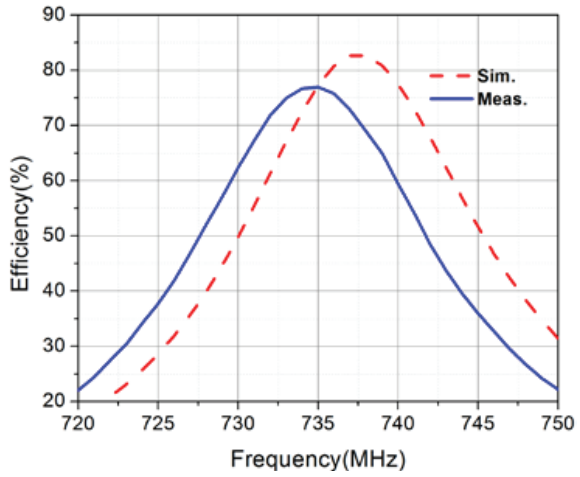

Fig. 7. The antenna efficiency.

Table 2: Comparison of several compact patch antennas operating in the UHF band below 1 GHz

Ref	Patch area	Thick-ness	BW /%	η /%	Gain /dBi
[12]	$0.16\lambda \times 0.16\lambda$	0.01λ	0.3	83	1
[19]	$0.077\lambda \times 0.077\lambda$	-	0.83	19.8	-3.9
[21]	$0.2\lambda \times 0.2\lambda$	0.028λ	0.5	-	-7.9
This work	$0.127\lambda \times 0.123\lambda$	0.03λ	0.93	77	2

in comparison with some other compact patch antennas operating in the UHF band below 1 GHz.

We have realized a small-sized UHF band patch antenna using the combination method of adding both a shorting wall and CSRRs. To make the antenna more compact, some other ways, e.g., a higher permittivity host substrate [12], [13] or magnetic material [14] may be incorporated into this powerful technique in future.

V. CONCLUSION

In conclusion, a small patch antenna is designed by combining two size-reduction methods as adding a shorting wall and CSRRs. Numerical calculations show that the resonant frequency can be significantly reduced by utilizing the combination method. One particular shorted patch antenna loaded with 2×2 CSRRs is experimentally studied, which is fabricated on a low permittivity substrate. The antenna resonates at 735 MHz. The patch size is $0.127\lambda \times 0.123\lambda$. The measured efficiency is acceptably high as 77% that can meet the demands of the UHF band communications.

ACKNOWLEDGMENT

This work is supported by the National Natural Science Foundation of China under Grant 11904222 and the Natural Science Foundation of Shanghai under Grant 16ZR1446100.

REFERENCES

[1] R. Garg, P. Bhartia, I. Bahl, and A. Ittipiboon, *Microstrip antenna design handbook*, Artech House, MA, 2001.

[2] D. R. Jackson, "Microstrip antennas," in *Antenna Engineering Handbook*, J. L. Volakis, Ed., McGraw Hill, NY, 2007, Ch. 7.

[3] E. J. Rothwell, and R. O. Ouedraogo, "Antenna miniaturization: definitions, concepts, and a review with emphasis on metamaterials," *J. Electromag. Waves Appl.*, vol. 28, pp. 2089-2123, 2014.

[4] S. Pinhas, and S. Shtrikman, "Comparison between computed and measured bandwidth of quarter-wave microstrip radiators," *IEEE Trans. Antennas Propag.*, vol. 36, pp. 1615-1616, 1988.

[5] R. Chair, K. F. Lee, and K. M. Luk, "Bandwidth and cross-polarization characteristics of quarter-wave shorted patch antennas," *Microw. Opt. Technol. Lett.*, vol. 22, pp. 101-103, 1999.

[6] K. F. Lee, Y. X. Guo, J. A. Hawkins, R. Chair, and K. M. Luk, "Theory and experiment on microstrip patch antennas with shorting walls," *IEE Proc.-Microw. Antennas Propag.*, vol. 147, pp. 521-525, 2000.

[7] R. L. Li, G. DeJean, M. M. Tentzeris, and J. Laskar, "Development and analysis of a folded shorted-patch antenna with reduced size," *IEEE Trans. Antennas Propag.*, vol. 52, pp. 555-562, 2004.

[8] H. Iwasaki, and Y. T. Lo, "A circularly-polarized small-size microstrip antenna with a cross slot," *IEEE Trans. Antennas Propag.*, vol. 44, pp. 1399-1401, 1996.

[9] L. Desclos, "Size reduction of patch by means of slots insertion," *Microw. Opt. Technol. Lett.*, vol. 25, pp. 111-113, 2000.

[10] N. Herscovici, M. F. Osorio, and C. Peixeiro, "Miniaturization of rectangular microstrip patches using genetic algorithms," *IEEE Antennas Wireless Propag. Lett.*, vol. 1, pp. 94-97, 2002.

[11] R. C. Hansen, and M. Burke, "Antenna with magneto-dielectrics," *Microw. Opt. Technol. Lett.*, vol. 26, pp. 75-78, 2000.

[12] J. Huang, "Miniaturized UHF microstrip antenna for a Mars mission," *IEEE Antennas and Propagation Society International Symposium*, pp. 486-489, 2001.

[13] J. S. Kula, D. Psychoudakis, W.-J. Liao, C.-C. Chen, J. L. Volakis, and J. W. Halloran, "Patch-antenna miniaturization using recently available ceramic substrates," *IEEE Antennas Propag. Mag.*, vol. 48, pp. 13-20, 2006.

[14] Z. Zheng, H. Zhang, J. Q. Xiao, and F. Bai, "Lowloss NiZn/Co2Z composite ferrite with almost equal values of permeability and permittivity for antenna applications," *IEEE Trans. Magn.*, vol. 49, pp. 4214-4217, 2013.

[15] X. M. Yang, Q. H. Sun, Y. Jing, Q. Cheng, X. Y. Zhou, H. W. Kong, and T. J. Cui, "Increasing the bandwidth of microstrip patch antenna by loading compact artificial magneto-dielectrics," *IEEE Trans. Antennas Propag.*, vol. 50, pp. 373-378, 2011.

[16] R. O. Ouedraogo, E. J. Rothwell, A. R. Diaz, K. Fuchi, and A. Temme, "Miniaturization of patch antennas using a metamaterial-inspired technique," *IEEE Trans. Antennas Propag.*, vol. 60, pp. 2175-2182, 2012.

[17] Y. Dong, H. Toyao, and T. Itoh, "Design and characterization of miniaturized patch antennas loaded with complimentary split ring resonator," *IEEE Trans. Antennas Propag.*, vol. 60, pp. 772-785, 2012.

[18] S. Li, A. Z. Elsherbeni, Z. Ding, and Y. Mao, "A metamaterial inspired compact miniaturized triple-band near field resonant parasitic antenna for WLAN/WiMAX applications," *Applied Computational Electromagnetics Society (ACES) Journal*, vol. 35, pp. 1539-1547, 2020.

[19] K. Buell, H. Mosallaei, and K. Sarabandi, "A substrate for small patch antennas providing tunable miniaturization factor," *IEEE Trans. Microw. Theory Technol.*, vol. 54, pp. 135-146, 2006.

[20] F. Bilotti, A. Toscano, and L. Vegni, "Design of spiral and multiple split-ring resonators for the realization of miniaturized metamaterial samples," *IEEE Trans. Antennas Propag.*, vol. 55, pp. 2258-2267, 2007.

[21] S. Jahani, J. Rashed-Mohassel, and M. Shahabadi, "Miniaturization of circular patch antennas using MNG metamaterials," *IEEE Antennas Wireless Propag. Lett.*, vol. 9, pp. 1194-1196, 2010.

[22] S. Kumar, and D. K. Vishwakarma, "Miniaturisation of microstrip patch antenna using an artificial planar magneto-dielectric meta-substrate," *IET Microw. Antennas Propag.*, vol. 10, pp. 1235-1241, 2016.

[23] X. Xu, and J. Wei, "Miniaturisation design of patch antenna using a low-profile mushroom type meta-substrate tailored with high permittivity," *IET Microw. Antennas Propag.*, vol. 12, pp. 1216-1221, 2018.

[24] G. Dai, X. Xu, and X. Deng, "Size-reduced equilateral triangular metamaterial patch antenna designed for mobile communications," *Applied Computational Electromagnetics Society (ACES) Journal*, vol. 36, pp. 1026-1030, 2021.

[25] Q. Huang, and X. Xu, "Design of a miniaturized UHF band patch antenna inspired by the metamaterial technology," *Asia-Pacific Conference on Antennas and Propagation*, pp. 1-2, 2020.

[26] H. Lu, X. Xu, and F. Sun, "Miniaturized UHF band microstrip antenna designed with spiral metamaterial inclusions," *International Applied Computational Electromagnetics Society Symposium*, pp. 1-2, 2021.

[27] J. D. Baena, J. Bonache, F. Martin, R. Marques, F. Falcone, T. Lopetegi, M. A. G. Laso, J. Garcia, I. Gil, and M. Sorolla, "Equivalent-circuit models for split-ring resonators and complementary split-ring resonators coupled to planar transmission lines," *IEEE Trans. Microw. Theory Tech.*, vol. 53. pp. 1451-1461, 2005.

[28] L. J. Chu, "Physical limitations of omnidirectional antennas," *J. Appl. Phys.*, vol. 19, pp. 1163-1175, 1948.

[29] J. S. McLean, "A re-examination of the fundamental limits on the radiation Q of electrically small antennas," *IEEE Trans. Antennas Propag.*, vol. 44, pp. 672–676, 1996.

Qianling Huang was born in Nantong, China, in 1996. She received the M.S. degree in electronics and communication engineering from Shanghai University, Shanghai, China, in 2020.Her research interest includes antenna miniaturization technology and electromagnetic metamaterials.

Xiaofei Xu received the B.S. degree in 2007 and the Ph.D. degree in 2011, both from Nanjing University, Nanjing, China.He is currently with the School of Communication and Information Engineering, Shanghai University, Shanghai, China.Dr. Xu's research areas include electromagnetics, antennas, and microwave technology. He has authored more than 50 papers published in peer-reviewed journals and conference proceedings. He also serves a number of journals and society workshops as the reviewer or organizer.

Ruiheng Zhang was born in Shanghai, China, in 1995. He received the M.S. degree in electronics and communication engineering from Shanghai University, Shanghai, China, in 2020. His current research interest includes antenna and RF technology for base stations and terminals for fifth-generation (5G) communications.

Study on the Electromagnetic Interference of Shielded Cable in Rail Weighbridge

Yang Yang[1,2], Feng Zhu[1*], Nan Lu[1], and Yingchun Xiao[1]

[1]School of Electrical Engineering
Southwest Jiaotong University, Chengdu 610031, China
280899254@qq.com, zhufeng@swjtu.cn, lunan946@qq.com, 1134748712@qq.com,

[2]Department of Railway Engineering
Sichuan College of Architectural Technology, Deyang 618000, China

Abstract **–**In view of the electromagnetic interference (EMI) of the signal shielded cable in the rail weighbridge, the interference source is analyzed on the basis of the field measurement and investigation, and methods of suppressing the crosstalk voltage of the shielded cable are proposed. First, the capacitive coupling model between the power line and the shielded cable is established, and the coupling model between the shielded layer and the core is developed. Later, the distribution parameters of the multi-conductor transmission line system are extracted by the commercial software ANSYS based on the finite element method. Then the coupling voltages of the shielded layer and the core can be calculated; compared with the measured results, the accuracy and effectiveness of the proposed method are verified. Finally, the EMI suppression methods are proposed and its effectiveness is verified. The EMI of the shielded cable is very common in engineering, and this method has a good reference value for solving the similar problems.

Index Terms **–** Capacitive coupling, crosstalk voltage, electromagnetic interference, rail weighbridge, shielded cable.

I. INTRODUCTION

The electronic rail weighbridge is an electronic weighing device for weighing railway vehicles and goods [1]. China's railway capacity is increasing with the development of railway transportation, and it is necessary to weigh the railway vehicles and their loaded goods more efficiently and accurately; so the electronic rail weighbridge must work in electromagnetic compatibility (EMC). However, research on the influence of shielding and grounding of railway field on electromagnetic interference (EMI) is still in an initial stage [2-4]. Therefore, the research on crosstalk of shielded signal cable of rail weighbridge has theoretical and practical application values [5].

Nowadays, the crosstalk researches of multi-conductor transmission lines are mainly concentrated in the high frequency band [6-9]; so they cannot be applied at low frequency for signal interference analysis. In some articles, single-end grounding of signal cable is proposed to solve the problem of EMI [10-12]. However, due to the complex electromagnetic environment in actual railway fields, even if the single-end grounding is used, there is still serious interference; so there is still lack of systematic theoretical analysis of railway electromagnetic environment. In a rail weighbridge EMI case, the rail weighbridge is set beside the National Traction Power Laboratory (NTPL) in Chengdu, China. The pressure sensor on the rail weighbridge is an electronic device that converts the weight of cargo and vehicles into an electrical signal. It is supposed to show a zero signal when there is nothing on the rail weighbridge, but in the EMI case, it shows a 320-mV electrical signal. The electric field intensity around the signal cable about 400 V/m is also measured by using an electric field tester, showing that the EMI is serious.

In Section II of this paper, the capacitive coupling model of signal transmission cable and power line under low frequency of railway weighbridge is established, and the formula for calculating the potential of the shielded layer as well as the crosstalk voltage between the shielded layer and the core of the signal cable is derived. In Section III, based on actual measurement and the finite element software ANSYS [13, 14], the coupling capacitance of multi-conductor line system is extracted and the interference voltage is calculated. In Section IV, the measures such as increasing the depth of grounding rods and improving soil moisture are proposed. Combined with an EMI case of railway weighbridge, the cause of interference signal is analyzed and eliminated. In Section V, the conclusion is drawn. The theoretical correctness is verified by comparing with the measured value in the field.

Submitted On: September 14, 2021
Accepted On: February 16, 2022

https://doi.org/10.13052/2022.ACES.J.370210

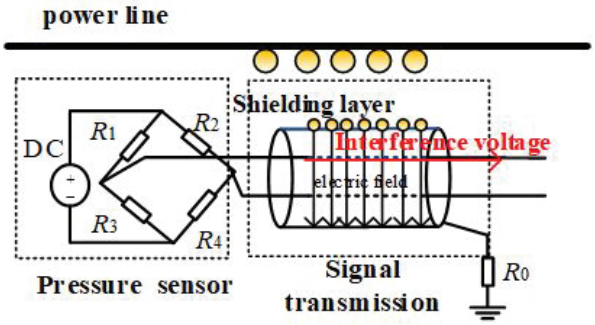

Fig. 1. Circuit and signal interference diagram of the pressure sensor.

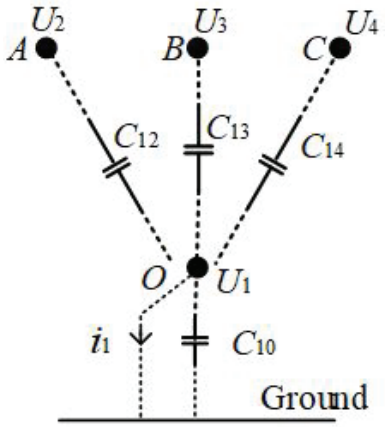

Fig. 2. Coupling model of power cord and shield wire.

II. SIGNAL CABLE INTERFERENCE MODEL OF RAIL WEIGHBRIDGE

The working circuit and signal interference diagram of the pressure sensor on the rail weighbridge is shown in Figure 1. The pressure sensor is mainly composed of four varistors to form the Wheatstone bridge (consists of R_1-R_4 and DC power supply). Its function is to convert the weight of the goods on the rail weighbridge into electrical signals. These electrical signals are sent through shielded cable to operational amplifier, filter, and other signal processing device, and finally the display will present the electrical signal to the user in terms of voltage signal and the weight of the goods.

The structure of the shielded cable used in the rail weighbridge is shown in Figure 1. It is composed of a copper mesh shielding layer and two core wires. Under ideal conditions, the shielding layer can protect the core wires from external electrical signal interference. However, when the shielded cable is very close to other wires, especially a power line with a large current, the power line can be regarded as a source of interference. Through capacitive coupling between multiple conductors, the shielding layer of the shielded cable can be regarded as the interfered object, and the induced charges will be generated on it. If the grounding resistance R_0 of the shielding layer is large, the electric field of the induced charges on the shielding layer will generate interference voltage on the cable core [15].

A. The crosstalk model of shielded layer and power line

When the signal cable is near the power line, due to the capacitive coupling between multiple conductors, the induced charges will be coupled on the shielded layer [16]. As shown in Figure 2, the shielded layer O is close to the power line. A, B, and C, respectively, represent the fire, zero, and ground wires of the power line. The capacitance between the shielded layer and the power lines A, B, and C is C_{12}, C_{13}, and C_{14}, the capacitance of the shielded layer to the ground is C_{10}, the interference voltage on the shielded layer is U_1, and the voltages on the three lines A, B, and C are U_2, U_3, and U_4.

According to the model of multi-conductor transmission lines, in a system consisting of three or more charged conductors, the charge of any conductor is affected not only by its own voltage but also by the voltages of the other conductors [17]. Then the charge Q_1 on the shielded layer can be expressed as [18]

$$Q_1 = \beta_{11}U_1 + \beta_{12}U_2 + \beta_{13}U_3 + \beta_{14}U_4 , \quad (1)$$

where β_{11} represents the electrostatic induction coefficient of the shielded layer; β_{12}, β_{13}, and β_{14} represent the mutual electrostatic induction coefficients of the signal cable and the three-phase transmission lines. The relation between β_{1n} and C_{1n} is [19]

$$\beta_{11} = C_{10} + C_{12} + C_{13} + C_{14}, \quad (2)$$

$$C_{1n} = -\beta_{1n}\ n = 2\ ,\ 3\ ,\ 4\ , \quad (3)$$

$$C_{10} = \beta_{11} + \beta_{12} + \beta_{13} + \beta_{14}. \quad (4)$$

According to the Thevenin theorem, the power line, shielding layer, and the ground can be regarded as a two-port network with an ideal voltage source in series with a resistor. The parameters of the voltage source and the resistor can be obtained by the following methods.

Consider two extreme cases: (1) perfect insulation of signal cable to ground; (2) short circuit of signal cable to ground. i_1 represents the short-circuit current of the signal cable when it short-circuits to the ground.

When the signal cable is perfectly insulated from the ground, $Q_1 = 0$. According to eqn (1), the open-circuit voltage of the signal cable is

$$U_1 = -\frac{\beta_{12}U_2 + \beta_{13}U_3 + \beta_{14}U_4}{\beta_{11}} . \quad (5)$$

When the signal cable is short-connected to the ground, the signal cable voltage U_1 is 0, and then its induced charge is

$$Q_1 = \beta_{12}U_2 + \beta_{13}U_3 + \beta_{14}U_4 . \quad (6)$$

In the case of alternating current 50 Hz, charge Q_1 is related to short-circuit current i_1 [20], which can be expressed as

$$i_1 = -j\omega Q_1. \tag{7}$$

According to the Thevenin theorem, the power line, the shielded layer, and the ground can be regarded as the two ends of the power supply with the open-circuit voltage U_1 and short-circuit current i_1. The internal impedance of power supply is

$$Z_1 = \frac{1}{j\omega\beta_{11}} = \frac{1}{j\omega(C_{10}+C_{12}+C_{13}+C_{14})}. \tag{8}$$

The grounding resistance R_0 of the shielded layer of the signal cable is related to the soil conductivity, temperature, humidity and grounding wire wiring measures at the grounding site [21, 22], and the grounding resistance value must comply with the national standard [23]. At this time, the disturbance voltage on the shielded layer of the signal cable is [24]

$$U_m = U_1 \frac{j\omega\beta_{11}R_0}{1+j\omega\beta_{11}R_0}. \tag{9}$$

In the ideal case, the earth is equipotential, but, in fact, there is a potential difference between any two points on the earth; so, the shielded layer will have great potential when the grounding device selection is inappropriate, the soil resistivity is excessive, or the potential gradient of the soil is large, especially near the high power equipment. Therefore, the potential of the shielded layer of the signal cable is equal to the vector sum of the ground potential and the induced voltage, and the calculation formula is as follows [25]:

$$U_s = \sqrt{(U_g)^2 + (U_m)^2}, \tag{10}$$

where U_s represents the total disturbance voltage of the shielded layer, U_g is the increased ground potential, and U_m is the induced voltage of the transmission line.

B. The coupling voltage of the shielded layer and core of the signal cable

For the sensor signal cable, the disturbance voltage on the shielded layer produces interference voltage on the core through electric field coupling, which will have a serious impact on the useful signal after amplification. The electric field intensity model generated by the shielded layer voltage is shown in Figure 3. The shielded layer with line charge density τ is $2l$ in length, and the center point of the conductor is selected as the origin to establish a Cartesian coordinate system.

According to the Coulomb's law and the concept of potential, the potential φ generated by point q on the shielded layer to any point P is [26]

$$\varphi = -\int_q^P \vec{E} \bullet d\vec{l} = \frac{\tau}{4\pi\varepsilon_0} \ln\left[\frac{\sin\theta_1(1-\cos\theta_2)}{\sin\theta_2(1-\cos\theta_1)}\right], \tag{11}$$

$$\sin\theta_1 = \frac{r}{\sqrt{r^2+(z+l)^2}}, \tag{12}$$

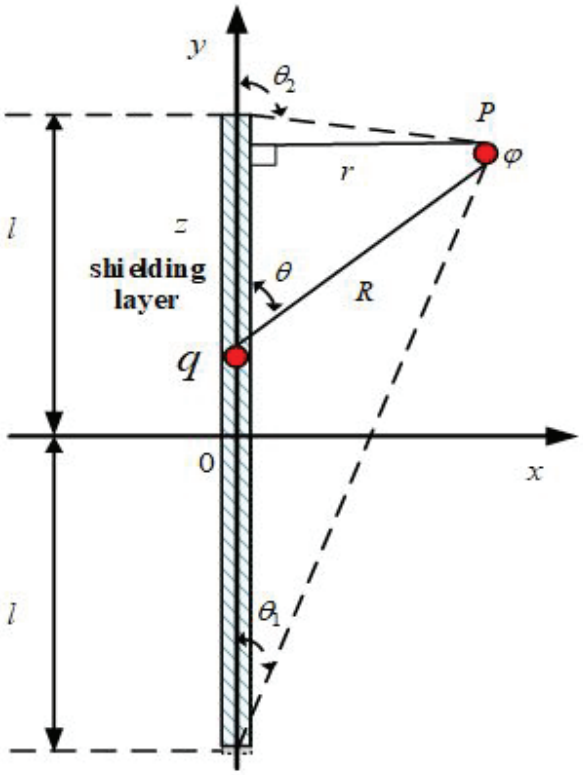

Fig. 3. A model of the electric field generated by the voltage of shielded layer.

$$\cos\theta_1 = \frac{z+l}{\sqrt{r^2+(z+l)^2}}, \tag{13}$$

$$\sin\theta_2 = \frac{r}{\sqrt{r^2+(z-l)^2}}, \tag{14}$$

$$\cos\theta_2 = \frac{z-l}{\sqrt{r^2+(z-l)^2}}, \tag{15}$$

where r and z are the horizontal and vertical distances of points P and q, the angle between the point q and the y-axis is θ, the angles between the two ends of the shielded layer and y-axis are, respectively, θ_1 and θ_2, and ε_0 is the vacuum permittivity. Replacing eqn (12)-(15) into eqn (11), it can be derived:

$$\varphi = \frac{\tau}{4\pi\varepsilon_0} \ln\left[\frac{\sqrt{r^2+(z-l)^2}-(z-l)}{\sqrt{r^2+(z+l)^2}-(z+l)}\right]. \tag{16}$$

In the actual situation, on the surface of the shielded layer, $z << l$ and $r << l$, eqn (16) can be derived:

$$\varphi = \frac{\tau}{2\pi\varepsilon_0} \ln\frac{2l}{r}. \tag{17}$$

According to the Gauss law, the electric field E can be expressed as

$$E = \frac{\tau}{2\pi\varepsilon_0}\frac{1}{r}. \tag{18}$$

Then the interference voltage U_d on the core of the signal cable can be obtained:

$$U_d = Ed, \tag{19}$$

where d is the distance between the shielded layer and the core of the signal cable.

III. ANALYSIS OF TEST AND SIMULATION RESULTS

A. A case study on the EMI of rail weighbridge

We have participated in an EMI case of a rail weighbridge. The physical layout of the rail weighbridge is shown in Figure 4. In the figure, the pressure sensor of the yellow rail weighbridge is connected with the outer chassis through a signal cable. The power line and signal cable behind the outer chassis are very close to each other. The internal structure of the outer chassis is shown in Figure 5. The collected data is transmitted to the amplifier through CH0, CH1, CH2, and CH3 channels.

It was found that even without cargo on the rail weighbridge, the voltage signal still displayed an interference voltage on the core of the cable, as shown in Figure 6. The exact value of the interference voltage derived from the exported table was 320 mV in maximum. The crosstalk voltage of the shielded layer was measured to be about 105 V, and the electromagnetic intensity beside the signal cable was measured to be about 400 V/m by using the electric field tester, as shown in Figure 7. There was a great interference voltage on the core of the signal cable, which affected the normal usage of the rail weighbridge.

B. Simulation and coupling capacitance extraction

In this case, the signal cable adopts RVVP double-core shielded cable, the insulating material is PVC (polyvinyl chloride), the shielding layer is copper braid, the cable diameter d is 7.6 mm, the diameter of the core is 3 mm, the power line adopts RVV three-core cable, the cable diameter is 7.9 mm, and the diameter of the core is 2.8 mm. The two cables are 1-mm apart in close proximity and 0.5 mm above the ground. The finite element model of the shielded cable and power line is shown in Figure 8.

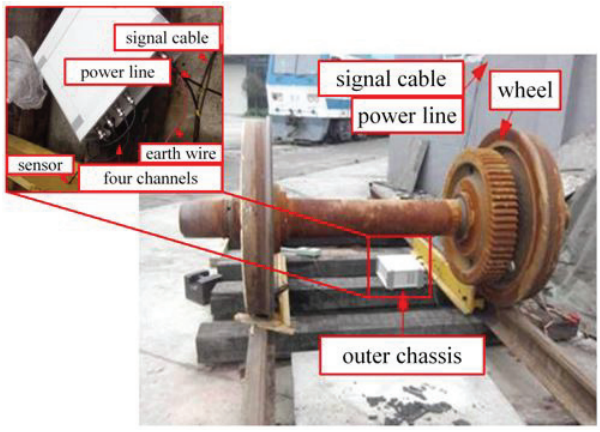

Fig. 4. Layout of the device for rail weighbridge.

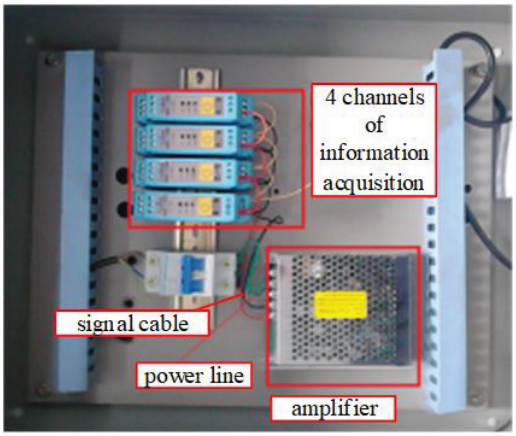

Fig. 5. Internal structure diagram of external chassis of rail weighbridge.

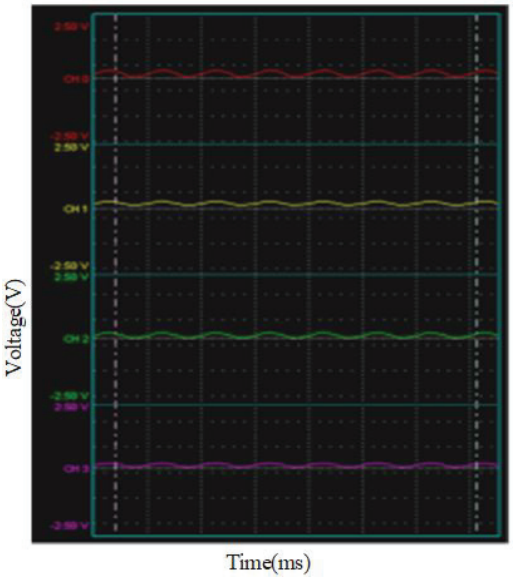

Fig. 6. Four channels of interference voltage signal displayed on the screen.

Through the analysis of finite element software ANSYS [27], the ground wire, fire wire, and zero wire in the power line constitute the multi-conductor transmission lines coupling system. The coupling capacitance between them can be extracted as 27.83, 27.62, and 6.29 pF, which represent C_{12}, C_{13}, and C_{14}, respectively, and the coupling capacitance C_{10} is 71.31 pF. Some actual parameters are obtained in the measurement: φ is 105 V,

Fig. 7. Testing picture of the electric field intensity.

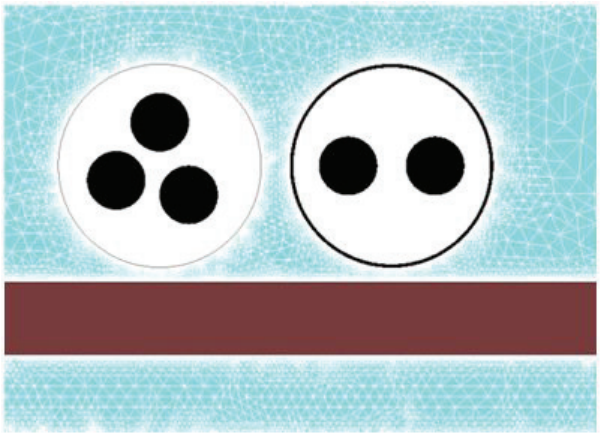

Fig. 8. Power line, signal cable, and ground modeled by finite element method.

l is 5 m, and r is 7.9 mm. According to formula (9) mentioned above, the shield-power cord crosstalk voltage U_m is 102.1 V. According to formulae (16) and (17), the electric field intensity of the shielded layer E is 413 V/m. Substituting the diameter d of the shielded cable as 7.6 mm into formula (19), the crosstalk voltage of the core of the signal cable which is represented by U_d is 316 mV.

The calculated values of the proposed method are basically consistent with the measured data, which verified the accuracy of the proposed method for interference prediction of railway weighbridge system.

IV. APPLICATION AND MEASURES FOR IMPROVEMENT

From the above, we know that the power line of the rail weighbridge system will generate interference voltage in the signal cable, resulting in a large error in the output signal voltage. The coupling capacitance of the shielded layer and the core, the length of the signal cable are fixed, they are not easy to be changed. Therefore, measures to reduce low-frequency crosstalk voltage of core can be mainly divided into increasing shielding protection measures and reducing ground potential [28, 29], as follows.

1) To improve the joint between the signal cable and the equipment, using the shielded cable with good shielded performance can reduce the coupling path of EMI.
2) To improve the grounding condition, increasing the contact area and depth of the grounding rod can reduce the soil resistivity.
3) When the surface potential gradient of the shielded cable is large, it is suitable to increase the number of grounding rods to reduce the surface potential difference.

After on-site inspection, there are some high-power equipment in the laboratory; so the induced voltage of the earth's surface is large, the depth grounding rod is not enough, and the soil is dry. Therefore, the methods of increasing the grounding depth from 0.1 to 0.6 m, increasing the moisture of soil, increasing the number of grounding rods from 1 to 4, and replacing the joints of the shielded cable are adopted.

After the improvement, the test shows that the interference voltage is basically reduced to 2 mV, and the electric field intensity near the power line is reduced to

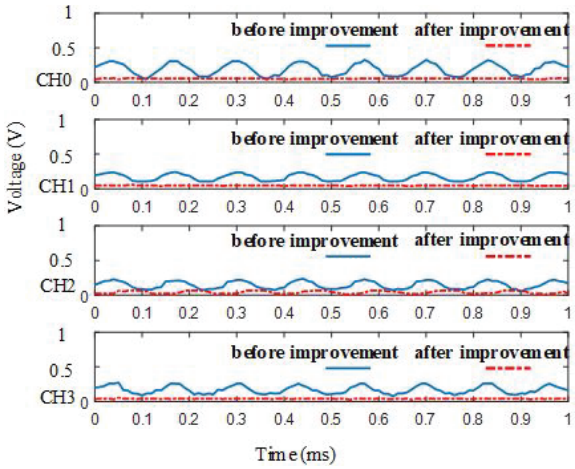

Fig. 9. Comparison of interference voltage of the signal before and after improvement.

about 5 V/m. The comparison of the signal interference voltage before and after the improvement in the display is shown in Figure 9, in which the solid blue line is the interference voltage before suppression, and the dashed red line is the interference voltage after suppression in the absence of pressure. By comparison, the maximum crosstalk voltage decreases from 320 to 2 mV, and the inhibition effect of the proposed method is significant.

V. CONCLUSION

This paper studies the EMI of the signal cable in railway weighbridge. The multi-conductor transmission lines model is established with the power line and signal cable, and the use of software for the simulation and calculation verifies the validity of the model. Then, as to an actual case of EMI, some applications such as replacing the shielded cable's joints and improving the grounding devices to restrain EMI had been proposed. Finally, the interference voltage on the signal cable had been eliminated. The inhibition effect of the proposed method is significant. This kind of EMI for shielded cable is very common in engineering, and the methods have good reference value for solving the similar problems.

ACKNOWLEDGMENT

This work was supported in part by the National Key R&D Program of China under Grant 2018YFC0809500.

REFERENCES

[1] Y. Zhou, H. Jiang, S. Li, A. An, and L. Bai, "Present situation of railway scale technology," *in Metering Technology of Track Scale .Beijing,China. Science Press*, pp. 2-5, 2017.

[2] Y. Cui, S. Yong, Z. Liu, and Y. Wang, "Research on shielding and grounding mode of railway signal cable," *Journal of the China Railway Society*, vol. 39, no. 17, pp. 77-82, Nov. 2017.

[3] B. Yi, Z. Wang. "Parameters calculation of shield cable and crosstalk between shielded layer and core," *High Voltage Engineering*, vol. 04, pp. 804-808, Apr. 2008.

[4] Z. Han, B. Li, and Z. Guo. "Discussion on earthing anti-jamming technology," *Measurement and Control Technology*, vol. 23, no. 12, pp. 74-77, Dec. 2007.

[5] F. Lin, Z. Yao, and X. Dai, "Numerical calculation of common-model interference coupled in a shielded cable," *High Voltage Engineering*, vol. 23, no. 4, pp. 9-11, Dec. 1997.

[6] C. Taylor, R. Satterwhite, and C. Harrison, 'The response of a terminated two-wire transmission line excited by a nonuniform electromagnetic field," *IEEE Transactions on Antennas & Propagation*, vol. 13, no. 6, pp. 987-989, Dec. 1965.

[7] V. Teppati, M. Goano, A. Ferrero, "Conformal-mapping design tools for coaxial couplers with complex cross section," *IEEE Transactions on Microwave Theory and Techniques*, vol. 50, no. 10, pp. 2339-2345, Nov. 2002.

[8] P. Xiao, W. Ran, and P. Du, "An analytic method of determining a critical cable spacing for acceptable crosstalk," *Applied Computational Electromagnetics Society (ACES) Journal,* vol. 35, no. 2, pp. 237-277, Feb. 2020.

[9] L. Li, W. Li, X. Wang, and W.-B. Li, "Crosstalk analysis between two parallel transmission lines," *Chinese Journal of Radio Science,* vol. 16, no. 2, pp. 271-274, Jun. 2002.

[10] Q. Yu, W. Liu, K. Yang, X. Ma, and T. Wang "Uncertainty quantification of the crosstalk in multiconductor transmission lines via degree adaptive stochastic response surface method," *Applied Computational Electromagnetics Society (ACES) Journal,* vol. 36, no. 2, pp. 174-183, Feb. 2021.

[11] A. Djordhevic and T. K. Sarkar, "Analysis of time response of lossy multiconductor transmission line networks," *IEEE Transactions on MTT*, vol. 35, no. 10, pp. 898-908, Nov. 1987.

[12] M. Z. M. Hamdalla, A. N. Caruso, and A. M. Hassan, "Predicting electromagnetic interference to a terminated wire using characteristic mode analysis," *Applied Computational Electromagnetics Society (ACES) Journal*, vol. 35, no. 11, pp. 1318-1319, Nov. 2020.

[13] Z. He, Z. Li, P. Liang, "ANSYS calculation method of temperature and current-carrying capacity for transmission lines," *Zhejiang Electric Power*, vol. 8, pp. 1-5, 2010.

[14] C. Zhu, W. Yan, S. Liu, and L. Geng, "Analysis on crosstalk for coplanar irregular-placed cables based on cascading method and cubic spline interpolation algorithm," *Applied Computational Electromagnetics Society (ACES) Journal,* vol. 35, no. 5, pp. 572-579, May 2015.

[15] G. Vijayaraghavan, M. Brown, and M. Barnes, "Equipment grounding," *in Practical grounding, bonding, shielding and surge protection. 3th ed. Butterworth-Heinemann*, pp. 24-37, 2004.

[16] C. R. Paul, "Solution of the transmission-line equation for three-conductor lines in homogeneous media," IEEE Trans. Electromagnetic compatibility. vol. 20, no. 1, pp. 216-222, Mar. 1978.

[17] J. Bai, G. Zhang, L. Wang, A. Duffy, C. Liu, and T. Shao, "Comparison of calculation methods of braided shield cable transfer impedance using FSV method," *Applied Computational Electromagnetics Society (ACES) Journal,* vol. 30, no. 2, pp. 140-147, Feb. 2015.

[18] C. R. Paul, Analysis of Multiconductor Transmission Lines. New York, USA: Wiley, 1994.

[19] C. Feng and X. Ma, An introduction to engineering electromagnetic fields, Higher Education Press, pp. 46-51, 2018.
[20] R. Morrison, "Electromagnetic compatibility," in grounding and shielding techniques. 4th ed. New York, Wiley, 1998.
[21] R. Xiong, Q. Yin, W. Yang, Y. Liu, and J. Li, "Improvement of shaped conductive backfill material for grounding systems," *Applied Computational Electromagnetics Society (ACES) Journal,* vol. 36, no. 4, pp. 442-449, Apr. 2021.
[22] J. Ma and F. P. Dawalibi, "Analysis of grounding systems in soils with finite volumes of different resistivities," *IEEE Power Engineering Review,* vol. 17, no. 2, pp. 596-601, Apr. 2002.
[23] *Code for Electrical Design of Civil Buildings*, JGJ16-2008, Ministry of Construction of the People's Republic of China, 2008.
[24] H. Lu, Z. Yu, and W. Li, *Electronic Information Specialty,* Xian, China, Xidian University Press, 2012.
[25] S. W. Blume, "Critical telecommunications circuits in HV environments," in *High Voltage Protection for Telecommunications,* Wiley-IEEE Press, pp. 121-142, 2011.
[26] D. K. Chen, *Field and Wave Electromagnetics*, Pearson education, pp. 49-72, 2013.
[27] Q. Q. Liu, Y. Zhao, C. Huang, W. Yan, and J. M. Zhou. "A new method for stranded cable crosstalk estimation based on BAS-BP neural network algorithm combined with FDTD method," *Applied Computational Electromagnetics Society (ACES) Journal,* vol. 35, no. 2, pp. 135-144, Feb. 2020.
[28] W. Huang, W. Liang, and X. Wen, "Method of reducing the grounding impedance of yangjiang nuclear power plant," *High Voltage Engineering*, vol. 36, no. 2, pp. 365-370, Feb. 2010.
[29] Z. Lu, S. Chang, and X. Wen, "Numerical analysis of grounding impedance for grounding grids with multi points short circuit current into the ground," *High Voltage Engineering,* vol. 30, no. 10, pp. 15-16, Oct. 2004.

Yang Yang was born in Shanxi, China, on April 19, 1989. She received the master's degree in control theory and control engineering from Northwestern Polytechnical University in 2014. She is currently working toward the Ph.D. degree in electrical engineering with Southwest Jiaotong University, Chengdu, China. At the same time, she is also a Lecturer with the Sichuan College of Architectural Technology. Her research interests include electromagnetic environment test and evaluation, electromagnetic compatibility analysis, and design in the field of rail transit.

Feng Zhu received the Ph.D. degree in railway traction electrification and automation from the Southwest Jiaotong University, Sichuan, China, in 1997. He is currently a Full Professor with the School of Electrical Engineering, Southwest Jiaotong University. His current research interests include locomotive over-voltage and grounding technology, electromagnetic theory and numerical analysis of electromagnetic field, and electromagnetic compatibility analysis and design.

Nan Lu was born in Anhui Province, China, on June 3, 1990. He received the master's degree in electrical engineering from the Anhui University of Science & Technology, Anhui, China, in 2016, and is currently working toward the Ph.D. degree in electrical engineering with Southwest Jiaotong University, Chengdu, China. His research interests include electromagnetic compatibility, electromagnetic environment test and evaluation, and transmission-line analysis.

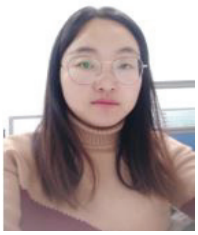

Yingchun Xiao was born in Gansu Province, China, in 1990. She received the B.S. degree in electronic information science and technology from the Lanzhou University of Technology, Lanzhou, China, in 2012, and is currently working toward the Ph.D. degree in electrical engineering with Southwest Jiaotong University, Chengdu, China. At the same time, she is a Lecturer with Lanzhou City College. Her research interests include electromagnetic environment test and evaluation, electromagnetic compatibility analysis and design, and identification and location of electromagnetic interference sources.

Solid Characterization Utilizing Planar Microwave Resonator Sensor

Ahmed Jamal Abdullah Al-Gburi[1], Zahriladha Zakaria[1,*], Imran Mohd Ibrahim[1], Rahmi S. Aswir[1], and Syah Alam[1,2]

[1]Fakulti Kejuruteraan Elektronik dan Kejuruteraan Komputer, Universiti Teknikal Malaysia Melaka, Hang Tuah Jaya, 76100 Durian Tunggal, Melaka, Malaysia
*zahriladha@utem.edu.my

[2]Department of Electrical Engineering, Universitas Trisakti

Abstract – This paper outlines the design and the implementation of a planar microwave resonator sensor for sensing application using the perturbation concept in which the dielectric characteristics of the resonator influence the quality factor (QF) and the resonance frequency. The designed sensor is fabricated using Roger 5880, and it is operating at 2.27 GHz in ranges of 1-3 GHz for testing solid materials. In addition, applying a specific experimental methodology, practical material is used as material samples such as those in Roger 5880, Roger 4350, and FR4. To investigate the microwave resonator sensor performance, an equivalent circuit model (ECM) is introduced. The proposed sensor has achieved a narrow bandwidth and high QF value of 240 at an operating frequency of 2.27GHz. Besides, the sensitivity and accuracy of the sensor is more than 80%, which makes this sensor an excellent solution to characterize the material, especially in discovering the material characteristics and quality.

Index Terms – Planar microwave resonator, solid sample, high *Q*-factor.

I. INTRODUCTION

A microwave sensor is possibly the most widely known sensor for the food sector, quality control, biomedical, and industrial use for material characterization detections [1–3]. Controls on the health and safety of fodder products are necessary in order to achieve the health and well-being of consumers whose presence can affect certain ingredients and end up causing specific diseases, such as allergic reactions, contaminating, and cancer. For such cases, the quality and safety of the product (e.g., drinks and cooking oils) must be ensured before even being marketed to the customers [3]. There have been two main types of resonant microwave methods: resonant and non-resonant methods for characterizing materials [4].

Microwave resonant technique is one of the potential methods which is used for highly accurate measurement of dielectric material characterization at a single or discrete frequency. According to the traditional method, material characterization was accomplished using high-sensitivity and precision waveguide, dielectric, and coaxial resonators [5]. However, the conventional resonator sensor is extremely large, costly to make, and requires a significant amount of material to be detected [material under test (MUT)] [5–8]. Besides that, this technique results in low sensitivity and *Q*-factor values, limiting the material's characterization range.

An objective of this report was to identify the shortcomings of the prior one by developing a new microwave sensor that is compatible, low in cost, small, easy to handle, and has a higher *Q*-factor [9–12]. A complementary split-ring resonator (SRR) was proposed to accurately measure the material's complex permittivity. The stated resonator operated at frequencies from 1.7 to 2.7 GHz [9]. Another study was conducted by utilizing a metamaterial resonator sensor for sensing applications. The proposed sensor was utilized at two main frequencies, 3.2 and 4.18 GHz, with *Q*-factors of 642 and 251, respectively [11]. A novel electromagnetic sensor operated at 1.4 GHz was proposed for real-time sensing liquid characterization [12].

In this study, a planar microwave resonator sensor is proposed to measure the corresponding permittivity for solid planar dielectric materials. The proposed method uses the sample under test as a substrate of a microstrip line with an impediment that has to be installed at various positions over the microstrip line for measurement determination. An equivalent circuit model (ECM) is proposed to confirm the design structure. Besides, this study looked into the drawbacks of the previous research studies through a new microwave sensor in terms of compatibility: low cost, simple structure, easy to fabricate, high *Q*-factor, and high precision.

II. SENSOR DESIGN AND CONFIGURATION

A. Design process

The proposed resonator sensor is performed at 2.27 GHz for frequencies of 1-3 GHz in order to explore

Submitted On: October 31, 2021
Accepted On: March 15, 2022
https://doi.org/10.13052/2022.ACES.J.370211

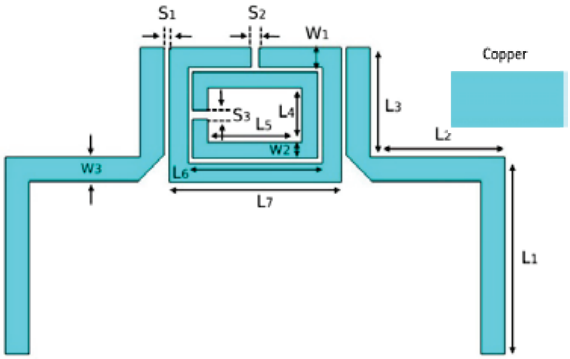

Fig. 1. The geometry of the proposed sensor.

Table 1: Proposed sensor parameters

S	V (in mm)	S	V (in mm)	S	V (in mm)
L	40	W	50	L_6	11.4
L_1	16.25	S_1	0.3	L_7	14.59
L_2	10.42	S_2	0.4	W_3	1.7
L_3	10.5	S_3	0.5	L_4	4.5
L_5	8	W_1	1.6	W_2	1.5

the type of materials employing the solid technique. The formed radiator is designed by utilizing a CST microwave studio. The total dimensions of the modeled radiator are about 50 mm × 40 mm, printed on Roger 5880 dielectric substrate comes with a thickness of 0.79 and 2.2 of dielectric constant and a loss tangent of 0.0009. The overall sensor geometry is duplicated in Figure 1 and recorded in Table 1.

It is worth mentioning that the need for an inner ring to the existing resonator is to allow more current to pass through the ring resonator, which leads to high e-field concentrations.

S = symbols and V = values.

The mathematical analysis of the proposed sensor through compatible folding arm loading the length and breadth of the patch, the length of the resonator is the half of the wavelength as presented in the following equation [12]:

$$L = \frac{c}{2\pi\sqrt{\varepsilon_{\text{eff}}}} \times \frac{1}{f_0}. \tag{1}$$

Based on the sensor length, the resonance frequency (f_0) can be determined using the following equation [13]:

$$f_0 = \frac{c}{2\,\pi r\sqrt{\varepsilon_{\text{eff}}}}, \tag{2}$$

where c is the speed of light ($8.98755179 \times 1016\ \text{m}^2/\text{s}^2$), L denotes the resonator length, and ε_{eff} is the effective dielectric constant of the stated resonator.

The width of microstrip patch antenna resonator W can be calculated using the following equation:

$$W = \frac{c}{2f_0\sqrt{\frac{\varepsilon_{r+1}}{2}}}. \tag{3}$$

The effective permittivity of the patch ε_{eff} can be calculated as proposed in eqn (4), for the fringing field and the wave propagation in the line [14].

$$\varepsilon_{\text{eff}} = \frac{\varepsilon r+1}{2} + \frac{\varepsilon r-1}{2}\left[\frac{1}{1+12\frac{h}{w}}\right] \tag{4}$$

where h is the height of the substrate and w is the width of the patch.

The Q-factor is acknowledged in this study as a quality factor embedded in a resonant circuit, which is involved as an infinite value together to reflect the unwanted energy with a specific resonant. It designates spectrum in relevant incidence at the center of frequency [15]

$$Q = \frac{2f_0}{\triangle f} \tag{5}$$

where Q represents the Q-factor, f denotes the center of frequency, and the resonant frequency is characterized as f_0.

B. Equivalent circuit model and analysis

Before analyzing the ECM configuration, it is very important to discover the sensing region of the proposed microwave sensor, which is based on the electric field distributions. The more electric field concentration is found to be near the square gap (red color), as shown in Figure 2(b). The 3D view of the proposed resonator is duplicated in Figure 2(a).

The sensitive area with the highest electric field concentration was located around the ring gap, and the excellent sensing region was only 378 nL. Setting the channel very close to the resonator sensor guarantees that the sample interacts with field lines concentrated by the resonator. An advance design software (ADS) is used in this stage to investigate the influence of material characteristics on the resonator sensor. The overall microwave sensor was designed with an effective length of 40 mm to operate at ranges from 1 up to 3 GHz.

The operational mechanism of the proposed ECM is mainly divided into two lump components: inductance (L) and capacitance (C) to achieve an LC circuit as duplicated in Figure 2(c). The ECM configuration is formed from the metallic co-planar with two square radiated rings. The metallic co-planar is equivalent inductance, as presented in [16], the ring resonators are structured from resonant inductance L_t, and the gaps between them are provided with a resonant capacitance (C_t) as suggested in [17] and calculated by approximating it between two identical co-planar strips with unlimited substrate thickness, as shown in eqn(6) and (7) [18]:

$$C_t = \varepsilon_0\frac{k'(m)}{k(m)}w + \varepsilon_0\varepsilon_{\text{substrate}}\frac{k'(m)}{k(m)}w + \varepsilon_0\frac{h_t}{s}w \tag{6}$$

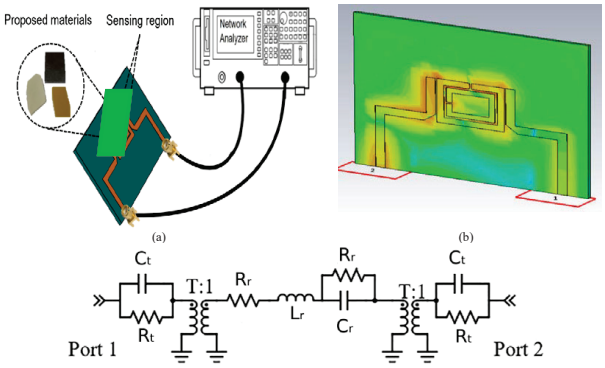

Fig. 2. Microwave sensor representation. (a) 3D view. (b) E-field. (c) ECM of all microwave sensors.

Table 2: Optimized values of the proposed ECM resonator

Circuit Parameters	Values
C_t	51 pF
R_t	100 k0
T	0.31
R_{r0}	0.9 M.
L_r	76 nH
C_{r0}	50 fF
R_r	5.4 O
$a.$	10

where w denotes the width of the resonator feed line, $k(m)$ is an elliptic integral, $k(m)$ is its complement, h_t is the copper thickness of the resonator feed line, and s is the spaces between the two inner and outer rings. The operational factor Z can be derived as

$$Z = \sqrt{\frac{s}{2*w+2*s}}. \tag{7}$$

Table 2 outlines the implemented ECM values of the proposed resonator. When samples are placed on top of the patch sensor's copper track, which has a high electric field concentration, the interaction of MUT and the structured patch electrical field results in changes in a resonant frequency which leads to affecting the functional parameters C_t and R_t, respectively, by presenting permittivity and loss variation in the sensor's profile. Permittivity variation was designed and simulated by sweeping the value of C_t, and the loss effect was simulated by evaluating simultaneous linear interpretation on R_t based on the following equation:

$$R_t = R_{r_0} + \alpha \frac{C_t - C_{t_0}}{C_{r_0}}, \tag{8}$$

where α is the empirical constant, C_{t0} denotes the initial value of matching gap capacitance, and R_{t0} describes the initial equivalent loss of the bare resonator's gap area.

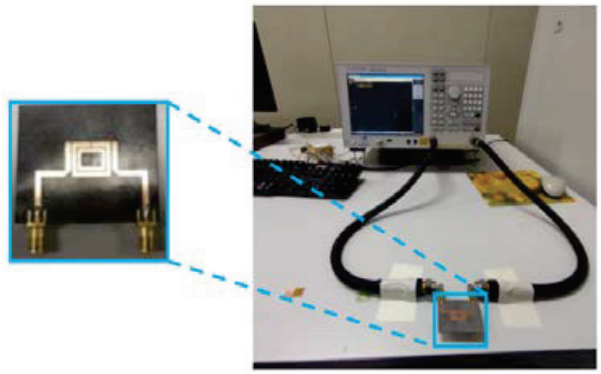

Fig. 3. Measurement setup using VNA.

C. Simulation process

The modeled sensor is designed by utilizing CST software. This sensor's classification is proposed based on the theoretical and mathematical analysis obtained from the justification parameters. Therefore, the tuning approach was proposed to deliver a more reliable insertion loss plot. Besides, the pair waveguide-ports are introduced to characterize the transverse electric and magnetic and their effect on the S-parameter.

The simulation process is carried out based on the MUT material characterization. The MUT characterization mainly depends on the red color region of the resonator electric-field as presented in Figure 2(b). The material units will be installed on the resonator patch, which leads to main electric field radiations. The sensitive area with the highest electric field concentration was located around the ring gaps and more from the left ring side of the resonator. Besides, the integration of material samples on the top of resonator sensors leads to a shifting in the resonant frequency.

D. Fabrication and measuring resonator

After understanding and upgrading the mathematical and the simulation process, the scheduled resonator is fabricated and measured in this study. The Roger 5880 is used for the fabrication process. The proposed microwave sensor is experimentally assessed by employing a VNA for frequencies of 1-3 GHz. The network analyzer verifies the sensor by connecting the two waveguide ports with 50 Ω. The MUT samples are installed at the radiated electric field of the radiated resonator patch.

The dimensions of the MUT are 10 mm × 12 mm for the types of materials such as FR4, Roger 5880, and Roger 4350. The fabrication and measurement process was set up by employing a VNA device, as shown in Figure 3.

The comparison between the simulation and measurement results of the modeled resonator is recorded in Table 3.

Table 3: Comparison simulation and measurement results

MUT	Simulation results						Measurement results					
	Q-factor	S21	BW	f (GHz)	Δf	Error%	Q-factor	S21	BW	f (GHz)	Δf	Error%
Free space	110.05	−1.796	0.04129	2.272	0	0	240	−10.9	0.02	2.4	0	0
Roger 5880	110.14	−1.862	0.03915	2.156	0.166	5.1056 (94.894)	140	−7.17	0.0329	2.31	0.09	3.75 (96.25)
Roger 4350	103.98	−2.2356	0.04043	2.102	0.17	7.4824 (92.517)	64.92	−8.25	0.06875	2.21	0.19	7.916 (92.084)
FR4	72.66	−4.9350	0.05373	1.952	0.32	14.0845 (85.9155)	168.8	−14.07	0.025	2.11	0.29	12.083 (87.917)

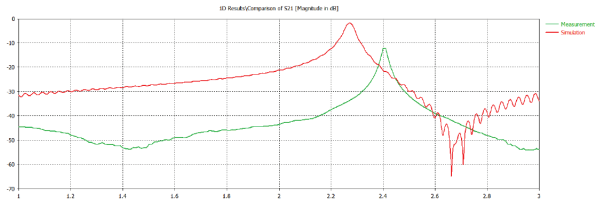

Fig. 4. Predicted and measured S21 results.

III. RESULT AND ANALYSIS

A. Resonant frequency

Figure 4 presents the simulated and measured transmission coefficient (S21) of the finalized sensor. From Figure 4, we can observe that the shifting in the resonant frequency defined the efficiency of the microwave sensor. During simulation, the resonant wavelength of the stated sensor is shifted from 2.272 for simulation to 2.4057 GHz for the measured one, with a slight variation of about 0.1337 GHz. The results of the resonant frequency regarding simulation results are appropriately matched. However, there are slightly shifted resonances compared to the measured results. This shifting because of a lack of feed lines and SMA connectors, and even the fabrication tolerances, can influence simulation accuracy.

B. Q-factor analysis

The Q-factor magnitude was calculated based on eqn (5). The proposed sensor was first operated at 2.272 GHz. Referring to eqn (5), the Q-factor is equal to 110 for simulation results; moreover, at the same frequency of 2.272 GHz, the measured Q-factor is about 240. It can be noticed that the measured Q-factor is higher than the simulated one.

The simulated and measured results slightly differ due to inaccuracies when fabricating using manual cutting tools, besides the inhomogeneous dielectric constant of the substrate [19]. The differences between simulations and measurements are also affected by the SMA connector losses in practice, as an ideal connector is modeled in simulations. Besides that, the amount of power fed into the antenna in measurements is also affected by the way the epoxy is applied to galvanically connect the SMA connector and fabric [20].

Furthermore, the Q-factor rises as the change in the resonance frequency reduces to the lowest frequency. Hence, a narrow bandwidth is expected, which points to improving and increasing the Q-factor value at its maximum magnitude.

Referring to the permittivity value of the experimented materials, which are FR4, Roger 4350, and Roger 5880, which have various thickness values of 1.6, 0.78, and 0.5mm. The simulated MUT materials are resonating at frequencies of 1.952, 2.1, and 2.156 GHz, respectively, meanwhile, for the measured part. The resonant frequencies are shifted due to the mutual coupling effect between the two co-planars on the resonator patch. The shifted frequencies were 2.11 GHz for FR4, 2.21, and 2.31 for Roger 5880 GHz at 2.4 GHz, sequentially. Figure 5 shows the simulated and measured transmission coefficient (S21) at different resonant frequencies.

C. Dielectric and loss tangent analysis

The shifted frequencies are strongly dependent on the impedance of the signal within the highest E-field concentrations and the MUT's permittivity. The relationship between resonance turned resonant frequency and the conventional permittivity can be categorized by the second polynomial method utilizing experimental outcomes as displayed in formula (9):

$$\varepsilon_r = -10.89x^2 + 37.288x - 25.779 \qquad (9)$$

where $\varepsilon_{\mathbf{r}}$ is the MUT permittivity.

Applying data shifts of resonance frequencies as shown in Figure 6, the curve fitting (CF) method is modeled based on the second-order polynomial role. The technical procedure is proposed for estimating the actual permittivity magnitude.

The outcomes of the estimated permittivity are recorded in Table 4. From Table 4, we can notice that

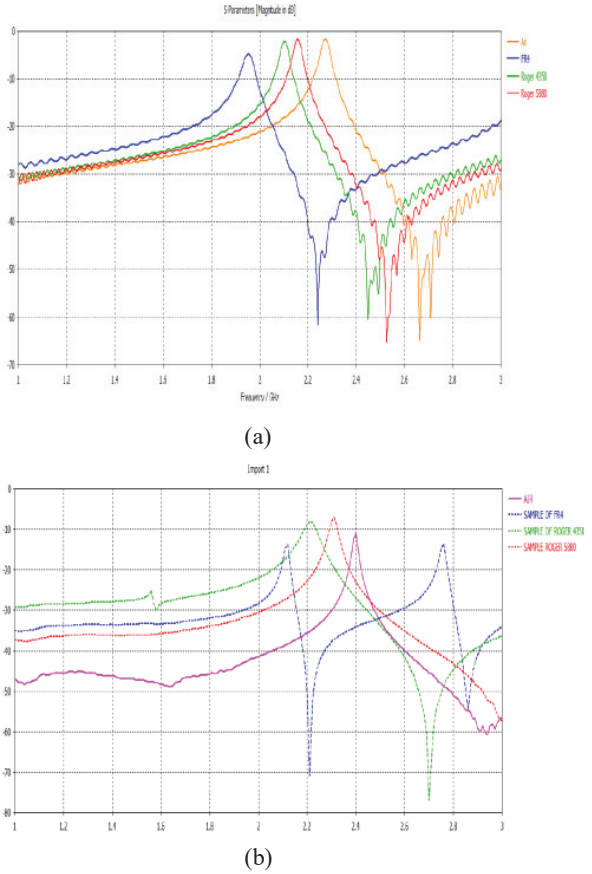

(a)

(b)

Fig. 5. Comparison of S21 MUT results for (a) simulation and (b) measurement.

the error in permittivity related to the second polynomial comparison is between 0.34% and 1.40%, respectively. The permittivity magnitude of the representation materials was an increase when the error got decreased.

The loss tangent is a frequency-dependent loss that produces a loss that is proportional to the frequency. When the tangent loss value is low, it shows a greater effect on the peak amplitude S21. So, when the tangent loss value is the smallest, the S21 parameter becomes smaller. The third-order polynomial expression established the link between loss tangent and resonant frequency change. The difference between the reference

Table 4: Analyzing permittivity values under MUT

MUT	Reference tan δ	Measured tan δ	% Error
Air	0	0	0
Roger 5880	0.0009	0.000897	0.33
Roger 4350	0.0037	0.003694	0.162
Fr4	0.025	0.024991	0.036

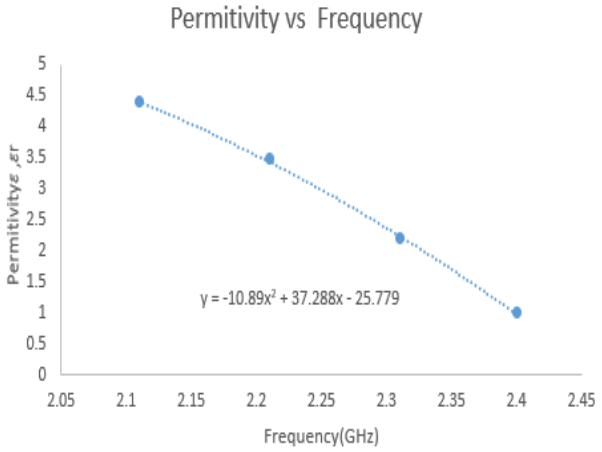

Fig. 6. Polynomial CP permittivity.

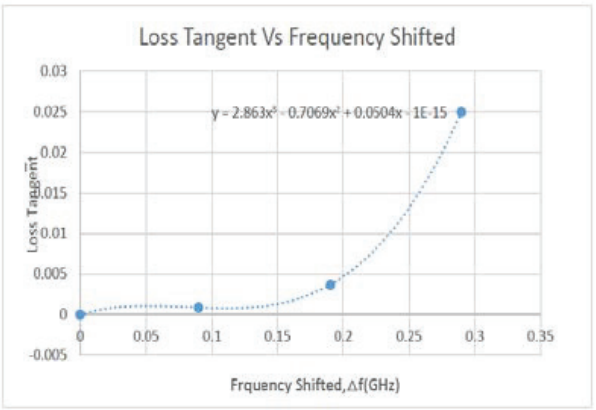

Fig. 7. Third-order polynomial curve fitting of loss tangent.

and measurement loss tangent was analyzed based on the percentage error trend line. From the third-order polynomial expression, the measurement tangent loss value can be obtained. The third-order polynomial expression is illustrated in Figure 7.

Figure 7 is structured from the particular input data collection regarding the model tangent loss to generate expression based on the CF method. It can be observed that the combination of $tan\delta$ and Δf is not consistent, and the result is described by the eqn (8). However, the relationship between both parameters can be described as a polynomial representation of third order to create an efficient mathematical equation as follows:

$$\text{Tan } \delta = -0.0278|\Delta f^3| + 0.0777|\Delta f^2| - 0.0248|\Delta f| - 7^{-15}. \quad (10)$$

IV. CONCLUSION

This paper presented a planar microwave resonator sensor which proves that it can be used to detect the

properties of solid material. Thus, high accuracy sensor works on 2.27 GHz. The sensor produces a high *Q*-factor value which is 240 compared to previous research. A mathematical model is developed for the determination of the dielectric constant and loss tangent of MUT. The polynomial CF was also applied to determine the dielectric properties of the material. The percentage error for permittivity of measurement and tangent loss is below 5%. The accuracy for this sensor is more than 85% which makes the sensor suitable to be applied in industrial.

V. FUTURE WORK

While the research is thriving, a few ideas for potential enhancements are presented as follows. Principally, to improve the sensor's sensitivity, the electric field should be highly concentrated. Besides, the area around the resonator will reflect all over the energies. Then, checking the soldering connectivity must be considered to block the loss in radiation behavior for both input and output terminals.

ACKNOWLEDGMENT

This work was supported by Universiti Teknikal Malaysia Melaka (UTeM).

REFERENCES

[1] S. N. Jha, "Measurement techniques and application of electrical properties for nondestructive quality evaluation of f oods-a review," *J. Food Sci. Technol*., vol. 48, no. 4, pp. 387–411, 2011.

[2] N. A. Rahman, Z. Zakaria, R. Abd Rahim, M. Alice Meor Said, A. Azuan Mohd Bahar, R. A. Alahnomi, and A. Alhegazi, "High quality factor using nested complementary split ring resonator for dielectric properties of solids sample," *Applied Computational Electromagnetics Society (ACES) Journal*, vol. 35, no. 10, pp. 1222–1227, 2020.

[3] J. Tang, "Unlocking potentials of microwaves for food safety and quality," *J. Food Sci*., vol. 80, no. 8, pp. E1776–E1793, 2015.

[4] P. M. Narayanan, "Microstrip transmission line method for broadband permittivity measurement of dielectric substrates," *IEEE Trans. Microw. Theory Tech*., vol. 62, no. 11, pp. 2784–2790, 2014.

[5] N. Abd Rahman, Z. Zakaria, R. Abd Rahim, R. A. Alahnomi, A. J. A. Al-Gburi, A. Alhegazi, W. N. Abd Rashid, and A. A. M. Bahar, "Liquid permittivity sensing using teeth gear-circular substrate integrated waveguide," IEEE Sensors Journal, pp. 1–8, 2022, doi: 10.1109/JSEN.2022.3166561.

[6] K. Shibata and M. Kobayashi, "Measurement of dielectric properties for thick ceramic film on an substrate at microwave frequencies by applying the mode-matchig method," 2016 *IEEE MTT-S Int. Conf. Numer. Electromagn. Multiphysics Model. Optim. NEMO* 2016, pp. 1–4, 2016.

[7] A. A. Mohd Bahar, Z. Zakaria, M. K. Md. Arshad, A. A. M. Isa, Y. Dasril, and R. A. Alahnomi, "Real time microwave biochemical sensor based on circular SIW approach for aqueous dielectric detection," *Sci. Rep*., vol. 9, no. 1, pp. 1–12, 2019.

[8] A. Azuan, M. Bahar, Z. Zakaria, S. Rosmaniza, A. Rashid, and A. A. Isa, "Microstrip planar resonator sensors for accurate dielectric measurement of microfluidic solutions," *in 3rd International Conference on Electronic Design (ICED)*, pp. 416–421, 2016.

[9] M. A. H. Ansari, A. K. Jha, and M. J. Akhtar, "Design and application of the CSRR-based planar sensor for noninvasive measurement of complex permittivity," *IEEE Sens. J*., vol. 15, no. 12, pp. 7181–7189, 2015.

[10] R. A. Alahnomi, Z. Zakaria, E. Ruslan, and A. A. M. Isa, "Optimisation analysis of microwave ring resonator for bio-sensing application," *Int. J. Appl. Eng. Res*., vol. 10, no. 7, 2015.

[11] S. R. Harry, Z. Zakaria, M. A. M. Said, R. Alahnomi, and M. Harris Misran, "Design of dual band meta-material resonator sensor for material characterization," *Applied Computational Electromagnetics Society (ACES) Journal*, vol. 36, no. 4, pp. 473–478, 2021.

[12] M. H. Zarifi, S. Farsinezhad, K. Shankar, and M. Daneshmand, "Liquid sensing using active feedback assisted planar microwave resonator," *IEEE Microwave and Wireless Components Letters*. 2015 Jul 14;25(9):621-3.

[13] M. S. Boybay and O. M. Ramahi, "Material characterisation using complementary split-ring resonators," *IEEE Trans. Instrum. Meas.*, vol. 61, no. 11, pp. 3039–3046, 2012, doi: 10.1109/TIM.2012.2203450.

[14] K. Chang and L.-H. Hsieh, "Microwave ring circuits and related structures," *Microw. Ring Circuits Relat. Struct*., 2005, doi: 10.1002/0471721298.

[15] D. K. Ghodgaonkar, V. V. Varadan, and V. K. Varadan, "Free-space measurement of complex permittivity and complex permeability of magnetic materials at microwave frequencies," *IEEE Trans. Instrum. Meas*., vol. 39, no. 2, pp. 387–394, 1990.

[16] S. Mohammadi, R. Narang, M. Mohammadi Ashani, H. Sadabadi, A. Sanati-Nezhad, and M. H. Zarifi, "Real-time monitoring of Escherichia coli concentration with planar microwave resonator sensor," *Microw. Opt. Technol. Lett*., vol. 61, no. 11, pp. 2534–2539, 2019.

[17] M. A. H. Ansari, A. K. Jha, and M. J. Akhtar, "Design and application of the CSRR-based planar sensor for noninvasive measurement of complex permittivity," *IEEE Sens. J*., vol. 15, no. 12, pp. 7181–7189, 2015.

[18] Cheng-Cheh Y, Chang K. Novel compact elliptic-function narrow-band bandpass filters using microstrip open-loop resona- tors with coupled and crossing lines. *IEEE Trans Microw Theory Tech*. 1998;46(7):952-958.

[19] A. Mehdi, K. Abdennacer and S. Mounir, "Analysis of the discrepancies fabricating error of microstrip antenna," *International Journal of Research and Reviews in Applied Sciences*, vol. 9, no. 3, pp. 405–412, 2011.

[20] K. Y. Yazdandoost and K. Sato, "Fabrication error in resonant frequency of microstrip antenna," *in Proc. Int. Conf. on Micromechatronics and Human Science, Nagoya, Japan*, pp. 41–44, 2001.

Ahmed Jamal Abdullah Al-Gburi is currently a Postdoctoral fellowship at UniversitiTeknikal Malaysia Melaka (UTeM).He received aPhD in Electronics Engineering from UTeM university within Graduate on Time (GoT).He has received the Best Paper Award from the IEEE Community and won several Gold, Silver, and Bronze medals in international and local competitions.

Zahriladha Zakaria is currently a Professor at UniversitiTeknikal Malaysia Melaka. His research areas include microwave filters, resonators, amplifiers and antennas, data communication and radio-wave propagation in wireless communication systems.

Imran Mohd Ibrahim a Senior Lecturer at UniversitiTeknikal Malaysia Melaka. He has published more than 80 journals articles and conference papers. His research interests are antennas and propagations.

Rahmi Silvia Binti Aswir received her Bachelor of Electronic Engineering with Honors from UniversitiTeknikal Malaysia Melaka. Her research areas include Sensors design.

SyahAlam was born in Jakarta, Indonesia. He received Bachelor Education of Engineering (S.Pd) degree in electrical engineering from Universitas Pendidikan Indonesia (UPI) and M.Eng (M.T) degree in telecommunication engineering from UniversitasTrisakti in 2010 and 2012, respectively.In 2021, he is pursuing his PhD at UniversitiTeknikal Malaysia Melaka (UTeM) in the field of RF and Microwave.

A Novel Technique for Dynamic Analysis of an Electromagnetic Rail Launcher using FEM Coupled with Simplorer

J. Lydia[1], R. Karpagam[1], and R. Murugan[2]

[1]Department of Electrical and Electronics Engineering, Easwari Engineering College,
Chennai 600089, India
lydia.jeec@gmail.com, karpagamraj2013@gmail.com

[2]Department of Electrical and Electronics Engineering,
St. Peter's College of Engineering and Technology, Chennai 600054, India
ramumurugan_r@rediffmail.com

***Abstract* –** The performance of a rail gun depends on the current density distribution over the rail and armature as it determines the force that accelerates the projectile of the rail gun. A finite element method (FEM) coupled with Simplorer was developed to model and study the performance of the rail gun. The rail gun was modeled using an ANSYS eddy current field solver to determine the current density distribution and equivalent rail gun circuit for the given rail gun geometry. The armature velocity was then calculated using Simplorer by coupling the obtained equivalent rail gun circuit and exciting the rails using a capacitor-based pulsed power supply (PPS) system. The FEM coupled with Simplorer method was verified by numerical calculations for the rectangular rails and also with other researchers' value, and that showed a good agreement between the results. Further, the current density distribution over rails and armature and velocity of the armature was calculated for different rail cross sections such as circular concave, circular convex, rectangular concave, rectangular convex, T-shaped concave, and T-shaped convex with a C-shaped armature. It was observed that the circular convex rail gun with C-shaped armature showed minimum current density distribution and gives a higher value of armature velocity compared with other rail gun structures. Thus, the circular convex armature was found to be suitable for the electromagnetic (EM) rail gun launching system.

***Index Terms* –** ANSYS coupled with Simplorer (ACS), current density, inductance gradient of rails, pulsed power supply system.

I. INTRODUCTION

A rail gun is a type of electromagnetic (EM) launch system that has great potential in EM applications and is widely studied [1, 2]. It has become a research hotspot in the field of military equipment with the advantages of having a simple structure, fast response, and accurate control. In the future, this technology may be used to launch small satellites into a low earth orbit or even into space at low cost [3, 4]. The simple rail gun has mainly three parts: two parallel rails, an armature, and a pulsed power supply (PPS) system. When pulse current flows along one rail, it crosses the armature, returns back along the second rail, and tends to accelerate the armature. Its work is based on a very basic EM concept known as the Lorentz force law, which can be shown by $F = \frac{1}{2}L'I^2$ where F is the force acting on the armature, I is the current passing through the armature, and L' is the inductance gradient of the rails [5]. The representation of a rail gun is shown in Figure 1.

The current density distribution in the rails and armature and inductance gradient of the rails plays an important role in a rail gun design as they determine the force that accelerates the armature with higher velocity. It also depends on the rail and armature shape, its cross sections, magnitude, and shape of the current pulse supplied to the rails. For the last several years, research has been carried out to calculate the same using 2D analysis by varying rail shapes and its dimensions by neglect-

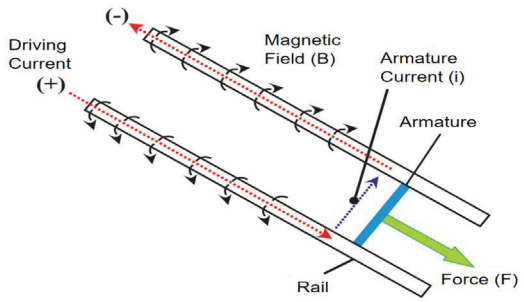

Fig. 1. A simple rail gun representation [6].

Submitted On: June 27, 2021
Accepted On: February 8, 2022

https://doi.org/10.13052/2022.ACES.J.370212

ing the armature effect [5–9]. Researchers also used 3D analysis using analytical methods such as finite element method (FEM) and finite difference method (FDM) by considering the armature effect, and the armature was assumed to be stationary [10–12]. These results were acceptable for lower values of armature velocity and were inconsistent for higher values of armature velocity [13]. Nowadays, researchers are focusing to develop field circuit coupling methods to study the performance of a rail gun under dynamic conditions of the armature [14, 15]. The EM coupled analysis using LS-Dyna was proposed to obtain a higher muzzle velocity, improved current density distribution, and inductance gradient of the tapered rails [16]. A hybrid robust optimization method was proposed to improve the energy efficiency of the rail gun using the polynomial chaos expansion method coupled with Latin hypercube design to study the influence of muzzle velocity, projectile diameter, projectile length, launch angle, and guidance coefficient [17]. The velocity and force acting on the armature were optimized by solving differential equations using the fourth-order Runge-Kutta method, and particle swarm optimization (PSO) algorithm was used to optimize the rail gun parameters [18]. The 3D transient finite element solver was adopted to solve the field circuit coupled problem and calculate the armature velocity of the rail gun [19, 20].

In this article, by using Maxwell's ANSYS software, which has an inbuilt electric field simulator named Simplorer, a method was developed to study the performance of the rail gun for various rails and armature shapes under dynamic conditions of the armature. The current density distribution in the rails and armature and the equivalent electric circuit of rail gun were obtained using the ANSYS eddy current field solver by sweeping the armature position. The armature velocity was calculated using Simplorer coupled with the ANSYS eddy current field solver by exciting the rail gun with the capacitor-based PPS system. The method was validated by numerical method by simulating the rectangular rail cross section and simulating the rail gun structure that was used by other researchers. The results obtained by ANSYS coupled with Simplorer (ACS) method showed good agreement between the results. Then, the work was extended to study the performance of the rail gun for various rail gun structures by calculating the current density distribution over the rails and armature and the velocity of the armature.

II. GOVERNING EQUATIONS

The inductance gradient L', magnetic flux density between the rails, the current density distribution, and the force acting on the rails are obtained using the eddy current solver [20].

In the analysis, the magnetic vector potential (A) is obtained as follows:

$$\nabla X\left(\frac{1}{\mu_0}\left(\nabla X\overrightarrow{A}\right)\right) = (\sigma + j\omega)\left(-j\omega\overrightarrow{A} - \nabla\varnothing\right), \quad (1)$$

where $\overrightarrow{A}$ is the magnetic vector potential, $\varnothing$ is the electric scalar potential, μ is the magnetic permeability, ω is the angular frequency, ε is the relative permittivity, and σ is the conductivity of the conductor.

The eddy current solver solves the magnetic vector potential to obtain the magnetic flux density as follows:

$$\nabla X\overrightarrow{A} = \overrightarrow{B}. \quad (2)$$

The magnetic field intensity and the current density distribution are calculated using the following relationships:

$$\overrightarrow{B} = \mu\overrightarrow{H}. \quad (3)$$

$$\nabla X\overrightarrow{H} = \overrightarrow{J}. \quad (4)$$

Then the energy stored in the system is given as

$$W_{avg} = \frac{1}{4}\iiint \overrightarrow{B}.\overrightarrow{H}\,dv. \quad (5)$$

The instantaneous energy of system is equal to

$$W_{inst} = \frac{1}{2}LI^2, \quad (6)$$

where I is the instantaneous value of current.

Using the above equations, the ANSYS Maxwell's solver calculates the inductance gradient of the rails which is given as

$$L' = 2\left(F/I^2\right). \quad (7)$$

Because the inductance value of the EM launcher is proportional to the position of the armature, the inductance of the rails are varied with respect to armature position, as given in the following:

$$L = (x_0 + \Delta x)L' = 2(x_0 + \Delta x)F/I^2, \quad (8)$$

where x_0 is the initial position of the armature and Δx is the displacement of the armature.

III. DESIGN CALCULATION OF PULSED POWER SUPPLY SYSTEM

The PPS system has an important function in the EM launcher system because it discharges a huge amount of electrical energy to the rails within a short duration. The PPS system, which is generally a capacitor-based system, gets energy from a high-voltage transformer and a rectifier circuit, which have advantages of mature development, simple control, operational reliability, and lower cost [21, 22]. The capacitor-based PPS system was made up of units called pulse forming units and they were assembled into many sections called modules. These modules were concurrently switched to get the desired velocity of the projectile by using thyristors [23, 24]. The design of PPS system depends on the muzzle velocity of the armature. To get the desired velocity of the armature, the PPS system stores enough energy to deliver the current required to accelerate the armature. The driving

current for obtaining the desired velocity of the armature, time period up to which the armature has contact with rails to get the desired velocity of the armature, and the amount of energy stored by the capacitor-based PPS were calculated using the numerical formula given below.

The muzzle velocity of the rail gun is given by the empirical formula [25]

$$V_{muzzle} = \sqrt{\frac{L'D}{m}} I, m/s \tag{9}$$

where L' is the inductance gradient of the rails (μH/m), D is the length of the rails (m), I is the driving current (A), and m is the mass of projectile (kg).

The driving current supplied to the rails was obtained by assuming the muzzle velocity of the armature. The time period up to which the projectile has contact with the rails to get the desired velocity of the projectile was obtained by substituting the driving current supplied to rails in eqn (2)

$$t = \sqrt{\frac{4mD}{L'I^2}}, \quad s \tag{10}$$

where t is the time period of the armature in the rails (s), m is the mass of the armature (kg), D is the length of the rails (m), L' is the inductance gradient of rails (μH/m), and I is the driving current (A).

The PPS system stores enough amount of energy and supplies the driving current to rails until the armature exits from the rails. The energy stored by the capacitor was calculated by assuming 10% efficiency, and it is given as follows:

Energy stored by the capacitor = (Energy stored in the rails at muzzle end)/(Efficiency of the rail gun).

The amount of energy stored in the rails at the muzzle end when the armature exits from the rails was calculated by

$$E_{muz} = \frac{1}{2} m v^2, \quad \text{Joules} \tag{11}$$

where E_{muz} is the energy stored at the muzzle end (Joules), m is the mass of the armature (kg), and v is the velocity of the armature (m/s).

The required voltage to energize the PPS capacitor was calculated by

$$\text{Energy stored by the capacitor} = \frac{1}{2} C v^2, \quad \text{Joules} \tag{12}$$

where C is the capacitance of the capacitor (F) and v is the required voltage to charge the capacitor.

IV. PROCESS OF DYNAMIC ANALYSIS OF RAIL GUN USING THE ACS METHOD

Figure 2 shows the process of ACS method which was used to study the performance of the rail gun. Initially, the properties of the materials, boundary conditions, and excitation of rails were assigned for a given

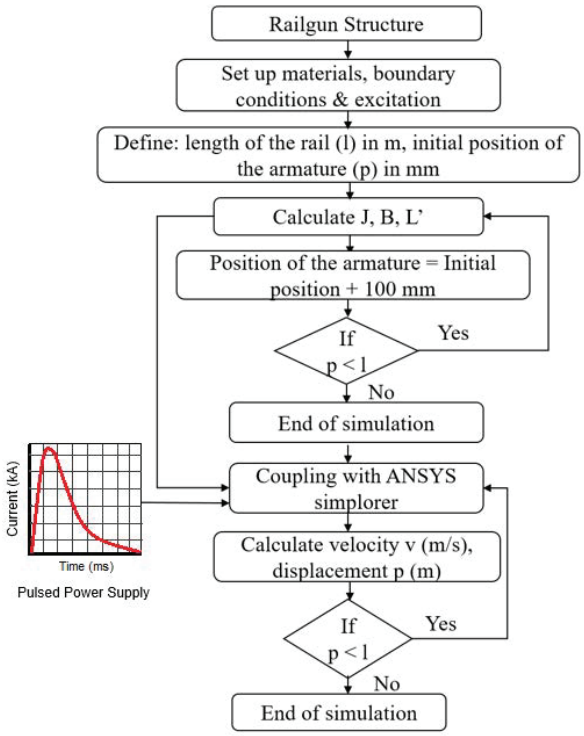

Fig. 2. Process of ACS method.

rail gun structure by creating meshes. The meshing was done over the length based on selecting the geometric region for a maximum of 1000 elements for armature and 2000 elements for rails. Then, the parametric sweep analysis was carried out to determine the current density distribution and magnetic density distribution over rails and armature and the inductance of the rails. Initially, in the parametric sweep analysis, the rail length and initial position of armature were assigned and current density (J), magnetic field distribution (B), and the inductance gradient (L') were calculated. Then, the armature position was incremented and, once again, J, B, and L' were calculated and the process was repeated until the armature reached the defined rail length. Then the equivalent rail gun circuit, which was obtained at the end of FEM analysis, was coupled with Simplorer and the armature velocity and displacement of the armature were calculated by exciting the rails with PPS system. In Simplorer, the rail gun circuit was excited with the PPS system and the position of armature and velocity of the armature were calculated. The solver checks the armature position, and when the armature position was less than the defined rail length, the position of the armature was once again given as input to the rail gun circuit and the velocity and position of the armature were calculated, and the process was repeated until the armature reached the defined rail length.

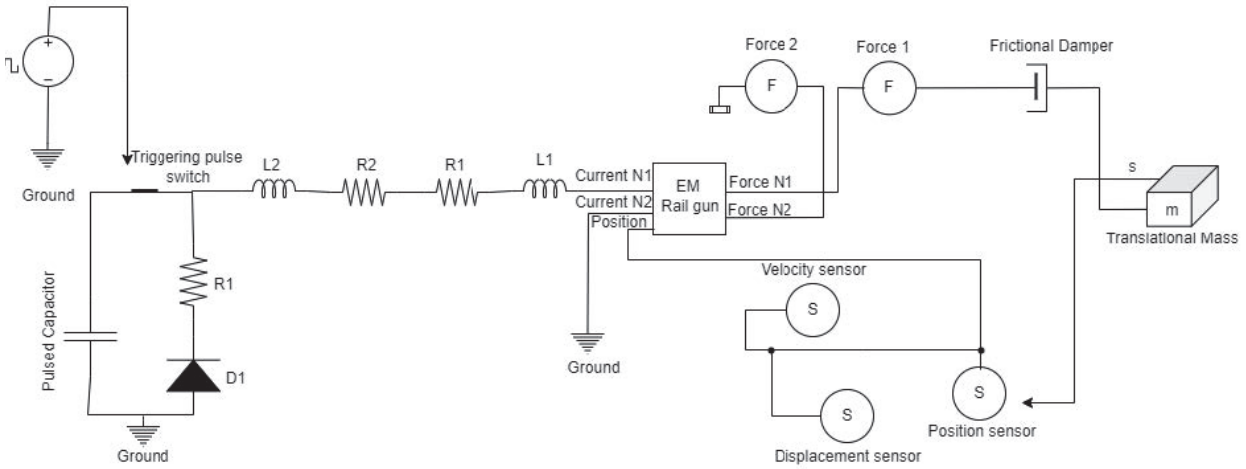

Fig. 3. Electrical equivalent circuit model of rail gun.

Figure 3 shows the electrical equivalent circuit model of the rail gun system coupled with ANSYS Simplorer. The capacitor is connected to the rails through cable (L2, R2) and the pulse shaping inductance (L1, R1) is used to generate the desired shape of current pulse. The capacitor is charged to rated voltage through high-voltage DC supply and it is connected to rails once it is charged to its rated value by closing the triggering pulse switch. The current delivered by the capacitor and the position of armature are given as inputs to the rail gun circuit (EM rail gun). The rail gun circuit calculates the force acting on the armature which is considered as a translational mass based on the current delivered by the capacitor and inductance gradient of the rails. The force is thus generated as a result of high discharge current that propels the armature mass (translational mass) with a frictional damper. The change in position of the armature motion is recorded using a position sensor. Then the velocity of the armature and the distance traveled by the armature is recorded using velocity and displacement sensor.

V. METHODS AND MATERIALS

To validate the concept of the ACS method for rail gun design, a rectangular rail cross section was used to accelerate the armature with a muzzle velocity of 1500 m/s. In this rail gun model, the length of rail was 1 m, the cross section area was 1500 mm^2, and the separation between rails was 20 cm. The armature length was 20 cm and mass of the armature was 100 g. The rails and armature were made up of a solid copper and aluminum conductor, and the properties of the materials used for simulation are given in Table 1.

To accelerate the armature with the desired velocity, the PPS system delivers the current until the armature exits from the rails. The PPS design parameters were calculated using the numerical formula as discussed in Section II and are given in Table 2.

Table 1: Rail and armature material properties

Parameters	Material	Conductivity (S/m)	Density (kg/m^3)
Rails	Copper	5.8×10^7	8940
Armature	Aluminum	3.5×10^7	2800

Table 2: Pulsed power supply system parameters

Rail gun parameters	H **= 40 mm** W **= 37.5 mm**	L' **= 0.483** μ**H/m [8]**
I **(kA)**	216	
t **(ms)**	1.3	
E_{muz} **(kJ)**	112.5	
Energy stored by the capacitor (MJ)	1.125 (for 10% of rail gun efficiency)	
Input voltage (kV)	3.75 (total capacitance of 160 mF)	
L1, L2	5 μH, 1 mH	

The current density distribution over the rails and armature and velocity of the armature depends on the contact pressure and friction between the rails and armature and the shape of current waveform. The effect of friction coefficient is not predominant at high velocity of the armature, and, therefore, its value is maintained as constant. Hence, in this work, it was assumed to be 0.1 [26]. Initially, the armature was kept at 0.1 m at the breech end and a current of 216 kA in the high frequency limit was applied to rails, and the current density distribution and velocity of the armature were obtained by sweeping the armature position with an increment of 100 mm using the ACS method as shown in Figures 4 and 5.

From the figures, it is observed that the current delivered by the PPS system is 216 kA and the velocity of the armature is 1500 m/s at 1.31 ms, which shows a good agreement with numerical calculations.

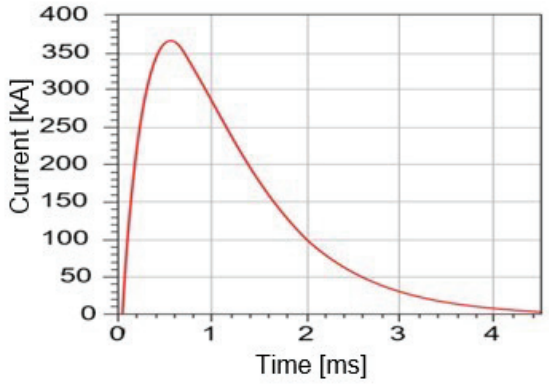

Fig. 4. Pulsed power capacitive discharge current.

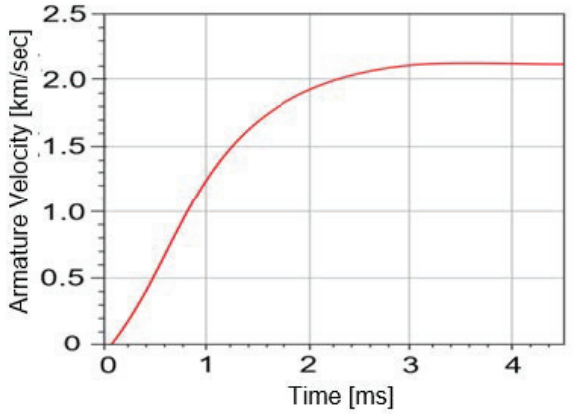

Fig. 5. Velocity of the armature.

To validate the ACS method further, the rail gun model of other researchers was simulated and the velocity of the armature was calculated, as shown in Figure 6. The simulated results were compared with values of other researchers and are given in Table 3.

From Table 3, it is observed that the values obtained using the ACS method show a good agreement with the values of other researchers.

Hence, in this work, the ACS method was used and simulated further to study the effect of rails and armature shape over current density distribution in rails and armature.

VI. RESULTS AND DISCUSSIONS

To study the effect of rails and armature shape over the current density distribution, different rail gun structures such as rectangular concave and convex, circular concave and convex, T-shaped concave, and convex rails with C-shaped armature, which are shown in Figure 7, were considered and simulated.

Figure 8 shows the current density distribution in the rails and armature for different rail gun structures

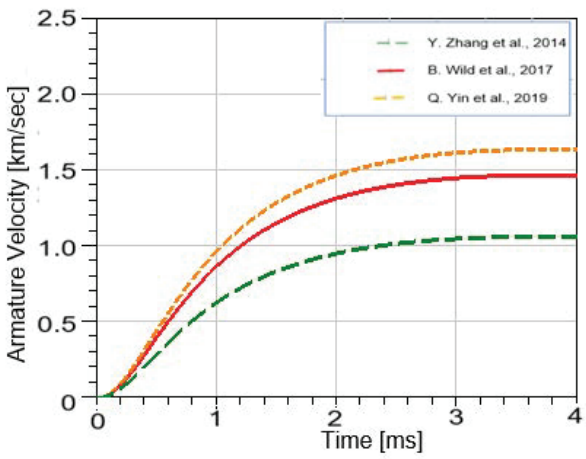

Fig. 6. Armature velocity of the other researchers.

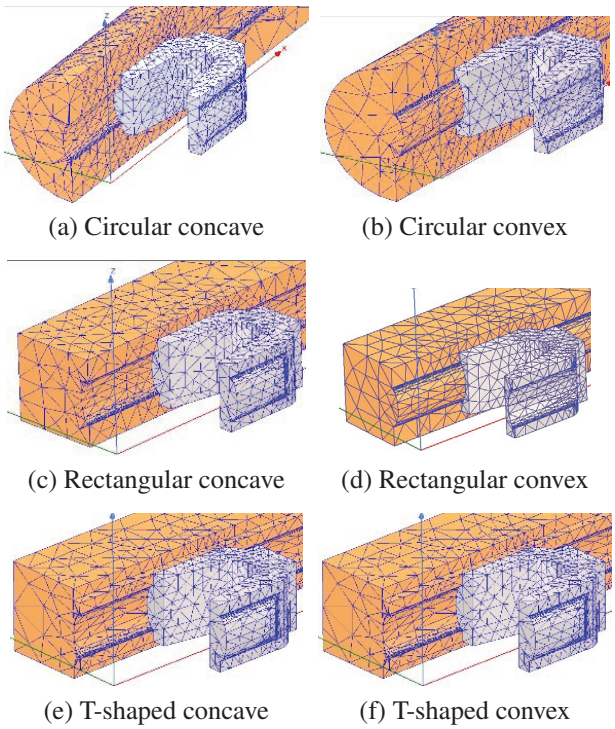

(a) Circular concave (b) Circular convex

(c) Rectangular concave (d) Rectangular convex

(e) T-shaped concave (f) T-shaped convex

Fig. 7. Different rail gun geometries.

Table 3: Comparison of other researchers' results

lAuthors name	Method used	Velocity (km/s)	Velocity (km/s) using ACS method
Zhang *et al.* (2014) [14]	Field circuit method	1.01 (2.5 ms)	1.01 (2.5 ms)
Wild *et al.* (2017)	Finite element method	1.45 (2.5 ms)	1.43 (2.5 ms)
Yin *et al.* (2019)	Finite element method	1.5 (2.6 ms)	1.55 (2.6 ms)

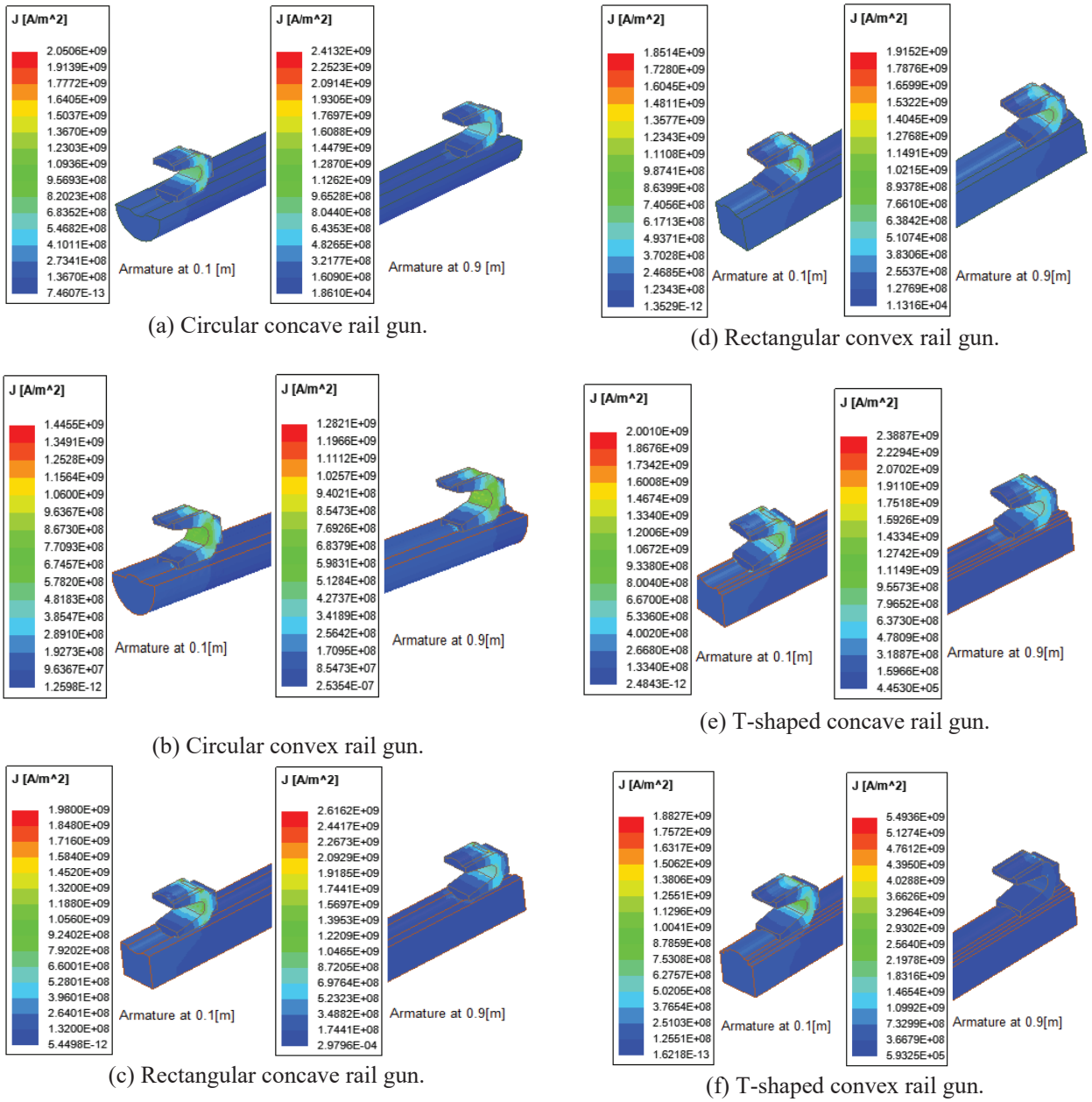

Fig. 8. (a)–(f). Current density distribution for different rail gun structures at 0.1 m and 0.9 m position.

obtained from the simulation at positions 0.1 and 0.9 m. From Figure 8, it is observed that current density distribution in the rails and armature is non-uniform when sliding along the rails. Moreover, the current distribution is higher over the corners and on the surface of the rails and armature edges. It is observed that the current does not penetrate deeper into the rails and armature when the armature is at the breech end, but it penetrates deeper into the rails and armature when the armature is at the muzzle end. This is mainly due to the velocity skin effect between the rails and armature. It is also observed that among the various rails and armature shapes, the circular convex rail gun shows minimum current density concentration in the armature of about 1.4455×10^9 A/m^2 at the breech end and 1.2821×10^9 A/m^2 at the muzzle end. Thus, the circular convex rails possess minimum current density concentration in the armature compared to the other rail gun structures. As the current hotspot is less, this armature model suits the launching process and the armature does not get destroyed before leaving the muzzle end of the rails. The ANSYS calculates the equivalent value of the rail gun inductance with respect

to armature positions by using the current density distribution and magnetic field distribution over rails and armature.

The expressions of resultant inductance (μH/m) of rails are given in eqn (13)–(18) for various configurations.

Circular convex rail gun:

$$L'_{\text{circ\_concave}} = -2.105(\rho)^2 + 491.5\rho + 45.41. \quad (13)$$

Circular convex rail gun:

$$L'_{\text{circ\_convex}} = -1.172(\rho)^2 + 483.5\rho + 45.19. \quad (14)$$

Rectangular concave rail gun:

$$L'_{\text{Rect\_concave}} = -0.964(\rho)^2 + 494.3\rho + 46.50. \quad (15)$$

Rectangular convex rail gun:

$$L'_{\text{Rect\_convex}} = -0.156(\rho)^2 + 480.8\rho + 45.70. \quad (16)$$

T-shaped concave rail gun:

$$L'_{\text{T\_concave}} = -0.655(\rho)^2 + 501.5\rho + 47.35. \quad (17)$$

T-shaped convex rail gun:

$$L'_{\text{T\_convex}} = -0.263(\rho)^2 + 487.0\rho + 46.40, \quad (18)$$

where ρ is the armature position.

The rail gun equivalent circuit was then coupled with Simplorer and excited by the capacitor-based PPS system, and the velocity and distance traveled by the armature were calculated and are shown in Figures 9 and 10.

The values of velocity and displacement of the armature for different rail structures are given in Table 4.

From Table 4, it is observed that the circular convex rail gun with C-shaped armature achieves velocity of about 1.99 km/s at 1.3 ms with armature displacement of 1.35 m compared with other rail gun structures. Hence, circular convex rails with C-shaped armature may be considered while designing the rail gun system.

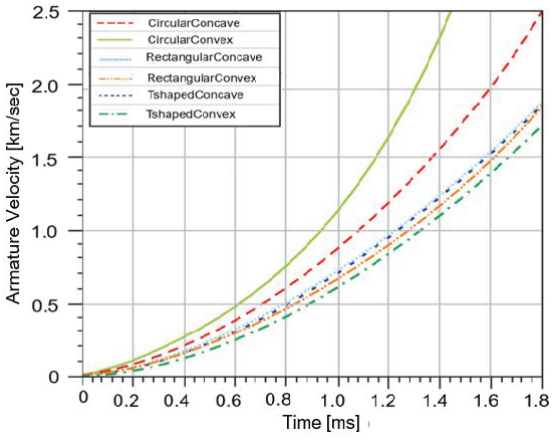

Fig. 9. Velocity of the armature for different rail gun structures.

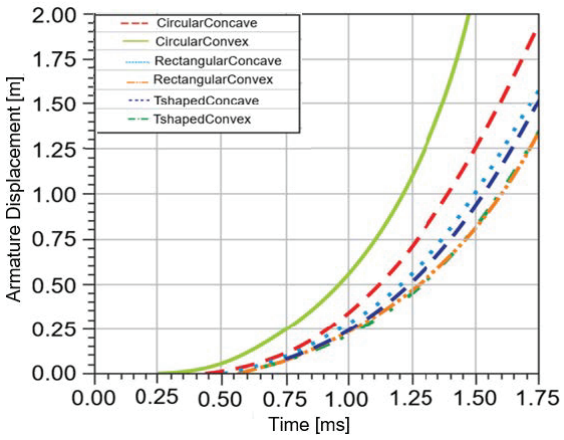

Fig. 10. Displacement of the armature for different rail gun structures.

Table 4: Velocity and displacement of the projectile for different rail gun structures

Geometric model	Velocity (km/s) at 1.3 ms	Distance (m) at 1.3 ms
Circular concave	1.3140	0.8065
Circular convex	1.9990	1.3524
Rectangular concave	1.1852	0.6924
Rectangular convex	1.0528	0.5703
T-shaped concave	1.1769	0.6377
T-shaped convex	1.0347	0.5604

VII. CONCLUSION

In this study, the ACS method was developed to study the performance of the rail gun. The method was validated for rectangular rail cross section with numerical calculations and further validated against various rail gun structures that were used by other researchers. The obtained results showed good agreement between the results. Then the current density distribution over rails and armature and velocity of the armature were calculated for different rail gun structures such as circular concave, circular convex, rectangular concave, rectangular convex, T-shaped concave, and T-shaped convex with a C-shaped armature for various rail gun structures. It was observed that the circular convex with C-shaped armature showed a lower current density distribution over rails and armature and gave a higher value of armature velocity compared with other rail gun structures. Thus, it can be concluded that the circular convex armature is suitable for the EM rail gun launching system.

ACKNOWLEDGMENT

The authors would like to thank all the reviewers and the editor for their valuable comments to enhance this manuscript. The authors wish to thank the Department of Science & Technology, Government of India, for funding the Research Infrastructure under the Scheme entitled "Funds for the Improvement of S&T Infrastructure (DST-FIST)" Ref. No. SR/FST/College – 110/2017.

REFERENCES

[1] S. Hundertmark, G. Vincent, D. Simicic, and M. Schneider, "Increasing Launch Efficiency with the PEGASUS Launcher," *IEEE Transactions on Plasma Science*, vol. 45, no. 7, pp. 1607-1613, Jul. 2017.

[2] I. R. McNab, "Developments in Pulsed Power Technology," *IEEE Transactions on Magnetics*, vol. 37, no. 1, pp. 375–378, Jan. 2001.

[3] H. D. Fair, "Guest Editorial the Past, Present, and Future of Electromagnetic Launch Technology and the IEEE International EML Symposia," *IEEE Transactions on Plasma Science*, vol. 41, no. 5, pp. 1024–1027, May 2013.

[4] C. Gong, X. Yu, and X. Liu, "Study on the System Efficiency of the Capacitive Pulsed-power Supply," *IEEE Transactions on Plasma Science*, vol. 43, no. 5, pp. 1441–1447, May 2015.

[5] M. N. S. Kumar, R. Murugan, "Analysis of Inductance Gradient and Current Density Distribution over Different Cross-section of Rails," *International Journal of Electrical and Computer Engineering,* vol. 8, no. 02, pp. 723-729, Apr. 2018.

[6] M. N. S. Kumar, R. Murugan, and P. Shivkumar, "Inductance Gradient and Current Density Distribution for T-shaped Convex and Concave Rail Cross-sections," *International Journal of Engineering & Technology (UAE),* vol. 7, no. 01, pp. 237-240, Mar. 2018.

[7] M. S. Bayati and A. Keshtkar, "Study of the Current Distribution, Magnetic Field, and Inductance Gradient of Rectangular and Circular Rail Guns," *IEEE Transactions on Plasma Science,* vol. 41, no. 5, pp. 1376-1381, May 2013.

[8] A. Keshtkar, S. Bayati, and A. Keshtkar, "Derivation of a Formula for Inductance Gradient using Intelligent Estimation Method," *IEEE 2008 14th Symposium on Electromagnetic Launch Technology*, pp. 1-4, Jun. 2008.

[9] M. S. Bayati and A. Keshtkar "Novel Study of the Rail's Geometry in the Electromagnetic Launcher," *IEEE Transactions on Plasma Science*, vol. 43, no. 5, pp. 1652-1656, May 2015.

[10] M. S. Bayati and K. Amiri, "Study of Various C-Shaped Armatures in Electromagnetic Launcher," *Applied Computational Electromagnetics Society Journal*, vol. 30, no. 9, pp. 1029-1034, Sep. 2015.

[11] D. Ceylan, M. Karagoz, Y. Cevik, B. Yildirim, H. Polat, and O. Keysan, "Simulations and Experiments of EMFY-1 Electromagnetic Launcher," *IEEE Transactions on Plasma Science,* vol. 47, no.7, pp. 3336-3343, Jul. 2019.

[12] J. Dong, J. Zhang, J. Li, Y. Gui, Y. Cui, S. Li, and N. Su, "The 100-kJ Modular Pulsed Power Units for Railgun," *IEEE Transactions on Plasma Science,* vol. 39, no. 1, pp. 275-278, Jan. 2011.

[13] W. Li, Y. Hu, J. Feng, Y. Zhang, and D. Jing, "Research on Armature Structure Optimization of Rail Gun Based on Multiple Linear Regression," *IEEE Transactions on Plasma Science,* vol. 47, no. 11, pp. 5042-5048, Nov. 2019.

[14] Y. Zhang, W. Qin, J. Liao, and J. Ruan, "Optimization Design of Multiparameters in Rail Launcher System," *Sensors & Transducers*, vol. 171, issue 5, pp. 115–120, May 2014.

[15] Y. Hu, P. Ma, M. Yang, and Z. Wang, "Validation and Optimization of Modular Railgun Model," *IEEE 2012 16th International Symposium on Electromagnetic Launch Technology (EML)*, pp. 1–6, May 2012.

[16] S. R. Praneeth, D. Chaudhuri, B. Singh, S. Chatterjee, and G. Bhuvaneswari, "Analysis of an Electromagnetic Railgun with Tapered Rails and Concave Armature Using 3-D FEM," *IEEE 2019 12th* International Symposium on Linear Drives for Industry Applications (LDIA), pp. 1-4, Jul. 2019.

[17] X. Shang, T. Chao, P. Ma, and M. Yang, "Simulation and Robust Optimization Design for Electromagnetic Railgun Performance," *IEEE Transactions on Plasma Science,* vol. 47, no. 6, pp. 2964-2970, Jun. 2019.

[18] A. Shiri and M. Allahyari, "Sensitivity Analysis and Optimization of Railguns Using Circuit Model," *IEEE Transactions on Plasma Science,* vol. 47, no. 11, pp. 5139-5147, Nov. 2019.

[19] C. Li, L. Chen, Z. Wang, J. Ruan, P. Wu, J. He, and S. Xia, "Influence of Armature Movement Velocity on the Magnetic Field Distribution and Current Density Distribution in Railgun," *IEEE Transactions on Plasma Science,* vol. 48, issue 6, pp. 2308-2315, Jun. 2020.

[20] Q. Lin, B. Li, "Field-circuit Coupled Analysis of a Series-augmented Electromagnetic Railgun," *IEEE Transactions on Plasma Science,* vol. 48, issue 6, pp. 2287-2293, Jun. 2020.

[21] B. E. Fridman, R. Sh. Enikeev, N. A. Kovrizhnykh, K. M. Lobanov, and R. A. Serebrov, "A 0.5 MJ 18 KV Module of Capacitive Energy Storage," *2019 IEEE Pulsed Power Conference*, vol. 39, no. 2, pp. 61-65, Jul. 2009.

[22] L. Dai, Y. Wang, Q. Zhang, W. Li, W. Lu, H. Dong, Q. Huang, and F. Lin, "Effect of Sequence Discharge on Components in a 600-kJ PPS Used for Electromagnetic Launch System," *IEEE 2012 16th International Symposium on Electromagnetic Launch Technology (EML)*, pp. 1-6, May 2012.

[23] X. Liu, X. Yu, and X. Liu, "Performance Analysis and Parameter Optimization of CPPS-based Electromagnetic Railgun System," *IEEE Transactions on Plasma Science*, vol. 44, no. 3, pp. 281-288, Mar. 2016.

[24] T. M. Abdo, A. L. Elrefai, A. A. Adly, and O. A. Mahgoub, "Performance Analysis of Coilgun Electromagnetic Launcher Using a Finite Element Coupled Model," *2016 Eighteenth International Middle East Power Systems Conference (MEPCON)*, pp. 506-511, Dec. 2016.

[25] E. Cholaki, S. Ahmadvand, E. Mahmodi, and M. H. Sahafi, "Design and Calculation of Railgun Velocity and Study on Frictional Effects," *3rd International Conference of Science & Engineering in Technology Era*, pp. 1-6, Aug. 2017.

[26] J. Gallant, P. Lehmann, "Experiments with Brush Projectiles in a Parallel Augmented Railgun," *IEEE Transactions on Magnetics*, vol. 41, issue 1, pp. 188-193, Jan. 2005.

J. Lydia is currently a Research Scholar, pursuing her Ph.D. degree under the Faculty of Electrical Engineering, Anna University, Chennai, India. She received the B.E. degree in Electrical and Electronics Engineering from Easwari Engineering College, Chennai, India. She received the M.E. degree in Power Electronics and Drives from the Karunya Institute of Technology and Sciences, Deemed University, in 2006.

She is currently an Assistant Professor with the Department of Electrical and Electronics Engineering, Easwari Engineering College and works in the fields of Electromagnetic Fields and High-Voltage Engineering. She is a member of ACES and MISTE.

R. Karpagam received the Ph.D. degree from the Indian Institute of Technology, Chennai, India, in 2013.

She is currently an Associate Professor with the Department of Electrical and Electronics Engineering, Easwari Engineering College, Chennai, India. Her research interests include Partial Discharge Studies, Space Charge Measurements in Epoxy Nanocomposites, and Power Electronics. She is a member of ACES and IET.

R. Murugan received the bachelor's degree in Electrical and Electronics Engineering from the University of Madras, Chennai, India, in April 1996. He received the master's degree in High-Voltage Engineering from the College of Engineering, Anna University, Guindy, Chennai, India, in February 1999 and the Ph.D. degree from the Electrical and Electronics Engineering Department, Anna University in 2011.

His main areas of research interest are Electromagnetic Field and High-Voltage Engineering.

Low-Frequency Transmitted Fields of a Source Inside a Magnetic Shell with Large Conductivity

Shifeng Huang, Gaobiao Xiao, and Junfa Mao

Key Laboratory of Ministry of Education of Design and
Electromagnetic Compatibility of High Speed Electronic Systems

Shanghai Jiao Tong University, Shanghai 200240, China
huangshifeng@sjtu.edu.cn; gaobiaoxiao@sjtu.edu.cn; jfmao@sjtu.edu.cn

Abstract – The method to evaluate the transmitted fields of a source inside a simply connected magnetic shell with large but finite conductivity at low frequencies is proposed in this paper. When modeling the magnetic shell with large conductivity, it is regarded as a penetrable object. Electric field integral equation (EFIE) is selected for the exterior region problem and magnetic field integral equation (MFIE) is chosen for the interior region problem. Each operator is decomposed with loop-star functions to overcome the problem of low-frequency breakdown. Numerical results verify the accuracy of the proposed method.

Keywords – Large conductivity, loop-star, low frequency, magnetic material, transmitted fields.

I. INTRODUCTION

The analysis of electromagnetic compatibility (EMC) is frequently carried out to keep a system or components of a system working properly [1, 2]. For example, components of a microelectronic system should work normally and not interfere with others at the same time. The protection of an electronic system with high sensitivity from the electromagnetic (EM) emission from a high power electrical equipment is usually needed on a platform like ships and airplanes. One common strategy to suppress EM interference (EMI) is to enclose the electronic or electrical equipment with a shield with large conductivity if possible. Hence, it is necessary to calculate the fields transmitted from a shielding shell. In some scenarios, the amplitude of EM fields leaked from a target is expected to be as small as possible so that it cannot be detected. This is of great importance for some underwater targets, such as submarines and unmanned underwater vehicles. Because those underwater targets are immersed in sea water, low-frequency EM waves can propagate to a large distance. The body of underwater targets may be filled with magnetic materials. At low frequencies, the shell cannot be modeled as perfect electrical conductor (PEC) because the skin depth is comparable to its thickness. Hence, it is necessary to model the fields transmitted from a magnetic shell with large but finite conductivity accurately at low frequencies.

The method based on quasi-static approximation is first developed by neglecting the displacement currents [3, 4]. However, this approximate method can only work well at low frequencies and may give wrong results at relatively higher frequencies, and the frequency when quasi-static method fails is difficult to predict.

Rigorous methods are proposed to model conductor with large but finite conductivity, like finite element method (FEM), volume integral equation (VIE) method, and surface integral equation (SIE) method. SIE method is preferred to model conductors with the advantage of only discretizing the surface of conductors. In SIE method, the conductor is modeled as a penetrable object. Appropriate equations from the interior and exterior problems are selected to describe the behavior of the fields in the interior of the conductor and the coupling between other objects, respectively [5–8]. Examples are the method using the generalized impedance boundary condition (GIBC) [7] and the differential surface admittance (DSA) [8].

The low-frequency breakdown (LFB) problem of electric field integral operator (EFIO) in the SIE method mentioned above has to be overcome. Some remedies have been proposed. The primal and dual projectors of solenoidal and non-solenoidal component are used to perform quasi-Helmholtz decomposition of operators in Poggio-Miller-Chang-Harrington-Wu-Tsai (PMCHWT) equation [9]. Two low-frequency stable equations with different augment techniques are proposed in [10] and [11]. To reduce the number of equivalent surface sources on the interface and improve the efficiency of solvers, single-source formulations are proposed with augment techniques for lossy conductors to cover the low-frequency band analysis [12, 13]. Well-conditioned formulation based on potential, instead of electric and

Submitted On: January 14, 2022
Accepted On: March 23, 2022

https://doi.org/10.13052/2022.ACES.J.370213

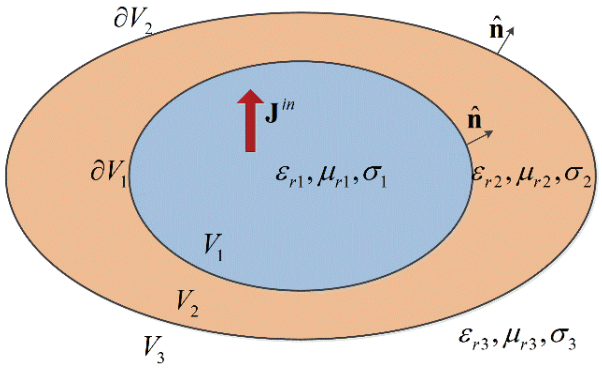

Fig. 1. Configuration of a source in a shell immersed in a homogeneous background media.

magnetic fields, is also reported to model good conductors [14].

In this work, the electric field integral equation (EFIE) in the exterior problem and the magnetic field integral equation (MFIE) in the interior problem of a shell are selected to model the shell with large conductivity and relative permeability, similar to [7]. The background media may also have large constitutive parameters, like sea water with large relative permittivity. Hence, PMCHWT equation are not chosen because it may fail to model objects with high contrast material parameters. The shell is thin with a thickness of several centimeters. The approximation in [7] due to small skin depth does not hold in this work because the skin depth may be comparable to the thickness. Furthermore, the LFB problem in [7] is not fully considered. Here, loop-star decomposition is performed on each operator in the equation for a simply connected shell. The low-frequency scaling of the decomposed coefficient matrix is analyzed and two sets of new rescaling coefficients are applied to improve the conditioning of the formular at low frequencies.

II. FORMULATION FOR THE SHELL

A. Equation formular at high frequency

A source in a magnetic shell with large but finite conductivity is shown in Figure 1. The source $\mathbf{J}^{\text{in}}$ is in region V_1 with parameters $(\mu_{r1},\varepsilon_{r1},\sigma_1)$ and bounded by surface ∂V_1. Region V_2 denotes the shell with parameters $(\mu_{r2},\varepsilon_{r2},\sigma_2)$. The shell is bounded by surfaces ∂V_1 and ∂V_2. The shell is immersed in a homogeneous background media V_3 with parameters $(\mu_{r3},\varepsilon_{r3},\sigma_3)$. $\hat{\mathbf{n}}$ is the outward unit vector of the surface. In our application, region V_1 is air with $\sigma_1 = 0$, region V_2 has large conductivity σ_2 and relative permeability μ_{r2}, and region V_3 is sea water with large relative permittivity ε_{r3} and $\sigma_3 = 4\ S/m$.

Based on extinction theorem, the EFIE and MFIE describing the internal problem of region V_1 can be written as

$$\hat{\mathbf{n}}\times\left[\mathscr{L}_{1E}\left\{\mathbf{J}_d^{1-}\right\}-\mathscr{K}_{1E}\left\{\mathbf{M}_d^{1-}\right\}+\mathbf{E}^{\text{in}}\right]=0,\ \mathbf{r}\in\partial V_1, \tag{1}$$

and

$$\hat{\mathbf{n}}\times\left[\mathscr{K}_{1H}\left\{\mathbf{J}_d^{1-}\right\}-\mathscr{L}_{1H}\left\{\mathbf{M}_d^{1-}\right\}+\mathbf{H}^{\text{in}}\right]=0,\ \mathbf{r}\in\partial V_1, \tag{2}$$

where $\mathbf{J}_d^{1-}$ and $\mathbf{M}_d^{1-}$ are the unknown equivalent surface electric current and magnetic current density on ∂V_1. $\mathbf{E}^{\text{in}}$ and $\mathbf{H}^{\text{in}}$ are the fields radiated by the source $\mathbf{J}^{\text{in}}$. The EFIE and MFIE describing the internal problem for region V_2 can be expressed as

$$\hat{\mathbf{n}}\times\left[\begin{array}{l}\mathscr{L}_{2E}\left\{\mathbf{J}_d^{1+}\right\}-\mathscr{K}_{2E}\left\{\mathbf{M}_d^{1+}\right\}\\ \quad+\mathscr{L}_{2E}\left\{\mathbf{J}_d^{2-}\right\}-\mathscr{K}_{2E}\left\{\mathbf{M}_d^{2-}\right\}\end{array}\right]=0,\ \mathbf{r}\in\partial V_1, \tag{3}$$

$$\hat{\mathbf{n}}\times\left[\begin{array}{l}\mathscr{L}_{2E}\left\{\mathbf{J}_d^{1+}\right\}-\mathscr{K}_{2E}\left\{\mathbf{M}_d^{1+}\right\}\\ \quad+\mathscr{L}_{2E}\left\{\mathbf{J}_d^{2-}\right\}-\mathscr{K}_{2E}\left\{\mathbf{M}_d^{2-}\right\}\end{array}\right]=0,\ \mathbf{r}\in\partial V_2, \tag{4}$$

and

$$\hat{\mathbf{n}}\times\left[\begin{array}{l}\mathscr{K}_{2H}\left\{\mathbf{J}_d^{1+}\right\}-\mathscr{L}_{2H}\left\{\mathbf{M}_d^{1+}\right\}\\ \quad+\mathscr{K}_{2H}\left\{\mathbf{J}_d^{2-}\right\}-\mathscr{L}_{2H}\left\{\mathbf{M}_d^{2-}\right\}\end{array}\right]=0,\ \mathbf{r}\in\partial V_1, \tag{5}$$

$$\hat{\mathbf{n}}\times\left[\begin{array}{l}\mathscr{K}_{2H}\left\{\mathbf{J}_d^{1+}\right\}-\mathscr{L}_{2H}\left\{\mathbf{M}_d^{1+}\right\}\\ \quad+\mathscr{K}_{2H}\left\{\mathbf{J}_d^{2-}\right\}-\mathscr{L}_{2H}\left\{\mathbf{M}_d^{2-}\right\}\end{array}\right]=0,\ \mathbf{r}\in\partial V_2, \tag{6}$$

where $\mathbf{J}_d^{1+}$ and $\mathbf{M}_d^{1+}$ are the equivalent surface electric current and magnetic current density on ∂V_1, respectively. $\mathbf{J}_d^{2-}$ and $\mathbf{M}_d^{2-}$ are the equivalent surface electric current and magnetic current density on ∂V_2, respectively. The EFIE and MFIE describing the internal problem of region V_3 can be written as

$$\hat{\mathbf{n}}\times\left[\left(\mathscr{L}_{3E}\left\{\mathbf{J}_d^{2+}\right\}-\mathscr{K}_{3E}\left\{\mathbf{M}_d^{2+}\right\}\right)\right]=0,\ \mathbf{r}\in\partial V_2, \tag{7}$$

$$\hat{\mathbf{n}}\times\left[\left(\mathscr{K}_{3H}\left\{\mathbf{J}_d^{2+}\right\}-\mathscr{L}_{3H}\left\{\mathbf{M}_d^{2+}\right\}\right)\right]=0,\ \mathbf{r}\in\partial V_2, \tag{8}$$

where $\mathbf{J}_d^{2+}$ and $\mathbf{M}_d^{2+}$ are the equivalent surface electric current and magnetic current density on ∂V_2, respectively. Due to the boundary condition on the interfaces, $\mathbf{J}_d^{i+}=-\mathbf{J}_d^{i-}$ and $\mathbf{M}_d^{i+}=-\mathbf{M}_d^{i-}$, with $i=1,2$.

The magnetic shell has large conductivity and is modeled as a penetrable object. Hence, the MFIE describing internal problem of region V_2 and EFIE describing external problem of region V_2 are selected:

$$\hat{\mathbf{n}}\times\left[\mathscr{L}_{1E}\left\{\mathbf{J}_d^{1-}\right\}-\mathscr{K}_{1E}\left\{\mathbf{M}_d^{1-}\right\}+\mathbf{E}^{in}\right]=0,\ \mathbf{r}\in\partial V_1, \tag{9}$$

$$\hat{\mathbf{n}}\times\left[\begin{array}{l}\mathscr{K}_{2H}\left\{\mathbf{J}_d^{1+}\right\}-\mathscr{L}_{2H}\left\{\mathbf{M}_d^{1+}\right\}\\ \quad+\mathscr{K}_{2H}\left\{\mathbf{J}_d^{2-}\right\}-\mathscr{L}_{2H}\left\{\mathbf{M}_d^{2-}\right\}\end{array}\right]=0,\ \mathbf{r}\in\partial V_1, \tag{10}$$

$$\hat{\mathbf{n}}\times\left[\begin{array}{l}\mathscr{K}_{2H}\left\{\mathbf{J}_d^{1+}\right\}-\mathscr{L}_{2H}\left\{\mathbf{M}_d^{1+}\right\}\\ \quad+\mathscr{K}_{2H}\left\{\mathbf{J}_d^{2-}\right\}-\mathscr{L}_{2H}\left\{\mathbf{M}_d^{2-}\right\}\end{array}\right]=0,\ \mathbf{r}\in\partial V_2, \tag{11}$$

$$\hat{\mathbf{n}}\times\left[\mathscr{L}_{3E}\left\{\mathbf{J}_d^{2+}\right\}-\mathscr{K}_{3E}\left\{\mathbf{M}_d^{2+}\right\}\right]=0,\ \mathbf{r}\in\partial V_2. \tag{12}$$

The equivalent surface sources $\mathbf{J}_d^{i+}$ and $\mathbf{M}_d^{i+}$ on the surface ∂V_i are expanded with RWG functions [15]

$$\mathbf{J}_d^{i+} = \sum_{n=1}^{N_i} j_n^i \mathbf{f}_n, \quad \mathbf{M}_d^{i+} = \sum_{n=1}^{N_i} m_n^i \mathbf{f}_n. \tag{13}$$

After testing eqn (9)–(12) with $\hat{\mathbf{n}} \times \mathbf{f}_m$, a matrix equation is obtained

$$\begin{bmatrix} \mathbf{L}_{1E} & \mathbf{K}_{1E} & \mathbf{0} & \mathbf{0} \\ \mathbf{K}_{2H} & -\mathbf{L}_{2H} & -\mathbf{K}_{2H} & \mathbf{L}_{2H} \\ \mathbf{K}_{2H} & -\mathbf{L}_{2H} & -\mathbf{K}_{2H} & \mathbf{L}_{2H} \\ \mathbf{0} & \mathbf{0} & \mathbf{L}_{3E} & \mathbf{K}_{3E} \end{bmatrix} \begin{bmatrix} \mathbf{j}^1 \\ \mathbf{m}^1 \\ \mathbf{j}^2 \\ \mathbf{m}^2 \end{bmatrix} = \begin{bmatrix} -\mathbf{V}_e^{\text{in}} \\ \mathbf{0} \\ \mathbf{0} \\ \mathbf{0} \end{bmatrix}. \tag{14}$$

The expressions of matrix entries are listed in the Appendix. Note that a rotated identity matrix $\mathbf{I}_{\text{X}}^p$ appears in $\mathbf{K}_{1E}$, $\mathbf{K}_{2H}$, $\mathbf{K}_{2H}$, and $\mathbf{K}_{3E}$. Once the equivalent surface sources $\mathbf{J}_d^{2+}$ and $\mathbf{M}_d^{2+}$ on ∂V_2 are solved, the transmitted fields in the background media can be obtained

$$\mathbf{E}_t = \mathscr{L}_{3E}\left\{\mathbf{J}_d^{2+}\right\} - \mathscr{K}_{3E}\left\{\mathbf{M}_d^{2+}\right\}, \ \mathbf{r} \in V_3, \tag{15}$$

$$\mathbf{H}_t = \mathscr{K}_{3H}\left\{\mathbf{J}_d^{2+}\right\} - \mathscr{L}_{3H}\left\{\mathbf{M}_d^{2+}\right\}, \ \mathbf{r} \in V_3. \tag{16}$$

B. Loop-star decomposition

At low frequencies, the LFB problem of operators has to be dealt with. In this work, the loop-star decomposition is adopted and the shell is assumed to be simply connected. Different from the work in [7], the loop-star scheme is applied to all operators in eqn (14). Specifically, after loop-star decomposition, the discretized operators in (14) become

$$\mathbf{U}_{iE/H}^{qH} = \begin{bmatrix} \mathbf{U}_{iE/H}^{LL} & \mathbf{U}_{iE/H}^{LS} \\ \mathbf{U}_{iE/H}^{SL} & \mathbf{U}_{iE/H}^{SS} \end{bmatrix}, (i = 1,2,3), \tag{17}$$

where $\mathbf{U}$ denotes $\mathbf{L}$ or $\mathbf{K}$. The scaling of entries in the decomposed operators $\mathbf{U}_{iE/H}^{qH}$ can be analyzed with Taylor expansions when frequency approaches zero. At low frequencies, the Green's function can be expanded as

$$g_i(\mathbf{r},\mathbf{r}') \approx \frac{1}{4\pi R}\left[1 - jk_iR - \frac{1}{2}(k_iR)^2 + \cdots\right], \tag{18}$$

and the dominant term of $g_i(\mathbf{r},\mathbf{r}')$ is $\mathscr{O}(1)$ as frequency approaches zero. Hence, the scaling of each sub-block in $\mathbf{L}_{iE}$ and $\mathbf{L}_{iH}$ is determined by the coefficients $k_i\eta_i$ and η_i/k_i of the vector and scalar potential terms. At low frequencies, if $\sigma_i \neq 0$, $\varepsilon_{\text{ieff}} \approx \sigma_i/j\omega$. Hence,

$$k_i\eta_i = \omega\mu_i = \mathscr{O}(\omega\mu_0), (i = 1,2,3), \tag{19}$$

$$\frac{\eta_1}{k_1} = \frac{1}{\omega\varepsilon_{1\text{eff}}} = \frac{1}{\omega\varepsilon_0} = \mathscr{O}\left(\frac{1}{\omega\varepsilon_0}\right), \tag{20}$$

$$\frac{\eta_i}{k_i} = \frac{1}{\omega\varepsilon_{\text{ieff}}} = \frac{j}{\sigma_i} = \mathscr{O}\left(\frac{1}{\sigma_i}\right), (i = 2,3). \tag{21}$$

Hence, the scaling of $\mathbf{L}_{1E}^{qH}$ is

$$\mathbf{L}_{1E}^{qH} = \mathscr{O}\begin{bmatrix} \omega\mu_0 & \omega\mu_0 \\ \omega\mu_0 & \frac{1}{\omega\varepsilon_0} \end{bmatrix}. \tag{22}$$

The scaling of $\mathbf{L}_{2E}^{qH}$ and $\mathbf{L}_{3E}^{qH}$ is

$$\mathbf{L}_{iE}^{qH} = \mathscr{O}\begin{bmatrix} \omega\mu_0 & \omega\mu_0 \\ \omega\mu_0 & \frac{1}{\sigma_i} \end{bmatrix}, (i = 2,3). \tag{23}$$

The scaling of $\mathbf{L}_{2H}^{qH}$ and $\mathbf{L}_{3H}^{qH}$ can be derived similarly as

$$\mathbf{L}_{iH}^{qH} = \mathscr{O}\begin{bmatrix} \sigma_i & \sigma_i \\ \sigma_i & \frac{1}{\omega\mu_0} \end{bmatrix}, (i = 2,3). \tag{24}$$

The gradient of Green's function can be expanded at low frequencies as

$$\nabla g(\mathbf{r},\mathbf{r}') \approx \frac{1}{4\pi}\left(\nabla\frac{1}{R} - \frac{k_i^2}{2}\frac{\mathbf{R}}{R} + \frac{jk_i^2}{3}\mathbf{R} + \cdots\right). \tag{25}$$

Note that the static term $\nabla(1/R)$ in (25) will be canceled between the interaction of two local loop functions [16]. Hence, the leading term of $\mathbf{K}_{iE/H}^{LL}$ is $\mathscr{O}(k_i^2)$. This does not happen in other sub-blocks in $\mathbf{K}_{iE/H}^{qH}$. The expression of k_i^2 in V_i is

$$k_i^2 = \begin{cases} \omega^2\mu_0\varepsilon_0, i = 1 \\ -j\omega\mu_i\sigma_i, i = 2,3 \end{cases}, \tag{26}$$

and the scaling of $\mathbf{K}_{iE/H}^{qH}$ can be derived as, accordingly,

$$\mathbf{K}_{iE/H}^{qH} = O\begin{bmatrix} \omega^2\mu_0\varepsilon_0 & 1 \\ 1 & 1 \end{bmatrix}, \ (i = 1), \tag{27}$$

$$\mathbf{K}_{iE/H}^{qH} = O\begin{bmatrix} \omega\mu_0\sigma_i & 1 \\ 1 & 1 \end{bmatrix}, \ (i = 2,3). \tag{28}$$

The scaling of rotated identity operator $\mathbf{I}_{\text{X}}^{p,qH}$ is [17]

$$\mathbf{I}_{\text{X}}^{p,qH} = O\begin{bmatrix} 0 & 1 \\ 1 & 1 \end{bmatrix}, \ (p = 1,2). \tag{29}$$

$$\mathbf{Z}_{\Lambda\Sigma} = \left[\begin{array}{cc|cc|cc|cc} \omega\mu_0 & \omega\mu_0 & \omega^2\mu_0\varepsilon_0 & 1 & 0 & 0 & 0 & 0 \\ \omega\mu_0 & \frac{1}{\omega\varepsilon_0} & 1 & 1 & 0 & 0 & 0 & 0 \\ \hline \omega\mu_0\sigma_2 & 1 & \sigma_2 & \sigma_2 & \omega\mu_0\sigma_2 & 1 & \sigma_2 & \sigma_2 \\ 1 & 1 & \sigma_2 & \frac{1}{\omega\mu_0} & 1 & 1 & \sigma_2 & \frac{1}{\omega\mu_0} \\ \hline \omega\mu_0\sigma_2 & 1 & \sigma_2 & \sigma_2 & \omega\mu_0\sigma_2 & 1 & \sigma_2 & \sigma_2 \\ 1 & 1 & \sigma_2 & \frac{1}{\omega\mu_0} & 1 & 1 & \sigma_2 & \frac{1}{\omega\mu_0} \\ \hline 0 & 0 & 0 & 0 & \omega\mu_0 & \omega\mu_0 & \omega\mu_0\sigma_3 & 1 \\ 0 & 0 & 0 & 0 & \omega\mu_0 & \frac{1}{\sigma_3} & 1 & 1 \end{array}\right]. \tag{30}$$

Eqn (14) $\mathbf{ZI} = \mathbf{V}$ becomes $\mathbf{Z}_{\Lambda\Sigma}\mathbf{I}_{\Lambda\Sigma} = \mathbf{V}_{\Lambda\Sigma}$ after loop-star decomposition. The scaling of $\mathbf{Z}_{\Lambda\Sigma}$ can be written as eqn (30). Apparently, the matrix of eqn (30) is ill-conditioned as frequency approaches zero. To improve the conditioning of $\mathbf{Z}_{\Lambda\Sigma}$, two diagonal matrices are defined as follows:

$$\mathbf{L} = \text{diag}(a_L, b_L, c_L, d_L, e_L, f_L, g_L, h_L), \tag{31}$$

$$\mathbf{R} = \text{diag}(a_R, b_R, c_R, d_R, e_R, f_R, g_R, h_R). \tag{32}$$

The preconditioned equation is

$$\mathbf{Ay} = \mathbf{b}, \tag{33}$$

where $\mathbf{A} = \mathbf{LZ}_{\Lambda\Sigma}\mathbf{R}$, $\mathbf{y} = \mathbf{R}^{-1}\mathbf{I}_{\Lambda\Sigma}$, and $\mathbf{b} = \mathbf{LV}_{\Lambda\Sigma}$. To improve the conditioning of matrix $\mathbf{A}$, the values of rescaling coefficients in matrices $\mathbf{L}$ and $\mathbf{R}$ are selected as follows:

$$a_L = \sqrt{\tfrac{1}{\omega\mu_0}}, b_L = \sqrt{\omega\varepsilon_0}, c_L = \sqrt{\tfrac{1}{\omega\mu_0}}, d_L = \sqrt{\omega\mu_0}, \\ e_L = \sqrt{\tfrac{1}{\omega\mu_0}}, f_L = \sqrt{\omega\mu_0}, g_L = \sqrt{\tfrac{1}{\omega\mu_0}}, h_L = \sqrt{\tfrac{1}{\omega\mu_0}}, \tag{34}$$

$$a_R = \sqrt{\tfrac{1}{\omega\mu_0}}, b_R = \sqrt{\omega\varepsilon_0}, c_R = \sqrt{\omega\mu_0}, d_R = \sqrt{\omega\mu_0}, \\ e_R = \sqrt{\tfrac{1}{\omega\mu_0}}, f_R = \sqrt{\omega\mu_0}, g_R = \sqrt{\omega\mu_0}, h_R = \sqrt{\omega\mu_0}. \tag{35}$$

The scaling of preconditioned matrix $\mathbf{A}$ is shown in equation (36).

$$\mathbf{A}=\left[\begin{array}{cc|cc|cc|cc}
1 & \omega\sqrt{\mu_0\varepsilon_0} & \omega^2\mu_0\varepsilon_0 & 1 & 0 & 0 & 0 & 0 \\
\omega\sqrt{\mu_0\varepsilon_0} & 1 & \omega\sqrt{\mu_0\varepsilon_0} & \omega\sqrt{\mu_0\varepsilon_0} & 0 & 0 & 0 & 0 \\
\hline
\sigma_2 & \sqrt{\frac{\varepsilon_0}{\mu_0}} & \sigma_2 & \sigma_2 & \sigma_2 & 1 & \sigma_2 & \sigma_2 \\
1 & \omega\sqrt{\mu_0\varepsilon_0} & \omega\mu_0\sigma_2 & 1 & 1 & \omega\mu_0 & \omega\mu_0\sigma_2 & 1 \\
\hline
\sigma_2 & \sqrt{\frac{\varepsilon_0}{\mu_0}} & \sigma_2 & \sigma_2 & \sigma_2 & 1 & \sigma_2 & \sigma_2 \\
1 & \omega\sqrt{\mu_0\varepsilon_0} & \omega\mu_0\sigma_2 & 1 & 1 & \omega\mu_0 & \omega\mu_0\sigma_2 & 1 \\
\hline
0 & 0 & 0 & 0 & 1 & \omega\mu_0 & \omega\mu_0\sigma_3 & 1 \\
0 & 0 & 0 & 0 & 1 & \frac{1}{\sigma_3} & 1 & 1
\end{array}\right]. \tag{36}$$

It is observed that much better conditioning of coefficient matrix is achieved. The $\mathbf{I}_{\Lambda\Sigma}$ can be recovered from $\mathbf{y}$ by

$$\mathbf{I}_{\Lambda\Sigma}=\mathbf{R}\mathbf{y}, \tag{37}$$

and the vector of RWG coefficients $\mathbf{I}$ can be recovered as follows:

$$\mathbf{I}=\begin{pmatrix}\mathbf{T}^1 & \\ & \mathbf{T}^2\end{pmatrix}\mathbf{I}_{\Lambda\Sigma}=\begin{pmatrix}\mathbf{T}^1 & \\ & \mathbf{T}^2\end{pmatrix}\mathbf{R}\mathbf{y}, \tag{38}$$

where $\mathbf{T}^p$ is the basis transformation matrix on surface ∂V_p.

The proposed method is stable with respect to the small perturbations of the geometry and material parameter in the framework of Gakerkin testing.

III. NUMERICAL EXAMPLES

The radiation of a vertical magnetic dipole in a spherical shell is calculated to validate the accuracy of the proposed method. The relative error is calculated with $20\log\left(\|\mathbf{x}-\mathbf{y}\|/\|\mathbf{y}\|\right)$, where $\mathbf{x}$ and $\mathbf{y}$ are the calculated and reference results. $\|\bullet\|$ is the l_2 norm.

The parameter $I_m dl$ of the magnetic dipole is 1 Vm. The dipole is placed along $+z$ direction at $(0,0,0.05\text{ m})$. The inner and outer radii of the shell are 0.3 and 0.33 m, respectively. The region V_1 is free space. The parameters of shell V_2 are $\varepsilon_{r2}=1$, $\mu_{r2}=100$, and $\sigma_2=1.0\times 10^7\,\mathrm{S/m}$. The parameters of background region V_3 are $\varepsilon_{r3}=81$, $\mu_{r3}=1$, and $\sigma_3=4\,\mathrm{S/m}$. The frequency is 0.1 Hz. The inner and outer spherical surfaces are discretized with an average edge length of 0.04 m, resulting in 2556 and 3099 RWG functions on the inner and outer surfaces, respectively. The current densities on the outer surface are shown in Figure 2. If the Mie analytical solution is the reference result, the relative errors of electric and magnetic current density on the inner surface are -36.1 and -31.6 dB, respectively; the corresponding relative errors of current densities on the outer surface are -40.9 and -35.9 dB, separately. The condition number reduced from 1.1×10^{22} to 2.4×10^9 after rescaling coefficients were applied.

The scattered fields in region V_1 along the line $\left(r=0.2\text{ m}, 0\le\theta\le\pi, \phi=\pi/4\right)$ are shown in Figure 3. The total fields in the shell along the line $\left(r=0.315\text{ m}, 0\le\theta\le\pi, \phi=\pi/4\right)$ are shown in Figure 4. The transmitted fields in the background media along the line $\left(r=1.2\text{ m}, 0\le\theta\le\pi, \phi=\pi/4\right)$ are shown in Figure 5.

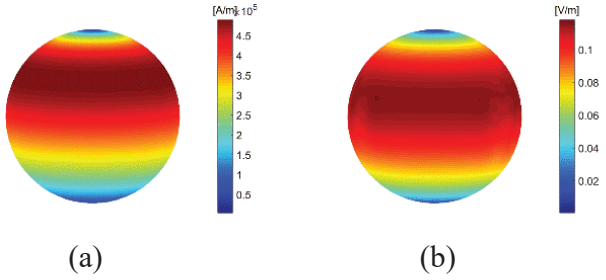

Fig. 2. (a) Electric current density on the outer surface. (b) Magnetic current density on the outer surface.

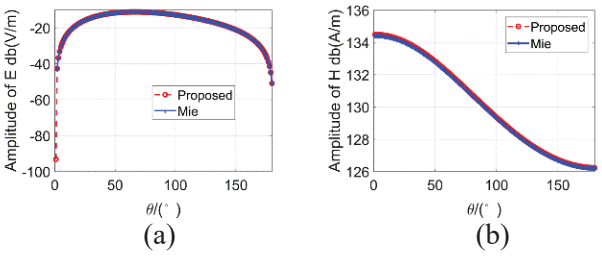

Fig. 3. Scattered fields along the line ($r=0.2\,\mathrm{m}$, $0\le\theta\le\pi, \phi=\pi/4$). (a) Electric field. (b) Magnetic field.

The transmitted electric and magnetic fields on the XOZ plane in the region $-20\le z\le 20, 1\le x\le 41, y=0$ are shown in Figures 6 and 7, respectively. The results calculated with proposed method agree well with reference results.

The transmitted fields of the spherical shell are also calculated at 50 Hz. The inner and outer surfaces of the shell are discretized into 8481 and 10212 RWG functions, respectively. The transmitted fields on the XOZ plane in the region $-20\le z\le 20, 1\le x\le 41, y=0$ are shown in Figures 8 and 9, respectively. It is observed that the amplitude of transmitted fields at 50 Hz is attenuated to a very small level. The reason is that the thickness

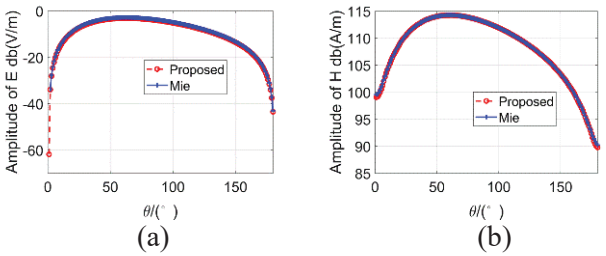

Fig. 4. Total fields along the line ($r=0.315\,\mathrm{m}$, $0\le\theta\le\pi, \phi=\pi/4$). (a) Electric field. (b) Magnetic field.

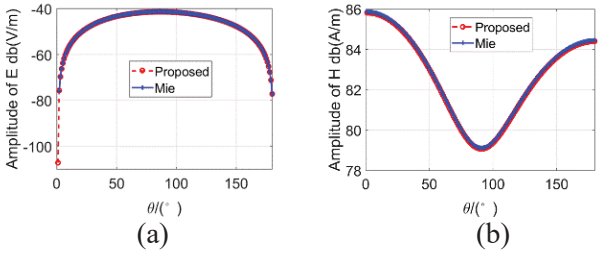

Fig. 5. Transmitted fields along the line ($r = 1.2\,\mathrm{m}$, $0 \le \theta \le \pi, \phi = \pi/4$). (a) Electric field. (b) Magnetic field.

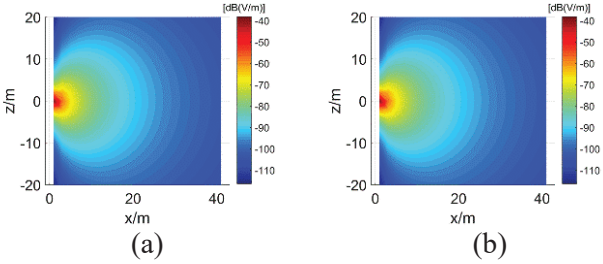

Fig. 6. Transmitted fields on the *XOZ* plane. (a) Electric field calculated with the proposed method. (b) Electric field calculated with Mie series solution.

of the shell is about 13 times of the skin depth at 50 Hz while 0.6 times of the skin depth at 0.1 Hz.

The proposed method can be easily extended to evaluate the transmitted fields of a source in a two-layered magnetic shell with large conductivity. We give the numerical results to verify the proposed method directly since the theory is similar. The inner and outer radii of the inner shell are $a = 0.3$ m and $b = 0.33$ m, respectively. The inner and outer radii of the outer shell are $c = 0.5$ m and $d = 0.53$ m, respectively. The regions $r < a$ and $b < r < c$ are free space. The parameters of shell $a < r < b$ and $c < r < d$ are $\varepsilon_{r2} = 1$, $\mu_{r2} = 100$, and $\sigma_2 = 1.0 \times 10^7\,\mathrm{S/m}$. The parameters of background region $d < r$ are $\varepsilon_{r3} = 81$, $\mu_{r3} = 1$, and $\sigma_3 = 4\,\mathrm{S/m}$. The

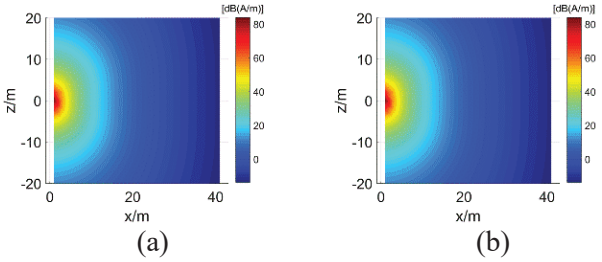

Fig. 7. Transmitted fields on the *XOZ* plane. (a) Magnetic field calculated with the proposed method. (b) Magnetic field calculated with Mie series solution.

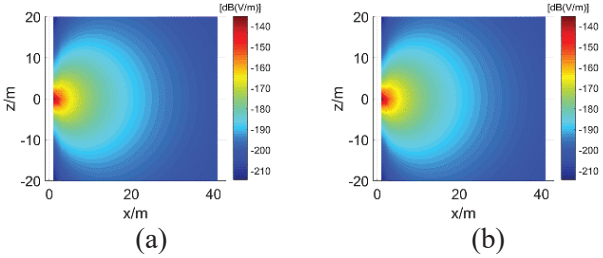

Fig. 8. Transmitted fields on the *XOZ* plane. (a) Electric field calculated with the proposed method. (b) Electric field calculated with Mie series solution.

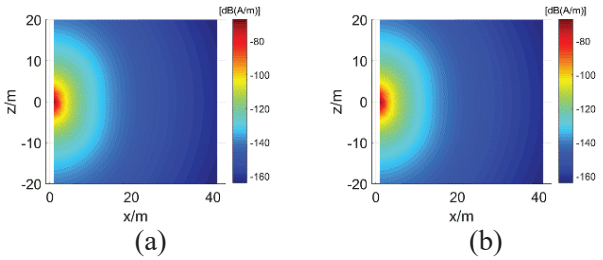

Fig. 9. Transmitted fields on the *XOZ* plane. (a) Magnetic field calculated with the proposed method. (b) Magnetic field calculated with Mie series solution.

frequency is 0.1 Hz. The inner and outer spherical surfaces of inner shell are discretized into 2556 and 3099 RWG functions, respectively. The corresponding total numbers of RWG functions on the inner and outer spherical surfaces of outer shell are 7032 and 7956, respectively. The electric current and magnetic current density on the surface $r = d$ are shown in Figure 10. Compared to Mie series solution, the relative errors of current densities are -49.6 and -41.9 dB, respectively.

The transmitted fields in the background media along the line $\left(r = 1.2\ \mathrm{m}, 0 \le \theta \le \pi, \phi = \pi/4\right)$ are shown in Figure 11. The transmitted electric and magnetic fields on the *XOY* plane in the region $-20 \le x \le 20, 1 \le y \le 41, z = 0$ are shown in Figures 12 and 13, respectively. They agree well with each other.

IV. CONCLUSION

In this work, evaluation of the transmitted fields from a magnetic shell with large but finite conductivity at low frequencies is proposed. The shell is modeled as a penetrable object. EFIE in the exterior problem and MFIE in the interior problem for the shell are selected to capture the wave behaviors outside and inside the shell. Furthermore, loop-star decomposition is carried out on operators in the formulation to overcome the LFB problem. Appropriate rescaling coefficients are applied to the decomposed equation to improve the conditioning at

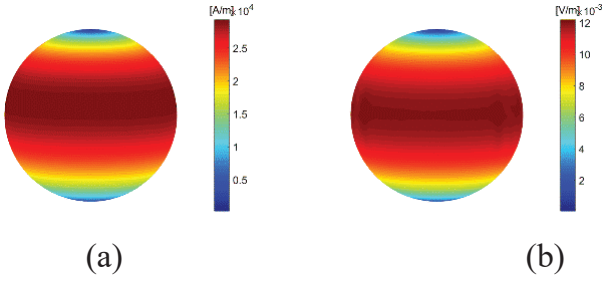

Fig. 10. (a) Electric current density on the surface $r = d$. (b) Magnetic current density on the surface $r = d$.

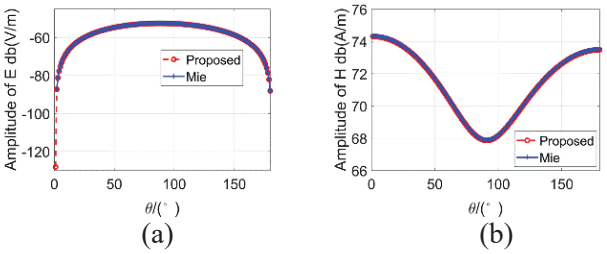

Fig. 11. Transmitted fields along the line $(r = 1.2\,\text{m}, 0 \le \theta \le \pi, \phi = \pi/4)$. (a) Electric field. (b) Magnetic field.

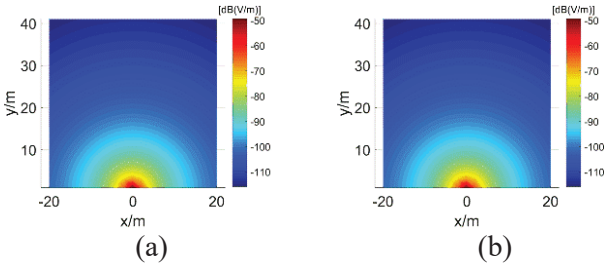

Fig. 12. Transmitted fields on the *XOY* plane. (a) Electric field calculated with the proposed method. (b) Electric field calculated with Mie series solution.

low frequencies. Presented numerical results validate the accuracy of the proposed method.

ACKNOWLEDGMENT

This work was supported by the National Nature Science Foundation of China under Grant 62188102.

APPENDIX

A. Expressions of operators

The explicit expression of operators $\mathscr{L}_{iE}$, $\mathscr{K}_{iE}$, $\mathscr{K}_{iH}$, and $\mathscr{L}_{iH}$ in region V_i are

$$\mathscr{L}_{iE}\left\{\mathbf{X}\left(\mathbf{r}'\right)\right\} = -jk_i\eta_i\int_S g_i\left(\mathbf{r},\mathbf{r}'\right)\mathbf{X}\left(\mathbf{r}'\right)dS' + \frac{\eta_i}{jk_i}\nabla\int_S g_i\left(\mathbf{r},\mathbf{r}'\right)\nabla'\cdot\mathbf{X}\left(\mathbf{r}'\right)dS', \tag{39}$$

$$\mathscr{K}_{iE}\left\{\mathbf{X}\left(\mathbf{r}'\right)\right\} = \int_S \nabla g_i\left(\mathbf{r},\mathbf{r}'\right)\times\mathbf{X}\left(\mathbf{r}'\right)dS', \tag{40}$$

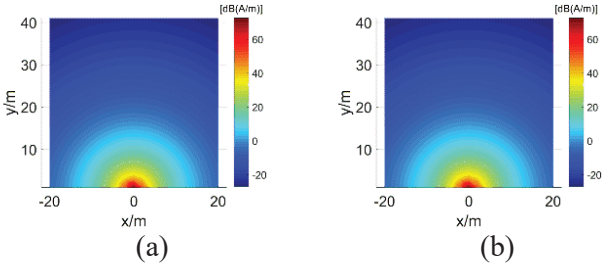

Fig. 13. Transmitted fields on the XOY plane. (a) Magnetic field calculated with the proposed method. (b) Magnetic field calculated with Mie series solution.

$$\mathscr{K}_{iH}\left\{\mathbf{X}\left(\mathbf{r}'\right)\right\} = \int_S \nabla g_i\left(\mathbf{r},\mathbf{r}'\right)\times\mathbf{X}\left(\mathbf{r}'\right)dS', \tag{41}$$

$$\mathscr{L}_{iH}\left\{\mathbf{X}\left(\mathbf{r}'\right)\right\} = \frac{1}{\eta_i^2}\mathscr{L}_{iE}\left\{\mathbf{X}\left(\mathbf{r}'\right)\right\}. \tag{42}$$

$\mathscr{K}_{iE}$ and $\mathscr{K}_{iH}$ include both residue term and Cauchy principal value term. $k_i = \omega\mu_i\varepsilon_{\text{ieff}}$ and $\eta_i = \mu_i/\varepsilon_{\text{ieff}}$ are the wave number and wave impedance in region V_i, respectively. $\varepsilon_{\text{ieff}} = \varepsilon_i + \sigma_i/j\omega$ is the effective permittivity in region V_i. $g_i\left(\mathbf{r},\mathbf{r}'\right) = e^{-jk_iR}/4\pi R$ is the Green's function in the region V_i.

B. Expressions of matrix entries in (14)

The expressions of matrix elements in (14) are as follows:

$$\mathbf{L}_{iE}(m,n) = jk_i\eta_i\int_{S_m}\mathbf{f}_m\cdot\int_{S_n} g_i\left(\mathbf{r},\mathbf{r}'\right)\mathbf{f}_n dr'dr + \frac{\eta_i}{jk_i}\int_{S_m}\nabla\cdot\mathbf{f}_m\cdot\int_{S_n} g_i\left(\mathbf{r},\mathbf{r}'\right)\nabla'\cdot\mathbf{f}_n dr'dr, \tag{43}$$

$$\mathbf{K}_{iE}(m,n) = \int_{S_m}\hat{\mathbf{n}}\times\mathbf{f}_m\cdot\int_{S_n}\nabla g_i\left(\mathbf{r},\mathbf{r}'\right)\times\mathbf{f}_n dr'dr, \tag{44}$$

$$\mathbf{K}_{iH}(m,n) = \int_{S_m}\hat{\mathbf{n}}\times\mathbf{f}_m\cdot\int_{S_n}\nabla g_i\left(\mathbf{r},\mathbf{r}'\right)\times\mathbf{f}_n dr'dr, \tag{45}$$

$$\mathbf{L}_{2H}(m,n) = \frac{jk_i}{\eta_i}\int_{S_m}\mathbf{f}_m\cdot\int_{S_n} g_i\left(\mathbf{r},\mathbf{r}'\right)\mathbf{f}_n dr'dr + \frac{1}{jk_i\eta_i}\int_{S_m}\nabla\cdot\mathbf{f}_m\cdot\int_{S_n} g_i\left(\mathbf{r},\mathbf{r}'\right)\nabla'\cdot\mathbf{f}_n dr'dr, \tag{46}$$

$$\mathbf{V}_e^{\text{in}}(m) = \int_{S_m}\mathbf{f}_m\cdot\mathbf{E}^{\text{in}}d\mathbf{r}. \tag{47}$$

REFERENCES

[1] M. A. Holloway, Z. Dilli, and N. Seekhao, and J. C. Rodgers "Study of basic effects of HPM pulses in digital CMOS integrated circuit inputs," *IEEE Trans. Electromagn. Compat.*, vol. 54, no. 5, pp. 1017-1027, Oct. 2012.

[2] H. Bagci. A. C. Yucel, J. S. Hesthaven, and E. Michielssen, "A fast Stroud-based collocation method for statistically characterizing EMI/EMC phenomena on complex platforms," *IEEE Trans. Magn.*, vol. 51, no. 2, pp. 301-311, May 2009.

[3] W. M. Rucker, R. Hoschek, and K. R. Richter, "Various BEM formulations for calculating eddy currents in terms of field variables," *IEEE Trans. Magn.*, vol. 31, no. 3, pp. 1336-1341, May 1995.

[4] D. Zheng, "Three-dimensional eddy current analysis by the boundary element method," *IEEE Trans. Magn*., vol. 33, no. 2, pp. 1354-1357, Mar. 1997.
[5] B. Song, Z. Zhu, J. D. Rockway, and J. White, "A new surface integral formulation for wideband impedance extraction of 3-D structures," *2003 IEEE/ACM International Conference on Computer Aided Design, San Jose, USA*, Nov. 2003.
[6] Y.-H. Chu and W. C. Chew, "A robust surface-integral-equation formulation for conductive media," *Microw. Opt. Technol. Lett*., vol. 46, no. 2, pp. 109-114, Jul. 2005.
[7] Z. G. Qian, W. C. Chew, and R. Suaya, "Generalized impedance boundary condition for conductor modeling in surface integral equation," *IEEE Trans. Microw. Theory Techn*., vol. 55, no. 11, pp. 2354-2364, Nov. 2007.
[8] D. De Zutter and L. Knockaert, "Skin effect modeling based on a differential surface admittance operator," *IEEE Trans. Microw. Theory Tech*., vol. 53, no. 8, pp. 2526-2538, Aug. 2005.
[9] T. L. Chhim, A. Merlini, L. Rahmouni, J. E. Ortiz Guzman, and F. P. Andriu, "Eddy current modeling in multiply connected regions via a full-wave solver based on the quasi-Helmholtz projectors," *IEEE Open J. Antennas Propag*., vol. 1, pp. 534-548, 2020.
[10] T. Xia, H. Gan, M. Wei, W. C. Chew, H. Braunisch, Z. Qian, and K. Ay, "An integral equation modeling of lossy conductors with the enhanced augmented electric field integral equation," *IEEE Trans. Antennas Propag*., vol. 65, no. 8, pp. 4181-4190, Aug. 2017.
[11] L. Zhang and M. S. Tong, "Low-frequency analysis of lossy interconnect structures based on two-region augmented volume-surface integral equations," *IEEE Trans. Antennas Propag*. Early Access. doi: 10.1109/TAP.2021.3118849.
[12] S. Sharma and P. Triverio, "SLIM: A well-conditioned single-source boundary element method for modeling lossy conductors in layered media," *IEEE Antennas Wireless Propag. Lett*., vol. 19, no. 12, pp. 2072-2076, Dec. 2020.
[13] M. Huynen, K. Y. Kapusuz, X. Sun, G. Van der Plas, E. Beyne, and D. Daniťl, "Entire domain basis function expansion of the differential surface admittance for efficient broadband characterization of lossy interconnects," *IEEE Trans. Microw. Theory Techn*., vol. 68, no. 4, pp. 1217-1233, Apr. 2020.
[14] S. Sharma and P. Triverio, "Electromagnetic Modeling of Lossy Materials with a Potential-Based Boundary Element Method," *IEEE Antennas Wireless Propag. Lett*., Early Access. doi: 10.1109/LAWP.2021.3132626.
[15] S. M. Rao, D. R. Wilton, and A. W. Glisson, "Electromagnetic scattering by surfaces of arbitrary shape," *IEEE Trans. Antennas Propag*., vol. 30, no. 3, pp. 409-418, May 1982.
[16] S. Y. Chen, W. C. Chew, J. M. Song, and J.-S. Zhao, "Analysis of low frequency scattering from penetrable scatterers," *IEEE Trans. Geosci. Remote Sens*., vol. 39, no. 4, pp. 726-735, Apr. 2001.
[17] S. Yan, J. M. Jin, and Z. Nie, "EFIE analysis of low-Frequency problems with loop-star decomposition and Calderón multiplicative preconditioner," *IEEE Trans. Antennas Propag*., vol. 58, no. 3, pp. 857-867, Mar. 2010.

Shifeng Huang received the B.S. and M.S. degrees from Wuhan University, Wuhan, China, in 2014 and 2017, respectively. He is currently working toward the Ph.D. degree in electronic engineering with Shanghai Jiao Tong University, Shanghai, China.

His current research interests include computational electromagnetics and its application in electromagnetic compatibility and scattering problems.

Gaobiao Xiao received the B.S. degree from the Huazhong University of Science and Technology, Wuhan, China, in 1988, the M.S. degree from the National University of Defense Technology, Changsha, China, in 1991, and the Ph.D. degree from Chiba University, Chiba, Japan, in 2002.

He has been a faculty member since 2004 with the Department of Electronic Engineering, Shanghai Jiao Tong University, Shanghai, China. His research interests are computational electromagnetics, coupled thermo-electromagnetic analysis, microwave filter designs, fiber-optic filter designs, phased array antennas, and inverse scattering problems.

Junfa Mao was born in 1965. He received the B.S. degree in radiation physics from the National University of Defense Technology, Changsha, China, in 1985, the M.S. degree in experimental nuclear physics from the Shanghai Institute of Nuclear Research, Chinese Academy of Sciences, Beijing, China, in 1988, and the Ph.D. degree in electronic engineering from Shanghai Jiao Tong University, Shanghai, China, in 1992.

Since 1992, he has been a Faculty Member with Shanghai Jiao Tong University. He was a Visiting Scholar with the Chinese University of Hong Kong, Hong Kong, from 1994 to 1995, and a Postdoctoral Researcher with the University of California at Berkeley, Berkeley, CA, USA, from 1995 to 1996. He has authored or coauthored more than 500 articles. His research interests include interconnect and package problems of integrated circuits and systems, and analysis and design of microwave components and circuits.

Prediction and Analysis of the Shielding Effectiveness and Resonances of a Cascaded Triple Enclosure Based on Electromagnetic Topology

Jin-Cheng Zhou and Xue-Tian Wang

School of Information and Electronics
Beijing Institute of Technology, Beijing 100081, China
zjc.chn@gmail.com, wangxuetian@bit.edu.cn

Abstract **–** A fast analytical method for predicting the shielding effectiveness (SE) and resonances of a parallelly–serially cascaded triple enclosure was proposed. Under the concept of electromagnetic topology, the observation points and the walls are treated as nodes and the space between them as tubes. An equivalent circuit model of the enclosures is derived in which the apertures on the front and rear walls of the two parallelly cascaded sub-enclosures are considered as a pair of three-port networks. To predict the SE at a particular monitoring point, we introduce the position factor. The results of the proposed method have a good agreement with the numerical methods while it is much faster. The proposed method can help in determining SE for cascaded enclosures. We can also find that the resonance effect affects each subenclosure through the apertures, which must be carefully considered in practice.

Index Terms **–** Shielding effectiveness, aperture coupling, general Baum–Liu–Tesche equation

I. INTRODUCTION

The development of high-power microwave (HPM), such as radar illuminating and electromagnetic pulses, in recent years has the potential to damage digital systems. Electromagnetic shielding is one of the most commonly used techniques to protect valuable electronics. The shielding performance of an enclosure with apertures is defined by the shielding effectiveness (SE), which is the ratio of the electric field at an observation point without and with the enclosure [1].

There are numerous approaches for calculating SE of the shielding enclosures with apertures, which can generally be divided into numerical methods and analytical formulations.

Numerical methods include finite-difference time-domain method [2], method of moments [3, 4], transmission line matrix (TLM) method [5]. Numerical methods can handle complicated structures, but they often consume more computational resources.

The analytical formulations are based on circuit models. For instance, Robinson's method [6, 7] and its developed methods [8–11] are based on transmission line parameters. In this type of method, the rectangular enclosure and the aperture are modeled by a short-circuited rectangular waveguide and a transmission line, respectively. However, the analytical formulations can hardly handle complex enclosure structures.

Electromagnetic topology (EMT) provides a useful tool for studying the coupling problems of complicated electrical systems, which treat the complex interaction problem into smaller and more manageable problems [12, 13]. By applying the EMT concept, the Baum–Liu–Tesche (BLT) equation can be derived to calculate the voltage and current responses at the nodes of a general multiconductor transmission line network. After transforming the enclosure and aperture into nodes, we can use the extended BLT equation to calculate the voltage and current at all nodes [14, 15]. In [16], a method is proposed to use the BLT equation to predict the SE of multiple cascaded enclosures, but the monitoring points are limited to the center axis of each front wall.

In this paper, we propose a fast algorithm based on the EMT to predict the SE for a parallelly–serially cascaded triple enclosure. The SE and resonances at any monitor point can be quickly and effectively predicted over a wide bandwidth range by introducing the aperture position factor.

The structure of this paper is as follows. The electromagnetic topological model and equivalent circuit are given along with the derivation of the extended BLT equation in Section II. Validation of the model is given in Section III, and Section IV summarizes the conclusions of this paper.

Submitted On: December 16, 2021
Accepted On: March 11, 2022

https://doi.org/10.13052/2022.ACES.J.370214

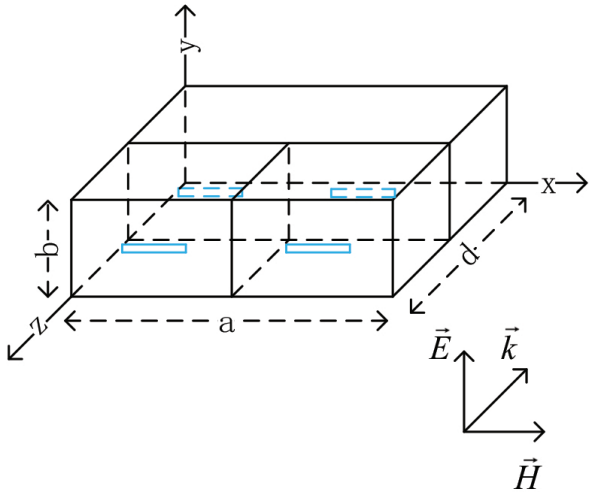

Fig. 1. Rectangular parallelly–serially cascaded enclosure and its coordinate system; all apertures are positioned centrally in the walls.

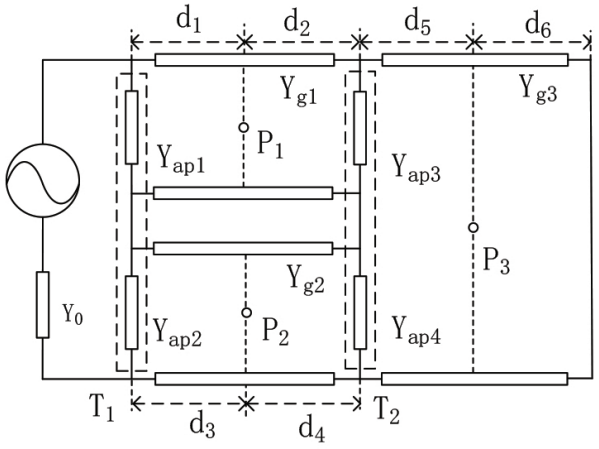

Fig. 2. Equivalent circuit of the parallelly–serially cascaded enclosure.

II. ELECTROMAGNETIC TOPOLOGICAL MODEL

In this paper, we focus on a parallelly–serially cascaded triple enclosure. The structure of this enclosure is shown in Figure 1. The overall size of the enclosure is $300 \times 100 \times 500$ mm, and the thickness of the enclosure wall is 1 mm.

The enclosure consists of three enclosures, and the subenclosure of the left-front one in Figure 1 is labeled as number 1 and has size $c \times b \times d_1$. The one on the right is labeled as number 2 and has the same size as Enclosure 1. And the rear one is labeled as number 3, and the size is $a \times b \times d_2$; it is also the biggest sub-enclosure. The left aperture ap_1 at the front wall of Enclosure 1 has a dimension of $l_1 \times w_1$ and the right aperture ap_2 has a dimension of $l_2 \times w_2$, and another pair of apertures ap_3 and ap_4 with dimensions $l_3 \times w_3$ and $l_4 \times w_4$ are located on the second wall. P_1, P_2, and P_3 are observation points located in the center of each subenclosure, respectively.

The equivalent circuit of the cascaded enclosures in Figure 1 is given in Figure 2. The impedance and propagation constants z_g and k_g are given by

$$k_g = k_0 \sqrt{1 - \left(\frac{m\lambda}{2a}\right)^2 - \left(\frac{n\lambda}{2b}\right)^2} \tag{1}$$

$$Z_g = Z_0 / \sqrt{1 - \left(\frac{m\lambda}{2a}\right)^2 - \left(\frac{n\lambda}{2b}\right)^2}. \tag{2}$$

The radiating source is represented by voltage V_0 and impedance of free space $Z_0 = 377\,\Omega$. Aperture is treated as a coplanar strip transmission line which is shorted at each end; its characteristic impedance is given by Gupta *et al* [17]:

$$Z_{ap} = C_a \frac{j}{2} \frac{l}{a} Z_{os} \tan\left(\frac{\mathrm{k_0 l}}{2}\right). \tag{3}$$

C_a is the position factor which is defined as [8, 11]

$$C_a = \sin\left(\frac{\mathrm{m}\pi}{\mathrm{a}} \mathrm{x_a}\right) \cos\left(\frac{\mathrm{n}\pi}{\mathrm{b}} \mathrm{y_a}\right). \tag{4}$$

x_a and y_a are the position coordinate, and m and n are mode indices. We can find that when the aperture is located at the center of the wall, TE_{01}, TM_{11}, and TE_{20} modes will not exist.

Since the cascaded enclosures have a thickness, we have effective width w_e

$$w_e = w - \frac{5t}{4\pi}\left[1 + \ln\frac{4\pi w}{t}\right] \tag{5}$$

where t is the thickness of the enclosure's wall and w is the width of the aperture. If the shape of the aperture is close to a slot ($w_e \leqslant \frac{b}{\sqrt{2}}$), we have

$$Z_{os} = 120\pi^2 \left[\ln\left(2\frac{1 + \sqrt[4]{1-(w_e/b)^2}}{1 - \sqrt[4]{1-(w_e/b)^2}}\right)\right]. \tag{6}$$

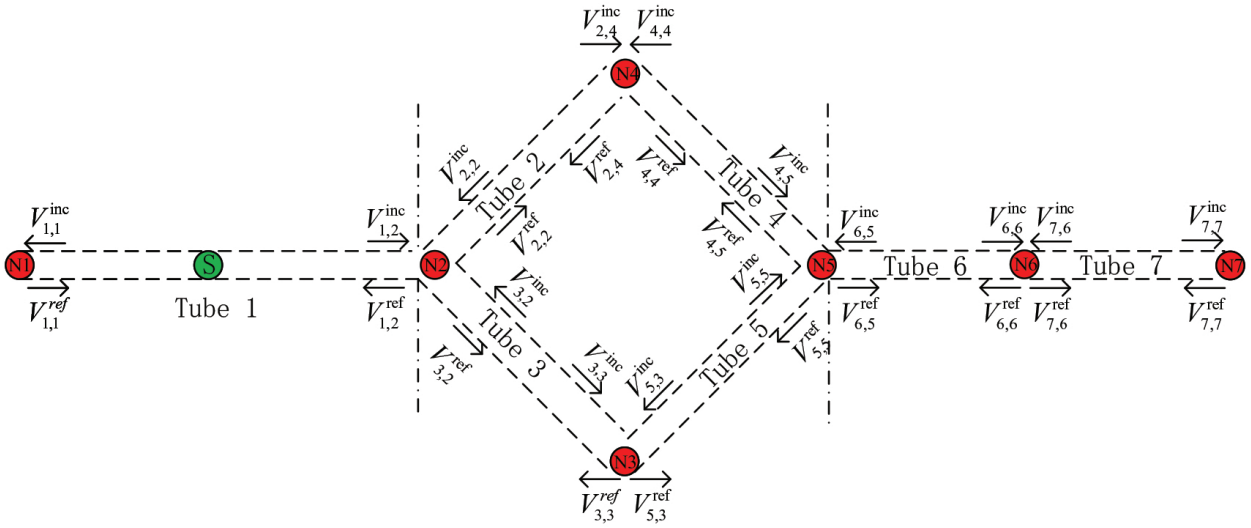

Fig. 3. Signal flow graph of cascaded enclosures.

$$\begin{bmatrix} V^r_{1,1} \\ V^r_{1,2} \\ V^r_{2,2} \\ V^r_{3,2} \\ V^r_{3,3} \\ V^r_{5,3} \\ V^r_{2,4} \\ V^r_{4,4} \\ V^r_{4,5} \\ V^r_{5,5} \\ V^r_{6,5} \\ V^r_{6,6} \\ V^r_{7,6} \\ V^r_{7,7} \end{bmatrix} = \begin{bmatrix} 0 & e^{\gamma_0 l_x} & 0 & 0 & 0 & 0 & 0 & 0 & 0 & 0 & 0 & 0 & 0 & 0 \\ e^{\gamma_0 l_x} & 0 & 0 & 0 & 0 & 0 & 0 & 0 & 0 & 0 & 0 & 0 & 0 & 0 \\ 0 & 0 & 0 & 0 & 0 & 0 & e^{T_1} & 0 & 0 & 0 & 0 & 0 & 0 & 0 \\ 0 & 0 & 0 & 0 & e^{T_3} & 0 & 0 & 0 & 0 & 0 & 0 & 0 & 0 & 0 \\ 0 & 0 & 0 & e^{T_3} & 0 & 0 & 0 & 0 & 0 & 0 & 0 & 0 & 0 & 0 \\ 0 & 0 & 0 & 0 & 0 & 0 & 0 & 0 & 0 & e^{T_4} & 0 & 0 & 0 & 0 \\ 0 & 0 & e^{T_1} & 0 & 0 & 0 & 0 & 0 & 0 & 0 & 0 & 0 & 0 & 0 \\ 0 & 0 & 0 & 0 & 0 & 0 & 0 & 0 & e^{T_2} & 0 & 0 & 0 & 0 & 0 \\ 0 & 0 & 0 & 0 & 0 & 0 & 0 & e^{T_2} & 0 & 0 & 0 & 0 & 0 & 0 \\ 0 & 0 & 0 & 0 & 0 & e^{T_4} & 0 & 0 & 0 & 0 & 0 & 0 & 0 & 0 \\ 0 & 0 & 0 & 0 & 0 & 0 & 0 & 0 & 0 & 0 & e^{T_5} & 0 & 0 & 0 \\ 0 & 0 & 0 & 0 & 0 & 0 & 0 & 0 & 0 & e^{T_5} & 0 & 0 & 0 & 0 \\ 0 & 0 & 0 & 0 & 0 & 0 & 0 & 0 & 0 & 0 & 0 & 0 & 0 & e^{T_6} \\ 0 & 0 & 0 & 0 & 0 & 0 & 0 & 0 & 0 & 0 & 0 & 0 & e^{T_6} & 0 \end{bmatrix} \begin{bmatrix} V^i_{1,1} \\ V^i_{1,2} \\ V^i_{2,2} \\ V^i_{3,2} \\ V^i_{3,3} \\ V^i_{5,3} \\ V^i_{2,4} \\ V^i_{4,4} \\ V^i_{4,5} \\ V^i_{5,5} \\ V^i_{6,5} \\ V^i_{6,6} \\ V^i_{7,6} \\ V^i_{7,7} \end{bmatrix} - \begin{bmatrix} V_0 \\ 0 \\ 0 \\ 0 \\ 0 \\ 0 \\ 0 \\ 0 \\ 0 \\ 0 \\ 0 \\ 0 \\ 0 \\ 0 \end{bmatrix}. \quad (7)$$

Figure 3 gives EMT for the triple enclosures shown in Figure 1. Node N_1 represents the observation point outside the enclosure which is equivalented by one-port network; nodes N_3, N_4, and N_6 denote observation points P_1, P_2, and P_3 inside the subenclosures respectively, and they are equivalented by two-port networks. The apertures are represented by nodes N_2 and N_5 as three-port network, and the shorted end is represented by N_7 as one-port network. Tube 1 denotes the electromagnetic wave propagation in free space, while Tube 2, Tube 3, Tube 4, Tube 5, and Tube 6 are the wave propagation between the observation points and the apertures in subenclosures. Tube 7 denotes the wave propagation to the short end of Enclosure 3.

As illustrated by Figure 3, we have a propagation matrix as shown in eqn (7):

l_x is the distance between electromagnetic wave and the apertures; $\gamma_0 = jk_0$ is the phase constant of freespace. T_i represents the phase constant of each subenclosure:

$$T_1 = \gamma_{g1} d_1, T_2 = \gamma_{g1} d_2 \quad (8)$$

$$T_3 = \gamma_{g2} d_3, T_4 = \gamma_{g2} d_4 \quad (9)$$

$$T_5 = \gamma_{g3} d_5, T_6 = \gamma_{g3} d_6. \tag{10}$$

Here, $\gamma_g = jk_0\sqrt{1-(m\lambda/2a)^2-(n\lambda/2b)^2}$, and d_i shown in Figure 2 represents the distance between each point in the planar wave propagation direction. We can also write eqn (7) as

$$\mathbf{V^{ref}} = \Gamma \times \mathbf{V^{inc}} - \mathbf{V_s}. \tag{11}$$

The scattering matrix S contains the scattering coefficients as shown in eqn (12). For the responses ordered by the tube number, this matrix is sparse, but not necessarily block diagonal, since the locations of the various scattering coefficients depend on how the junctions in the network are numbered and interconnected:

$$\begin{bmatrix} V^r_{1,1} \\ V^r_{1,2} \\ V^r_{2,2} \\ V^r_{3,2} \\ V^r_{3,3} \\ V^r_{5,3} \\ V^r_{2,4} \\ V^r_{4,4} \\ V^r_{4,5} \\ V^r_{5,5} \\ V^r_{6,5} \\ V^r_{6,6} \\ V^r_{7,6} \\ V^r_{7,7} \end{bmatrix} = \begin{bmatrix} \rho^1 & 0 & 0 & 0 & 0 & 0 & 0 & 0 & 0 & 0 & 0 & 0 & 0 & 0 \\ 0 & S^2_{11} & S^2_{12} & S^2_{13} & 0 & 0 & 0 & 0 & 0 & 0 & 0 & 0 & 0 & 0 \\ 0 & S^2_{21} & S^2_{22} & S^2_{23} & 0 & 0 & 0 & 0 & 0 & 0 & 0 & 0 & 0 & 0 \\ 0 & S^2_{31} & S^2_{32} & S^2_{33} & 0 & 0 & 0 & 0 & 0 & 0 & 0 & 0 & 0 & 0 \\ 0 & 0 & 0 & 0 & S^3_{11} & S^3_{12} & 0 & 0 & 0 & 0 & 0 & 0 & 0 & 0 \\ 0 & 0 & 0 & 0 & S^3_{21} & S^3_{22} & 0 & 0 & 0 & 0 & 0 & 0 & 0 & 0 \\ 0 & 0 & 0 & 0 & 0 & 0 & S^4_{11} & S^4_{12} & 0 & 0 & 0 & 0 & 0 & 0 \\ 0 & 0 & 0 & 0 & 0 & 0 & S^4_{21} & S^4_{22} & 0 & 0 & 0 & 0 & 0 & 0 \\ 0 & 0 & 0 & 0 & 0 & 0 & 0 & 0 & S^5_{11} & S^5_{12} & S^5_{13} & 0 & 0 & 0 \\ 0 & 0 & 0 & 0 & 0 & 0 & 0 & 0 & S^5_{21} & S^5_{22} & S^5_{23} & 0 & 0 & 0 \\ 0 & 0 & 0 & 0 & 0 & 0 & 0 & 0 & S^5_{31} & S^5_{32} & S^5_{33} & 0 & 0 & 0 \\ 0 & 0 & 0 & 0 & 0 & 0 & 0 & 0 & 0 & 0 & 0 & S^6_{11} & S^6_{12} & 0 \\ 0 & 0 & 0 & 0 & 0 & 0 & 0 & 0 & 0 & 0 & 0 & S^6_{21} & S^6_{22} & 0 \\ 0 & 0 & 0 & 0 & 0 & 0 & 0 & 0 & 0 & 0 & 0 & 0 & 0 & \rho^6 \end{bmatrix} \begin{bmatrix} V^i_{1,1} \\ V^i_{1,2} \\ V^i_{2,2} \\ V^i_{3,2} \\ V^c_{3,3} \\ V^i_{5,3} \\ V^i_{2,4} \\ V^i_{4,4} \\ V^i_{4,5} \\ V^i_{5,5} \\ V^i_{6,5} \\ V^i_{6,6} \\ V^i_{7,6} \\ V^i_{7,7} \end{bmatrix}. \tag{12}$$

$\rho^1 = 0$ is the free space, and $\rho^6 = -1$ is the short end of the Enclosure 3. S^3 , S^4, and S^5 represent P_1 , P_2, and P_3:

$$S^3 = S^4 = S^6 = \begin{bmatrix} 0 & 1 \\ 1 & 0 \end{bmatrix}. \tag{13}$$

S^2 and S^5 can be obtained from network T_1 and T_2 in Figure 2 respectively. Since the apertures are orthogonal to the propagation direction, we cannot determine the transmission between them; so we neglect the coupling between aperture 1 and aperture 2 and, hence, $S^2_{23} = S^2_{32} = 0$:

$$S^2_{11} = (Y_0Y_{g2} + Y_0Y_{ap2} + Y_0Y_{ap1} + Y_0Y_{g1} - Y_{g1}Y_{g2} - Y_{g1}Y_{ap2} - Y_{g2}Y_{ap1} - Y_{ap1}Y_{ap2})/Y_t^2$$

$$S^2_{12} = 2(Y_0Y_{g2} + Y_0Y_{ap2})/Y_t^2$$

$$S^2_{13} = 2(Y_0Y_{g1} + Y_0Y_{ap1})/Y_t^2$$

$$S^2_{21} = 2(Y_0Y_{g1} + Y_{g1}Y_{g2} + Y_{g1}Y_{ap2})/Y_t^2$$

$$S^2_{22} = (Y_0Y_{g1} + Y_{g1}Y_{g2} + Y_{g1}Y_{ap2} - Y_0Y_{ap1} - Y_{g2}Y_{ap1} - Y_{ap1}Y_{ap2} - Y_0Y_{ap2} - Y_0Y_{g2})/Y_t^2$$

$$S^2_{31} = 2(Y_0Y_{g2} + Y_{g1}Y_{g2} + Y_{g2}Y_{ap1})/Y_t^2$$

$$S^2_{33} = Y_0Y_{g2} + Y_{g1}Y_{g2} + Y_{g2}Y_{ap1} - Y_0Y_{ap2} - Y_{g1}Y_{ap2} - Y_0Y_{ap2} - Y_0Y_{g1} - Y_{ap1}Y_{ap2}$$

$$Y_t^2 = Y_0Y_{g2} + Y_0Y_{ap2} + Y_0Y_{ap1} + Y_0Y_{g1} + Y_{g1}Y_{g2} + Y_{g1}Y_{ap2} + Y_{g2}Y_{ap1} + Y_{ap1}Y_{ap2}.$$

For the same reason mentioned above, $S^5_{12} = S^5_{21} = 0$:

$$S^5_{11} = (Y_{g1}Y_{g3} + Y_{g1}Y_{g2} + Y_{g1}Y_{ap4} - Y_{g3}Y_{ap3} - Y_{g2}Y_{ap3} - Y_{g3}Y_{ap4} - Y_{g2}Y_{g3} - Y_{ap3}Y_{ap4})/Y_t^5$$

$$S^5_{13} = 2(Y_{g1}Y_{g3} + Y_{g1}Y_{g2} + Y_{g1}Y_{ap4})/Y_t^5$$

$$S^5_{22} = (Y_{g2}Y_{g3} + Y_{g1}Y_{g2} + Y_{g2}Y_{ap3} - Y_{g3}Y_{ap4} - Y_{g1}Y_{ap4} - Y_{ap3}Y_{ap4} - Y_{g3}Y_{ap3} - Y_{g1}Y_{g3})/Y_t^5$$

$$S^5_{23} = 2(Y_{g2}Y_{g3} + Y_{g1}Y_{g2} + Y_{g2}Y_{ap3})/Y_t^5$$

$$S^5_{31} = 2(Y_{g2}Y_{g3} + Y_{g3}Y_{ap4})/Y_t^5$$

$$S^5_{32} = 2(Y_{g1}Y_{g3} + Y_{g3}Y_{ap3})/Y_t^5$$

$$S^5_{33} = (Y_{g1}Y_{g3} + Y_{g3}Y_{ap3} + Y_{g3}Y_{ap4} + Y_{g2}Y_{g3} - Y_{g1}Y_{g2} - Y_{g2}Y_{ap3} - Y_{g1}Y_{ap4} - Y_{ap3}Y_{ap4})/Y_t^5$$

$$Y_t^5 = Y_{g1}Y_{g3} + Y_{g1}Y_{ap3} + Y_{g1}Y_{ap4} + Y_{g1}Y_{g2} + Y_{g2}Y_{g3} + Y_{g2}Y_{ap3} + Y_{g3}Y_{ap4} + Y_{ap3}Y_{ap4}.$$

The values of Y_0, Y_{gn}, and Y_{apn} are derived from the equivalent circuit and eqn (2), and (3). For ap_3 and ap_4, they are located on the front wall of Enclosure 3; so the width is 300 mm and $x_a = a/4$.

We can also write eqn (12) as

$$\mathbf{V^{ref}} = \mathbf{S} \times \mathbf{V^{inc}}. \tag{14}$$

The voltage response is defined as $\mathbf{V} = \mathbf{V^{ref}} + \mathbf{V^{inc}}$ and, denotes the voltage response at the central point of the $z = z_p$ plane; then we have the extensional BLT equation [14]:

$$\mathbf{V} = (\mathbf{E} + \mathbf{S}) \times (\Gamma - \mathbf{S})^{-\mathbf{1}} \times \mathbf{V_s}. \tag{15}$$

Here, E is a unit matrix, Γ is the propagation matrix as shown in eqn (7), and S is the scattering matrix. V_s is the source matrix, and since we have only one source in Tube 1, the V_s has only one element in the first line.

The total voltage equal to the sum of the voltages in the different propagation modes, the SE at point P is calculated by $\mathrm{SE} = -20\log(\mathrm{V_p}/\mathrm{V_0})$.

III. RESULTS AND DISCUSSION

In this section, we use CST-MWS, a 3D electromagnetic simulation program, to check the validity of the model presented in Section II. The incident plane wave propagates along the $+z$ axis, and the frequency range is between 0.2 and 2.2 GHz.

Enclosures 1, 2, and 3 shown in Figure 1 have dimensions of $150 \times 100 \times 240, 150 \times 100 \times 240$, and $300 \times 100 \times 260$ mm, respectively. And the sizes of each aperture are defined as $60 \times 10, 50 \times 10, 60 \times 10$, and 70×10 mm, respectively. And the P_1, P_2, and P_3 are in (75, 50, 380), (225, 50, 380), and (150, 50, 130), respectively.

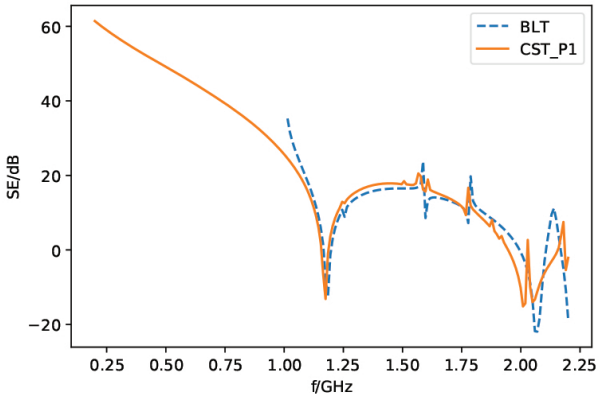

(a)

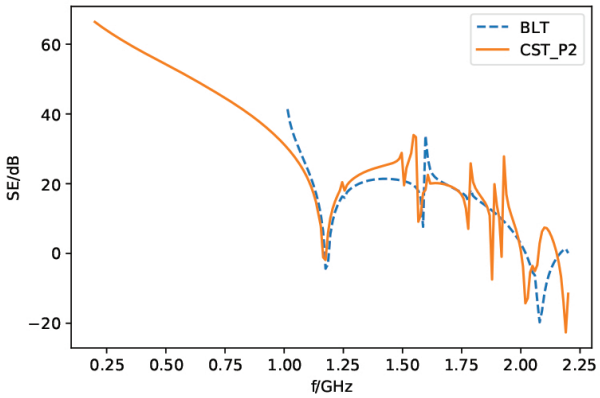

(b)

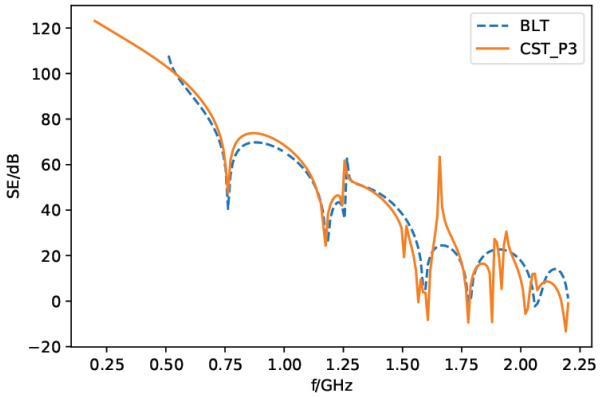

(c)

Fig. 4. Comparison between the SE result from the BLT equation with that of CST for observe points 1, 2, and 3, respectively.

A. Results of different enclosures

Figure 4(a) shows SE at P_1, and this is also the center of Enclosure 1. It can be observed that the result calculated by the proposed method is in good agreement with the simulation result of CST. The minimum SE values due to the resonance effect are just located at the resonance points which can be calculated by eqn (16):

$$f_{mnh} = \frac{C}{2}\sqrt{\left(\frac{m}{a}\right)^2 + \left(\frac{n}{b}\right)^2 + \left(\frac{h}{d}\right)^2} \tag{16}$$

where m, n, and h are determined by the wave modes in the enclosure. In Enclosure 1, the resonant frequency is 1179.24 MHz for the TE_{101} mode and 1600.78 MHz for the TE_{102} mode. 1000 MHz is the cutoff frequency of TE_{10} mode Enclosure 1, and the cutoff frequency of TE_{30} in Enclosure 1 is 3000 MHz; consequently, the higher-order propagation modes are blocked.

Figure 4(b) shows the SE at P_2, which have a similar SE of P_1 due to the same dimension size. The difference of SE results from the different dimensions of the apertures.

Figure 4(c) shows the SE at P_3, and compared with SE at the observation point P_1, the SE at the center of Enclosure 3 improves by 20 dB in most frequency ranges, except at the resonance points. From Figure 4(c), it can be seen that the result of SE with the proposed method is in good agreement with that of CST-MWS. Figure 4(c) shows the resonant frequencies of different transmission modes, such as 763.44 (TE_{101}), 1154.49 (TE_{201}), 1257.52 (TE_{102}), 1607.12 (TE_{301}), 1801.54 (TE_{103}), and 2081.54 MHz (TE_{401}). As we have seen in Section II, ap_3 and ap_4 are not at the center of the front wall of Enclosure 3, so TE_{201} and TE_{401} modes appear in Enclosure 3; Note that the TE_{201} mode is also TE_{101} mode in Enclosure 1 and Enclosure 2, which further weakens the SE in Enclosure 3. We can conclude that the shielding capacity of the inner enclosures is obviously much better than that of the outer enclosure, and the resonant modes of the different enclosures influence each other through the apertures; this must be considered in practice. By observing eqn (16), we can also see that reducing the size of the enclosure will increase the resonant frequency; in other words, separating the outer enclosure into two smaller enclosures helps to improve the SE of the inner enclosure.

B. Results of different positions

By applying the position factor in eqn (4), we obtain voltage distribution at any observation point: $v_p^{'} = v_p C_a$; then an off-center observation point can be considered in this way. We have moved the observation points to new positions, and the new points P_1', P_2', and P_3' are located in (30, 50, 380), (225, 80, 380), and (150, 50, 100).

Figure 5(a) shows the SE at P_1', and we can see that the SE at P_1' is about 5 dB higher than at P_1, indicating that the off-center point has a better SE.

Figure 5(b) shows the SE at P_2'. Unlike the case of P_1', the SE of P_2' is very close to P_2. Since TE_{10} is the main mode in Enclosure 2, it leads to a consistent voltage distribution in the y-axis direction.

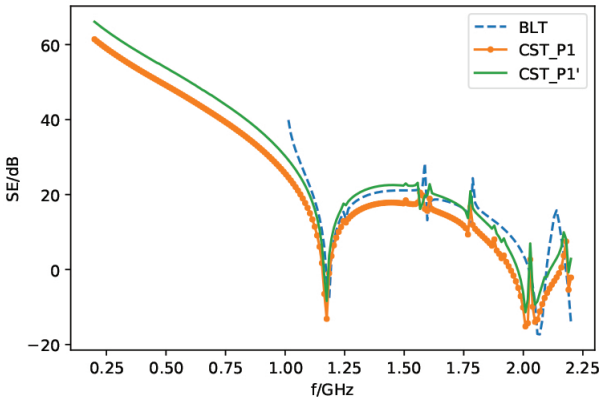

(a)

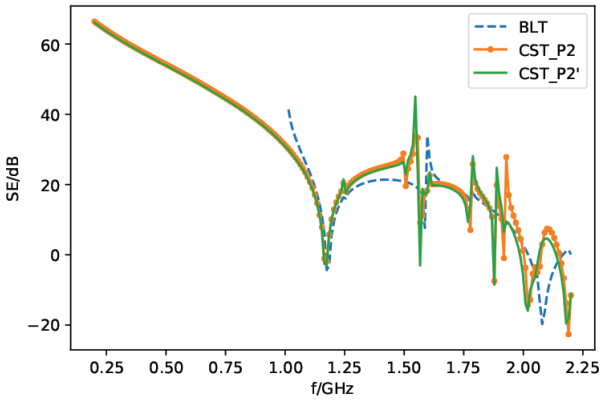

(b)

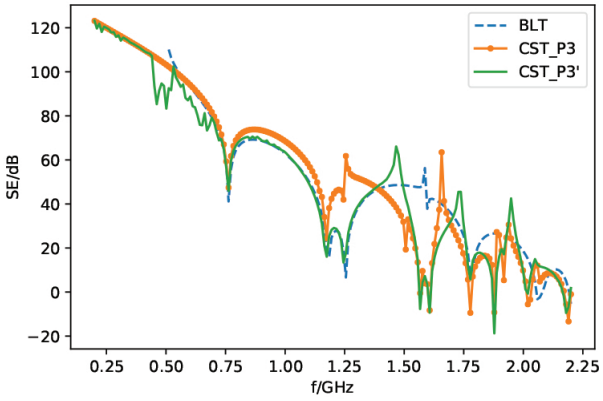

(c)

Fig. 5. Comparison between the SE results from P_1', P_2', and P_3' with the same position and the original position P_1, P_2, and P_3 of CST.

Figure 5(c) shows the SE at P_3'. We vary the z coordinate by changing d in the propagation matrix. It can be observed that the results of SE for the same enclosure differ greatly between two different monitor points.

All cases were calculated on the same computer running a 2.2-GHz Intel i7-8750 CPU. The CST takes 25–30 minutes for a simulation with 200 frequency points, while the fast algorithm takes no more than 0.2 seconds for the same case, indicating the high computational efficiency of the fast algorithm compared to the CST simulation.

IV. CONCLUSION

In this paper, we propose a fast algorithm based on EMT theory and the BLT equation to analyze the shielding performance of an apertured triple enclosure illuminated by an external plane wave. We derive a double three-port scattering matrix to describe the coupling relationship of the triple enclosure. By introducing the position factor c_a, the SE and resonances at any observation point can be easily predicted. Several observation points are presented to demonstrate the validity and accuracy of the algorithm. The proposed method has a good agreement with numerical method over a wide frequency range, while it can significantly improve the computation speed. This algorithm also proves that the BLT equation can handle complex enclosures by changing the EMT relationship.

REFERENCES

[1] T. Cvetković, V. Milutinović, N. Dončov, and B. Milovanović, "Numerical Investigation of Monitoring Antenna Influence on Shielding Effectiveness Characterization," *The Applied Computational Electromagnetics Society Journal (ACES)*, pp. 837-846, 2014.

[2] S. Georgakopoulos, C. Birtcher, and C. Balanis, "HIRF penetration through apertures: FDTD versus measurements," *IEEE Transactions on Electromagnetic Compatibility*, vol. 43, no. 3, pp. 282-294, Aug. 2001.

[3] R. Araneo and G. Lovat, "Fast MoM Analysis of the Shielding Effectiveness of Rectangular Enclosures With Apertures, Metal Plates, and Conducting Objects," *IEEE Transactions on Electromagnetic Compatibility*, vol. 51, no. 2, pp. 274-283, May 2009.

[4] B. Audone and M. Balma, "Shielding effectiveness of apertures in rectangular cavities," *IEEE Transactions on Electromagnetic Compatibility*, vol. 31, no. 1, pp. 102-106, Feb. 1989.

[5] B.-L. Nie, P.-A. Du, Y.-T. Yu, and Z. Shi, "Study of the Shielding Properties of Enclosures With Apertures at Higher Frequencies Using the Transmission-Line Modeling Method," *IEEE Transactions on Electromagnetic Compatibility*, vol. 53, no. 1, pp. 73-81, Feb. 2011.

[6] M. P. Robinson, T. M. Benson, C. Christopoulos, J. F. Dawson, M. D. Ganley, A. C. Marvin, S. J. Porter, and D. W. P. Thomas, "Analytical formulation for the shielding effectiveness of enclosures with apertures," *IEEE Transactions on Electromagnetic Compatibility*, vol. 40, no. 3, p. 9, 1998.

[7] M. P. Robinson, J. D. Turner, D. W. P. Thomas, J. F. Dawson, M. D. Ganley, A. C. Marvin, S. J. Porter, T. M. Benson, and C. Christopoulos, "Shielding effectiveness of a rectangular enclosure with a rectangular aperture," *Electronics Letters*, vol. 32, no. 17, pp. 1559-1560, Aug. 1996, publisher: IET Digital Library.

[8] F. Po'ad, M. Jenu, C. Christopoulos, and D. Thomas, "Analytical and experimental study of the shielding effectiveness of a metallic enclosure with off-centered apertures," in *2006 17th International Zurich Symposium on Electromagnetic Compatibility*, pp. 618-621, IEEE, Singapore, 2006.

[9] C.-C. Wang, C.-Q. Zhu, X. Zhou, and Z.-F. Gu, "Calculation and Analysis of Shielding Effectiveness of the Rectangular Enclosure with Apertures," *The Applied Computational Electromagnetics Society Journal (ACES)*, pp. 535-545, 2013.

[10] M.-C. Yin and P.-A. Du, "An Improved Circuit Model for the Prediction of the Shielding Effectiveness and Resonances of an Enclosure With Apertures," *IEEE Transactions on Electromagnetic Compatibility*, vol. 58, no. 2, pp. 448-456, Apr. 2016.

[11] B.-L. Nie and P.-A. Du, "An Efficient and Reliable Circuit Model for the Shielding Effectiveness Prediction of an Enclosure With an Aperture," *IEEE Transactions on Electromagnetic Compatibility*, vol. 57, no. 3, pp. 357-364, Jun. 2015.

[12] F. Tesche, "Topological concepts for internal EMP interaction," *IEEE Transactions on Antennas and Propagation*, vol. 26, no. 1, pp. 60-64, Jan. 1978.

[13] C. E. Baum, "Electromagnetic Topology for the Analysis and Design of Complex Electromagnetic Systems," in J. E. Thompson and L. H. Luessen, editors, *Fast Electrical and Optical Measurements: Volume I — Current and Voltage Measurements/ Volume II — Optical Measurements*, NATO ASI Series, pp. 467-547, Springer Netherlands, Dordrecht, 1986.

[14] F. M. Tesche, J. M. Keen, and C. M. Butler, "Example of the use of the BLT equation for EM field propagation and coupling calculations," *URSI Radio Science Bulletin*, vol. 2005, no. 312, pp. 32-47, Mar. 2005.

[15] F. M. Tesche, "On the Analysis of a Transmission Line With Nonlinear Terminations Using the Time-Dependent BLT Equation," *IEEE Transactions on Electromagnetic Compatibility*, vol. 49, no. 2, pp. 427-433, May 2007.

[16] Kan Yong, Yan Li-Ping, Zhao Xiang, Zhou Hai-Jing, Liu Qiang, and Huang Ka-Ma, "Electromagnetic topology based fast algorithm for shielding effectiveness estimation of multiple enclosures with apertures," *Acta Physica Sinica*, vol. 65, no. 3, p. 030702, 2016.

[17] K. Gupta, R. Garg, I. Bahl, and P. Bhartia, *Microstrip Lines and Slotlines*, Artech House, 1996.

Jincheng Zhou was born in Jiangsu, China, in 1990. He received the B.A. degree from Xi'an Technological University, China, in 2008. He is currently working toward the Ph.D. degree with at the School of Information and Electronics, Beijing Institute of Technology. His research interests include radio propagation, EMC, and EM protection.

Xuetian Wang was born in Jiangsu, China, in 1961. He received the Ph.D. from the Department of Electronic Engineering, Beijing Institute of Technology in 2002. He has been working with t Beijing Institute of Technology as a Researcher since August 2001, and he has been a Professor since 2003. His research interests include EMC, EM protection, and electromagnetic radiation characteristics.

Analysis of Nonlinear Characteristics and the Factors Affecting the Operation of the Active Magnetic Bearings Rotor System Considering Alford Force

Siyuan Zhang[1], Jin Zhou[2], Xiaoming Han[1], and Yanchao Ma[1]

[1]College of Mechanical and Electrical Engineering
Nanjing University of Aeronautics and Astronautics, Nanjing 210016, China
zhangsiyuan@nuaa.edu.cn, hanxiaoming@nuaa.edu.cn, mayanchao@nuaa.edu.cn

[2]National Key Laboratory of Science and Technology on Helicopter Transmission
Nanjing University of Aeronautics and Astronautics, Nanjing 210016, China
zhj@nuaa.edu.cn

Abstract – Based on a test rig supported by active magnetic bearings (AMBs), this paper focuses on the study of the nonlinear dynamic characteristics and the factors affecting the operation of a rotor system under the coupling of magnetic bearing force and Alford force. In order to solve the nonlinear dynamic response of rotor system, a dynamic equation of the rotor which introduces Alford force and the electromagnetic force of the AMBs controlled by PID is established. By changing the control parameters (k_P and k_D), operation parameters (rotational speed), and structural parameters (clearance between impeller and volute), the equation is solved by using Runge−Kutta method. The results show that the rotor system exhibits complex nonlinear dynamic characteristics under the coupling action of Alford force and magnetic bearing force. The rotor system appears different dynamic behaviors such as single period, multi multi-period, and quasi quasi-period when changing the control parameters. Among all the control parameters, adjusting k_D is more effective to ensure system stability. The amplitude of rotor increases from 8.2 μm to 11.9 μm with the increase of speed from 6000 rpm to 10,000 rpm, while that decreases from 9.6 μm to 8.2 μm with the increase of clearance between impeller and volute from 1mm to 4 mm. Therefore, under the influence of Alford force, apart from the control parameters, the operation parameters and structural parameters of magnetic bearings also affect the operation of the rotor system supported by the AMBs.

Index Terms – Active magnetic bearings, Alford force, Rotor rotor dynamics, Nonlinearnonlinear.

I. INTRODUCTION

The stable operation of rotor system is the premise of normal operation of rotating machinery. However, because of the manufacturing and assembly problems, the impeller and volute are relatively eccentric, thus leading to the uneven distribution of tip clearance unevenly distribution as well as the difference in blade efficiency and pressure distribution around the circumference. According to Bernoulli principle, the blade with small clearance is more efficient and dose does more work and, therefore, receives more aerodynamic load. In consequence, apart from the resultant torque, a transverse force acting on the impeller axis which increases with the increase of impeller eccentricity is generated by the circumferential aerodynamic force. The transverse force is a self-excited force of the rotor which may eventually cause the instability of the rotor. Consequently, it is necessary to explore the influence of this force coupling on the rotor system.

GE found this phenomenon in the test of a gas turbine. The vibration was not effectively eliminated by dynamic balance method but finally solved by changing the structure. At that time, people did not pay more attention to this phenomenon. Until 1958, Thomas first raised this problem in the study of the stability of steam turbine [1]. Alford studied this problem and established a mechanical model [2]. Therefore, this force is usually called Alford force. Since then, many scholars have studied Alford force. Cheng *et al*. who combined rolling bearing force with Alford force and used the Runge−Kutta method to solve the dynamic equations of the system found that excessive bearing clearance and rotor eccentricity will reduce the stability of the system [3]. Jung *et al*. did a limit-cycle analysis of auto-balancer system considering Alford force. The results showed that for certain combinations of bearing parameters and operating speeds, the global asymptotic stability of the synchronous balanced condition can be guaranteed [4]. Yada *et al*. analyzed the open/close nozzle mode and the open/close ratio of the symmetrical

Submitted On: October 28, 2021
Accepted On: January 26, 2022

https://doi.org/10.13052/2022.ACES.J.370215

part of the partial intake turbine in the turbopump of the rocket engine. It is found that the Alford force varies with the rotation angle at a certain opening/closing ratio and put forward the universal rules to provide guidelines for follow-up research [5]. Taking the flexible shaft and elastic disk rotor system as the research object, Yang *et al*. established the vibration differential equation with the modal synthesis method and solved the equation by using the Runge−Kutta method. The results showed that the increase of speed and disk radius will lead to the increase of rotor response, which can help to improve the stability of the system by adjusting the support position [6]. Li *et al*. analyzed the impact of nonlinear coupling factor and blade-bending vibration to dynamic characteristics of rotor-bearing system and the results indicated that the Alford force caused by blade tip clearance makes the motion state of the system more complex [7].

Based on the rolling bearing rotor system, many scholars have studied the factors that affect the operation of rotor system considering Alford force. However, in recent years, with the application and development of electromagnetic technology, permanent magnet generator [8–10], maglev planar motor [11–13], and magnetic bearings [14–16] have been widely concerned because of its advantages of no friction, high speed, and long life. In addition, active magnetic bearings (AMBs) that can be actively controlled has have been successfully applied in many industrial products [17]. Therefore, it is necessary to study the factors affecting the stability of the rotor system supported by the AMBs under Alford force. There are few researches on it, nevertheless. Wang *et al*. who established the finite element model of the coupling of magnetic bearing force and Alford force under PID control algorithm used the Newmark-β method to solve the dynamic response of the rotor system. The results showed that under the action of magnetic bearing force and Alford force, the system shows complex dynamic characteristics and the control parameters have great influence on the characteristics of rotor system. But, this paper only does the simulation research [18].

In this paper, an AMB test rig is taken as the research object, a dynamic equation which considers the coupling effect of Alford force and magnetic bearing force under the PID controller is established, and the rotor response is solved with the Runge−Kutta method. The results show that after considering Alford force, the system has significant nonlinear characteristics. Meanwhile, by changing the control parameters (k_P and k_D), operating parameters (rotational speed), as well as structural parameters (clearance between impeller and volute), the characteristics of the system have changed greatly. It shows that different from the traditional bearing, the magnetic bearing should take not only structural characteristics but also the control parameters into account.

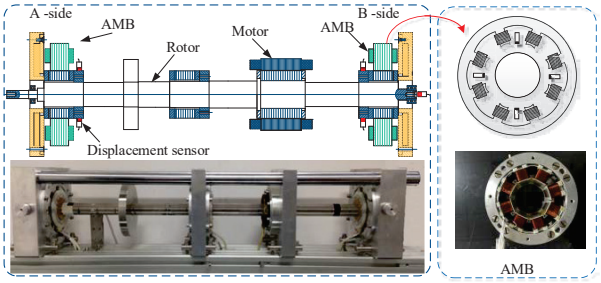

Fig. 1. Active magnetic bearing rotor system structure.

II. MODELING OF THE AMBs ROTOR SYSTEM CONSIDERING ALFORD FORCE

A. The AMBs rotor system model

A typical AMB rotor system structure is shown in the Figure 1. It is limited to 5 five degrees of freedom by AMBs and driven to rotate by motor.

The electromagnetic force produced by an electromagnet in a magnetic bearing can be expressed as

$$f_x = \frac{\mu_0 A N^2}{4}\left(\frac{I_0}{C_0}\right)^2. \tag{1}$$

The magnetic bearing adopts differential arrangement in one degree of freedom and the resultant force under the action of a pair of magnets is:

$$\begin{aligned} f_x &= f_{x1} - f_{x2} \\ &= \frac{\mu_0 A N^2}{4}\left[\left(\frac{I_0 + i_x}{C_0 + x\cos\alpha}\right)^2 - \left(\frac{I_0 - i_x}{C_0 - x\cos\alpha}\right)^2\right]. \end{aligned} \tag{2}$$

The Taylor expansion is carried out at i_x = 0, x = 0 and the higher order term is ignored, . The magnetic bearing force on the rotor can be expressed as:

$$\begin{aligned} f_{\mathrm{AMB}} &= \frac{\mu_0 A N^2 I_0^2 \cos^2\alpha}{C_0^3} x + \frac{\mu_0 A N^2 I_0 \cos\alpha}{C_0^2} i_x \\ &= k_h x + k_i i_x, \end{aligned} \tag{3}$$

where μ_0 is the vacuum permeability, A is the area of a single magnetic pole, N is the total number of turns of the coil on a pair of magnetic poles, C_0 is the unilateral air gap when the rotor is at the magnetic center, I_0 is the coil bias current, i_x is the coil control current, k_h is the displacement stiffness coefficient, and k_i is the current stiffness coefficient.

B. Alford force model

Many scholars have focused on the modeling of Alford force. The first model given by Thomas is as follows:

$$f = \frac{m_o \lambda u}{2} \cdot \frac{d\xi_{sp}}{d\delta} \cdot e, \tag{4}$$

where m_o is the total gas flow, λ is the pressure coefficient, u is the tangent speed at the center of the blade, ζ_{sp} is the local efficiency loss, δ is the tip clearance, and e is the eccentricity.

Alford made a further study and established the model as:

$$f = \frac{T\beta e}{DH}, \tag{5}$$

where, T is the torque on the impeller, D is the diameter at the center of the blade, H is the blade height, β is the efficiency coefficient, and e is the eccentricity.

However, their models have some limitations. First, their models are based on the local efficiency loss of impeller. What's more, it is difficult to get some parameters of the model. In Thomas' model, $\frac{d\xi_{sp}}{d\delta}$ is irregular and difficult to calculate. In Alford's model, similar to the correction factor, β is a variable value that can be adjusted to meet the matching between theory and experiment by adjusting that value. Since then, many scholars have revised and improved the Alford force model [19–20]. Among them, based on fluid mechanics and momentum theorem, Chai *et al.* combined the impeller structure parameters to carry out theoretical modeling and used numerical methods to verify the reliability of the model [21]. This paper applies the model established by Chai *et al*. The details are as below follows:

$$\begin{aligned}
&f_{\mathrm{ALFORD}} = A_1 \cdot e + A_3 \cdot e^3,\\
&e = \sqrt{x^2 + y^2},\\
&A_1 = \left(R_T{}^2 - R_B{}^2\right)^2 \pi C R_T / \left(R_T{}^2 - R_B{}^2 + 2R_T\bar{\delta}\right)^2,\\
&A_3 = 3\left(R_T{}^2 - R_B{}^2\right)^2 \pi C R_T{}^3 / \left(R_T{}^2 - R_B{}^2 + 2R_T\bar{\delta}\right)^4,\\
&C = V^2 \sin\beta_1 \rho_0 \left(\cos\beta_1 + \zeta\cos\beta_2\right),\\
&\begin{cases} f_{ax} = f_a \cdot \cos\theta \\ f_{ay} = f_a \cdot \sin\theta \end{cases} \left(\tan\theta = \frac{y}{x}\right),
\end{aligned} \tag{6}$$

where e is the eccentricity, R_T is the tip radius, R_B is the root radius, β_1 is the inlet angle, β_2 is the outlet angle, ρ_0 is the airflow density, ζ is the speed coefficient, $\bar{\delta}$ is the average tip clearance, V is the inlet speed, and f_{ax}, f_{ay} are the component forces of the Alford force in the x and y directions.

C. System dynamics equation

Alford force and magnetic bearing force are substituted into the rotor system and the system dynamics equation is as follows:

$$m\ddot{x}_0 = f_{\mathrm{AMB}} + m\bar{e}\varpi^2 \sin\varpi T + f_{\mathrm{ALFORD}}. \tag{7}$$

The AMBs are different from rolling bearings as the control algorithm also affects the support characteristics of the AMBs. This paper adopts PID controller which is widely used in industry, and the bearing force under the PID controller can be expressed as:

$$f_{\mathrm{AMB}} = k_x x_0 + k_i[k_P x_0 + k_I \int_0^T S x_0 dS + k_D \dot{x}_0], \tag{8}$$

Table 1: Parameters of magnetic bearing and impeller

Parameter name	Symbol	Value	Unit
Mass	m	14.56	kg
Current stiffness	k_i	338.54	N/A
Displacement stiffness	k_h	2.502e6	N/μm
Tip radius	R_T	29	mm
Root radius	R_B	7.5	mm
Inlet angle	β_1	25	°
Outlet angle	β_2	30	°

where m is the rotor mass, and k_P, k_I, and k_D are the proportional, integral, and differential coefficients.

Formulae (8) and (6) are substituted into eqn (7) and the dimensionless transformation is introduced to facilitate computation.

Taking $\frac{x_0}{c_0} = x, \frac{\bar{e}}{c_0} = e, \bar{\omega}\sqrt{\frac{c_0}{g}} = \omega$, formula (7) is changed into:

$$\begin{aligned}
\dddot{x}(t) = {} & \frac{k_1}{\omega^2}\dot{x}(t) + \frac{k_2}{\omega^2}\dot{x}(t) + \frac{k_3}{\omega^3}x(t)\\
& + \frac{k_4}{\omega}\ddot{x}(t) + e\cos t + \frac{k_5}{\omega^2}\dot{x}(t).
\end{aligned} \tag{9}$$

In formula (9):

$$\begin{aligned}
&k_1 = \frac{k_x c_0}{mg}, k_2 = \frac{k_i k_P c_0}{mg}, k_3 = \frac{k_i k_I c_0}{mg}\sqrt{\frac{c_0}{g}},\\
&k_4 = \frac{k_i k_D}{m}\sqrt{\frac{c_0}{g}}, k_5 = \frac{A_1 c_0}{mg}.
\end{aligned}$$

Transform formula (9) into matrix form:

$$\begin{bmatrix} \dot{x}_1 \\ \dot{x}_2 \\ \dot{x}_3 \end{bmatrix} = \begin{bmatrix} 0 & 1 & 0 \\ 0 & 0 & 1 \\ \frac{k_3}{\omega^3} & \frac{k_1+k_2+k_5}{\omega^2} & \frac{k_4}{\omega} \end{bmatrix} \begin{bmatrix} x_1 \\ x_2 \\ x_3 \end{bmatrix} + \begin{bmatrix} 0 \\ 0 \\ 1 \end{bmatrix} e\cos t. \tag{10}$$

Due to the strong nonlinear characteristics of the system, the Runge−Kutta method is used to solve the dynamics equation of the system and the results are analyzed.

III. SYSTEM CHARACTERISTIC ANALYSIS

In order to explore the influence of Alford force, simulation is carried out. In the simulation, the magnetic bearing rotor system and impeller parameters are shown in the Table 1.

The Poincare map is obtained according to the solution of the motion equation. As shown in Figure 2, without considering the influence of Alford force, the system is characterized by a single point on Poincare map at 100 Hz, and it shows that the system behaves as a typical single period motion. After introducing Alford force, the Poincare map shows a bunch of outward divergent points and the system is in multi-period motion. When the rotating speed is increased to 500 Hz, the Poincare map is similar to that at 100 Hz, but the divergence is stronger than that at 100 Hz, which indicates that the system is in multi-period motion and with a stronger non-linearity. Fast Fourier transform (FFT) analysis at the speed of 500 Hz shows that apart from the main frequency, there is

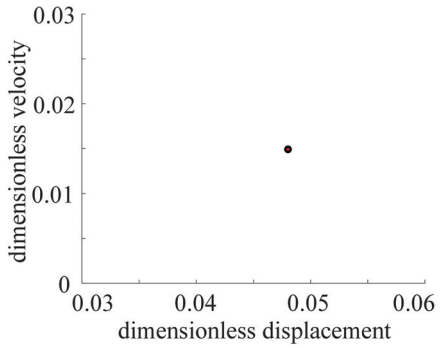

(a) Poincare map without Alford force at 100 Hz.

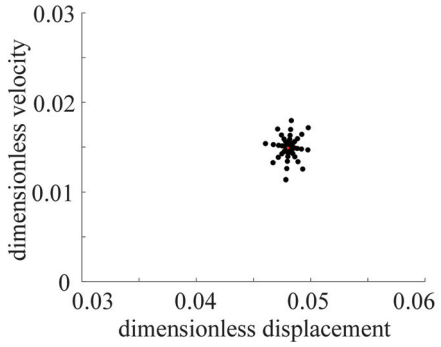

(b) Poincare map considering Alford force at 100 Hz.

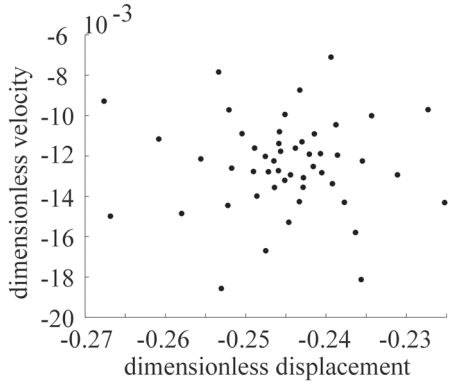

(c) Poincare map considering Alford force at 500 Hz.

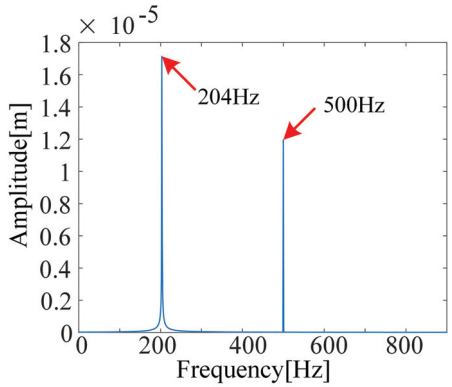

(d) FFT analysis at 500 Hz.

Fig. 2. Dynamics behavior of the system.

still a frequency of 204 Hz which verifies the existence of Alford force.

As mentioned above, the supporting characteristics of the AMBs can be changed by adjusting control parameters. In this paper, with the adoption of the PID controller. k_P and k_D are expressly explored as they have a great influence on the system characteristics. Figure 3 is the Poincare map and phase trajectory diagram of the system when k_D is 0.0015 and 0.015, respectively. The Poincare map appears as a closed ellipse and the phase trajectory is relatively miscellaneous when k_D is 0.0015. At this time, the whole system is in quasi-periodic motion. When k_D is 0.015, the Poincare map and the phase trajectory are single, which means the system is in single periodic motion. The results show that the system runs more stably with the increase of k_D. This is because in the AMBs rotor system, adjusting k_D is equivalent to changing system damping which can effectively improve the stability of system operation.

Figure 4 is the Poincare map as well as the phase trajectory diagram of the system when k_P is 1 and 3, respectively. Compared with k_D, k_P has less influence on the system. Whether k_P is 1 or 3, the Poincare maps of the system are divergent points and the phase trajectories are multiple mixed lines. In this case, the system is in multi-periodic motion. The small influence of k_P is due to the fact that in the AMBs rotor system, adjusting k_P is equivalent to changing the system stiffness.

IV. EXPERIMENTAL SETUP

In order to verify the accuracy of the above analyses, an AMBs rotor system test rig is used to conduct the experiment. The experimental setup is shown in Figure 5.

First, the experiment is conducted without installing the volute. Assuming that the circumference of the impeller is a uniform field without differential pressure, so no influence of Alford force will be considered. As shown in Figure 6, the amplitude response of the rotor at a speed of 100 Hz in this state is obtained. Then through installing the volute to create Alford force, the amplitude response of the rotor in this state is obtained. Comparing that with the amplitude response of the rotor without volute, the results are shown in Figure 7. It shows that the amplitude of the rotor increases by about 2 μm within the range of all running speeds after installing the volute considering the effect of Alford force.

ISO 14839-2 defines the vibration displacement level of a magnetic bearing rotor system under steady conditions [22]. In Figure 8, $x_{\max}$ and $y_{\max}$ are the maximum amplitudes measured by the sensor in the radial direction, and $D_{\max}$ is the maximum radial displacement of the rotor.

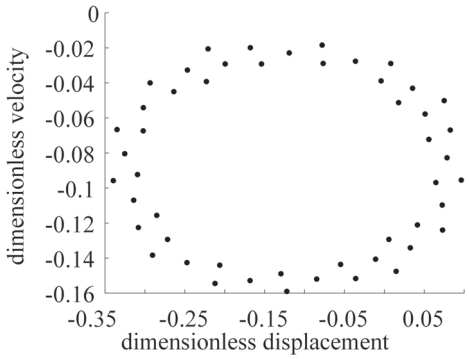

(a) Poincare map with $k_D = 0.0015$.

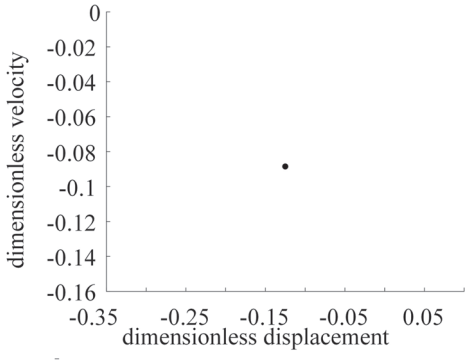

(b) Poincare map with $k_D = 0.015$.

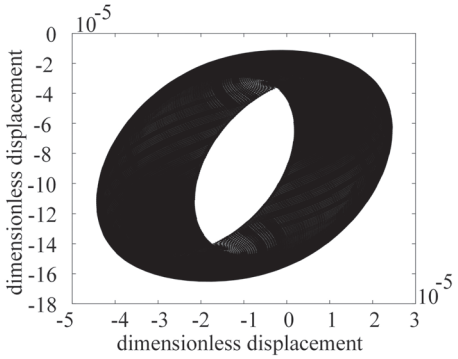

(c) Phase trajectory with $k_D = 0.0015$.

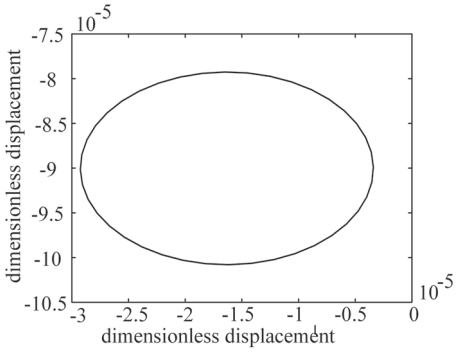

(d) Phase trajectory with $k_D = 0.015$.

Fig. 3. Dynamics behavior of the system under different k_D.

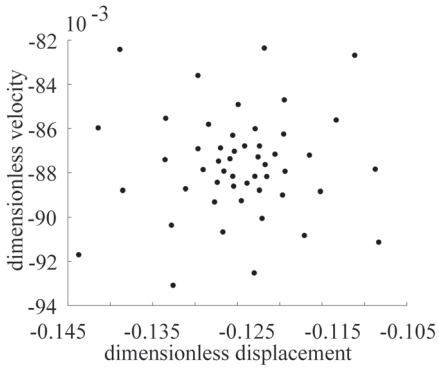

(a) Poincare map with $k_P = 1$.

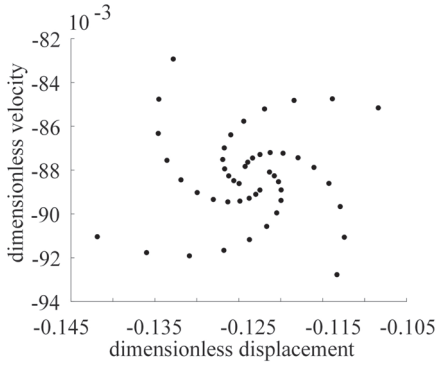

(b) Poincare map with $k_P = 3$.

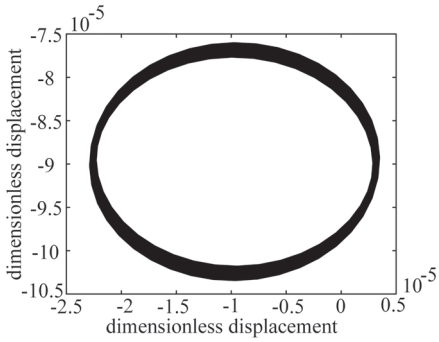

(c) Phase trajectory with $k_P = 1$.

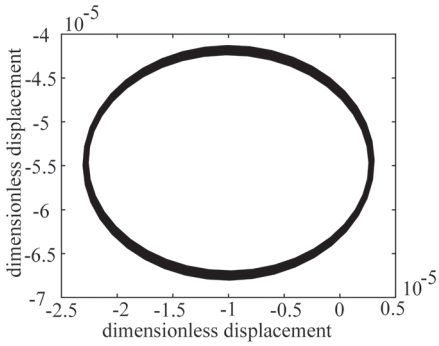

(d) Phase trajectory with $k_P = 3$.

Fig. 4. Dynamics behavior of the system under different k_P.

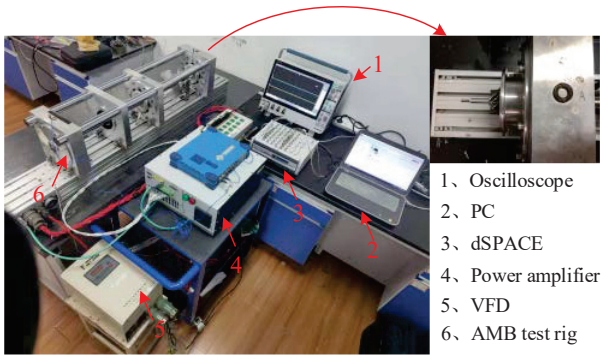

Fig. 5. Experimental setup.

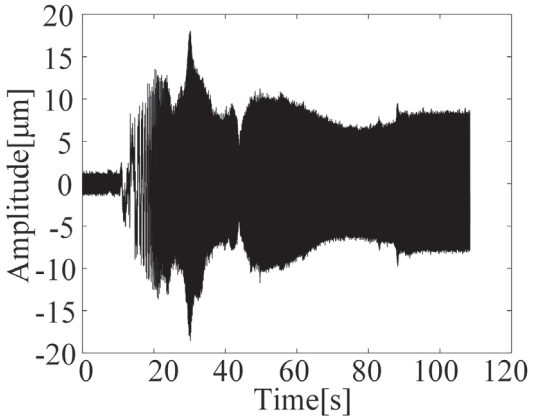

Fig. 6. Rotor response without the Alford force.

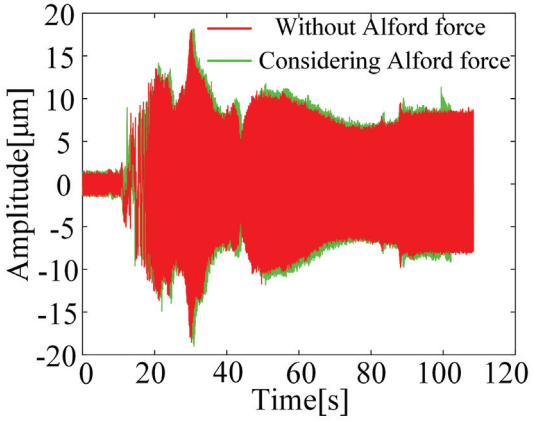

Fig. 7. Comparison of rotor response with and without Alford forces.

So,

$$D_{\max} = \max \left| \sqrt{x^2(t) + y^2(t)} \right|, \tag{11}$$

where $x(t)$, and $y(t)$ is are the rotor position coordinates.

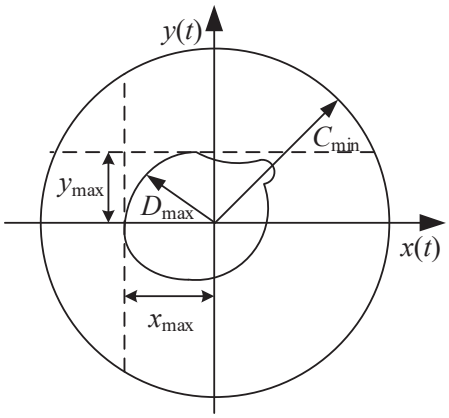

Fig. 8. Rotor orbit of vibration displacement.

Table 2: Recommended criteria of zone limits

Level	$D_{\max}/C_{\min}$
A	$A < 0.3$
B	$0.3 \leq a < 0.4$
C	$0.4 \leq a < 0.5$
D	$0.5 \leq a$

$C_{\min}$ means the gap between protective bearing and the rotor. In this paper, $C_{\min} = 0.125$ mm.

Based on the above testing principles and methods, the vibration displacement level curve of both ends of the rotor are obtained, as shown in Figure 9. With the effect of impeller, the amplitude of terminal A is larger than B.

As shown in Table 2, the ISO 14839-2 standard defines the level of vibration displacement of a rotor in a magnetic levitation system, where $a = D_{\max}/C_{\min}$.

Combined with the recommended level of standards in the table, the amplitude ratio of vibration displacement at both ends is less than 0.3, indicating that the rotor vibration displacement level of the test rig is within

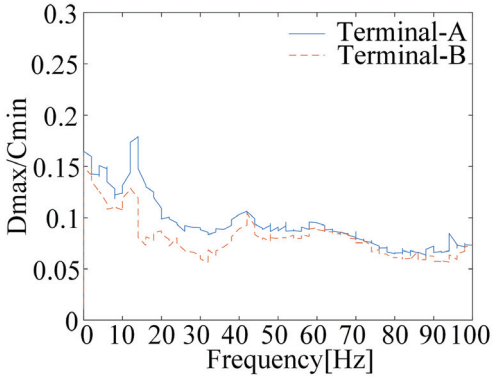

Fig. 9. Rotor vibration level.

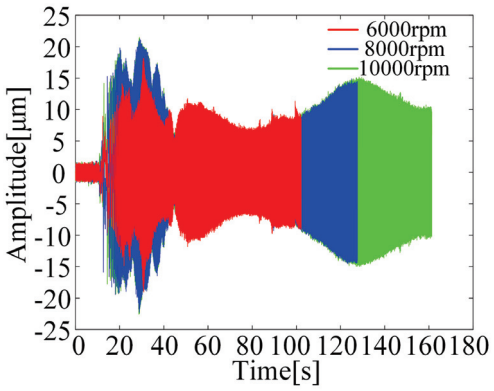

Fig. 10. Rotor response under different rotational speeds.

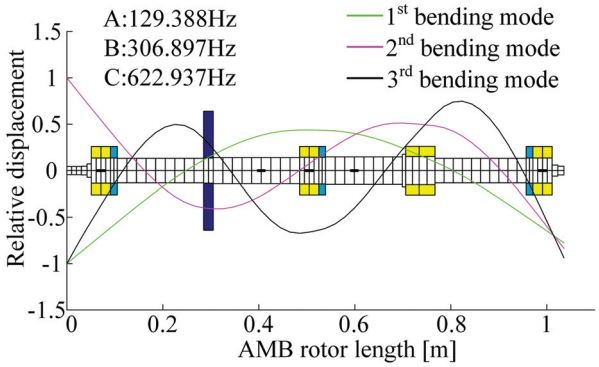

Fig. 11. Rotor modal analysis.

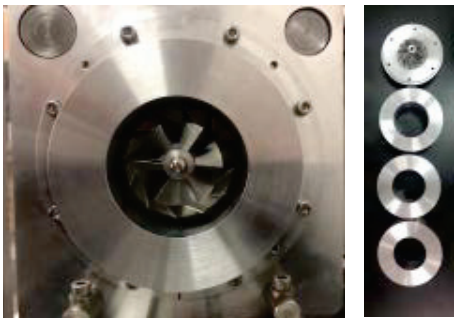

Fig. 12. Sleeve with different clearance.

level A, which provides a guarantee for subsequent research.

Figure 10 shows the amplitude of the rotor considering Alford force at different speeds. It can be seen that the amplitude of the rotor increases from 8.2 μm to 11.9 μm with the increase of the rotating speed from 6000rpm to 10,000 rpm. While at 8000 rpm, the amplitude of the rotor is the largest, reaching 14.7 μm, because 8000 rpm is close to first-order frequency. The modal shape and frequency of the rotor in the free-−free state

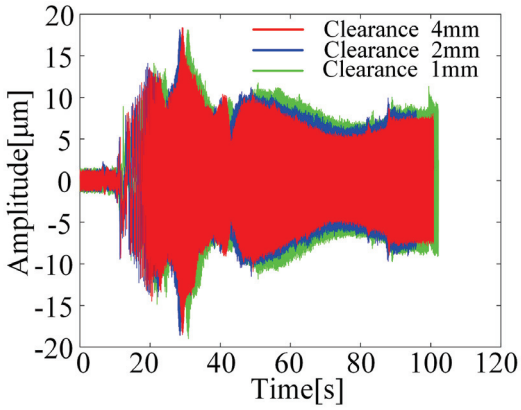

Fig. 13. Rotor response under different clearance.

are obtained by simulation, as shown in Figure 11, and the first-order mode frequency is 130 Hz, which verified the above analysis.

Alford force is caused by the clearance difference. In this paper, sleeves with different inner diameters are machined to produce different Alford forces and the structure is shown in the Figure 12. The response of the rotor with different clearances is obtained and shown in the Figure 13 which reveals that with the increase of the clearance from 1mm to 4 mm, the amplitude of the rotor decreases from 9.6 μm to 8.2 μm. This means that a larger gap produces a smaller Alford force. Due to the large clearance, the flow field between the cylinder and impeller is more uniform and the pressure difference is smaller, thus leading to a smaller Alford force.

V. CONCLUSION

Taking an AMBs rotor system test rig as the research object, this paper not only analyzes the dynamic characteristics of the rotor system under the coupling action of Alford force and magnetic bearing force but also explores the factors affecting the operation of the system. The results reveals that the rotor system shows more complex characteristics when considering Alford force. The specific conclusions are as follows:.

1) Without considering Alford force, the whole system behaves in a typical single period motion. At the same time, the test rig meets the level-A standard without the influence of Alford force, which guarantees the follow-up research. After considering the Alford force, the whole system behaves in a multi-period motion, which indicates that it has strong nonlinear characteristics.
2) It can be concluded that when the control parameters k_P and k_D, the rotational speed, and the clearance between impeller and volute are changed,

k_P has little influence on the rotor operation and k_D of which selection should be paid more attention to when setting the parameters is more obvious. In addition, the coupling effect is more obvious with the increase of speed, ; therefore, when the system operates at high speed, we need to pay more attention. Last but not least, the clearance between impeller and volute also affects the state of the system. With the increase of clearance, the effect is relatively reduced. In further design, the effect can be reduced by increasing the clearance appropriately.

ACKNOWLEDGMENT

This work was supported in part by National Key Laboratory of Science and Technology on Helicopter Transmission (under Grant No. HTL-A-20K03) and in part by the National Nature Science Foundation of China (under Grant No. 52075239).

REFERENCES

[1] H. J. Thomas, "Unstable oscillations of turbine rotors due to steam leakage in the sealing glands and the buckets," *Bullet in Scientifique A.J.M*, vol. 71, pp. 223-236, 1958.

[2] J. S. Alford, "Protecting turbomachinery from self-excited whirl," *ASME Journal of Engineering for Power*, no. 05, pp. 333-344, 1965.

[3] M. Cheng, G. Meng, and B. Y. Wu, "Effect of Alford force and ball bearing on dynamic characteristics of a rotor system," *Journal of Vibration and Shock*, vol. 30, no. 12, pp. 164-168, 2011.

[4] D. Y. Jung and H. A. DeSmidt, "Limit-Cycle analysis of planar Rotor/Autobalancer system influenced by Alford force," *Journal of Vibration & Acoustics*, vol. 138, no. 2, pp. 021018.1-021018.14, 2016.

[5] K. Yada, M. Uchiumi, and K. I. Funazaki, "Thomas/Alford force on a Partial-Admission turbine for the rocket engine turbopump," *Journal of Fluids Engineering*, vol. 141, no. 01, 2018.

[6] W. Yang, H. Yuan, L. Hui, and K. Zhang, "Dynamic analysis of flexible shaft and elastic disk rotor system based on the effect of Alford force," *Shock & Vibration*, no. PT.2, pp. 3545939.1-3545939.13, 2019.

[7] B. Li, L. Zhang, and Y. Y. Cao. "Dynamic characteristic analysis for Rotor-bearing system with Alford force considering blade vibration," *Journal of Ship Mechanics*, vol. 24, no. 1, 2020.

[8] I. Ahmad, J Ikram, M. Yousuf, R. Badar, S. S. H. Bukhari, and J.-S. Ro, "Performance improvement of Multi-rotor axial flux vernier permanent magnet machine by permanent magnet shaping," *IEEE Access*, vol. 9, pp. 143188-143197, 2021.

[9] S. Ali, J Ikram, C. P. Devereux, S. S. H. Bukhari, S. A. Khan, N. Khan, and J.-S. Ro, "Reduction of cogging torque in AFPM machine using Elliptical-Trapezoidal-Shaped permanent magnet," *Applied Computational Electromagnetics Society (ACES) Journal*, vol. 36, no. 8, pp. 1090-1098, 2021.

[10] S. Amin, S. Madanzadeh, S. Khan, S. S. H. Bukhari, F. Akhtar, and J.-S. Ro, "Effect of the magnet shape on the performance of coreless axial flux permanent magnet synchronous generator," *Electrical Engineering*, 2021.

[11] T. S. Ou, C. X. Hu, Y. Zhu, M. Zhang, and L. Zhu, "Intelligent feedforward compensation motion control of maglev planar motor with precise reference modification prediction," *IEEE Transactions on Industrial Electronics*, vol. 68, no. 9, pp. 7768-7777, 2021.

[12] W. R. Wang, G. J. Yang, J. H. Yan, H. Ge, and P. Zhi, "Magnetic levitation planar motor and its adaptive contraction backstepping control for logistics system," *Advances In Mechanical Engineering*, vol. 13, no. 3, 2021.

[13] M. Y. Chen, C. F. Tsai, and L.C. Fu. "A novel design and control to improve positioning precision and robustness for a planar maglev system," *IEEE Transactions on Industrial Electronics*, vol. 66, no. 9, pp. 4860-4869, 2019.

[14] H. Z. Wang, K. Liu, J. B. Wei, and H. Hu, "Analytical modeling of air gap magnetic fields and bearing force of a novel hybrid magnetic thrust bearing," *IEEE Transactions on Magnetics*, vol. 57, no. 10, 2021.

[15] Q. Liu, L. Wang, and Y. Y. Li, "Single-structured hybrid gas-magnetic bearing and its rotor dynamic performance," *Nonlinear Dynamic*, vol. 104, no. 1, pp. 333-348, 2021.

[16] K. K. Nielsen, C. R. H. Bahl, N. A. Dagnaes, I. F. Santos, and R. Bjørk, "A passive permanent magnetic bearing with increased axial lift relative to radial stiffness," *IEEE Transactions on Magnetics*, vol. 57, no. 3, 2021.

[17] G. Schweitzer and E. Maslen, *Magnetic Bearing: Theory, Design, and Application to Rotating Machinery*. Springer, Berlin, Germany, 2012.

[18] X. H. Wang, G. G Yan, Y. G. Hu, and R. Tang, "The influence of Alford force and active magnetic bearing on the dynamic behavior of a rotor system," *Journal of Vibration and Shock*, vol. 39, no. 08, pp. 222-229, 2020.

[19] J. Colding-Jorgensen, "Predicting of rotor dynamic destabilizing forces in axial flow compressors," *ASME Journal of Fluids Engineering*, vol. 114, no. 11, pp. 621-625, 1992.

[20] F. Erich, "Rotor whirl forces induced by the tip clearance effect in axial flow compressors," *ASME*

Journal of Vibration and Acoustics, vol. 115, no. 10, pp. 509-515, 1993.

[21] S. Chai, Y. Zhang, and Q. Qu, "An analysis on the air exciting-vibration force of steam turbine," *Engineering Science*, vol. 3, no. 04, pp. 68-72, 2001.

[22] ISO, ISO14839-2 Mechanical vibration—Vibration of rotating machinery equipped with active magnetic bearings—Part 2: Evaluation of vibration, British: Subcommittee GME/21/5, 2004.

Siyuan Zhang was born in Jiangsu, China, in 1992. He received the M.S. degree from Shihezi University. He is currently working toward the Ph.D. degree in Mechanical mechanical design and theory in with the Nanjing University of Aeronautics and Astronautics (NUAA).

His research interests include active magnetic bearings and vibration control.

Jin Zhou was born in Jiangsu, China, in 1972. She received her the Ph.D. degree in mechanical engineering from the China University of Mining and Technology (CUMT), China, in 2001.

From 2012 to 2013, she was a Visiting Scholar in with the Rotating Machinery and Control Laboratory (ROMAC) of the University of Virginia. She was the member of Program Committee of the *14th International Symposium on Magnetic Bearings* (2014) and the Program Chair of the *16th International Symposium on Magnetic Bearings* (2018). She was an elected member of International Advisory Committee for ISMB in 2018. Her research interests include magnetic bearings and vibration control.

Xiaoming Han was born in Shandong, China, in 1997. He received histhe B.S. degree in 2019 from Qingdao University in 2019. He is currently working toward the M.S. degree in with the Nanjing University of Aeronautics and Astronautics (NUAA).

His research focuses on magnetic bearings.

Yanchao Ma was born in Shandong, China, in 1996. He received his the B.S. degree in 2019 from the Civil Aviation University of China (CAUC) in 2019. He is currently working toward the M.S. degree in with the Nanjing University of Aeronautics and Astronautics (NUAA).

His research focuses on magnetic bearings.